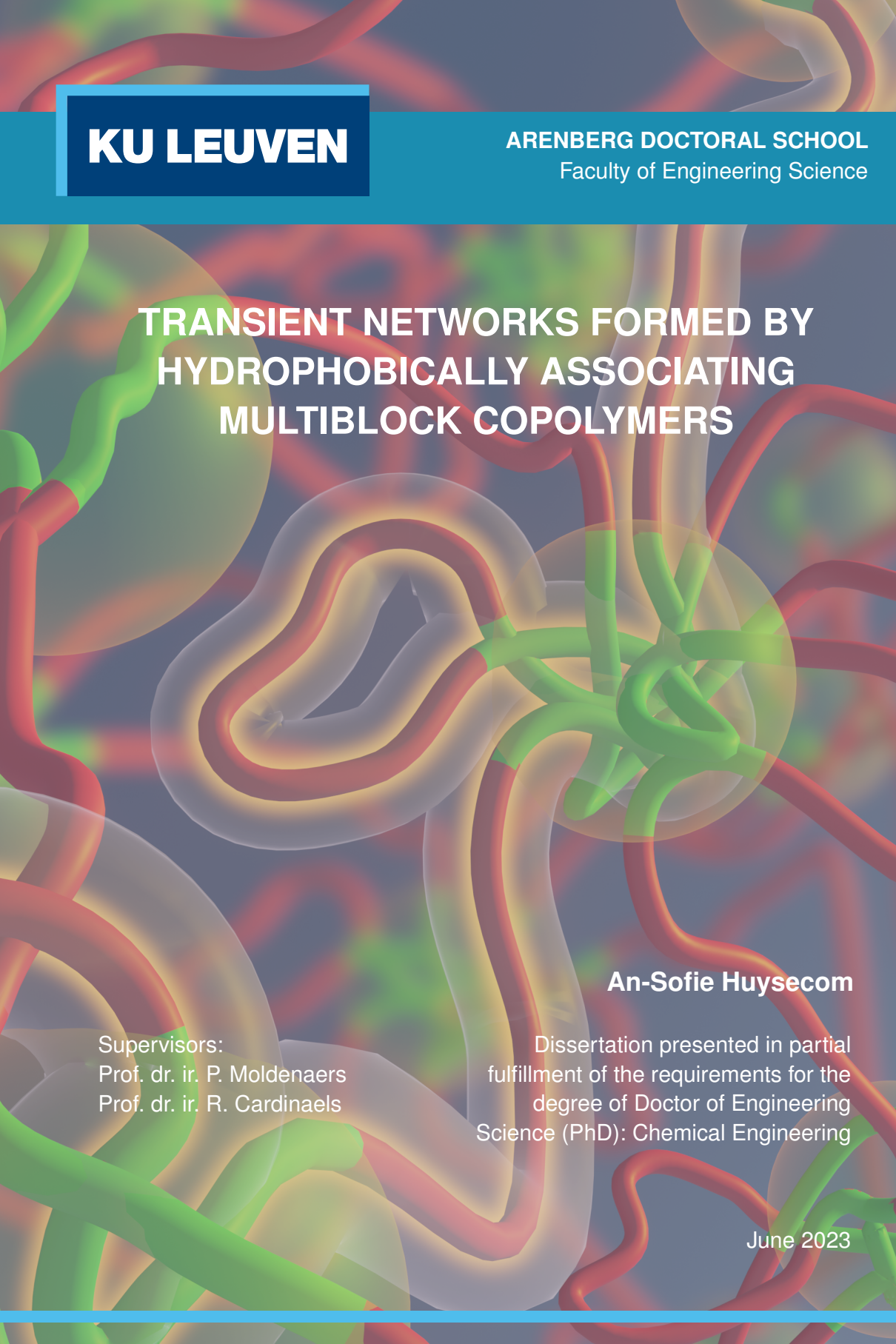

KU LEUVEN

ARENBERG DOCTORAL SCHOOL
Faculty of Engineering Science

TRANSIENT NETWORKS FORMED BY HYDROPHOBICALLY ASSOCIATING MULTIBLOCK COPOLYMERS

An-Sofie Huysecom

Supervisors:
Prof. dr. ir. P. Moldenaers
Prof. dr. ir. R. Cardinaels

Dissertation presented in partial fulfillment of the requirements for the degree of Doctor of Engineering Science (PhD): Chemical Engineering

June 2023

Transient networks formed by hydrophobically associating multiblock copolymers

An-Sofie HUYSECOM

Examination committee:
Prof. dr. ir. Y. Willems, chair
Prof. dr. ir. P. Moldenaers, supervisor
Prof. dr. ir. R. Cardinaels, supervisor
Prof. dr. ir. E. Koos
Prof. dr. ir. S. Kuhn
Prof. dr. ir. W. Thielemans
Prof. dr. ir. E. Van Ruymbeke
(UC Louvain, Belgium)
Prof. dr. ir. H. Heuts
(TU Eindhoven, The Netherlands)

Dissertation presented in partial fulfillment of the requirements for the degree of Doctor of Engineering Science (PhD): Chemical Engineering

June 2023

© 2023 KU Leuven – Faculty of Engineering Science
Uitgegeven in eigen beheer, An-Sofie Huysecom, Celestijnenlaan 200J box 2424, B-3001 Leuven (Belgium)

Alle rechten voorbehouden. Niets uit deze uitgave mag worden vermenigvuldigd en/of openbaar gemaakt worden door middel van druk, fotokopie, microfilm, elektronisch of op welke andere wijze ook zonder voorafgaande schriftelijke toestemming van de uitgever.

All rights reserved. No part of the publication may be reproduced in any form by print, photoprint, microfilm, electronic or any other means without written permission from the publisher.

Preface

The end of a five-year PhD journey, the end of an era... Writing this dissertation is the ultimate step in completing this chapter of my life and has prompted me to acknowledge the many protagonists in my PhD story.

First of all, I would like to warmly thank my supervisors *Paula Moldenaers* and *Ruth Cardinaels* for giving me the opportunity to embark on this challenging PhD journey, which contributed to my personal development in many more ways than just scientific. Thank you for giving me the freedom to pursue my own lines of research, for continuously supporting me along the way and for entrusting me with various (didactical) responsibilities. I will forever cherish the numerous opportunities I was given to attend international conferences and summer schools, to meet scientists from all over the world and to engage in research collaborations both in Belgium and abroad. This PhD dissertation would not be what it is today if it wasn't for their critical eye and thorough research approach. *Ruth*, in addition to your scientific input, I specifically want to thank you for the other, non-scientific conversations we had. It often made me put things into perspective, kept me motivated and rekindled my enthusiasm. I would also like to express my gratitude to the other members of the examination committee, *Erin Koos, Simon Kuhn, Wim Thielemans, Evelyne Van Ruymbeke* and *Hans Heuts*, who carefully read my PhD thesis and provided constructive feedback to increase the quality of this work. I also highly appreciated the other, useful discussions I had with *Christ Glorieux* and *Jan Thoen* (Department of Physics, KU Leuven), *Charles-André Fustin* (UCLouvain) and *Kay Saalwächter* (Martin-Luther-Universität), whose insights have certainly contributed to my research output. Finally, I wish to thank the Research Foundation Flanders (FWO) for their financial support.

However, the setting of my PhD story has probably been the single most important contributing factor to its successful completion. It was really a pleasure working in the open-minded atmosphere at SMaRT, surrounded by highly motivated and helpful people. Special thanks to *Anja, Nico* and *Carlo*, for taking such good care of the SMaRT infrastructure and for creating a safe and smoothly functioning working environment. Also a word of appreciation to *Marie-Claude* and *Ann* for their administrative support.

Finally, a big thank you to all professors at SMaRT for providing us with countless opportunities to celebrate outside of work, such as rheoschool and conference dinners, Christmas and/or Easter parties, lab weekends, BBQs and departmental parties. The additional birthday parties, games nights and trips abroad that were regularly organized by the PhD students, just prove that we were and continue to be one warm SMaRT family.

Being part of this family for more than five years, I have met so many wonderful people without whom my PhD journey would not have been the same. *Dries*, you are so much more than a former colleague to me. Sharing this entire experience with you was a true privilege. We went through the ups and downs of a PhD journey together and found these universal feelings of great dispair, extreme happiness, towering frustrations and the occasional existential crisis along our way. Fortunately, there was always one address for a good laugh: office 02.516 window seat (or zaal Pavo). *Tess, Charlotte* and *Margot*, I really enjoyed keeping Flemish alive with you at SMaRT. Even though a PhD and everything that comes along with it can sometimes be 'aartsmoeilijk', you girls managed to make it feel much lighter for me. Your positive attitude and slightly more youthful enthusiasm were often contagious and just what I needed. *Roberta* and *Bram*, you both were the best mentors during my master thesis and the beginning of my PhD, and kept supporting me throughout the years (albeit sometimes from a distance). *Roby*, a special thanks for the endless conversations we had in the beginning years, it made the long days more bearable.

Over the years, I had the pleasure of being surrounded by the best office mates. It was quite a transition though, from *Mathieu, Jasper, Helene* and *Moritz* in the 'spheer' office with dirty jokes, a song-of-the-day and goodbye parties with hats and confetti, to *Charlotte, Souhaila* and *Alina* in an 'all girls' office with a lot of girls talk and chocolate - thank you *Souhaila* for that extra sugar now and then. However, a nice and open atmosphere was always ensured in which lots of laughter, frustrations and sometimes tears were shared. Finally, also many many thanks to all other present and former members of SMaRT (and MCS), who all contributed to the great dynamics: *Stijn, Jessica, Stelios, Jens, Iurii, Kenneth, Luca, Lingyue, Yanshen, Alexis, Joel, Xiangmeng, Tobias, Vince, Jarno, Jelle, Maxwell, Yannick, Sebastian, Steffen, Irene, Robin, Jan, Susanna, Karel, Michael, Greet, Maya, Akankshya, Avanish, Charlotte, Kristien, Jeroen, Maarten, Mouna* and the short-stay visitors. I also had the opportunity to perform parts of my research in other labs, in which I always felt very welcomed. Thanks to *Rowanne* for her introduction to chemical synthesis at UCLouvain and to *Gertrude* and *Samuel* for their help with ITC and SAXS experiments at Kulak in Kortrijk. I also want to thank *Romy, Manuel, Kjell* and *Toon*, the master thesis students that I had under my wings during my PhD, for their interest in the research (often very far from my own) and their hard-working attitudes.

All education starts with your parents, and I could not be happier with mine. Everything I have achieved, experienced and obtained so far, I owe to them. *Moeki*, you know

you are my biggest example, my older best friend and, as appeared to be necessary quite often during my PhD, my personal therapist. *Papieke*, even though you might be a little disappointed that I do not have my own startup company yet, I know you are immensely proud and will continue to support me in all of my endeavors. Infinite thanks to both of you for your endless support, great advice and unconditional love. I also want to thank my brother and the rest of my family and friends for not asking too often about my PhD progress, but instead providing great distractions from science in the form of dinner parties, weekend trips and shopping sprees. *Omake*, ik vind het jammer dat je dit niet meer kan meemaken, maar ik weet zeker dat je super trots zou zijn en zou genieten van dat glaasje cava of twee op de receptie achteraf (zoals die andere keer een aantal jaar geleden). And last but not least, a huge thanks should go out to my boyfriend *Ben*. We first met 5 days before I started my PhD journey and here we are, more than 5 years, a company, a house, 2 years of a global pandemic, a few crises and a PhD later, standing stronger than ever. You are my biggest support, my greatest distraction, my scientific (computer) helpline and so much more. You always keep me going in a healthy - thanks to your amazing cooking skills and your gentle nudge to start biking - and balanced way - thanks to our holiday trips away from science. I may not always show it, but all of that truly means the world to me. Having survived a PhD together, I am pretty sure we can basically handle anything and I can't wait to see us bring that to reality. Onto next, even bigger adventures together!

I have also realized over these five years that the preface is probably the most widely read part of a PhD dissertation. Therefore, I decided to include some nice pictures reminding me (and maybe you) of the many fun, scientific and not-so-scientific, opportunities these five years have given me, and for which I will be forever grateful.

— An-Sofie Huysecom
June 26th 2023














PARADIS




2019 ECIS
Leuven 8-13 September


06105379




2019 ECIS
Leuven 8-13 September


33rd Conference of
The European Colloid
and Interface Society











Abstract

Supramolecular chemistry has opened up an impressive toolbox for the development of novel polymeric systems. Whether exploited to create self-assembled architectures in dilute solutions, or to serve as non-permanent crosslinks in more concentrated polymer networks or hydrogels, supramolecular interactions induce superior, often stimuli-responsive properties. For biomedical applications such as drug delivery and tissue engineering, the thermoreversible hydrophobic association of poly(ethylene oxide) (PEO) and poly(propylene oxide) (PPO) block copolymers in aqueous solutions has emerged as a promising interaction type. The microphase separation of such amphiphilic molecules does not only govern the broadly tunable microstructure and associated rheological properties, but also enables efficient encapsulation and controlled release of therapeutic agents within the self-assembled hydrophobic cores. The current literature extensively reports on the fundamentals and applications of PEO-PPO-PEO triblock copolymers (commercially available as Pluronics®), while other copolymer architectures such as multiblock copolymers are poorly discussed. Therefore, this dissertation focuses on gaining a fundamental understanding of the behavior of alternating PEO-PPO multiblock copolymers in increasingly complex aqueous media, thus demonstrating their potential as attractive alternatives to triblock copolymers.

In the first part of this dissertation, their behavior in simple aqueous solutions is elucidated. Different characterization techniques including rheology, scanning and titration calorimetry and light transmittance are used to determine the phase transitions and associated energetic contributions of two types of alternating PEO-PPO multiblock copolymers (commercially available as ExpertGel®) with different hydrophobicity. In addition, the morphological evolution upon micellization is examined using light and X-ray scattering. The combination of these techniques allows the identification of the relevant temperature and concentration regimes in which polymer solutions, micellar solutions, micellar networks or macroscopic phase separation are obtained. Not only the importance of hydrophobicity in dictating the phase behavior, but also that of the copolymer architecture, i.e. the configuration and amount of the PEO and PPO blocks, is highlighted by comparing their behavior with that of triblock copolymers and longer

multiblock copolymers with similar hydrophobicity. The subsequent chapters further explore the micellar networks formed at higher concentrations and temperatures to establish the relationships between their microstructure and rheological properties. Unlike Pluronic® triblock copolymers, multiblock copolymers contain intermediate PEO blocks that can act as elastic bridges connecting two micellar PPO cores. The as such obtained polymer networks have the rheological characteristics of a transient network. Due to the presence of multifunctional micellar crosslink interactions between multisticker polymers, they are of particular interest to generate fundamental insights in transient networks of multisticker polymers. A mechano-statistical transient network model originally developed for telechelic triblock copolymers having hydrophobic end groups, is therefore extended and generalized to alternating multiblock copolymers bearing multiple hydrophobic blocks along their polymer backbone. Hereto, a combinatorics approach is used that takes into account the configurational complexity of multisticker polymers. The combination of the theoretical model with experimental input about the spatial distribution of micellar nodes as inferred from small-angle X-ray scattering, allows the microscopic network topology to be translated into macroscopic elasticity. The good agreement between model predictions and rheological elasticity reveals a concentration-dependent evolution from loop- and superstructure-dominated networks with limited elasticity to bridge-dominated networks with high node functionalities and increased elasticity. The rheological fingerprints of the micellar networks exhibit broad, sticky Rouse-like relaxation and reflect the need for multiple sticker dissociation events to allow complete chain relaxation. The scaling of the characteristic relaxation times with concentration questions the assumptions made in conventional transient network relaxation frameworks and mandates a novel microscopic view thereon. A hybrid model combining concepts from other transient network models with the insights from our mechano-statistical network model, thereby not neglecting the intrinsic chain dynamics, can explain the peculiar relaxation behavior.

The second part of this dissertation broadens the versatility and expands the complexity by combining PEO-PPO multiblock copolymer networks with a second supramolecular network in a thermoresponsive double network. The addition of a labile metal-ligand network of 4-arm PEO-star polymers crosslinked by telechelic zinc(II)-terpyridine complexes induces two distinct modes of relaxation, on which temperature has a contrasting effect and which can therefore be linked to the single network contributions. As a result of the topological constraints imposed by the presence of a second network and the possible formation of internetwork entanglements, the double network has a synergistic elasticity with significantly delayed relaxation dynamics as compared to the single networks. Unfortunately, the rheological reproducibility of the double networks is poor, mainly due to the microstructural complexity of the network formed by multiblock copolymers. In summary, this work demonstrates the broad tunability and potential of hydrophobically associating multiblock copolymers by highlighting the relationships between the building block architecture, the microstructure and the final rheological properties.

Beknopte samenvatting

Supramoleculaire chemie heeft een indrukwekkende toolbox geopend voor de ontwikkeling van nieuwe polymere systemen. Of ze nu worden gebruikt om zelfgeassembleerde architecturen te creëren in verdunde oplossingen, of om te dienen als niet-permanente crosslinks in meer geconcentreerde polymeernetwerken of hydrogels, supramoleculaire interacties zorgen voor superieure, vaak op stimuli reagerende eigenschappen. Voor biomedische toepassingen zoals de toediening van geneesmiddelen en weefselmanipulatie, is de thermoreversibele hydrofobe associatie van poly(ethyleenoxide) (PEO) en poly(propyleenoxide) (PPO) blokcopolymeren in waterige oplossingen naar voren gekomen als een veelbelovend interactietype. De microfasenscheiding van dergelijke amfifiele moleculen bepaalt niet alleen de breed afstembare microstructuur en de bijbehorende reologische eigenschappen, maar maakt het ook mogelijk therapeutische middelen efficiënt in te kapselen in de zelfgeassembleerde hydrofobe kern. De huidige literatuur gaat uitgebreid in op de fundamenten en toepassingen van PEO-PPO-PEO triblokcopolymeren (commercieel verkrijgbaar als Pluronics®), terwijl andere copolymeerarchitecturen, zoals multiblokcopolymeren beperkt worden behandeld. Daarom richt dit proefschrift zich op het verkrijgen van een fundamenteel begrip van het gedrag van alternerende PEO-PPO multiblokcopolymeren in steeds complexere waterige media, om zo hun potentieel aan te tonen als aantrekkelijke alternatieven voor triblokcopolymeren.

In het eerste deel van dit proefschrift wordt hun gedrag in eenvoudige waterige oplossingen opgehelderd. Verschillende experimentele karakterisatiestechnieken, waaronder reologie, scan- en titratiecalorimetrie en lichttransmissie, worden gebruikt om de faseovergangen en bijbehorende energetische bijdragen van twee soorten alternerende PEO-PPO multiblokcopolymeren (commercieel verkrijgbaar als ExpertGel®) met verschillende hydrofobiciteit te bepalen. Daarnaast wordt ook de morfologische evolutie tijdens micelvorming onderzocht met behulp van licht- en röntgenverstrooiing. De combinatie van deze technieken maakt het mogelijk de relevante temperatuur- en concentratieregimes te identificeren waarin polymeeroplossingen, micellaire oplossingen, micellaire netwerken of macroscopische fasescheiding worden verkregen. Niet alleen het belang van de hydrofobiciteit

bij het dicteren van het fasegedrag, maar ook dat van de copolymeerarchitectuur, d.w.z. de configuratie en hoeveelheid van de PEO- en PPO-blokken, wordt belicht door hun gedrag te vergelijken met dat van triblokcopolymeren en langere multiblokcopolymeren van gelijkaardige hydrofobiciteit. In de daaropvolgende hoofdstukken worden de micellaire netwerken die ontstaan bij hogere concentraties en temperaturen nader onderzocht om de relaties tussen hun microstructuur en de resulterende reologische eigenschappen te bepalen. In tegenstelling tot Pluronic® triblok copolymeren bevatten multiblokcopolymeren tussenliggende PEO-blokken die kunnen fungeren als elastische bruggen tussen twee micellaire PPO kernen. De als zodanig verkregen polymeernetwerken hebben de reologische kenmerken van een transiënt netwerk, en zijn van bijzonder belang voor fundamentele inzichten door de aanwezigheid van multifunctionele micellaire crosslink-interacties tussen multisticker polymeren. Een mechanisch-statistisch transiënt netwerkmodel, oorspronkelijk ontwikkeld voor telechelische triblock copolymeren met hydrofobe eindgroepen, wordt daarom uitgebreid en veralgemeend tot alternerende multiblock copolymeren met meerdere hydrofobe blokken in hun polymeerketen, door gebruik te maken van een combinatorische benadering die rekening houdt met de configurationele complexiteit van dergelijke multisticker polymeren. De combinatie van het theoretische model met experimentele input over de ruimtelijke verdeling van de micellaire knooppunten zoals afgeleid uit kleine-hoek röntgenverstrooiing, maakt het mogelijk de microscopische netwerktopologie te vertalen naar macroscopische elasticiteit. De goede overeenstemming tussen modelvoorspellingen en reologische elasticiteit laat een concentratie-afhankelijke evolutie zien van door lussen en superstructuren gedomineerde netwerken met beperkte elasticiteit naar door bruggen gedomineerde netwerken met hoge knooppuntfunctionaliteit en verhoogde elasticiteit. De reologische vingerafdrukken van de micellaire netwerken vertonen een brede, kleverige Rouse-achtige relaxatie en weerspiegelen de nood aan meerdere stickerdissociaties om volledige ketenrelaxatie mogelijk te maken. De schaling van de karakteristieke relaxatietijden met de concentratie stelt de aannames in de conventionele kaders voor het verklaren van de relaxatie(s) in transiënte netwerken ter discussie en vereist een nieuwe microscopische kijk hierop. Een hybride model dat concepten van andere transiënte netwerkmodellen combineert met de inzichten van ons mechanisch-statistisch netwerkmodel, waarbij de intrinsieke ketendynamiek niet wordt verwaarloosd, kan het bijzondere relaxatiegedrag verklaren.

Het tweede deel van dit proefschrift verbreedt de veelzijdigheid en breidt de complexiteit verder uit door PEO-PPO multiblokcopolymeernetwerken te combineren met een tweede supramoleculair netwerk in een thermoresponsief dubbel netwerk. De toevoeging van een labiel metaal-ligandnetwerk van 4-armige PEO-ster polymeren verknoopt door telechelische zink(II)-terpyridinecomplexen induceert twee verschillende relaxatiemodi, waarop temperatuur een contrasterend effect heeft en die daarom kunnen worden gekoppeld aan de afzonderlijke netwerkbijdragen. Als gevolg van de topologische beperkingen die worden opgelegd door de aanwezigheid van een

tweede netwerk en de mogelijke vorming van verstrengelingen tussen de netwerken, heeft het dubbele netwerk een synergetische elasticiteit met aanzienlijk vertraagde relaxatiedynamiek in vergelijking met de enkelvoudige netwerken. Helaas is de reologische reproduceerbaarheid van de dubbele netwerken slecht, voornamelijk door de microstructurele complexiteit van het netwerk gevormd door multiblokcopolymeren. Samenvattend demonstreert dit werk de brede afstembaarheid en het potentieel van hydrofoob associërende multiblokcopolymeren door de relaties tussen de bouwsteenarchitectuur, de microstructuur en de uiteindelijke reologische eigenschappen te belichten.

List of Abbreviations and Symbols

Abbreviations

Symbol	Definition
ASC	Adiabatic scanning calorimetry
CMC	Critical micelle concentration
CMT	Critical micelle temperature
DCM	Dichloromethane
DCN	Dual-crosslink network
DLS	Dynamic light scattering
DMSO	Dimethyl sulfoxide
DN	Double network
DSC	Differential scanning calorimetry
DWC	Double wall Couette
EG	ExpertGel
EO	Ethylene oxide
FT-IR	Fourier-transform infrared
GPC	Gel permeation chromatography
HC	Hydrophobic clustering
HEUR	Hydrophobically modified urethane-ethoxylate
ICP-OES	Inductively coupled plasma-optical emission spectroscopy
IPN	Interpenetrating polymer network
ITC	Isothermal titration calorimetry
KD	Krieger-Dougherty
LLC	Lyotropic liquid crystal
LCST	Lower critical solution temperature
LT	Light transmittance

ML	Metal-ligand
NMR	Nuclear magnetic resonance
PAA	Poly(acrylic acid)
PAM/PAAm	Poly(acryl amide)
PAMPS	Poly(2-acrylamido-2-methylpropanesulfonic acid)
PCL	Poly(caprolactone)
PEO/PEG	Poly(ethylene oxide) or poly(ethylene glycol)
PP	Plate-plate
PPO/PPG	Poly(propylene oxide) or poly(propylene glycol)
PO	Propylene oxide
RENT	Real elastic network theory
SAOS	Small amplitude oscillatory shear
SANS	Small angle neutron scattering
SAXS	Small angle X-ray scattering
SLD	Scattering length density
SLS	Static light scattering
SMDI	Saturated methylene diphenyl diisocyanate
SS	Stainless steel
THF	Tetrahydrofuran
tpy	Terpyridine
UV-VIS	Ultraviolet-visible light

Roman symbols

Symbol	Definition	SI unit
A	Pre-exponential factor	[s]
a	Number of hydrophobic blocks	[-]
A_2	Second virial coefficient	[molL/g^2]
a_E	Length between entanglements	[m]
b	Kuhn length	[m]
B	Energy barrier for bridge exchange	[J]
c	Mass concentration	[g/L]
c^*	Overlap concentration	[g/L]
c^{**}	Transition concentration from semi-dilute to concentrated	[g/L]
C_∞	Flory's characteristic ratio	[-]
c_e	Entanglement concentration	[g/L]
c_p	Specific heat capacity	[J/gK]
c_T	Number concentration of telechelic chains	[1/m^3]
$c_{network}$	Critical network concentration	[g/L]

c_{syr}	Concentration in syringe	[g/L]
c_{uni}	Unimer concentration	[g/L]
$Đ$	Dispersity	[-]
D	Diameter	[m]
D	Diffusion coefficient	[m/s^2]
d	Distance	[m]
$E_{a,diss}$	Activation energy for sticker dissociation	[J/mol]
$E_{a,flow}$	Activation energy for flow	[J/mol]
$E_{a,relax}$	Activation energy for relaxation	[J/mol]
f	Crosslinking functionality	[-]
f_{EO}	Weight fraction of EO monomers relative to EO + PO	[-]
F_1	Bridge probability	[-]
F_2	Loop probability	[-]
F_b	Energy barrier for micelle debridging	[J]
$g^{(2)}(\tau)-1$	Normalized intensity autocorrelation function	[-]
$g(r)$	Radial distribution function	[-]
g_T	Number of monomers in thermal blob	[-]
G	Gibbs free energy	[J]
G	Shear modulus	[Pa]
G_0 or G_p	Plateau modulus	[Pa]
G'	Elastic or storage modulus	[Pa]
G''	Viscous or loss modulus	[Pa]
h	Gallery spacing	[m]
H	Enthalpy	[J]
H_b	Bob height	[m]
$H(\tau)$	Relaxation time spectrum	[Pa]
i	Number of bridges in multiblock configuration	[-]
I_{bckg}	Background scattering intensity	[cm^{-1}]
I_0	Intensity scaling factor	[-]
$I(q)$	Scattering intensity	[cm^{-1}]
K	Contrast factor	[-]
K_1	Equilibrium constant ML mono-complex	[-]
K_2	Equilibrium constant ML bis-complex	[-]
l	Bond length	[m]
m	Mass	[kg]
M_0	Monomer molecular weight	[Da]
M_E	Molecular weight between entanglements	[Da]
M_S	Molecular weight between stickers	[Da]
M_w	Molecular weight	[Da]

$\overline{M}_n$	Number average molecular weight	[Da]
$\overline{M}_w$	Weight average molecular weight	[Da]
n	Refractive index	[-]
n	Number of monomers	[-]
n	Number density of chains	[1/m^3]
n_m	Number of micelles in close proximity	[-]
N	Number of (Kuhn) segments	[-]
N_a	Average amount of associating blocks of a chain in a node	[-]
N_{agg}	Aggregation number	[-]
N_b	Average amount of bridges of a chain in a node	[-]
N_c	Average amount of chains in a node	[-]
N_d	Average amount of bridges per chain	[-]
P	Power	[W]
$P(\Psi)$	Node distribution function	[-]
$P(q)$	Form factor	[cm^{-1}]
q	Scattering vector	[m^{-1}]
r	Radius or end-to-end distance	[m]
r_c	Core radius	[m]
r_{span}	Span length	[m]
R_g	Radius of gyration	[m]
R_H	Hydrodynamic radius	[m]
R_{HS}	Hard sphere radius	[m]
$R(q)$	Excess Rayleigh ratio	[-]
S	Entropy	[J/K]
$S(q)$	Structure factor	[-]
t	Time	[s]
T	Temperature	[°C or K]
T_{gel}	Gelation temperature	[°C or K]
U	Energy barrier for micelle deformation	[J]
v	Solvent quality	[-]
x	Mol fraction	[-]
z	Excluded volume interaction parameter	[-]

Greek symbols

Symbol	Definition	SI unit
α	Correction factor	[-]
β	Broadness	[-]
β_S	Sticker dissociation rate	[1/s]

$\beta_{S,0}$	Thermal vibration frequency	[1/s]
γ	Strain	[-]
$\dot{\gamma}$	Shear rate	[1/s]
Γ	Decay rate	[1/s]
Δ	Difference	[-]
$[\eta]$	Intrinsic viscosity	[L/g]
η	Viscosity	[Pa s]
η^*	Complex viscosity	[Pa s]
η'	Dynamic viscosity	[Pa s]
η''	Elastic viscosity	[Pa s]
η_0	Zero-shear viscosity	[Pa s]
η_{rel}	Relative viscosity	[-]
η_{sp}	Specific viscosity	[-]
θ	Angle	[° or rad]
λ	Wavelength	[m]
ν	Number density of elastically active chains	[1/m^3]
ρ	Scattering length density	[m^{-2}]
ϕ	Volume fraction	[-]
Ψ	Node functionality	[-]
$\langle\Psi\rangle$	Average node functionality	[-]
χ	Flory interaction parameter	[-]
τ	Relaxation time	[s]
τ_0	Time constant	[s]
τ_1	Fast relaxation time	[s]
τ_2	Slow relaxation time	[s]
τ_C	Core dissociation time	[s]
τ_h	Micellar hopping time	[s]
τ_N	Network relaxation time	[s]
τ_S	Sticker dissociation time	[s]
τ_{break}	Chain dissociation time	[s]
τ_{chain}	Chain relaxation time	[s]
ω	Angular frequency	[rad/s]

Subscripts

Subscript	Definition
crit	Critical
max	Maximum
mic	Micellar
min	Minimum
sol	Solvent

Constants

Symbol	Definition	value
k_b	Boltzmann constant	$1.3806 \cdot 10^{-23}$ $\mathrm{kgm^2s^{-2}K^{-1}}$
N_{Av}	Avogadro's number	$6.022 \cdot 10^{23}$ $\mathrm{mol^{-1}}$
R	Universal gas constant	8.314 $\mathrm{JK^{-1}mol^{-1}}$

Contents

Abstract ix

Beknopte samenvatting xi

List of Abbreviations and Symbols xv

Contents xxi

1 Introduction 1

1.1 Context and motivation 1

1.2 Aims and outline 3

2 State of the art 5

2.1 Supramolecular self-assembly 5

2.1.1 Hydrophobic association 7

2.1.2 Metal-ligand complexation 14

2.2 Supramolecular polymer networks 16

2.2.1 Networks formed by hydrophobic association 17

2.2.2 Networks formed by metal-ligand complexation 25

2.3 Theoretical frameworks for transient network rheology 30

2.3.1 Telechelic stickers 32

2.3.2 Stickers along the chain 37
2.4 Supramolecular double networks 41
2.4.1 Based on hydrophobic association 43
2.4.2 Based on metal-ligand complexation 44

3 Materials and methods 47
3.1 Materials 47
3.1.1 Commercial PEO-PPO multiblock copolymers 47
3.1.2 Terpyridine-functionalized 4-arm PEO stars 57
3.1.3 Network preparation 61
3.2 Characterization methods 62
3.2.1 Rheometry 62
3.2.2 Differential scanning calorimetry 66
3.2.3 Adiabatic scanning calorimetry 67
3.2.4 Isothermal titration calorimetry 68
3.2.5 Light transmittance 68
3.2.6 Light scattering 69
3.2.7 Small-angle X-ray scattering 70
3.2.8 Data analysis 72

I SINGLE NETWORKS by hydrophobic association 73

4 Mapping their phase behavior by a multitude of techniques 75
4.1 Phase boundaries 76
4.1.1 Micellization temperature 76
4.1.2 Cloud point 83
4.1.3 Phase diagram 84

4.2 Thermodynamics of micellization 87
4.2.1 Scanning calorimetry 90
4.2.2 Titration calorimetry 92
4.3 Micellar sizes and topology 96
4.3.1 Dynamic light scattering 96
4.3.2 Static light scattering 99
4.3.3 Small-angle X-ray scattering 102
4.3.4 Viscosity scaling 103
4.4 Conclusions 106

5 Unravelling their network topology and elasticity using a novel transient network model 107

5.1 Generalized mechano-statistical transient network model 108
5.1.1 Configuration probabilities 109
5.1.2 Node functionality 111
5.1.3 Elastically active bridges 112
5.2 Critical network concentration 117
5.3 Micellar network topology 121
5.3.1 SAXS intensity profile 121
5.3.2 Radial distribution function 126
5.4 Network elasticity and model performance 130
5.4.1 Model performance 131
5.4.2 Critical assessment 134
5.5 Conclusions 137

6 Understanding their sticky Rouse-like relaxation dynamics 139

6.1 Identification of characteristic relaxation times 140
6.2 Temperature and concentration dependence 143

6.2.1 Temperature dependence 143
6.2.2 Concentration dependence 146
6.3 Comparison with theoretical frameworks 148
6.3.1 Existing models 148
6.3.2 Hybrid model 152
6.4 Conclusions 154

II DOUBLE NETWORKS combining hydrophobic association and metal-ligand complexation 155

7 Identifying the multiple dynamics and synergy in double networks 157
7.1 Double network model system 158
7.1.1 Characterization of the relaxation process 158
7.1.2 Selection of metal-ligand network 162
7.1.3 Time-dependent network formation 166
7.2 Multiple dynamics and synergy 169
7.2.1 Synergistic elasticity 171
7.2.2 Relaxation delay 172
7.3 Reproducibility issues 174
7.4 Conclusions 176

8 Conclusions and outlook 179
8.1 Conclusions 179
8.2 Outlook 183

A Appendix to Chapter 4 187
A.1 Additional figures discussed in Chapter 4 187

B Appendix to Chapter 5 195

B.1 Transient network model for telechelic triblock copolymers 195
B.2 Approximation of the aggregation number based on the core volume . 196
B.3 Additional figures discussed in Chapter 5 198

List of Figures **205**

List of Tables **211**

Bibliography **213**

Curriculum vitae **245**

List of publications **247**

Chapter 1

Introduction

1.1 Context and motivation

Whether used in simple everyday products or serving as highly customized solutions in niche applications, polymers are indispensable in our daily lives. Since the discovery of synthetic polymers more than a century ago, research into the synthesis, properties and applications of polymers has emerged as one of the largest areas in interdisciplinary materials science. Their macromolecular nature, i.e. the fact that they consist of many monomers connected by covalent chemical bonds, has opened up an impressive toolbox for creating a wide range of materials depending on the polymer composition (homo- or copolymer), architecture (linear, branched, star or ring) and molecular weight. In the last few decades, supramolecular self-assembly processes which are omnipresent in nature, have inspired polymer scientists to also exploit non-covalent, physical interactions in synthetic polymer systems, thereby introducing promising and often stimuli-responsive properties like self-healing and shape memory. Different types of non-covalent interactions including van der Waals interactions, hydrogen bonding, ionic interactions, metal-ligand complexation and hydrophobic association, have been used in dilute and concentrated solutions, as well as in the bulk state. The strength, functionality, position and density of these interactions dictate the final mechanical properties and further add degrees of freedom to obtain highly specific and tailored structures and properties.

Of particular interest for soft matter research is the exploitation of supramolecular chemistry in aqueous polymer solutions. In dilute state, the physical association between 'sticky' groups results in self-assembled architectures. A well-known example of such polymeric assembly is micellization of amphiphilic block copolymers, in

which entropy-driven hydrophobic association is responsible for the self-assembly process. The hydrophobic core of these microphase-separated structures is often used to solubilize hydrophobic components in hydrophilic environments and is exploited in drug delivery applications and selective separation processes. The physical and stimuli-responsive driving forces behind the self-assembly process do not only allow efficient encapsulation but also controlled release of their cargo as a function of temperature, pH or other external stimuli. At more elevated polymer concentrations, non-covalent interactions can serve as non-permanent crosslinks in supramolecular polymer networks and hydrogels. The obtained networks often combine characteristics of both physical and chemical networks such as a high mechanical strength and toughness, substantial swelling and large but reversible deformations. Therefore, supramolecular polymer networks have proven to be useful in a plethora of advanced applications including tissue engineering and soft robotics. From a fundamental point of view, supramolecular polymer networks have attracted the interest of polymer physicists and rheologists due to their transient nature, which allows studying both their elastic and dissipative properties within the timescales accessible by rheology. Whereas most studies in literature consider model polymer systems with either multifunctional end group stickers or bi- or trifunctional side group stickers, the case of multifunctional stickers along the polymer backbone is often excluded from theoretical frameworks. The many configurational possibilities of a single chain with inter- and intramolecular associations, combined with the often non-negligible size of the associative interactions significantly increase the complexity of the system and will be the main topic of the first part of this dissertation.

Even more advanced and tunable, is the combination of a supramolecular polymer network with another polymer network, either covalent or non-covalent, in a double or interpenetrating network structure. Depending on the double network composition as well as the difference in binding strength of both types of crosslinks, two (or more) distinct dynamic modes with complementary features can be obtained. For example, the slow relaxation of a network generated by strongly interacting stickers induces a solid-like behavior, thereby providing resistance against flow and creep, whereas the faster relaxing network exhibits liquid-like behavior due to its ability to dissipate energy, ultimately resulting in increased toughness and limited crack propagation. This ‘double’ mechanical behavior facilitates a controlled balance between the properties of the individual networks and promotes synergistic final properties. Such double networks present an additional opportunity to engineer materials with complex time- and rate-dependent properties and further broaden the spectrum of smart polymeric materials. However, most studies consider double networks as soft non-linear deformable solids and have therefore focused almost exclusively on their elastic properties. The multiscale dynamics in supramolecular double networks and its ensuing viscoelasticity has hardly been addressed in literature despite its crucial importance in processing and end-use applications. Therefore, the second part of this dissertation will exploit rheology to probe the viscoelastic properties and structure of supramolecular double networks.

1.2 Aims and outline

This doctoral dissertation situates in the field of supramolecular polymer self-assembly and network formation and mainly aims at understanding the structure-property relationships in transient networks formed by micellar interaction nodes in aqueous media. **Chapter 2** gives a broad introduction to supramolecular self-assembly and network formation, with the main emphasis on hydrophobic association and metal-ligand complexation in aqueous solutions. It also includes a discussion of the existing theoretical frameworks describing the (non-)linear rheological response of supramolecular polymer networks. The limited amount of studies on fully supramolecular double networks probed by rheology, are also introduced. In **Chapter 3**, the materials and characterization methods used in the subsequent chapters are discussed. In **PART I** of this dissertation, the main focus lies on single networks formed by alternating multiblock copolymers bearing multiple hydrophobically associating blocks along their polymer backbone. In **PART II**, these multisticker micellar networks are combined with networks formed by metal-ligand complexation in a double network configuration. The main objectives of this dissertation can be summarized as follows:

1. To fully map for the phase behavior of medium-length alternating poly(ethylene oxide)-poly(propylene oxide) (PEO-PPO) multiblock copolymers in aqueous solutions as a function of temperature and concentration, and to understand the underlying thermodynamic driving forces for these phase transitions as well as the related morphological changes. For this purpose, a multitude of characterization techniques including rheology, scanning and titration calorimetry, light and X-ray scattering and light transmittance will be exploited in **Chapter 4**.

2. To unravel the network topology and resulting elasticity of transient networks formed by PEO-PPO multiblock copolymers in aqueous solutions at elevated concentrations and temperatures. Hereto, a mechano-statistical transient network model as originally developed for telechelic triblock copolymers bearing their associating groups as end groups, is extended and generalized to alternating multiblock copolymers bearing multiple associating blocks along the polymer backbone. Using a combinatorics approach over all possible chain configurations of multiblock copolymers, the model allows to gain insights in the network topology, the related statistical probabilities of bridge and loop formation of a soluble hydrophilic block and their effect on the macroscopic rheological properties of the networks in **Chapter 5**.

3. To understand the relaxation dynamics in transient networks formed by PEO-PPO multiblock copolymers, which have multiple hydrophobic blocks along their chain forming large-scale micellar crosslinking nodes and for which no

broad consensus regarding their relaxation principles has been obtained so far. In **Chapter 6**, the concentration and temperature dependencies of the characteristic relaxation times question the assumptions often made in the conventional theoretical frameworks and help drawing a more general picture about the sticky Rouse-like relaxation processes in multisticker transient networks.

4. To create double polymer networks exclusively based on supramolecular crosslinking interactions with different transient dynamics, in order to pinpoint the synergistic effects of the double network structure on its elasticity and relaxation processes. This goal is reached by combining the temperature-responsive network formed by hydrophobic association of PEO-PPO multiblock copolymers with a faster relaxing network formed by metal-ligand complexation of telechelic terpyridine-functionalized 4-arm PEO star polymers. In **Chapter 7**, linear shear rheology is used as the main toolbox to study the time- and temperature-dependent behavior of the double network structure and to examine its behavior compared to that of the single networks.

A schematic overview of the main content of this dissertation and the relevant research questions can be found in Figure 1.1. In the last chapter of this dissertation, **Chapter 8**, the main conclusions and perspectives for future work are presented.

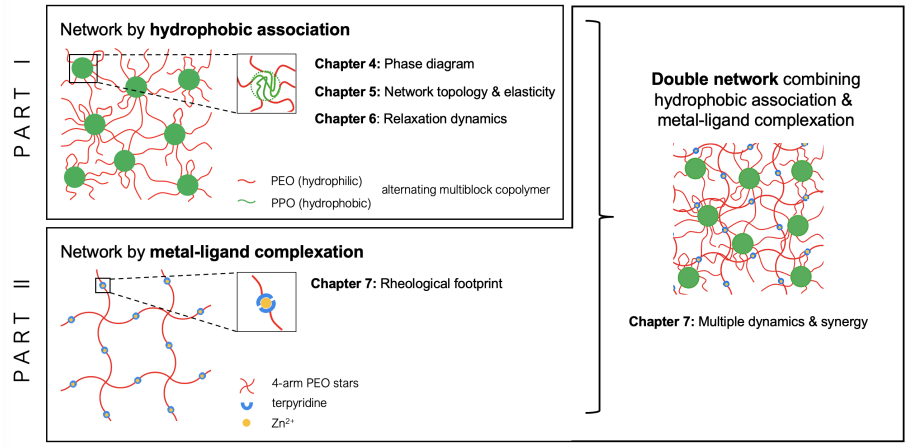

Figure 1.1: Schematic overview of this PhD dissertation and relevant research questions treated in each chapter.

Chapter 2

State of the art

Parts of this chapter are taken from the following publications and adapted to be better integrated in this dissertation:

An-Sofie Huysecom, Christ Glorieux, Jan Thoen, Wim Thielemans, Charles-André Fustin, Paula Moldenaers and Ruth Cardinaels, "Phase behavior of medium-length hydrophobically associating PEO-PPO multiblock copolymers in aqueous media", *Journal of Colloid and Interface Science*, 641:521-538, 2023

An-Sofie Huysecom, Wim Thielemans, Paula Moldenaers and Ruth Cardinaels, "A generalized mechano-statistical transient network model for unravelling the network topology and elasticity of hydrophobically associating multiblock copolymers in aqueous solutions", *Macromolecules*, 56(2):612-633, 2023

2.1 Supramolecular self-assembly

When receiving the Nobel prize for their work on host-guest chemistry in 1987, Lehn and his fellow laureates Pedersen and Cram defined supramolecular chemistry as '*chemistry beyond the molecule'*, which refers to the hierarchical structures formed by intermolecular, non-covalent associations between two or more species [1]. Since then, supramolecular chemistry had gained increasing attention and developed into an active field of research, which is usually subdivided into the following subcategories [2]: host-guest complexes [3], self-assembled architectures [4], supramolecular polymers [5], supramolecular gels [6] and supramolecular polymer networks [2, 7, 8]. In

'supramolecular polymers' monomeric (or short polymeric) units are connected by directional, non-covalent interactions. The length of such supramolecular polymers largely depends on the stability of the supramolecular bonds. A typical example is the formation of long supramolecular polymer chains by bi-functional metal-ligand association of telechelic polymers [9]. The term 'supramolecular gels' refers to low molecular weight precursors which assemble in a three-dimensional gel structure by physical interactions [6]. 'Supramolecular polymer networks', on the other hand, consist of conventional polymer chains functionalized with binding motifs, either as telechelic end groups, as side groups along the polymer chain, or incorporated in the polymer backbone, which can associate by both intra- and intermolecular physical interactions. Supramolecular polymer networks are either utilized in the bulk, or as supramolecular hydro- or organogels, i.e. swollen in water or another solvent [8]. In this dissertation, only self-assembled polymer architectures and supramolecular polymer networks in aqueous media are considered. Many types of non-covalent, physical interactions have been employed in supramolecular chemistry, including hydrogen bonding [10], π-π stacking [11], ionic (Coulombic) interactions [12] and metal-ligand complexation [13, 14]. Figure 2.1 compares the binding strength of these interactions with that of covalent bonds and proves the wide span in strength of physical interactions. Metal-ligand interactions specifically, span almost the entire interval and can range from very labile interactions (10 kJ/mol) to interactions as stable as covalent bonds (400 kJ/mol), depending largely on the choice of metal and to a lesser extent on the ligand [15]. Combinations of different interaction types have also been reported to create exotic architectures [16–18] or multidynamic polymer networks [19, 20].

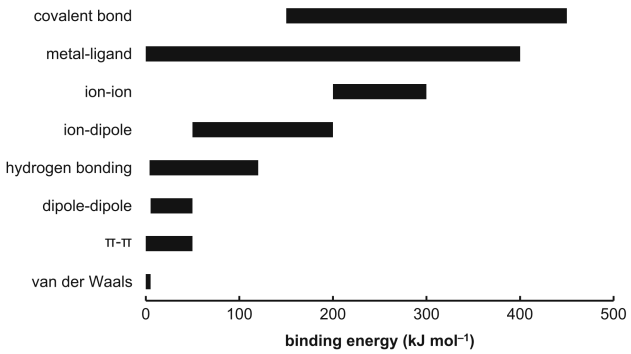

Figure 2.1: Comparison of the binding energy of covalent and different types of non-covalent interactions, reproduced from [21].

The wide variety of interaction types with their characteristic features, together with the nature of the macromolecular building blocks allows precise molecular control over supramolecular polymer assemblies, thereby resulting in a broad range

of tunable properties. Hence, owing to its great potential to significantly expand the polymer material palette by relatively simple molecular design, supramolecular polymer chemistry is referred to as *'playing LEGO with macromolecules'* by some pioneering scientists in the field of metal-ligand complexation [14]. In what follows, the two non-covalent interaction types employed in this dissertation, i.e. hydrophobic association (or micellization) and metal-ligand complexation, are discussed.

2.1.1 Hydrophobic association

The self-assembly of amphiphilic block copolymers in selective solvents (usually water) has been widely studied since the 1950's [22–25]. Such block copolymers contain both hydrophilic (A) and hydrophobic (B) blocks. Driven by the hydrophobic effect, the amphiphilic molecules spontaneously phase separate into microscopic hydrophobic domains stabilized by the hydrophilic blocks, thereby forming micellar assemblies with various morphologies [26]. The hydrophobic effect and the ensuing spontaneous self-assembly is governed by entropy. The introduction of hydrophobic blocks in water, causes a disruption of the hydrogen bonds between water molecules and a subsequent reorientation of these water molecules to maximize their remaining hydrogen bonding capacity. This goes hand in hand with a decrease in the degree of disorder. To satisfy the second law of thermodynamics ($\Delta S > 0$), the hydrophobic blocks cluster together, thereby reducing their contact area with water and minimizing the disruption of the H-bond network of the surrounding water molecules. The resulting increase in entropy of water widely overcomes the reduction in entropy due to the hydrophobic clustering and makes the self-assembly process spontaneous [24]. The transition usually occurs at a characteristic temperature and concentration, referred to as the Critical Micelle Temperature (CMT) and Critical Micelle Concentration (CMC), respectively, and is specific for each combination of amphiphile and solvent. Below CMC or CMT, the amphiphilic copolymers exist as individual unimers in solution, whereas upon exceeding the CMC or CMT, the unimer concentration is constant and the additional copolymers aggregate into micellar assemblies. By increasing the concentration above the CMC, progressively more micelles are being formed.

The micellar assemblies formed by amphiphilic copolymers at low concentrations can have various morphologies such as spherical or cylindrical micelles, bilayer vesicles or lamellar phases. At more elevated concentrations, the micellar aggregates often pack in their most favorable configuration, thereby forming a crystal-like, ordered 'mesophase'. Figure 2.2 shows a typical phase diagram indicating different lyotropic liquid crystal (LLC) phases as a function of amphiphile concentration and temperature. The characteristic progression of mesophases as a function of concentration generally evolves from a micellar solution over a cubic and/or hexagonal phase to a lamellar phase upon increasing the concentration. Besides the amphiphile concentration and temperature, the micellar assemblies and resulting phase behavior are also highly

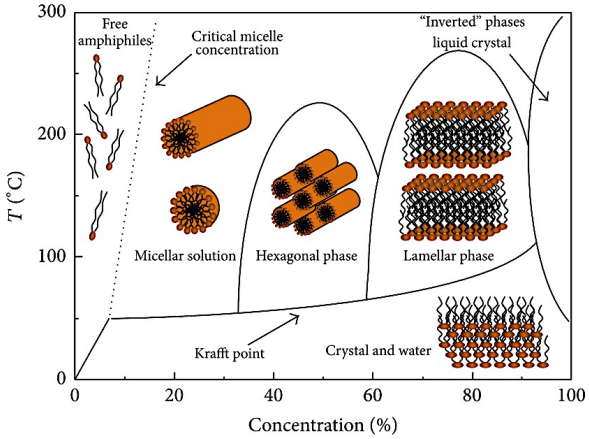

Figure 2.2: Typical amphiphile phase diagram indicating the (meso)phase transitions as function of concentration and temperature, reproduced from [24].

influenced and hence tunable by changes in the pressure, pH or addition of additives. The different mesophases also all have distinct mechanical properties. While the cubic and hexagonal phases often form elastic gel-like structures with a significant yield stress, lamellar structures were found to have little to no yield stress [27].

Micellar assemblies and their ensuing complex phase behavior have often been used in biomedical applications [28] as drug delivery systems [29, 30] and tissue engineering scaffolds [31–34]. The small hydrophobic domains can act as microcarriers [35] for therapeutic agents, such as drugs or (stem) cells, and allow controlled release of their cargo [36, 37]. A widely used hydrophilic polymer in such biomedical applications is poly(ethylene oxide) (PEO, -CH2-CH2-O-) (also called poly(ethylene glycol (PEG) at low molecular weights) due to its excellent water solubility, its biocompatibility and lack of toxicity or immunogenicity [38–41]. Classic examples of PEO-based amphiphilic block copolymers contain poly(propylene oxide) (PPO, -CH(CH3)-CH2-O-) blocks in different configurations. Owing to the increased hydrophobicity and hence dehydration of the PPO blocks upon increasing temperatures (> 15°C [42]), such block copolymers undergo thermoreversible microscopic phase separation and form ordered structures with various morphologies [43, 44]. Undoubtedly, the architecture of the PEO-PPO block copolymers, i.e. the block lengths and their configuration as linear or branched di-, tri- or multiblock copolymers, as well as the overall molecular weight of the molecules play a crucial role in the location of the phase boundaries, the morphology of the micellar aggregates as well as their final mechanical properties [45]. The next two sections elaborate on the micellization and resulting phase behavior of both triblock and alternating multiblock copolymers of PEO and PPO.

Triblock copolymers

The ABA triblock copolymers of PEO and PPO (PEO_x-PPO_y-PEO_x) are often referred to as poloxamers and are commercially available as Pluronics® with different PEO (x) and PPO (y) block lengths [44]. Due to the wide variety of block lengths, they have often been studied to obtain fundamental insights in the micellization and phase behavior as a function of hydrophobicity and overall molecular weight [27, 43]. Figure 2.3 (a) shows the different available Pluronics®. The crystalline packing of Pluronic® micelles in lyotropic liquid crystalline phases at more elevated concentrations, gives rise to a polymorphism similar to conventional surfactants. However, the characteristic thermotropic behavior of Pluronics® induces transitions between mesophases not only as a function of concentration, but also under the influence of temperature [27], and makes the phase behavior of PEO-PPO-PEO triblock copolymers even richer. Therefore, the phase behavior of Pluronics® has been studied by a multitude of techniques including dye solubilization [43], calorimetry [46], light scattering [47, 48], X-ray scattering [49], neutron scattering [50, 51] as well as linear [52] and non-linear rheology [53, 54].

Due to the temperature dependent hydrophobicity of the PPO block, the CMC of Pluronics® is highly temperature dependent. Figure 2.3 (b) shows the linear temperature dependency of the CMC (or concentration dependency of the CMT) for different Pluronics® as obtained by Alexandridis *et al.* using dye solubilization in water [43, 44] and proves that the CMC can vary by multiple orders of magnitude in a small temperature window. The CMC (or CMT) decreases upon increasing the hydrophobic block length (e.g. F108 as compared to F88) or upon increasing the (relative) hydrophobic weight fraction (e.g. P103 as compared to F108) [43, 44]. Instead of a sharp transition, differential scanning calorimetry (DSC) measurements revealed that the micellization process of PEO-PPO-PEO triblocks spans over a wide temperature interval of at least 5 to 10°C [45, 49, 55, 56], which is attributed to the progressive incorporation of triblock copolymers into micelles, possibly due to some polydispersity and/or the presence of impurities [27]. The structural changes of the dilute micellar assemblies as a function of temperature during this broad process has been widely examined, but a general consensus is missing. Some authors, on the one hand, report an increase of the micellar aggregation number N_{agg}, i.e. the amount of copolymers segregated in one micelle, upon increasing temperature. Combined with a further dehydration of the PPO blocks, this results in a constant hydrodynamic radius (R_H) of the often spherical core-shell micelles on the order of 10 nm [44, 55, 57]. Figure 2.3 (c) displays the temperature evolution of the apparent R_H as determined by dynamic light scattering (DLS) for Pluronic® P68 at different concentrations in aqueous solutions and indeed shows that the radius remains constant above CMT [55]. Mortensen *et al.*, on the other hand, have found an increase in both the aggregation number and the micellar size with increasing temperature [50] for Pluronic® P85. Nonetheless, most authors have concluded that far above the critical micellar transition N_{agg} does not

significantly change with concentration, nor with temperature [27, 50], and is usually on the order of 50-100 for Pluronic® spherical micelles in isotropic solutions [27].

Upon further increasing the temperature above the CMT, the hydrophobicity of the PEO blocks in Pluronics® also increases and the micellar geometry changes from spherical to more prolate ellipsoidal [50]. Upon increasing the concentration, rod-like structures are formed leading to a hexagonal mesophase. Further increase in temperature and/or concentration results in an ordered lamellar structure. By using polarized optical microscopy, small angle neutron scattering (SANS) and transmission electron microscopy, Wanka *et al.* characterized the phase behavior of different types of Pluronics® as isotropic, cubic, hexagonal, lamellar or multiphasic phases [27]. Note that both the polymer solution and micellar solution are isotropic in nature. They found that triblocks with small PEO blocks directly form a hexagonal mesophase, whereas for triblocks with small overall EO/PO ratios both the cubic and hexagonal LCC phases are absent. Pluronics® with high EO/PO ratios usually only form a cubic mesophase, as can be seen for F127 in Figure 2.3 (d). The transition from isotropic solution to a cubic crystalline ordering goes hand in hand with a drastic and sharp increase in elasticity and creates a gel-like material. In Figure 2.3 (e), the temperature evolution of the linear dynamic moduli, i.e. the storage modulus G' and the loss modulus G'' (left y-axis), for a 20 wt% F127 aqueous solution, proves that at a characteristic gel formation temperature (T_{gel}, second dashed vertical line in Figure 2.3 (e)), the elastic modulus G' starts dominating over the viscous modulus G''. This LLC transition is also accompanied by an additional calorimetric process in DSC thermograms (right y-axis, also see inset in Figure 2.3 (e)), in addition to the endothermic micellization observed at lower temperatures. The linear rheological frequency sweeps of 20 wt% F127 solutions at different temperatures in Figure 2.3 (f) indeed reveal a transition from a purely viscous, terminal flow behavior ($G' \sim \omega^2$ and $G'' \sim \omega^1$) at low temperatures to a typical fingerprint of a gel material with $G' \sim G'' \sim \omega^\alpha$ (with $0.5 < \alpha < 0.8$ [58]) and $G' > G''$ over the entire frequency range at temperatures above 30°C [52]. Besides temperature, also other external factors such as pressure [59, 60], or the presence of co-solvents [61, 62] or ionic liquids [63–67] affecting the pH or ionic strength, can influence the phase behavior of Pluronics®. Moreover, combinations of different types of Pluronics® [56, 68, 69] or Pluronics® with other surfactants [70] have also been exploited by some scientists as a way to further tailor their phase behavior.

The reverse counterparts of Pluronics® having a BAB configuration, i.e. so-called 'reverse Pluronics®', exhibit significantly different phase behavior [43, 71–75]. Whereas ABA triblock copolymers form micelles with PEO 'hairs' in the outer corona, BAB triblock copolymers form so-called flowerlike micelles in which soluble PEO blocks loop back to the same micellar PPO core, thereby forming flower petals in the outer corona. For such PPO-PEO-PPO triblock copolymers, an optimal balance between PEO and PPO block lengths is crucial for the solubility of the copolymer at low temperatures, and the ensuing formation of micellar assemblies upon heating. Alexandridis *et al.*

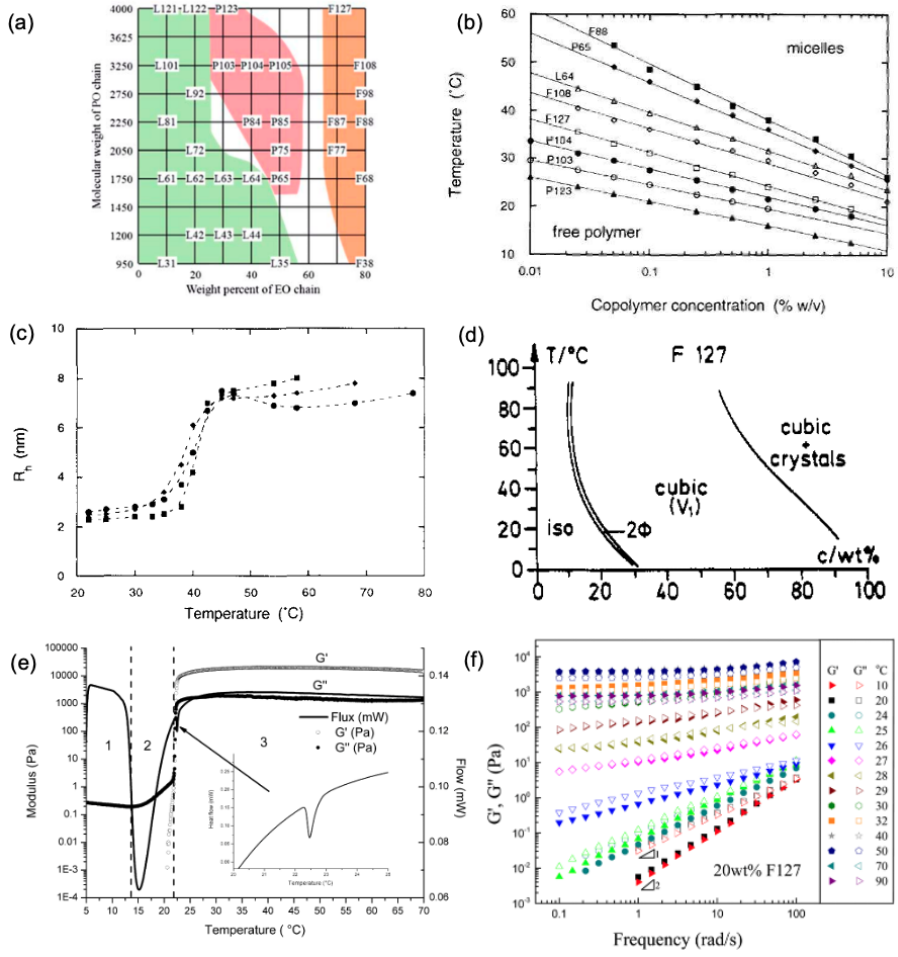

Figure 2.3: (a) Nomenclature of different commercial grades of Pluronics®, reproduced from [40]. (b) Concentration dependence of the CMT (or temperature dependence of the CMC) for different types of Pluronics® as indicated in the graph, reproduced from [44]. (c) Temperature evolution of the hydrodynamic radius of P68 Pluronic® at different concentrations (square symbol is 12.5 g/L, circle symbol is 25.0 g/L and diamond symbol is 51.7 g/L) in aqueous solutions, reproduced from [55]. (d) Phase diagram of F127 solutions indicating the isotropic, cubic and multiphasic mesophases as function of temperature and concentration, reproduced from [27]. (d) Temperature evolution of the dynamic moduli (left y-axis) and the heat flow (right y-axis) for a 20 wt% F127 solution, reproduced from [45]. (e) Dynamic moduli as a function of frequency for a 20 wt% F127 solution at different temperatures as indicated in the graph, reproduced from [52].

observed no micelle formation for reverse Pluronics® of type 25R4 in dilute solutions [43], which is supported by a theoretical calculation of Ten Brinke *et al.* who found that the significant entropy loss upon loop formation of soluble middle blocks prevents the formation of flowerlike micelles in many BAB triblock copolymers [76]. However, according to Balsara's modified theoretical entropic calculations, loop formation is possible depending on the molecular weight of the middle block [77]. By studying two grades of reverse Pluronics® (25R2 and 25R4) with similar PPO block length but different PEO block length, D'Errico *et al.* concluded that 25R2 triblocks with short PEO blocks did not form any spherical micelles at low concentration, nor any LLC mesophases at more elevated concentrations, whereas 25R4 triblocks exhibited similar phase transitions as Pluronics®. They underwent transitions from an isotropic solution over hexagonal and lamellar LLC phases to a phase separated structure upon increasing concentration, but also lack the formation of isolated flowerlike micelles at low concentrations [72, 73] as concluded by Alexandridis *et al.* [43]. Mortensen *et al.*, on the other hand, studied 25R8 reverse Pluronics® with a much longer middle PEO as compared to 25R4, which form an interconnected micellar network at elevated concentrations in aqueous solutions instead of liquid crystalline phases as observed by D'Errico [71].

Multiblock copolymers

The limited viscosity increase and the related poor mechanical strength, limited stability as well as short residence times and unacceptably high permeability obtained using triblock copolymer aqueous solutions and hydrogels [80], combined with the fact that the gel forming capabilities of Pluronics® are highly influenced by the presence of other components such as individual PEO chains [81, 82], limit their practical applicability and drives research into other types of PEO-PPO amphiphiles. Unlike most research on PEO-PPO di- or triblock copolymers and their differences, alternating PEO-PPO multiblock copolymers have been the subject of only a limited amount of studies. Such multiblock copolymers also form thermo-responsive self-assembled structures and networks, and might display superior behavior as compared to Pluronics®. Cohn *et al.* [80, 83–85] synthesized alternating and random multiblock copolymers by covalently coupling relatively short PEO and PPO polymers using different types of binding moieties such as phosgene, carbonyl chloride, diacyl chloride or hexamethylene diisocyanate. Similarly, Wang *et al.* [86, 87] covalently linked PEO and PPO blocks using triphosgene as a coupling agent. Sun *et al.* [78] prepared PEO-PPO multiblock copolymers by disulfide coupling of thio-terminated Pluronics®. All these authors found a gradual but significant increase in viscosity upon subjecting aqueous solutions of medium length alternating PEO-PPO multiblock copolymers to increasing temperatures. Their multiblocks containing 3 to 4 repeating PEO-PPO units were compared to Pluronics® with similar hydrophobicity and were found to give rise to a more pronounced viscosity enhancement at equal concentrations, as well

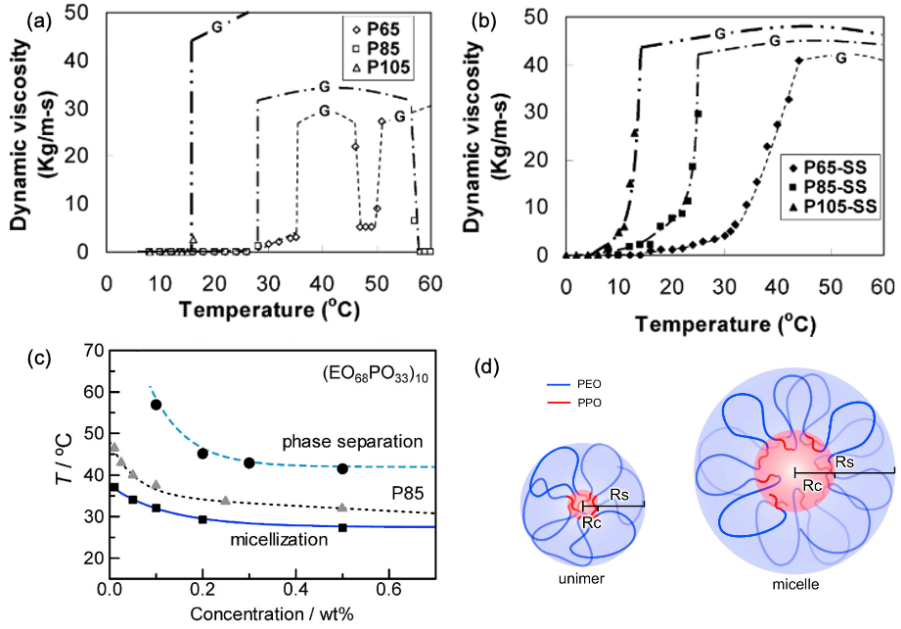

Figure 2.4: Temperature evolution of the viscosity of 30 wt% aqueous solutions of Pluronics® (except P65 at 40 wt%) (a) and alternating PEO-PPO multiblock copolymers (b) with similar hydrophobicity, reproduced from [78]. (c) Phase diagram obtained for $(EO_{68}PO_{33})_{10}$ aqueous solutions indicating the micellization and phase separation boundaries. The micellization transition for Pluronic® P85 with similar hydrophobicity is also shown, all reproduced from [79] (d) Schematic illustrations of both unimer and multimer micelles formed below and above the CMT, respectively, of alternating multiblock copolymers, reproduced from [79].

as larger micellar aggregates. Note that the self-assembled structures of alternating PEO-PPO multiblocks can constitute of both PEO hairs and loops in the hydrophilic corona. Figures 2.4 (a) and (b) display the temperature evolution of the viscosity for different types of Pluronics® and PEO-PPO alternating multiblock copolymers with similar hydrophobicity (indicated with 'SS'), respectively, as obtained by Sun *et al.* for 30 wt% aqueous solutions (except P65 which is 40 wt%) [78]. The graphs illustrate the higher viscosities obtained at lower transition temperatures for multiblock copolymers as compared to their triblock copolymer counterparts. Moreover, Sosnik *et al.* [80] elaborated on the effect of the segment sequence in the copolymer architecture and figured that an alternating sequence leads to a more pronounced viscosity increase as compared to a random multiblock configuration [80]. Nonetheless, a thorough investigation of the exact micellization behavior, the energetic driving forces as well as

the related rheological properties remains elusive in these studies.

Horiuchi *et al.* [88, 89] and Rikiyama [79] *et al.*, on the other, have studied the association and micellization behavior, respectively, of alternating multiblock copolymers with 6 to 10 repeating PEO-PPO units by a multitude of techniques. They found that micelle formation and phase separation occur at lower temperatures compared to Pluronics® of similar hydrophobity. Their phase diagram is presented in Figure 2.4 (c) for aqueous solutions of a $(EO_{68}PO_{33})_{10}$ alternating multiblock copolymer as well as for Pluronic® P85 solutions. The CMT was determined by the dye solubilization method [79] and the phase separation temperature (or cloud point) was inferred from light transmission measurements [88]. Moreover, Rikiyama *et al.* observed interesting aggregation behavior of unimers even below the CMT, indicative of significant hydrophobic driving forces within one multiblock copolymer [79]. Figure 2.4 (d) schematically illustrates the unimer micelles with a size of 8-10 nm, formed below the CMT, as well as the larger multimer micelles of 20-27 nm diameter formed above the CMT, as inferred from synchrotron small angle X-ray scattering (SAXS) intensity profiles [79]. Although their studies have pointed out interesting features of the micellization of multiblock copolymers at dilute concentrations, clear insights into their phase behavior at more elevated concentrations and a correlation with their ensuing rheological properties is missing in their work.

2.1.2 Metal-ligand complexation

Another commonly employed physical interaction type in polymeric systems is metal-ligand complexation. In a metal-ligand complex, ligands coordinate to a central metal atom or ion based on the Lewis bond approach [90]. The conditions for forming such a complex are that the ligand (the Lewis base) needs to have at least one free electron pair, while the metal (the Lewis acid) needs to have free orbitals in its valence shell. The ligand then donates its free electron pair(s) to the metal to form the coordination complex. The amount of binding ligands to one metal ion is given by the coordination number. For their electron donating properties, non-ionic ligands usually rely on one or more oxygen or nitrogen atoms. Ideal candidates as electron acceptors, on the other hand, are transition metals due to their partially filled d-orbital and the ensuing ability to create cations with an incomplete d-orbital in the valence shell. The broad catalogue of possible ligands together with the many applicable metal ions, which make up almost half of the periodic table and often have different stable oxidation states, make metal-ligand combinations enormously versatile [91].

In polymer systems, ligands can be incorporated in the polymer chain as either telechelic groups [92], side groups [93, 94], or in the polymer backbone [95, 96], thereby giving access to a variety of structural motifs as illustrated for bi-functional metal-ligand complexes in Figure 2.5 [97]. The strongly increased number of synthetic routes to

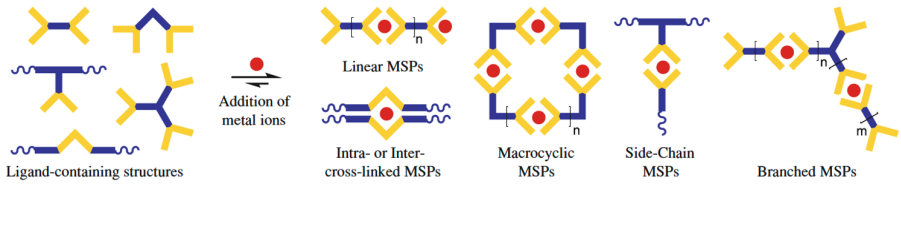

Figure 2.5: Schematic representation of different bi-functional metallo-supramolecular polymer architectures in which the polymer chains are in blue, the ligands in yellow and the metal ions in red, reproduced from [91].

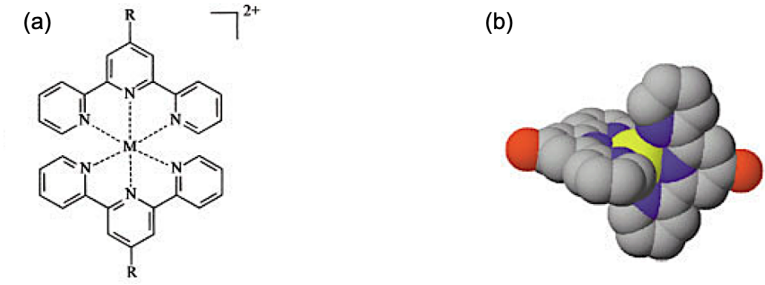

Figure 2.6: Bis-complex formed between two 2,2':6',2"-terpyridine groups and a central divalent metal ion: (a) schematic representation in which *M* is the metal ion and *R* is usually a polymer chain and (b) three-dimensional model showing the octahedral geometry of the complex with the metal ion in yellow, the nitrogen atoms of terpyridine in blue and the polymer chains in red, both images reproduced from [14].

achieve (post-)functionalization of polymers with ligands [14, 91] proves the great scientific attention for this so-called metallo-supramolecular polymer science. One of the most commonly employed ligands in polymeric systems is 2,2':6',2"-terpyridine [13, 14]. In Figure 2.6, this ligand can be seen in its typical bis-complex with a divalent metal ion (M) as a schematic representation (a) as well as in a three-dimensional model (b). It has three nitrogen atoms as electron donors and has therefore a relatively strong chelating effect. The equilibrium constants of terpyridine with different transition metal ions in water for both their mono- (K_1) and bis-complexes (K_2) are given in Table 2.1, as determined by Holyer *et al.* using stopped-flow experiments. The equilibrium constants correspond to the following 'reactions' for the formation of mono- and biscomplexes

Table 2.1: Equilibrium constants K_1 and K_2 for mono- and bis-complexes of 2,2':6',2"-terpyridine with different divalent transition metal ions in water, data taken from [103].

Metal ion	log K_1	log K_2
Mn(II)	4.4	
Fe(II)	7.1	13.8
Co(II)	8.4	9.9
Ni(II)	10.7	11.1
Zn(II)	6	
Cd(II)	5.1	

and are an indication of the interaction strength of the metal-ligand association.

$$\mathrm{M} + \mathrm{L} \rightleftharpoons \mathrm{ML} \text{ with } K_1 = \frac{[ML]}{[M][L]} \text{ (mono-complex)} \tag{2.1}$$

$$\mathrm{ML} + \mathrm{L} \rightleftharpoons \mathrm{ML_2} \text{ with } K_2 = \frac{[ML_2]}{[ML][L]} \text{ (bis-complex)} \tag{2.2}$$

The values in Table 2.1 show that bis-complexes are usually favored over mono-complexes and that the metal-ligand interaction strengths comply with the Irving-Williams series predicting Mn(II) < Fe(II) < Co(II) < Ni(II) < Cu(II) > Zn(II) irrespective of the nature of the ligands and the coordination number [98]. The strength of the metal-ligand bond in polymeric systems is not only dependent on the employed metal, but is also influenced by other external stimuli such as temperature [99], pH [100], the solvent [101] and the presence of competing counterions [102].

2.2 Supramolecular polymer networks

In recent years, supramolecular polymer networks have received a great deal of attention not only from material scientists for the development of novel, custom-made materials for different applications, but also from polymer physicists to unravel fundamental polymer principles. Such physical networks are formed by macromolecules containing 'sticky' groups, which undergo transient non-covalent interactions and form the crosslinking nodes of a 3-dimensional, sample spanning polymer network that restricts flow. The final network structure, mechanical properties and dynamics are not only

determined by the strength and functionality of the sticky groups, but also by their location and the respective ability of polymer segments to entangle and/or crystallize [7, 104]. An important subclassification of supramolecular polymer networks relies on whether the network is present in a gel or bulk state. A gel can be defined as a material with solid-like properties in which a significant fraction (usually more than 70 wt%) of liquid or gas is present. Most supramolecular polymer gels are hydro- or organogels, containing water or an organic solvent, respectively. A supramolecular bulk network, on the other hand, consists of viscous (molten) polymers which owe their solid-like character to non-covalent interactions other than entanglements [8]. Since this dissertation focuses on networks formed in aqueous media, the main focus in what follows will be on supramolecular hydrogels. Different physical interactions, such as hydrogen bonding [105–109], ionic interactions [110–112], metal-ligand complexation [101, 113, 114] and inclusion complexation [115, 116] have been employed in physical hydrogels. The transient character of the physical crosslinks delivers properties in between those of entangled polymer solutions and those of permanently crosslinked, chemical hydrogels. It also provides the networks with excellent self-healing [117–119], stimuli-responsive [120, 121] and shape-memory [107, 122] properties. Therefore, physical polymer gels have proven to be useful in a plethora of advanced applications including microfluidics [123], superabsorbents [124], (bio)sensors [125] and artificial muscles [126]. Whereas the previous section focused on the driving forces behind hydrophobic association and metal-ligand complexation, and their effects on the properties of dilute polymer solutions, the next two sections discuss polymer hydrogels formed by these two non-covalent interaction types at more elevated polymer concentrations, with the main emphasis on their linear rheological properties.

2.2.1 Networks formed by hydrophobic association

Hydrophobic association of amphiphilic block copolymers results in micellization at low concentrations above the CMC. At more elevated concentrations, however, interactions between individual micellar assemblies might result in the formation of a (visco)elastic network or gel. Fundamentally different underlying principles have been observed based on the block lengths and molecular architecture of the block copolymers [127]. Figure 2.7 illustrates some of these different principles. In case (a), hairy spherical micelles formed by AB diblock or ABA triblock copolymers jam together in liquid crystalline lattices with gel-like characteristics [128–130]. Such liquid crystalline gels have been observed for a wide set of Pluronic® micelles (cfr. supra) [27]. This type of ‘colloidal’ gel formation (often called ‘glasses’) is not considered here in the context of supramolecular polymer networks due to the absence of well-defined, intermolecular crosslink interactions between different polymer chains. In such gels, the physical interaction does thus not act as a network crosslink, but rather facilitates

morphological changes which in turn allow colloidal jamming and/or entanglements between the A block hairs. BAB triblock copolymers shown in case (b), on the other hand, have end-capped hydrophilic blocks and assemble in flowerlike micelles at low concentrations. At higher concentrations, these end-capped hydrophilic A blocks potentially connect two different micellar cores, instead of looping back to the same core. The presence of such 'bridges' results in the formation of a sample-spanning, viscoelastic polymer network [131–135] with its properties governed by the amount and lifetime of these bridges [127]. In this case, the hydrophobic association thus effectively behaves as a multifunctional network crosslink. Note that the crosslink functionality is determined by the aggregation number, i.e. the amount of hydrophobic B blocks per core, and can therefore become rather high as compared to other conventional and often bi-functional physical interactions such as hydrogen bonding and inclusion complexation. Case (c) represents polymers with multiple hydrophobic branches along the chain, thereby forming more complex and less well-defined structures. Nonetheless, they also assemble into transient network structures at elevated concentrations. If the hydrophobic interaction is too strong in very concentrated solutions, phase separation is usually observed in all cases [127]. The networks formed by case (b) and case (c), and their characteristic rheological fingerprints, will be treated in the following paragraphs. The focus will be on hydrophobic association in water, even though many examples of 'solvophobic' association in other polar [35], ionic [136, 137] and apolar solvents exist [138].

In addition to the examples shown in Figure 2.7, some block copolymers tend to aggregate in long, wormlike micelles depending on their molecular structure and

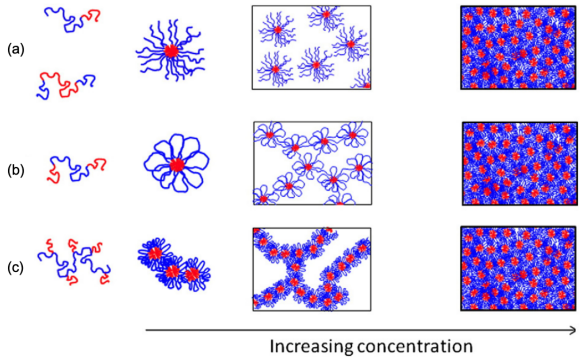

Figure 2.7: Schematic representation of different network principles of amphiphilic block copolymers with the hydrophilic blocks (A) in blue and the hydrophobic blocks (B) in red. Case (a) represents AB or ABA block copolymers forming hairy micelles, case (b) represents BAB block copolymers forming flower-like micelles and case (c) represents hydrophobic branches, reproduced from [127].

external environment (e.g. pH, ionic strength) [139, 140]. Such wormlike micelles are referred to as 'living' polymers, as they constantly break and reform, and have the potential to physically entangle above a certain critical concentration, thereby forming a transient viscoelastic network resembling an entangled polymer solutions [140]. However, their rheological response is not only governed by the physics of polymer entanglements, but also by the reversible kinetics of the self-assembly process [139, 140]. Most studies focus on wormlike micelles formed by head-tail surfactants, but there also exist examples of wormlike micelles formed by amphiphilic block copolymers consisting of PEO and poly(butadiene) [141–145].

BAB triblock copolymers

Amphiphilic BAB triblock copolymers have their hydrophobic stickers as telechelic end groups. Important model systems of such telechelic triblocks are hydrophobically modified urethane–ethoxylate (HEUR) polymers consisting of hydrophilic PEO end-capped by hydrophobic groups such as aliphatic alcohols using urethane bonds. These hydrophobically modified water soluble polymers are often referred to as 'associative thickeners' and find their main use in waterborne paints [146]. Aqueous solutions of HEUR have been studied extensively by both linear and non-linear rheology [147–152]. Figure 2.8 (a) shows the linear elastic (G') and viscous (G'') moduli as a function of angular frequency ω for 7 w/v% HEUR polymers with hydrophobic linear alcohol blocks containing 16 carbon atoms and 35 kDa hydrophilic PEO blocks (indicated as C16/35 representing the block lengths) at 298 K, as reproduced from Annable *et al.* [147]. The linear rheological response follows the ideal Maxwell model (solid lines), predicting:

$$G' = \frac{G_0 \cdot (\omega\tau)^2}{1+(\omega\tau)^2} \tag{2.3}$$

$$G'' = \frac{G_0 \cdot (\omega\tau)}{1+(\omega\tau)^2} \tag{2.4}$$

in which G_0 is the plateau modulus and τ the characteristic relaxation time. This model describes viscoelasticity as a simple serial combination of an elastic spring and a viscous dashpot. The plateau modulus gives an indication of the polymer network elasticity. In analogy with rubber elasticity theory, each bridge in principle contributes 1 k_BT to the elastic plateau modulus, giving rise to the well-known affine network theory [153] stating that:

$$G_0 = \nu k_B T \tag{2.5}$$

in which ν is the number density of elastically active chains, k_B is the Boltzmann constant and T the absolute temperature. Also other network theories predicting elasticity have been derived taking into account (local) structural defects, such as the phantom network theory [153] and the real elastic network (RENT) theory [154, 155]

in which the interaction functionality plays a crucial role. For micellar systems with very high functionalities, however, the phantom network and RENT theories approach the affine network theory, which makes the latter widely used [147, 152, 156, 157]. The single relaxation time τ of a Maxwellian respons is the characteristic timescale at which viscous, terminal flow kicks in. In BAB networks, it is fully governed by the dissociation of a hydrophobic block from a micellar node and hence of the order of the bond lifetime [147]. The internal modes of conformational relaxation are usually too fast to be probed by rheology [127]. HEUR systems represent ideal

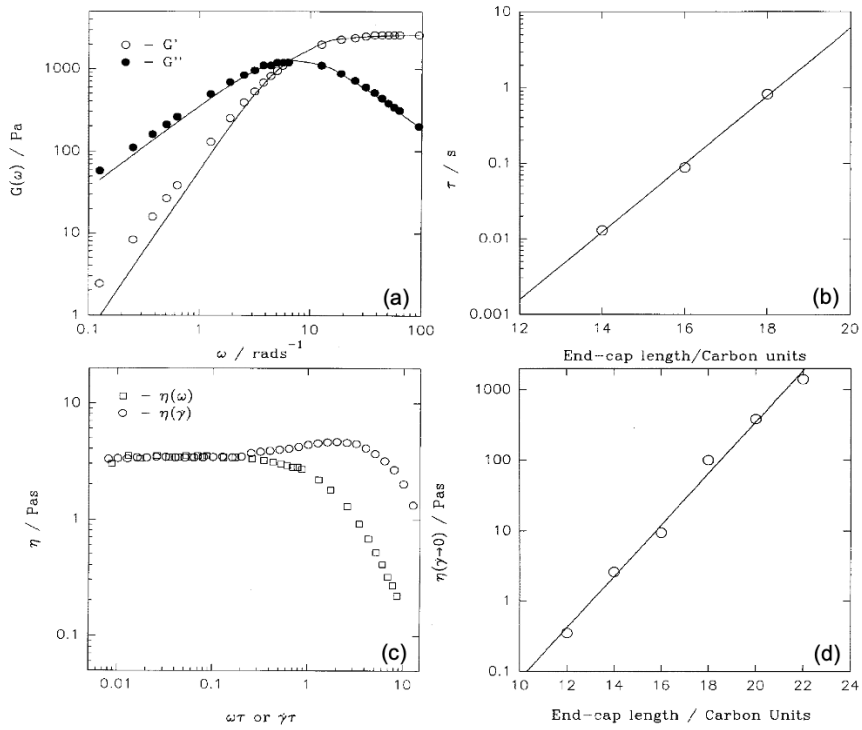

Figure 2.8: Rheological properties of networks formed by HEUR polymers with hydrophobic linear alcohol blocks and 35kDa hydrophilic PEO blocks at 298 K: (a) elastic (G') and storage modulus (G'') as a function of angular frequency ω for a network of 7 w/v% 16C/35 HEUR with the solid lines representing the Maxwell curve fits, (b) evolution of the relaxation time (τ) as function of hydrophobic block length for hydrophilic block lengths of 35 kDa at 4 w/v% concentrations, (c) shear viscosity η as a function of shear rate $\dot{\gamma}$ for 1.5 w/v% solutions of 16C/36 and (d) evolution of the zero-shear viscosity (η_0) as function of hydrophobic block length for hydrophilic block lengths of 35 kDa at 2w/v% concentrations. All figures are reproduced from [147].

model systems of BAB triblocks due to the ease of block length variation as well as the possibility to easily tune the nature of the hydrophobic block (e.g. fluorinated alkyl chains [158]). This in turn allows fundamental and systematic studies of the structure-property relationships. Figure 2.8 (b) shows the evolution of the relaxation time τ as function of the hydrophobic block length expressed as the amount of C atoms in the hydrophobic blocks, in HEUR systems with 35 kDa PEO middle blocks at 4 w/v%. This clearly indicates that the dynamic response of the networks is highly tunable by variation of the molecular design of the triblocks, i.e. the end-cap chain length and the relative length as compared to the hydrophilic block length. The non-linear rheology of HEUR polymers in aqueous media also has characteristic features. Figure 2.8 (c) shows the shear viscosity η as a function of rotational shear rate $\dot{\gamma}$ for 1.5 w/v% C16/35 HEUR polymers at 298 K. Also the complex viscosity η^* as function of angular frequency ω, as obtained by a linear oscillatory test protocol, is displayed. The discrepancy between both viscosities proves that the Cox-Merz rule, stating that:

$$\eta^*(\omega) = \eta(\dot{\gamma}) \text{ at } \omega = \dot{\gamma}, \tag{2.6}$$

is violated in such transient networks. At low shear rates, the viscosity is constant and the material behaves Newtonian, whereas at higher shear rates the viscosity first increases (shear thickening) after which it decreases (shear thinning). The shear thickening is believed to find its origin in either the shear-induced formation of more bridges or non-Gaussian stretching of the bridges [150, 159, 160]. The breakage of elastic bridges at higher shear rates, on the other hand, causes shear thinning behavior [127]. Figure 2.8 (d) shows the evolution of the zero-shear viscosity (obtained at $\dot{\gamma} \to 0$) versus the end-cap chain length of 35 kDa PEO HEUR systems at 2 w/v%. Increasing the length of the hydrophobic blocks leads to an exponential increase of the viscosity over several decades. The slopes in Figures 2.8 (b) and (d) are similar and governed by the activation energy for disengagement of a hydrophobic block from a micellar core, which is proportional to the block length [147].

Next to the nature and length of the hydrophobic multistickers, the concentration of HEUR polymers also plays a crucial role in its rheological properties. Figure 2.9 (a) presents the concentration evolution of the plateau modulus (left y-axis) and relaxation time (right y-axis), as obtained by Sprakel *et al.* using the Maxwell model for fitting the rheological frequency sweep data of C16/35 HEUR polymers at 293 K. The linear trends in these log-log plots show that both G_0 and τ exhibit a power law dependence on the concentration with exponents 2.3 and 0.75, respectively. Hence, the relative amount of elastically active chains does not remain constant upon varying the concentration, but increases with concentration. Also the viscosity at low shear rates strongly depends on the concentration, with a power law dependence of $\sim c^{3.9}$, whereas the pure 35 kDa PEO chains have a $\sim c^{2.1}$ dependency, as shown in Figure 2.9 (b).

Besides linear alkanes as hydrophobic blocks telechelically attached to hydrophilic PEO chains, the introduction of stimuli-responsive hydrophobic blocks, whose

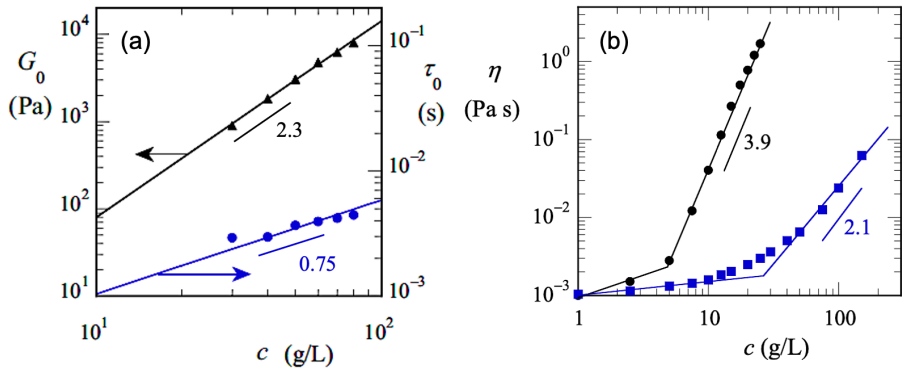

Figure 2.9: Rheological properties of networks formed by HEUR polymers with hydrophobic linear alkyl chains of $C_{16}H_{33}$ and 35 kDa hydrophilic PEO blocks at 293 K: (a) evolution of the plateau modulus (G_0, triangle, left y-axis) and the relaxation time (τ, circle, right y-axis) obtained from Maxwell model fits as function of concentration with the solid lines representing the power law fits with the exponents indicated in the graph and (b) low shear viscosity η as function of concentration for pure 35 kDa PEO polymers (square) and for hexadodecyl-modified 35 kDa PEO associative polymers, with the solid lines representing the power law fits with the exponents indicated in the graph. All figures are reproduced from [161].

hydrophobicity is governed by an external stimulus such as temperature or pH, results in the formation of networks with a temperature or pH sensitive 'on/off switch'. Sanabria-De Long *et al.* studied networks formed by triblock copolymers of PEO with telechelic amorphous or crystalline poly(lactide) blocks [134, 135, 162, 163]. By controlling the crystallization of the hydrophobic blocks, they obtained hydrogels with highly tunable mechanical properties due to the combination of both hydrophobic association and crystallization as crosslink interactions. Bae *et al.* end-functionalized PEO chains with poly(caprolactone) (PCL) blocks for the formation of thermoreversible and biodegradable hydrogels [133] with a sol-gel-sol transition upon increasing the temperature. However, prolonged annealing of the low temperature sol phase resulted in an opaque gel, which the authors attribute to the kinetically slow crystallization of the PCL blocks at low temperatures [164]. Other hydrophobic blocks including poly(oxybutylene) [132, 165], poly(N-(2-hydroxypropyl)methacrylamide lactate) [166, 167] and PPO [71, 74, 75] have been exploited for the formation of thermoreversible supramolecular polymer networks based on B-PEO-B triblocks. The latter, so-called 'reverse Pluronics®' have been the subject of a limited amount of studies as compared to regular Pluronics®, which usually focus exclusively on their micellization and phase transitions (as discussed above) instead of their potential network formation and the ensuing rheological fingerprint. Mortensen *et al.* performed

a structural investigation of reverse Pluronic® 25R8 and verified the formation of uniform micellar networks in which PPO hydrophobic cores are connected by PEO bridges at more elevated concentrations and temperatures [71]. Although Mortensen *et al.* used rheology to probe the phase transitions, they did not provide insights into the potential transient character of supramolecular networks formed by reverse Pluronics® as they only considered one particular probing frequency in their study.

Multiblock copolymers

More complex as compared to telechelic BAB triblocks, is the hydrophobic association between the hydrophobic B blocks of multiblock copolymers. Such 'multisticker' polymers have the possibility to form more than one elastic bridge originating from one chain. Similar to telechelic triblocks, the size and nature of the B blocks dictate both the steady and transient dynamic properties, but the distribution of B blocks as either equally-spaced or statistical should also be considered. Moreover, the B blocks can contain the hydrophobically associating block as (long) side chains or truly incorporated into their polymer backbone. This multitude of features makes hydrophobically associating multiblock copolymers an equally interesting model system to gain systematic insights into the rheological behavior of transient networks as compared to telechelic systems, despite their rheological fingerprint being more complex.

Polyacrylamide (PAM) and its derivates have been widely employed as hydrophilic blocks in multisticker multiblock copolymers with aliphatic [168–170], aromatic [171], or fluorinated hydrophobic blocks [172] often prepared by micellar polymerization to control the homogeneous introduction of hydrophobic blocks in the chain [173]. Regalado *et al.* hydrophobically modified PAM with low amounts of N,N-dihexylacrylamide using free radical micellar polymerization, resulting in equally spaced multiblock copolymers. Figure 2.10 (a) displays the frequency dependent response of the dynamic moduli G' and G'' for a 5 wt% network prepared using 140 kDa PAM with 2 mol% of N,N-dihexylacrylamide, distributed as 7 hydrophobes per micelle during polymerization thereby resulting in 7 hydrophobic monomers per hydrophobic block. A clear viscoelastic response with a (much) broader distribution of relaxation times as compared to telechelic systems with often only one single relaxation time describing the dynamics [127], is obtained. The Maxwell model fit, shown as solid lines, indeed proves that the rheological response of networks formed by hydrophobically associating polymers only complies with the Maxwell model at low frequencies (i.e. the terminal behavior). Interestingly, this typical broad response is general, as networks with different synthesis characteristics and therefore variable block lengths all exhibit similar behavior [168]. In Figure 2.10 (b) and (c) the plateau modulus and relaxation time as obtained from the low frequency Maxwell model fit (corresponding to the slowest relaxation mode), respectively, are shown as a function of concentration in a log-

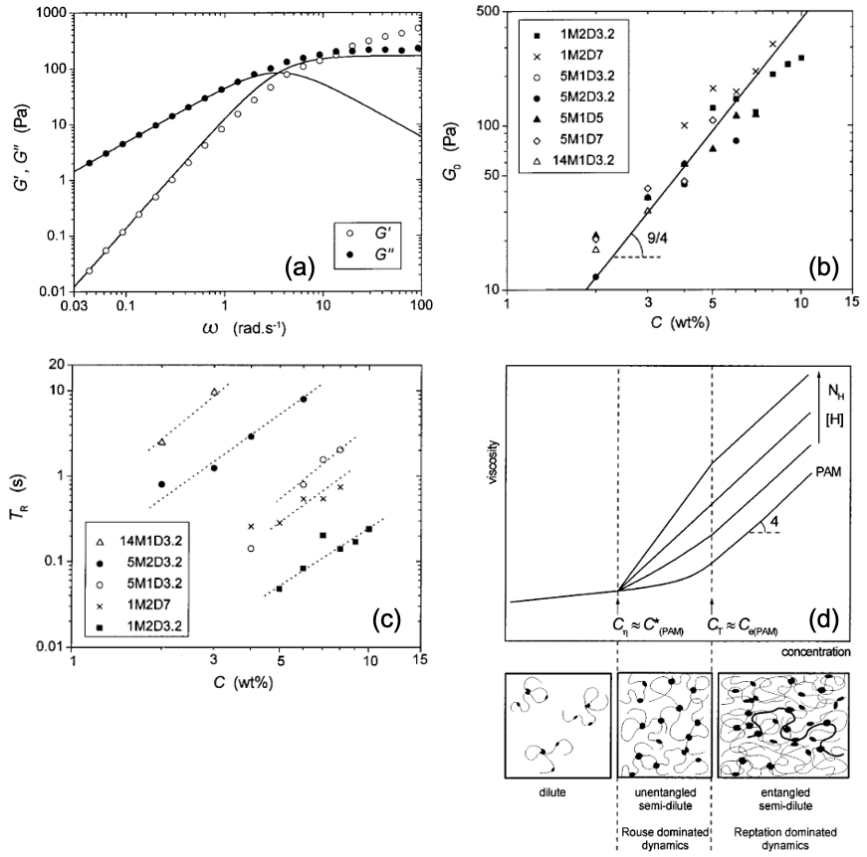

Figure 2.10: (a) Elastic (G') and storage modulus (G'') as a function of angular frequency ω for a network of 5 wt% 140 kDa PAM hydrophobically modified with 2 mol% dihexylacrylamide, incorporated as 7 repeating units in each hydrophobic block. The solid lines represent the low frequency Maxwell model fits. (b) Concentration evolution of the plateau modulus (of the slowest relaxation mode) for different types of hydrophobically associating multisticker polymers displaying a power law dependence with exponent 9/4. The name code includes M_w indicated as the first digit(s) prior to 'M', $[H]$ indicated as the digit prior to letter 'D' and N_H indicated as the last digit(s). (c) Concentration evolution of the longest relaxation time for different types of hydrophobically associating multisticker polymers displaying a power law dependence with exponents 2-3 and demonstrating the influence of M_w, $[H]$ and N_H. (d) Schematic illustration of the zero shear viscosity versus concentration for different types of hydrophobically associating multisticker polymers, indicating the different concentration regimes: dilute, semidilute unentangled en semidilute entangled. All figures reproduced from [168].

log plot for multisticker networks with different characteristics. These characteristics include the molecular weight of the PAM (M_w), the mol% of hydrophobe ($[H]$), and the amount of hydrophobes in a hydrophobic block (N_H). The Maxwellian plateau modulus seems to be independent of the characteristics of the multisticker polymers and obeys a power law dependence on the concentration with an exponent of 9/4. The relaxation time, on the other hand, significantly increases upon increasing M_w, $[H]$ or N_H which can be attributed to the presence of entanglements (reflected in M_w), an increase in the sticker density (reflected in $[H]$) or in the hydrophobicity of the hydrophobic blocks (reflected in N_H). The power law exponent of the relaxation time versus concentration was found to be on the order of 2 to 3. For the zero shear viscosity, a similar trend, i.e. an increase upon increasing M_w, $[H]$ or N_H, was also detected. Figure 2.10 (d) schematically demonstrates the pronounced viscosity increase as function of concentration upon increasing the density ($[H]$) and hydrophobicity (N_H) of the stickers in the hydrophobically modified PAM networks of Regalado *et al.*. It also illustrates the different concentration regimes, i.e. dilute, semidilute unentangled and semidilute entangled, which are evident from the distinct power law dependencies of the zero shear viscosity on the concentration. Analogous conclusions about the linear oscillatory response as well as the viscosity evolution of PAM multisticker networks were made by Cram *et al.* who studied networks of N,N'-dimethylacrylamide polymers containing dodecyl or octadecyl side groups statistically distributed along the chain [174]. Their study thus shows that the broad, non-Maxwellian rheological frequency response and the influencing molecular parameters are universal regardless of whether the nature of the multisticker polymers is 'blocky' or random. Besides simple hydrocarbon hydrophobic groups, also thermoresponsive blocks such as poly(N-isopropylacrylamide) [175] and PPO [176] have been incorporated in PAM polymers for the development of thermoreversible, multisticker networks.

Multiblock copolymers of PEO as hydrophilic block with poly(lactic acid) [177], PCL [178] or PPO [78, 80, 83, 85, 179] as hydrophobic blocks have also been reported, but these studies usually only focus on the thermogelling properties and construct a phase diagram with the sol-gel-sol transitions by either studying the viscosity (at a relatively low shear rate) or the dynamic moduli (at a relatively high frequency) as function of temperature. A characteristic rheological fingerprint as function of frequency for insights in the transient behavior of the supramolecular networks at different time scales or the evolution of the rheological network characteristics such as G_0 and τ with concentration is often lacking in these studies.

2.2.2 Networks formed by metal-ligand complexation

In contrast to the high functionality of hydrophobic crosslinking nodes, the functionality of a metal-ligand association is given by the coordination number and is usually on the order of 1 to 6 for transition metals [91]. The position and functionality of the ligands

influence its network forming capabilities. For linear polymer chains with two telechelic ligands (ditopic ligands) for example, networks can only be formed if functionalities above 2 are obtained (type I in Figure 2.11). This is usually achieved using either large transition metal ions such as rhodium(I) and iridium(I) [180], or using lanthanide metal ions such as neodymium (II), europium(III) and lanthanum(III) [102, 181]. Star-shaped or branched polymers with multiple telechelic ligands on their 'arms' or branches (multitopic ligands) [182, 183], as well as polymers with side-chain ligands [184, 185] or ligands incorporated in the polymer backbone [186, 187] (polymeric ligands), on the other hand, can all form networks even at functionalities of 2 (type II in Figure 2.11).

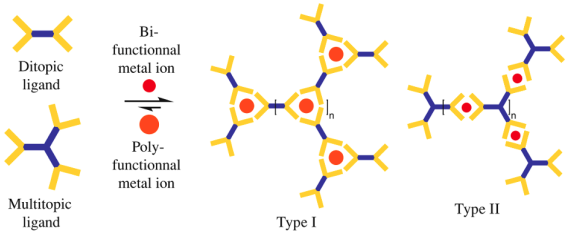

Figure 2.11: Schematic representation of different network principles of telechelic metallo-supramolecular polymers in which the polymer chains are in blue, the ligands in yellow and the metals in red. Type I consists of linear polymer chains with telechelic ligands (i.e. ditopic ligands) crosslinked by polyfunctional metal ions. Type II consists of star-shaped polymer chains with telechelic ligands (i.e. multitopic ligands) crosslinked by bi-functional metal ions, reproduced from [91]

Networks that rely on polymeric ligands combined with a relatively large amount of metal ions, have been widely covered in literature. For example, in the 1980's poly(acrylic acid) [188], polysaccharide [189], and cellulose derivatives [190] were found to form pH-dependent gels in combination with metal ions. More recently, pyridine-based (co-)polymers [186, 191], as well as conjugated polymers [187, 192] with advanced optical properties have received particular attention. Due to the wide variety of functional groups that can coordinate a metal ion, the synthetic feasibility of such polymeric ligands is the only factor restricting its diversity [91]. Therefore, this straightforward and extensively used route to obtain type II metallo-supramolecular polymer networks, is not discussed further in this dissertation. Instead, we focus on an alternative route in which the coordinating moieties are telechelically added to the polymer chains by post-functionalization, resulting in either di- or multitopic ligands. Whereas there are plenty examples of such type I [180], type II [182–185] or combination [102] supramolecular networks formed in organic solvents, there are only a few examples of corresponding hydrogels.

Vermonden *et al.* constructed type I metallosupramolecular hydrogels by crosslinking a concentrated solution of ditopic ligands, consisting of two pyridine-2,6-dicarboxylate groups connected to oligo(ethylene oxide) spacers with 4 to 8 repeating units, with trifunctional neodymium(III) or lanthanium(III) ions [181, 193]. However, they concluded that the networks predominantly consist of long linear supramolecular chains with entanglements as their main network junctions, similar to wormlike micelles. Hence, the trifunctional metal-ligand associations of their ditopic ligands did not serve as true crosslinks in the network structure, but rather created cyclic defects in the long supramolecular polymers.

For the development of type II supramolecular hydrogels based on multi-arm star polymers, poly(ethylene oxide) has emerged as an ideal polymer candidate due to its promising potential in biomedical and pharmaceutical applications. Inspired by the fascinating chemistry behind mussel byssal threads, Holten-Andersen *et al.* created type II supramolecular hydrogels based on four-arm PEO stars telechelically modified with catechol and addition of iron(III) ions [195]. The stoichiometry of these complexes changes from mono-, over bis- to tri-complexes upon deprotonation of the catechol hydroxyl groups at increasing pH, thereby resulting in a strongly pH-responsive hydrogel. In addition to catechol, also 3,4-dihydroxyphenylalanin [196] and histidine ligands [194, 197] are mussel-inspired ligands commonly employed in star-shaped PEO-based hydrogels. Grindy *et al.* studied the effects of the PEO arm length, the PEO concentration as well as the metal-to-ligand stoichiometry on the elasticity and relaxation time of four-arm PEO networks crosslinked by nickel(II)-histidine complexes [194]. Figure 2.12 (a) shows the linear dynamic moduli G' and G'' as a function of angular frequency for such networks with different concentrations and different arm molecular weights. The solid lines are the Maxwell model fits (see Equations 2.3 and 2.4)) and show good agreement with the data. Figure 2.12 (b) and (c) show the Maxwellian plateau modulus G_N and the relaxation time τ, respectively, as a function of polymer volume fraction for different molecular weights (in a log-log plot). The relaxation time is less strongly influenced by the concentration as compared to the plateau modulus. A scaling exponent of 9/4 for the plateau modulus versus volume fraction is obtained, as also previously obtained for telechelic, hydrophobically associating HEUR polymers. When keeping the metal-ligand pair constant, they found that the elasticity can further be tuned by the star arm length and concentration as well as the metal-to-ligand ratio, whereas the relaxation time is only governed by the latter [194].

A final class of PEO-based star polymers uses telechelic terpyridine ligands for their crosslink interaction with metal ions (cfr. supra). Extensive work was done by Rossow *et al.* who studied hydrogels constructed by telechelic terpyridine-functionalized four-arm PEO stars in water and different organic solvents using various transition metals including cobalt(II), zinc(II) and manganese(II) [101, 198]. Figures 2.13 (a) and (b) show the linear rheological response of cobalt(II) and zinc(II) networks, respectively,

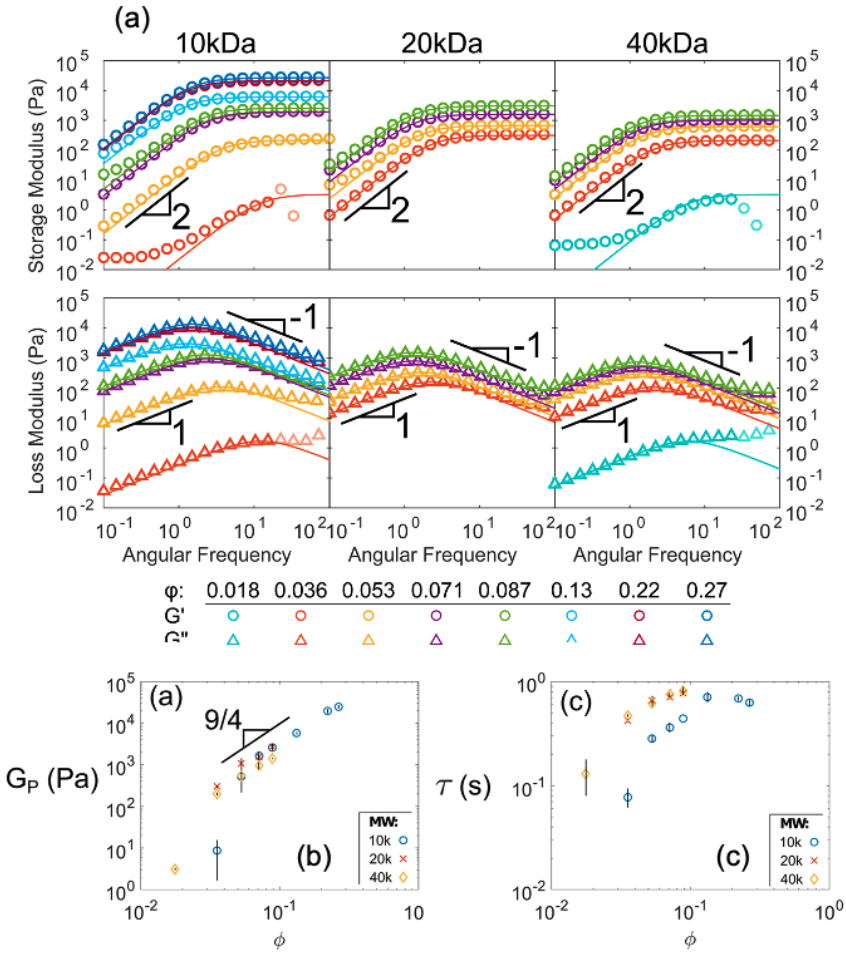

Figure 2.12: Rheological properties of 4-arm PEO metallosupramolecular hydrogels crosslinked by nickel(II)-histide complexes in a ratio of $[Ni^{2+}]$:[His] = 1:2 at 20 °C: (a) elastic (G') and storage modulus (G'') as a function of frequency for different concentrations (ϕ = 0.018-0.266) and molecular weights (10, 20, 40 kDa) with the solid lines representing the Maxwell model fits. Evolution of the (b) plateau modulus G_p and (c) the relaxation time (τ) as function of the polymer volume fraction, with the solid line in (b) indicating the slope of 9/4. All figures are reproduced from [194].

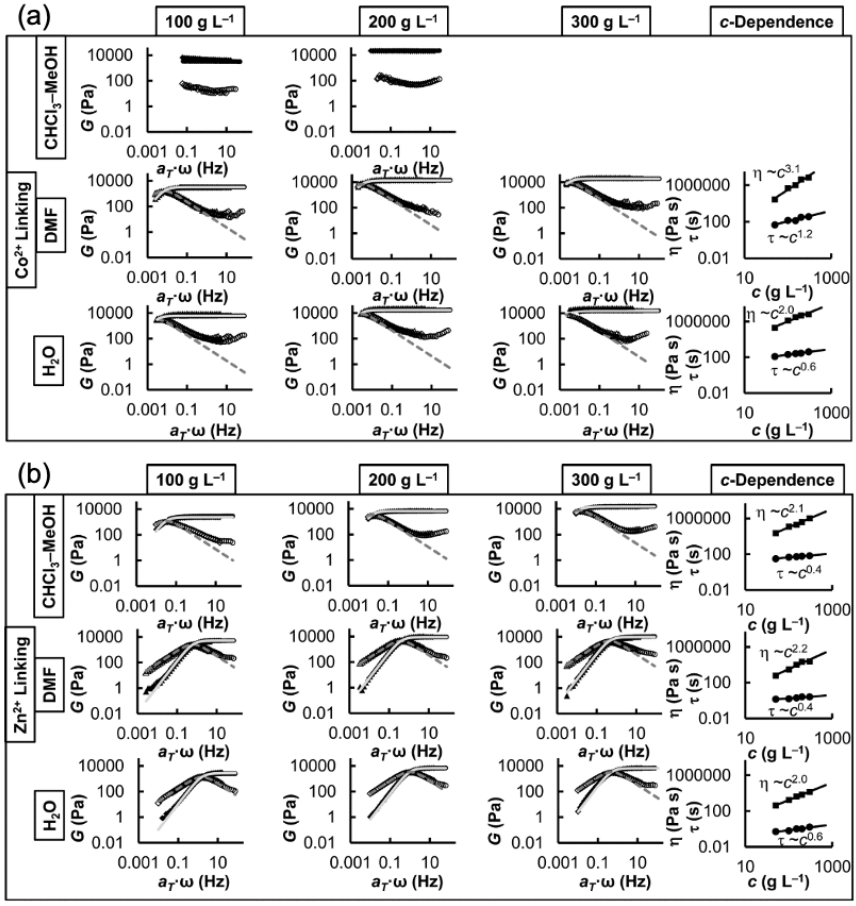

Figure 2.13: Rheological properties of 4-arm PEO metallosupramolecular hydrogels crosslinked by terpyridine complexes with different metal ions in a ratio of $[M^{2+}]$:[tpy] = 1:2 (a) cobalt(II) crosslinking and (b) zinc(II) crosslinking. The different rows represent the different solvents chloroform-methanol (1:1), dimethylformamide and water. The different columns show different polymer concentrations (100, 200 and 300 g/L). The dynamic moduli G' and G'' are obtained by time-temperature superposition of measurements at 25°C and at 40°C. Mastercurves at 25°C are shown. The solid lines represent the Maxwell model fits. The last column shows the evolution of the relaxation time (τ) and the viscosity (η) as function of polymer concentration with the solid lines representing the power law fits. The obtained power law exponents are also shown. All figures are reproduced from [101].

in different solvents (rows) and at different concentrations (columns). The dynamic moduli as a function of angular frequency again comply with the Maxwell model of Equations 2.3 and 2.4 (shown as solid lines). The last column in Figures 2.13 (a) and (b) displays the concentration dependence of the obtained relaxation time τ and the viscosity η in log-log plots with the scaling exponents indicated in the plots. The results show that very different rheological behavior can be obtained depending on the metal ion, solvent and concentration. Networks crosslinked by zinc(II) are significantly more labile at 25°C as compared to those crosslinked by cobalt(II), with their terminal relaxation almost three decades apart. The scaling exponents of τ and η show a weak concentration dependence of the relaxation time as compared to the viscosity and do no particularly agree with any existing rheological frameworks predicting the rheology of transient networks (cfr. infra). Besides a macroscopic assessment of the network elasticity and dynamics, microstructural investigations by static light scattering revealed a minor amount of nano-scale structural defects in networks constructed by zinc(II)-terpyridine complexes, making these networks potential model networks [198], whereas networks constructed by cobalt(II) showed significant heterogeneity. In addition to this structural evidence, the number density of elastically active chains ν, as inferred from the plateau modulus G_0 (see Equation 2.5), revealed for cobalt(II) networks more elastically active chains than theoretically possible based on the polymer shape and concentration. This, combined with the higher flow activation energy of these networks as compared to those with zinc(II), indeed proves that in cobalt(II) networks, there probably exists additional building block connectivity such as junction clustering, resulting in mechanical reinforcement but also a heterogeneous network topology [198].

2.3 Theoretical frameworks for transient network rheology

During the last few decades, many authors have tried to fundamentally understand and predict the linear and non-linear rheological properties of supramolecular polymer networks and gels based on so-called transient network models. The often Maxwellian linear rheological behavior of networks formed by telechelic ‘stickers’ suggests a universal response based on the position of the stickers as telechelic end groups. Therefore, we group the theoretical frameworks based on the sticker position, even though other influencing factors such as the functionality (and size) of the crosslink interactions as well as the possible presence of entanglements play a crucial role.

Table 2.2: Characteristics of different theoretical frameworks as well as the scaling laws describing the concentration dependency of the linear rheological properties G_0, τ_N and τ_S in different concentration regimes, with ν the Flory exponent ($\nu = 0.588$ for a good solvent) and z accounts for excluded volume interactions ($z = 0.225$ for a good solvent).

Model	Authors	Sticker position	Interaction functionality	Entanglements	Concentration regime	G_0	τ_N	τ_S
Tanaka-Edwards transient network model	Tanaka-Edwards [199–202]	telechelic	f $\gg$ 2	no		$\sim c^1$	$\sim c^0$	
Cates model	Cades-Candau [139,203]	telechelic	f $\gg$ 2	yes	c > c*	$\sim c^{\frac{3\nu}{3\nu-1}} \approx 2.3$	$\sim c^{1.4-1.5}$	
Telechelic micellar model	Semenov [204]	telechelic	f $\gg$ 2	possible	c > c* c $\gg$ c*	$\sim (\frac{c}{c^*} - 1)^{\frac{6\nu}{3-2\nu}} \approx 1.93$ $\sim c^{\frac{3\nu-4/3}{3\nu-1}} \approx 0.56$	$\sim \exp(f_1(c,\nu))$ $\sim \exp(f_2(c,\nu))$	
Sticky-Rouse model	Baxandall-Rubinstein-Semenov [205–207]	multisticker	f = 2	no	c < c_{ren} [i] c_{ren} < c < c_s [ii] c_s < c < c_e [iii]	$\sim c^{\frac{3\nu+z}{3\nu-1}} \approx 2.60$ $\sim c^{\frac{3\nu+z}{3\nu-1}} \approx 2.60$ $\sim c^1$	$\sim c^{\frac{2+2z}{3\nu-1}} \approx 3.20$ $\sim c^{\frac{6+7z}{6\nu-2}} \approx 4.96$ $\sim c^{\frac{z}{6\nu-2}} \approx 0.17$	$\sim c^{\frac{2+3z}{6\nu-2}} \approx 1.81$ $\sim c^{\frac{z}{6\nu-2}} \approx 0.17$
Sticky-reptation model	Leibler-Rubinstein-Semenov [208,209]	multisticker	f = 2	yes	c_e < c < c_{ren} [i] c_{ren} < c < c_s [ii] c_s < c < c_{le} [iii] c_{le} < c < 1 [iv]	$\sim c^{\frac{3\nu}{3\nu-1}} \approx 2.3$ (entanglements plateau)	$\sim c^{\frac{3+2z}{3\nu-1}} \approx 2.90$ $\sim c^{\frac{4+3.5z}{6\nu-2}} \approx 3.13$ $\sim c^{\frac{1+0.5z}{3\nu-1}} \approx 1.46$ $\sim c^{\frac{1.75+0.5z}{3\nu-1}} \approx 2.44$	$\sim c^{\frac{2+3z}{6\nu-2}} \approx 1.81$ $\sim c^{\frac{z}{6\nu-2}} \approx 0.17$ $\sim c^{\frac{3+2z}{12\nu-4}} \approx 0.15$
Multisticker micellar model	Semenov [210]	multisticker	f $\gg$ 2	possible	c > c*	$\sim c^{1-1/(9\nu-3)} \approx 0.56$	$\sim \exp(f(c,\nu))$	

[i] Unrenormalized bond lifetime, transfer from intra- to intermolecular associations;
[ii] Renormalized bond lifetime, transfer from intra- to intermolecular associations;
[iii] Renormalized bond lifetime, mainly intermolecular associations;
[iv] Renormalized bond lifetime, entanglements between stickers $M_S > M_E$.

It should be highlighted that the following sections do not in any way attempt to provide a complete overview of all possible network frameworks, but rather cites some pioneering and widely exploited theories. Additionally, our discussion is mainly limited to the linear rheological behavior in view of the content of this dissertation, since an extensive discussion of the non-linear rheological properties would take us too far. Table 2.2 summarizes the typical characteristics of most of the theoretical frameworks mentioned below. The scaling laws predicting the concentration dependencies of the linear rheological properties, i.e. the network plateau modulus G_0, the network (or longest) relaxation time τ_N and the sticker dissociation time τ_S, in different concentration regimes are also shown.

2.3.1 Telechelic stickers

Tanaka-Edwards and modifications

The transient network models originally developed by Green and Tobolsky [211], Yamamoto [212] and Lodge [213] for entangled polymer solutions, and later modified by Tanaka and Edwards [199–202] for unentangled telechelic, physically associating polymers, predict a single relaxation time, which represents the lifetime of a network strand and hence remains constant as a function of concentration. It is correlated to the sticker dynamics as:

$$\tau_N = \beta_S^{-1} = \tau_0 \exp\frac{\Delta G}{k_B T}, \tag{2.7}$$

in which β_S is the sticker dissociation rate, $\tau_0 = \beta_{S,0}^{-1}$ is a time constant characteristic of the thermally activated attempt rate at which a sticker dissociates from the crosslink interaction (i.e. the inverse of the 'thermal vibration frequency' $\beta_{S,0}$) and ΔG is the potential energy barrier for changing from the associated to the dissociated state. The plateau modulus of the network ($G_0 = \nu k_B T$), on the other hand, linearly increases with concentration, since the number density of elastically active chains ν is proportional to the number density of chains n (and hence the concentration), according to the following equation as derived by Tanaka and Edwards

$$\nu = n \cdot \frac{\exp(\Delta G/k_B T)}{1+\exp(\Delta G/k_B T)}. \tag{2.8}$$

As a consequence, the zero-shear viscosity ($\eta_0 = G_0 \cdot \tau_N$) also linearly evolves with concentration. To account for the peculiar non-linear rheological response of transient networks, Tanaka and Edwards argued that the association or creation rate α and dissociation rate β of the sticky interactions should differ and that the dissociation rate β should depend on the HEUR chain's shear rate dependent end-to-end distance r according to $\beta = \beta_0 f(r)$. For ideal Gaussian chains, the exponential $f(r)$ function

(see Table 2.3) made the analytical calculations too complex. Therefore, without any physical evidence, Tanaka and Edwards proposed a quadratic function $f(r) = c_1 + c_2 r^2$ in their model derivations.

Experimental observations of the linear rheological properties in telechelic transient networks do not obey the simple Tanaka-Edwards scaling relationships with concentration and show stronger dependencies [147]. Moreover, the Tanaka-Edwards model fails to predict some common non-linear rheological features of transient networks, such as shear thickening, using their proposed $f(r)$ functions for the dissociation rate [150–152]. Therefore, they form the basis for more generalized constitutive modeling as performed by other authors including Marrucci *et al.* [159], Vaccaro *et al.* [214] and Tripathi *et al.* [152], or for the Brownian dynamics simulations of Van den Brule *et al.* [215, 216]. These modified Tanaka-Edwards models account for additional effects such as non-Gaussian chain stretching, free and dangling chains, multiple sticker dissociation and reassociation events prior to complete chain relaxation, as well as shear-induced enhancement and dissociation of associative interactions responsible for shear thickening and thinning behavior, respectively. All these effects have an influence on the shear rate and chain size dependence of both the creation ($\alpha = \beta_0 f_\alpha(r)$) and dissociation rate ($\beta = \beta_0 f_\beta(r)$). As a matter of comparison, the $f(r)$ functions as derived in some of these modified models are summarized in Table 2.3.

Table 2.3: Comparison of the $f(r)$ model expressions of the association rate ($f_\alpha(r)$) and dissociation rate ($f_\beta(r)$) in various transient network models, in which c_1, c_2, c_3 and c_4 are model-specific constants, $r = \sqrt{\langle r^2 \rangle}$ is the average end-to-end distance of a bridging chain, γ is the total strain and $\dot{\gamma}$ is the shear rate. Adapted from [152].

Model	$f_\alpha(r)$ for association	$f_\beta(r)$ for dissociation
Green-Tobolsky [211]	1	1
Tanaka-Edwards [199–202]	c_1	$\exp(c_2 r)$ (Gaussian) $c_3 + c_4 r^2$
Wang [217]	$c_1 + c_2 \beta_0^{-2} \dot{\gamma}^2$	$1 + c_3 r^2 / r_{eq}^2$
Ahn-Osaki [218]	$\exp(c_1 \gamma)$	$\exp(c_2 \gamma)$
Van den Brule-Hoogerbrugge [215]	$c_1 r / r_{eq}$	2
Vaccaro-Marrucci [214]	$c_1 + c_2 r / r_{eq}$	$1/(1 - r^2 / r_{max}^2)$

Annable

The modified Tanaka-Edwards transient network theories still fail to explain the strong effect of concentration on the network's linear rheological properties, especially the elastic modulus [147]. Therefore, a different approach as compared to constitutive modeling was taken by Annable *et al.*, who developed a so-called mechano-statistical transient network model for unentangled, telechelic BAB triblock copolymers [147, 148]. In their model, they take into account that an intermediate A block can either form a bridge (with a probability $F_1 = 1 - F_2$) and thereby contribute to elasticity, or a loop (with a probability F_2) which is elastically inactive and more likely to be formed at low concentrations, resulting in a steeper concentration dependency of the plateau modulus. Additionally, Annable *et al.* also argue that the presence of 'superstructures' such as superloops and -bridges, which are more abundantly present at low concentrations, influence the rheological properties. The former do not contribute to elasticity at all (much like single-chain loops), whereas the latter consist of successive single-chain bridges of which each does not uniquely contribute to elasticity as a single bridge, but as as a fraction of one superbridge. In addition, superbridges also speed up the relaxation due to their increased dissociation probability. Based on their model, Annable *et al.* predict a topological evolution from a loop- and superstructure-dominated network to a bridge-dominated network upon increasing concentration, which is responsible for the macroscopic mechanical behavior. Their fairly simple approach resulted in accurate predictions of the evolution of the number density of elastically active chains and relaxation times for HEUR polymers, as inferred from

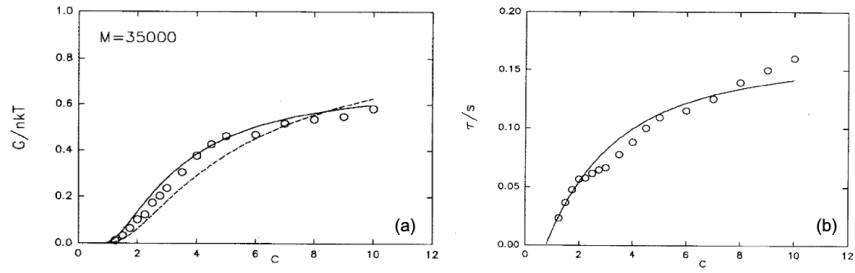

Figure 2.14: Rheological properties of networks formed by HEUR polymers with 16C hydrophobic linear alcohol blocks and 35kDa hydrophilic PEO blocks at 298 K: (a) evolution of the fraction of elastically active chains ($\nu/n = G_0/nk_BT$) as a function of HEUR concentration with the solid and dashed lines representing the mechano-statistical transient network model as derived by Annable *et al.* [147] using 70% and 100% end-cap efficiency, respectively, and (b) evolution of the relaxation time (τ) as function of concentration with the solid line as the model prediction using 70% end-cap efficiency. All figures are reproduced from [147].

linear shear rheology, and showed agreement with their predictions from simplified Monte-Carlo simulations [147]. Figures 2.14 (a) and (b) show the concentration evolution of the fraction of elastically active chains ($\nu/n = G_0/nk_BT$) and the single (Maxwellian) relaxation time, respecitively, for 16C/35 HEUR chains with the solid lines in (a) and (b) representing the mechano-statistical model predictions of Annable *et al.* using an end-cap efficiency of 70%, and the dashed line in (a) using an end-cap efficiency of 100%. The model succeeds in predicting the rheological data quite well, with both rheological parameters first increasing non-linearly and then leveling off as function of concentration. This seems to be an accurate representation of the elasticity evolution, but the continued increase of the relaxation time with concentration at high concentrations indicates that the mechano-statistical model is probably too simplistic for describing the relaxation behavior. A possible explanation resides in the concept of multiple dissociation and reassociation events of a hydrophobe prior to complete bridge relaxation (as introduced in the modified Tanaka-Edwards models), which becomes increasingly important at higher concentrations and is not considered by Annable *et al.* [147, 148].

Cates-Candau

It is important to note that in the above network frameworks, it is assumed that the sticker dissociation is the rate-limiting step, implying that the chain relaxation is infinitely fast as compared to the sticker dissociation. This can be justified by the absence of chain entanglements and considering Rouse-like chain dynamics. In the model derived by Cates for networks formed by wormlike micelles [203], on the other hand, the competition between the timescales for chain scission by dissociation of the micellar interaction (τ_{break}) and chain relaxation (τ_{chain}) plays a crucial role. This finds its origin in the 'living' nature of wormlike micelles, which form entangled networks, but whose chain dimensions heavily depend on possible breakage events. Therefore, Cates models their behavior by adopting classical reptation theory for entangled polymers, which can be accelerated by the dissociation of the chain. He thereby assumes that the chains break with equal probability per unit time and length, and that chain recombination occurs at a rate proportional to the concentration of chain fragments. If $\tau_{break} \ll \tau_{chain}$, the network relaxation is governed by chain (reptation) relaxation. If $\tau_{break} \gg \tau_{chain}$, on the other hand, the stress relaxation was found to be dominated by chain scission, similar to the assumptions made in the above mentioned theoretical frameworks. In case $\tau_{break} \approx \tau_{chain}$, both timescales come into play and an average relaxation time $\tau_N = \sqrt{\tau_{break}\tau_{chain}}$ is observed. In a later work, Cates and Candau derived the scaling exponents of G_0 and τ_N with concentration as shown in Table 2.2 based on a mean-field approach including excluded volume interactions. Nyrkova and Semenov extended the Cates-Candau model by allowing multiple self-recombinations of broken chains based on spatial correlation effects, thereby considering the effective (or renormalized) τ_{break} as the time it takes for a

chain to, upon breakage, associate with a different new chain [219]. Even though the Cates-Candau model and its modifications have been derived for living polymers, they have been successfully applied to other supramolecular transient networks as well [161, 193, 220, 221].

Telechelic micellar model

Instead of considering individual polymer chains, a very different approach for networks constructed through multifunctional sticker interactions and hence non-negligible crosslink sizes, was proposed by Semenov *et al.* [204]. They analyzed such micellar networks as a dense suspension of spherical micelles with a significant attractive interaction due to polymer bridging. In the micellar gel regime, the interactions between micelles are assumed to be dominated by excluded volume repulsions rather than attractive polymer bridging, with its elasticity fully governed by micellar compression. Stress relaxation, on the other hand, requires at least half of the micelles to change their position in the network, i.e. to hop over a distance on the order of their size. Such micellar hopping induces an exchange of bridges, but also an additional deformation of the gel. Moreover, for such micellar hopping events to take place, all of the connecting bridges should be relaxed. Depending on whether the energy barrier for deformation (U) or the energy barrier for bridge exchange (B) dominates, the network relaxation scales as $\tau_N \sim \exp(\Delta F_b + U)$ or $\tau_N \sim \exp(\Delta F_b + B)$ in which ΔF_b represent the energy needed for 'debridging' a micelle from all of its neighbors. As such, complex exponential scalings of τ_N versus concentration are obtained. The obtained characteristic scaling relations of G_0 and τ_N with concentration are given in Table 2.2. Inspired by the work of Semenov, Pham *et al.* constructed scaling laws based on a short-range interaction potential between soft spheres [222]. Governed by the compression of the soft sphere micelles, this 'micellar transient network model' predicts a quadratic scaling of the plateau modulus with concentration. Meanwhile, the relaxation time evolves with an exponential scaling as a function of concentration and reflects the need for micellar reorganization and hopping to completely relax all stress stored in the network, very similar to the scaling relations developed by Semenov [204]. Amin *et al.* argue that the dissociation of a sticker from all of its sticky interactions in one micelle is energetically unfavorable and they suggest stress relaxation through a 'partner exchange' mechanism instead of single sticker hopping, as inferred from hybrid molecular dynamics/Monte Carlo simulations [223]. This exchange requires two association clusters to first merge and form a bigger cluster, which then subsequently breaks up in two smaller clusters, but with different partners.

Since micellar model approaches also fail to quantitatively capture the complex concentration dependency of the rheological properties [156], Xu *et al.* proposed a hybrid transient network model in which the micelle is the fundamental building block, rather than individual chains, but in which the elasticity is still governed by bridging

chains instead of compression [224]. By comparing the micelle model and Annable's mechano-statistical network model [147], Meng *et al.* ultimately conclude that at low network concentrations, the micellar picture is more accurate due to significant excluded volume repulsions between micelles and highly stretched bridges, whereas at higher network concentration, the effective screening of excluded volume interactions results in Gaussian, bridging chains fully responsible for the network's rheology (cfr. Annable and (modified) Tanaka-Edwards theories) [156]. This multitude of different (hybrid) models shows that there is still no consensus on the exact structure-property relationships in transient networks, especially those with large-scale crosslinking nodes, and proves the need for additional theoretical, experimental or simulation studies [146]. In this regard, Mordvinkin *et al.* recently exploited multiple-quantum NMR on unentangled, telechelically associating polymers forming micellar networks to extract bond lifetimes. By correlating these timescales and their temperature dependencies with the ones obtained from linear rheology, they showed that even for networks formed by micellar crosslinking nodes, the terminal relaxation is governed by single chain relaxation principles rather than micellar reorganization [225, 226].

2.3.2 Stickers along the chain

Unlike telechelic polymers exhibiting ideal Maxwellian behavior, non-telechelic associative polymers, having 'sticky' groups distributed along the chain, show more complex linear rheological behavior [127, 227]. A limited amount of studies try to capture their rheological response based on constitutive modeling, thereby exhibiting only qualitative agreement with experimental data [228–230], whereas simulations usually succeed in predicting the response more accurately, but lack an a priori physical interpretation of the system's behavior [231, 232]. Amongst the existing transient network models considering multisticker polymers, the theoretical frameworks developed by Leibler, Rubinstein, Colby and Semenov are probably the most widespread. These are known as the 'sticky Rouse' [205–207] and 'sticky reptation' models [208, 209] for unentangled and entangled multisticker associative polymer solutions, respectively, and were developed based on a single-chain approach with pairwise interactions between the sticky groups.

Sticky Rouse

Due to the multisticker nature of a chain with S stickers per chain ($S > 2$), the size of the elastically active strands is smaller than that of the entire chain [206, 207]. Therefore, the relaxation of an entire polymer chain is attained by repeated dissociation and association processes of all S stickers belonging to the chain. This is in contrast to the telechelic case, in which the dissociation of one of the stickers allows full chain relaxation. Figure 2.15 (a) and (b) schematically represent a typical frequency- (or

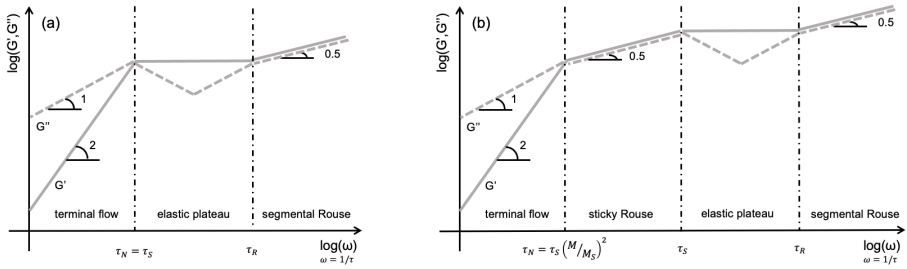

Figure 2.15: Schematic representation of the characteristic evolution of G' (solid line) and G'' (dashed line) as a function of frequency for (a) a telechelically associating polymer network and (b) a multisticker associating polymer network. The different regimes probed at different time scales are indicated.

time-)dependent rheological fingerprint for both telechelic and multisticker unentangled associative networks, respectively. At very short timescales (or very high frequencies) below the Rouse time τ_R, segmental Rouse-like relaxations are probed. Above τ_R and at timescales shorter than the sticker dissociation time τ_S, a network with an elastic plateau is probed in both cases. Once a sticker dissociates at τ_S, i.e. the lifetime of a bond, a telechelic network can fully relax ($\tau_N = \tau_S$) resulting in terminal flow behavior. In a multisticker network, on the other hand, the sticker dissociation triggers a Rouse-like relaxation mechanism, the so-called sticky Rouse regime with a characteristic slope of 0.5 representing the relaxation of individual gel strands when one of their stickers dissociates [205]. Assuming uncorrelated and independent sticker dissociation events in the entire chain, the network relaxation time (or longest relaxation time) is related to the sticker dissociation time as $\tau_N \sim N^2 \tau_S$, in which N represents the amount of network strands per chain. In the absence of loops and with a negligible size of the associating stickers, N can be calculated as M/M_S with M the molecular weight of the entire chain and M_S the molecular weight between stickers. In that case, both τ_S and τ_N are independent of the concentration. However, Rubinstein and Semenov also recognized the significant presence of loops, or intramolecular associations, at lower concentrations and have therefore theoretically derived the gradual concentration dependent transition form intra- to intermolecular associations. Moreover, they introduced the concept of a renormalized bond lifetime, which takes into account multiple dissociation and reassociation events of a sticker before it eventually really detaches and recombines with another partner. This mechanism is especially important for high concentrations of strong association interactions. Note that this concept has already been exploited in the modified Tanaka-Edwards transient network models [152,159,215] and in the Cates model as well [219]. Both the effects of intramolecular associations and renormalized sticker dissociation times induce a particular concentration dependency of both τ_N and τ_S, as shown in Table 2.2 for the different network concentration regimes.

Sticky reptation

The concepts of the sticky reptation model are very similar to those of the sticky Rouse model, except that the entanglements serve as additional junctions and that the chains relax according to a reptation mechanism. Based on whether the entanglements, with a characteristic molecular weight between the entanglements M_E, are present abundantly in every network strand ($M_E < M_S$), or just occasionally along the chain ($M > M_E > M_S$), different rheological fingerprints of the elastic modulus G' are obtained as shown in Figure 2.16. In case $M_E < M_S$ (orange in Figure 2.16) and upon dissociation of a sticker at τ_S, a fraction M_S/M of the chain can reptate over a distance on the order of the end-to-end segment size between stickers, i.e. $a_E\sqrt{M_S/M_E}$ in which a_E is the length between entanglements. Complete network relaxation happens upon reptation over a distance equal to the entire chain's contour length $a_E(M/M_E)$ and therefore

$$\tau_N = \frac{M}{M_S}\cdot\tau_S\cdot\left(\frac{a_E(M/M_E)}{a_E\sqrt{M_S/M_E}}\right)^2 = \tau_S\cdot\frac{M}{M_S}\cdot\frac{M^2M_E}{M_E^2M_S} = \tau_S M^3 M_S^{-2} M_E^{-1}.$$

In case $M_E > M_S$ (blue in Figure 2.16), an entangled strand can relax according to the sticky Rouse principle along the contour of the confining tube, due to the presence of many stickers along this strand, resulting in a characteristic slope of 0.5 with a relaxation time of the entangled strand $\tau_E = \tau_S(M_E/M_S)^2$. The relaxation time of the overall network, i.e. the sticky reptation time, is than $\tau_N = \tau_E(M/M_E)^3 = \tau_S M^3 M_S^{-2} M_E^{-1}$ [233, 234]. Hence, the expression for the longest relaxation time is the same as in the case $M_E < M_S$, but the rheological fingerprint has a typical double plateau, as first predicted by Leibler [208] and observed in some experimental systems [235]. The plateau at high frequencies corresponds to the elasticity induced by the associative stickers plus the entanglements, whereas the one at low frequencies represents the entanglements alone. Rubinstein and Semenov derived the scaling laws for both the reptation time τ_N and the (renormalized) bond life time τ_S in different concentration regimes, as summarized in Table 2.2.

Despite the extensive theoretical background of these 'sticky' models, experimental rheological data often show limited agreement with the model predictions [236–239]. Moreover, most associative polymer solutions obeying similar scaling relations as predicted by the 'sticky' frameworks, almost never fulfill the assumption of simple pairwise association [168, 174, 240]. Nonetheless, some interesting studies on (melt) networks with ionic [241, 242] or hydrogen bonding interactions [243–245], show striking agreement with the sticky models by taking into account polydispersity in the molecular weight and/or the number of stickers per chain. Interestingly, some authors even verify the renormalization concept of the sticker lifetime in rheology by probing the bare lifetime using additional experimental techniques such as dielectric spectroscopy [244, 246, 247].

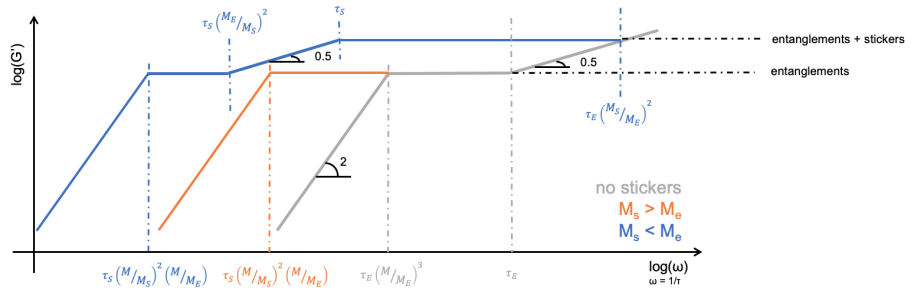

Figure 2.16: Schematic representation of the characteristic evolution of G' as a function of frequency for different scenarios: grey represents non-associative polymers without stickers, orange $M_s > M_e$ and blue $M_s < M_e$. The characteristic timescales and their expressions are indicated.

Multisticker micellar model

Alternatively, transient networks with large-scale crosslinking nodes formed by multisticker associative polymers were also treated by Semenov *et al.* according to a collective approach (cfr. supra), in which the dynamics of the overall aggregate assembly dominate over single chain relaxations [210]. In their approach, they suggest to neglect the renormalization of the bond life time by stating that the aggregation number varies around an average value N_{agg} due to which micelles with N_{agg} or $N_{agg} \pm 1$ stickers are equally probable and a sticker hopping event has an estimated energy change lower than the thermal energy k_bT. Similar to the micellar model for telechelic stickers [204], the network relaxation time or 'micellar hopping time' τ_h obeys an exponential scaling with concentration, usually in the form of $\sim \exp(c^n)$. Different

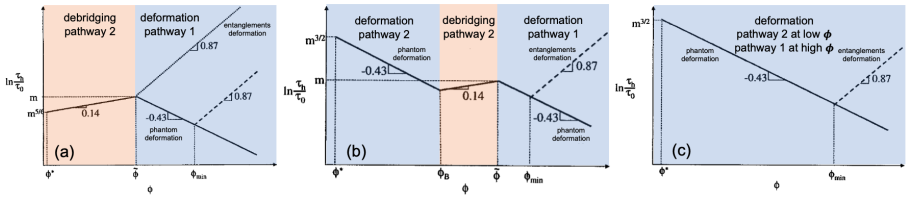

Figure 2.17: Concentration dependence of the logarithm of the network relaxation time (micelle hopping time τ_h) in different concentration regimes and for different scenario's in log-log plots: (a) large, (b) intermediate and (c) small activation energy. The limits of the different concentration regimes $\phi^*, \widetilde{\phi}, \phi_{min}, \phi_B$ are function of v, N_{agg}, the total activation energy for sticker dissociation, the chain length between stickers and the entanglement molecular weight. Figures are adapted from [210].

values for the exponent n are predicted in different concentration regimes depending on the dominant (fastest) kinetic pathway [210]. In this regard, pathway 1 requires conformational relaxation of all involved chains for micellar hopping to happen. Due to the long conformational relaxation times of entangled chains, however, pathway 2 allows a faster relaxation mechanism for non-overlapping micelles by first transforming all bridges of one micelle to loops, i.e. 'debridging', and subsequently moving the micelle to a new position without any sticker dissociation but with substantial deformation. If entanglements are involved, a deformation of the entanglements should also be taken into account besides the phantom deformation related to the micellar corona. Depending on whether debridging or deformation is the bottleneck for the hopping process to take place according to pathway 2, different scenario's and hence scaling exponents are possible. In Figures 2.17 (a), (b) and (c) the scaling laws of $\ln(\tau_h/\tau_0)$ versus concentration (or volume fraction ϕ) in which τ_0 represents the microscopic sticker diffusion time, in different concentration regimes are shown in which the dominant relaxation pathway and mechanisms are indicated. The transition from kinetic pathway 2 to kinetic pathway 1 typically occurs at the micellar overlap concentration $\tilde{\phi}$. Whether scenario (a), (b) or (c) is valid depends on how the total activation energy for sticker dissociation relates to the aggregation number and the entanglement molecular weight. Regardless of Semenov's very extensive work, an experimental verification of this 'micellar model' for multisticker associative polymers is lacking up to date.

2.4 Supramolecular double networks

As discussed in the previous sections, supramolecular chemistry and the ensuing possibilities for the formation of transient polymer networks and hydrogels with broadly tunable rheological properties greatly expand the polymer material palette. Another route that significantly contributes to the wide spectrum of polymeric materials is the combination of different polymer networks in so-called 'interpenetrating polymer networks' (IPNs). IPNs are 'alloys' of two or more separate polymer networks, in which at least one of the networks is crosslinked in the presence of the other network. These multicomponent polymeric systems usually exhibit synergistic properties as compared to the separate network contributions and have been an active field of polymer research since their first discovery in 1960 [248, 249]. Since the 2000s, the double network (DN) hydrogels, a special subset of IPN hydrogels in which two polymer networks with distinct mechanical features are asymmetrically combined, i.e. as a majority and a minority network, have attracted much attention for their ability to induce exceptional mechanical properties [250–253]. Especially in the biomedical field, such DNs hold a promising potential to mimic the properties of natural tissue, thereby overcoming the typical bottlenecks of poor mechanical performance of single network hydrogels [252]. In 2003, Gong *et al.* introduced the concept of a 'sacrificial' minority

network in their pioneering work on DN hydrogels [254]. Such a network is usually a rigid and brittle, densely crosslinked network [254–256]. Upon combination of this sacrificial network with a soft, loosely crosslinked majority network in a DN structure, Gong *et al.* obtained materials with superior mechanical properties as compared to the single networks [254–256]. Figure 2.18 (a) shows the stress-strain curves of poly(2-acrylamido-2-methylpropanesulfonic acid) (PAMPS) and poly(acryl amide) (PAAm) single networks, as well as a PAMPS-PAAm DN (containing 90 wt% of water) under compression and proves the significant increase in strength, fracture strain and toughness of the DN as compared to the individual single network contributions. In Figure 2.18 (b) pictures illustrate the ability of the PAMPS single network (left) and the PAMPS-PAAm DN (right) to sustain a high compression. The strongly increased toughness originates from the sacrificial bonds of the PAMPS network, which dissipate substantial amounts of energy upon breakage and thereby limit crack propagation. The second network then provides elasticity and the ability to maintain its original configuration and structure [256].

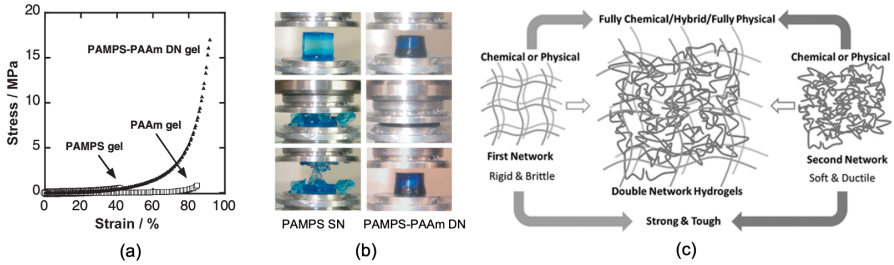

Figure 2.18: (a) Compressive nominal stress-strain curves for a PAMPS-PAAm double network, and PAMPS and PAAm single networks. (b) Photographs of a PAMPS single network (left) and a PAMPS-PAAm double network (right) before, during and after a high compression load, both (a) and (b) reproduced from [254] (c) Schematic illustration of a double network comprising of a rigid and brittle minority network and a soft and ductile majority network, reproduced from [250].

The concept of a sacrificial network, as schematically illustrated in Figure 2.18 (c), was first introduced for chemical DNs with covalent crosslinks in both networks, but has since been applied to associative, supramolecular polymers in either hybrid or fully physical DNs as well [251]. Hybrid DNs consist of a physical network that acts as the sacrificial minority network, combined with a covalently crosslinked second network. The reversibility of the sacrificial network imparts interesting, additional features such as self-recovery and fatigue resistance and effectively combines the benefits of both chemical and physical networks into one single polymeric material. In hybrid DNs, energy is continuously dissipated through repeated and reversible breakage of the sacrificial, physical associations under deformation, referred to as

'chain pulling-out' [252]. In physical DNs, on the other hand, both networks are formed based on two orthogonal types of physical and hence reversible crosslink interactions, resulting in true and autonomous self-healing behavior. Both networks can take part in energy dissipation via 'reversible chain association-dissociation' mechanisms [252]. Moreover, the combination of different, often stimuli-responsive physical associations allows orthogonal and selective control of the networks by environmental stimuli such as temperature, light, pH and ionic strength. The major disadvantage of such fully physical DNs is their susceptibility to long-term creep. Since the seminal work of Gong *et al.*, many different types of DN hydrogels have been reported, with a majority consisting of biopolymers and their derivatives such as chitosan, starch, alginate and gelatin [249, 252, 257].

For the construction of fully physical IPN or DN hydrogels, dynamic covalent bonds such as Schiff base bonds (imine, acylhydrazone and oxime), Diels-Alder bonds, disulfide bonds and boronic ester bonds have emerged as the most commonly used interaction types in the majority network due to their slow dynamics as compared to other supramolecular associations [258]. Such bonds are covalent and hence static in nature, but possess the ability to undergo dynamic bond exchange upon application of an external stimulus such as temperature (e.g. vitrimers), light or pH. As a result thereof, they possess shape memory properties, i.e. they can, induced by their external stimulus as a trigger, return from a deformed state to their initial shape, and they are less prone to creep. Here, we focus on all, but very limited amount of studies using rheology as the main tool to probe the elasticity and (partial) relaxation dynamics of physical and multiresponsive DN or IPN hydrogels with either hydrophobic association or metal-ligand complexation.

2.4.1 Based on hydrophobic association

Klymenko *et al.* report IPN hydrogels constructed by two different types of amphiphilic BAB triblock copolymers, one having a central PEO hydrophilic block and one with a central poly(acrylic acid) block [259]. Both triblocks form independent transient micellar networks by physical, hydrophobic association of their telechelic end-blocks, as illustrated in Figure 2.19 (a). The exchange dynamics of the PEO-based network are fast and independent of pH, whereas the network formed by PAA triblocks is strongly pH-sensitive. Its dynamics depend on the degree of ionization, i.e. it is fast at a high degree of ionisation obtained at neutral pH and slow at a low degree of ionization at pH = 5. Interestingly, under the influence of UV radiation the clustered hydrophobic blocks connected to the PEO blocks form in-situ and irreversible, covalent crosslinks, thereby converting the transient network to a permanent covalent network. In the IPN structure, the authors thus had control over the networks via either UV or pH as on/off switches for one of the networks, and figured that the percolation concentration of both networks was reduced as compared to their single network response, albeit

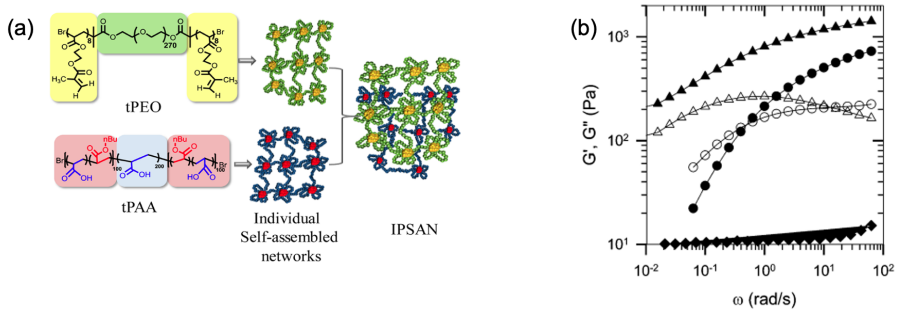

Figure 2.19: (a) Schematic illustration of an IPN combining two hydrophobically associating triblock copolymer networks: a UV-responsive PEO network and a pH responsive PAA network. (b) Dynamic moduli G' (filled symbols) and G'' (open symbols) as function of frequency for IPN networks before (circles) and after UV irradiation (triangles). The single PEO network after UV irradiation is also shown (diamonds). Both figures reproduced from [259].

to a different extent. They concluded that the presence of a second network favors bridging over loop formation in micellar networks, which has a beneficial effect on the rheological properties, i.e. increased elasticity and delayed relaxation time (at least below the network saturation concentration at which all chains form bridges). Upon covalent crosslinking of the PEO network, the rheological fingerprint of the elastic modulus G' versus frequency in Figure 2.19 (b) reveals a high frequency elastic plateau corresponding to the combined PEO and PAA network, a partial relaxation of the dynamic PAA network at intermediate frequencies and a low frequency plateau corresponding to the covalent PEO network [259].

2.4.2 Based on metal-ligand complexation

Yang *et al.* prepared a series of tunable IPN hydrogels by the orthogonal incorporation of pH-sensitive Schiff base bonds and metal-ligand coordination bonds in the polymer main chains [260]. Using linear shear rheology, they studied four different types of IPN hydrogels by combining either a very stable oxime or a less stable acylhydrazone dynamic covalent bond, with either a long-lifetime Fe^{2+}-terpyridine or a more dynamic Zn^{2+}-terpyridine metal-ligand complex. Figure 2.20 (a) schematically illustrates the different crosslinking interactions as employed by Yang *et al.*. They found that the IPNs exhibit a higher plateau modulus as compared to a mere addition of the single network moduli and attribute this to possible entanglements between the two networks, which are trapped in between two stickers and provide additional physical network junctions. Due to the static nature of the dynamic covalent bonds at neutral pH, they observe

partial relaxation through the sticky Rouse mechanism governed by the more fastly relaxing metal-ligand crosslinks (Zn^{2+}-terpyridine). Nonetheless, as inferred from Figure 2.20 (b), the complete relaxation of the metal-ligand network is delayed in the IPN structure (red) as compared to the single network (magenta). At low pH, Yang *et al.* observed an inversion of the relaxation times in IPN networks combining the more long-lifetime Fe^{2+}-terpyridine complexes with the more pH-sensitive acylhydrazone dynamic covalent bonds, thereby resulting in the pH as an external stimulus to promote different dynamics in the IPNs [260].

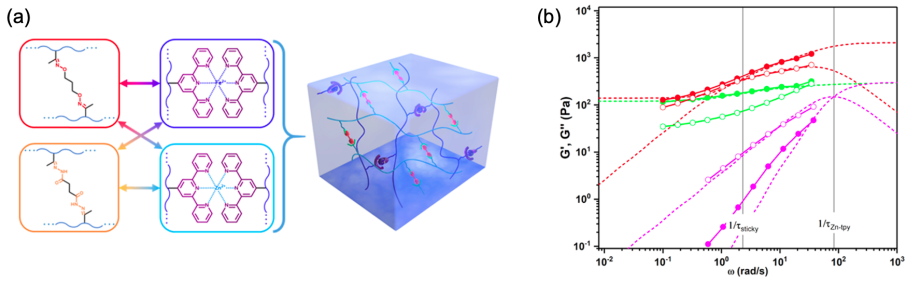

Figure 2.20: (a) Schematic illustration of an IPN combining different metal-ligand and dynamic covalent bonds. (b) Dynamic moduli G' (filled symbols) and G'' (open symbols) as function of frequency for a single Zn^{2+}-terpyridine metal-ligand network (magenta), a single acylhydrazone network (green) and an IPN combining both networks (red). Both reproduced from [260].

In a follow-up work, Yang *et al.* compared networks containing Zn^{2+}-terpyridine bis-complexes and oxime dynamic covalent bonds as either a dual-crosslink single network (DCN) in which both association types are present within one single polymer chain, as an IPN or as a DN (see Figure 2.21 (a)) [261]. Note that in the DN structure, a highly asymmetric distribution of crosslinks is present, i.e. a very densely crosslinked metal-ligand network serves as the sacrificial minority network and a sparsely crosslinked dynamic covalent network forms the majority network. Figure 2.21 (b) shows that for all network strategies, the linear rheological behavior is characterized by the presence of two elastic plateaus separated by a partial relaxation as governed by the faster dissociating metal-ligand interactions. All three network topologies result in a significant and synergistic increase of the elasticity as compared to the individual contributions, but with a different origin. In the IPN and DN structures, the increased elasticity is attributed to inter-network entanglements, whereas in the DCN the significantly increased density of elastically-active stickers as compared to the single networks is responsible for the synergistic plateau modulus. Even compared to the IPN and DN hydrogels, the DCN results in a significantly higher elasticity, as can be seen in Figure 2.21 (b). The authors argue that a possible cooperativity between

the stickers in the DCN structure could be the reason behind this large difference, since the formation of one type of crosslink can facilitate the formation of the other type of crosslink within the same chain. Interestingly, by studying the response of the single networks in the presence of the other network's precursors (without the crosslinkers), they revealed that the presence of uncrosslinked chains induces a 'screening' effect and promotes the formation of elastically inactive intrachain associations, especially for the more labile metal-ligand network. In the case of both crosslinks being active, on the other hand, the above mentioned screening effect was absent and they suggest that the topological constraints of the other network, even promote effective crosslinking [261] (as also concluded by Klymenko *et al.* [259]).

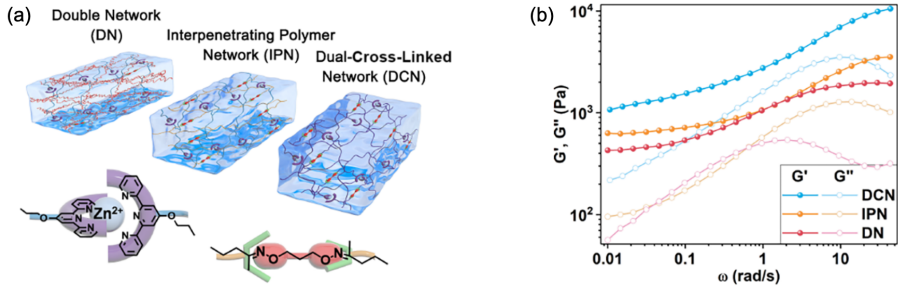

Figure 2.21: (a) Schematic illustrations of the dual-crosslink single network (DCN), the IPN and the DN hydrogels combining metal-ligand and dynamic covalent bonds. (b) Dynamic moduli G' (filled symbols) and G'' (open symbols) as function of frequency for all three network strategies. Both reproduced from [261].

Chapter 3

Materials and methods

Parts of this chapter are taken from the following publications and slightly adapted to be better integrated in this dissertation:

An-Sofie Huysecom, Christ Glorieux, Jan Thoen, Wim Thielemans, Charles-André Fustin, Paula Moldenaers and Ruth Cardinaels, "Phase behavior of medium-length hydrophobically associating PEO-PPO multiblock copolymers in aqueous media", *Journal of Colloid and Interface Science*, 641:521-538, 2023

An-Sofie Huysecom, Wim Thielemans, Paula Moldenaers and Ruth Cardinaels, "A generalized mechano-statistical transient network model for unravelling the network topology and elasticity of hydrophobically associating multiblock copolymers in aqueous solutions", *Macromolecules*, 56(2):612-633, 2023

3.1 Materials

3.1.1 Commercial PEO-PPO multiblock copolymers

ExpertGel® (EG) polymers of type 312 and 412 were kindly donated by PolymerExpert (France) and used without further purification. ExpertGel molecules are linear multiblock copolymers of alternating poly(ethylene oxide) (PEO) and poly(propylene oxide) (PPO) blocks. The exact structure of ExpertGel® molecules is inferred from experimental Fourier Transform Infrared Spectroscopy (FT-IR), Gel Permeation Chromatography (GPC) and ^{1}H Nuclear Magnetic Resonance Spectroscopy (^{1}H-NMR),

combined with the information found in the original patent from PolymerExpert describing ExpertGel® molecules (US7339013B2 [262] and equivalents in other countries) as well as an application patent (US11191714B2 [263]). They are formed by connecting two PEO_x-PPO_y-PEO_x triblock copolymers (also referred to as Pluronics®, a trademark of BASF) using poly(propylene glycol)-12/dicyclohexylmethane-4,4'-diisocyanate (PPG-12/SMDI) copolymer, and terminated by additional PEO blocks. The links are formed by urethane chemistry between a terminal hydroxy group and the reactive isocyanate of SMDI. Figure 3.1 shows a schematic overview of the repeating unit present in EG312 and EG412, in which the number of monomers in each PEO, PPO and PPG block is indicated. EG312 consists of Pluronic® F108 (poloxamer 338, PEO_{141}-PPO_{44}-PEO_{141} on average), whereas EG412 consists of Pluronic® F127 (poloxamer 407, PEO_{101}-PPO_{56}-PEO_{101} on average). The linking PPG-12/SMDI copolymer contains on average 4 repeating PPG-12/SMDI units. A characterization comparison is made with their precursor Pluronics® F108 and F127, which were commercially acquired from Sigma-Aldrich, now Merck (Belgium), as BioReagent powder suitable for cell culture and characterized without further purification.

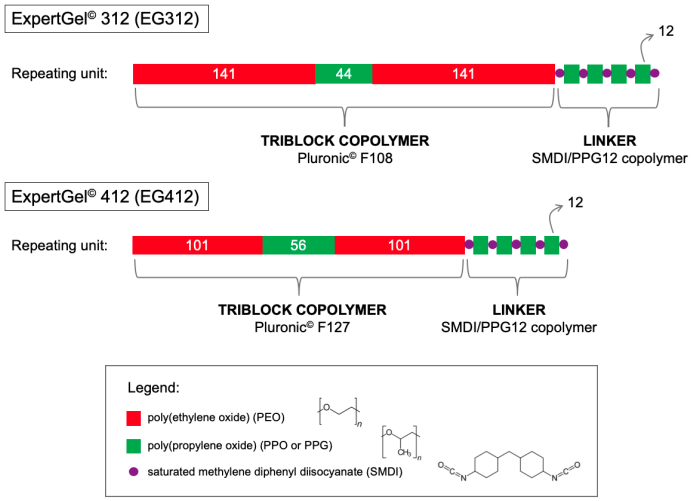

Figure 3.1: Schematic overview of the repeating unit in both ExpertGel® molecules with an indication of the amount of monomers in each block.

Characterization

Fourier-transform infrared spectroscopy FT-IR spectra were recorded using a Bruker Vertex 70 FT-IR spectrometer at room temperature for ExpertGel® 312 and 412 and their precursor Pluronics® F108 and F127, respectively. An attenuated total

reflectance mode was used with a diamond crystal. Sixty-four scans were accumulated in the range 4000-400 cm^{-1} with a resolution of 2 cm^{-1}. Figure 3.2 (a) and (b) show the FT-IR spectra for Pluronic® F108 and ExpertGel® 312, and for Pluronic® F127 and ExpertGel® 412, respectively. The relevant peak positions and the corresponding energy absorption processes are summarized in Table 3.1. The differences between Pluronics® and ExpertGel® are indicated in bold. They originate from the urethane linkers in ExpertGel multiblock copolymers, which connect Pluronic® molecules through a reaction between the isocyanate group (N=C=O) in SMDI and the terminal hydroxy (OH) groups in Pluronics®. No clear isocyanate stretching band is observable around 2270 cm^{-1}, meaning no residual SMDI is present in ExpertGel®. The location of the amide I (C=O stretch) and II (N-H bend and C-N stretch) bands in ExpertGel indicates that the vast majority of the connections between 2 Pluronic molecules are formed by urethane bonds (amide I at 1715 cm^{-1}), with a small fraction of urea bonds (amide I at 1645 cm^{-1}). The latter can be formed as a side reaction in the presence of water. The absence of amide bands belonging to biuret (amide I at 1731 cm^{-1} [264]) or allophanate bonds (amide I at 1807 and 1775 cm^{-1} [265]) proves that the multiblock copolymer structure is linear, rather than branched.

Table 3.1: FT-IR peak positions and their origin in ExpertGel samples: ν = stretching vibration with subscripts s = symmetrical, as = asymmetrical and δ = bending vibration with subscripts ip = in-plane and op = out-of-plane. For the abundantly present -CH_2 groups, the four different bending vibrations are indicated with δ_s = symmetric in-plane bending (scissoring), ρ = asymmetric in-plane bending (rocking), ω = symmetric out-of-plane bending (wagging) and τ = asymmetric out-of-plane bending (twisting).

Wavenumber [cm^{-1}]	Vibrational origin	Wavenumber [cm^{-1}]	Vibrational origin
3515	ν(O-H)	1342	ω(C-H)
3332	ν(N-H)	1280	τ(C-H)
2876	$\nu_{(a)s}$(C-H)	1241	τ(C-H)
1715	ν(C=O) urethane	1097	ν_{as}(C-O-C)
1645	ν(C=O) urea	962	ν_s(C-O-C)
1530	δ_{ip}(N-H), ν(C-N)	842	ρ(C-H)
1466	δ_s(C-H)		

Gel permeation chromatography GPC was performed using an Agilent system with two PSS gram columns (10 μm beads, porosity: 100 Å and 1000 Å) connected to an Agilent differential refractometer. N,N-dimethylformamide + 2.5 mM NH_4PF_6

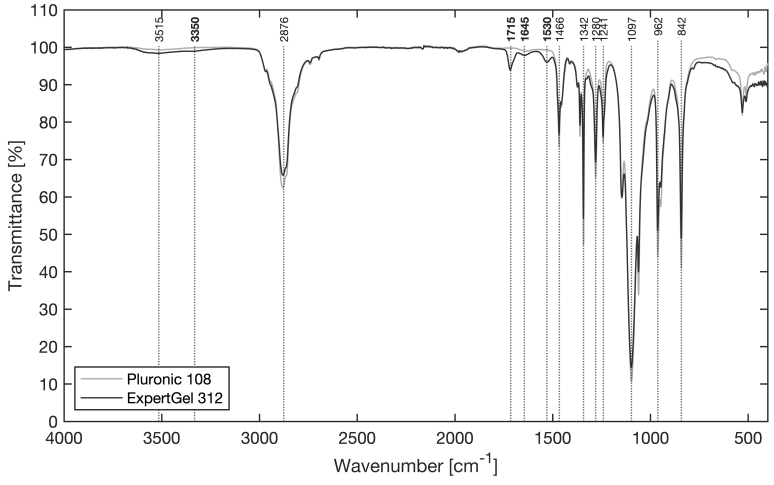

(a)

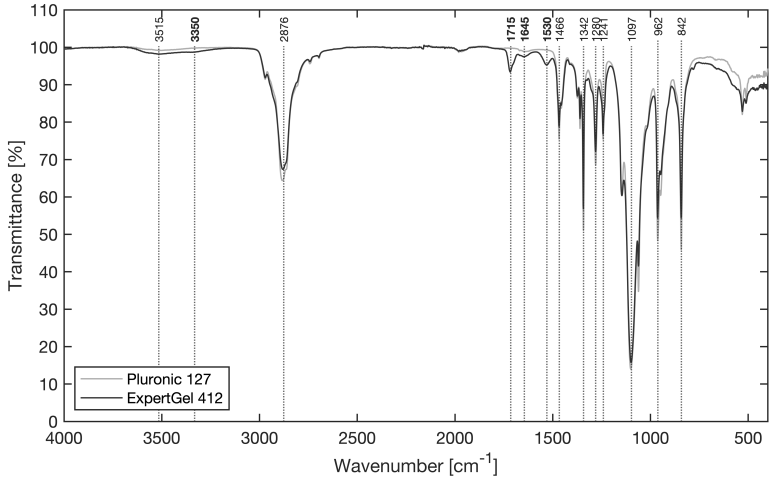

(b)

Figure 3.2: FT-IR spectra of (a) Pluronic® F108 and ExpertGel® 312, and (b) Pluronic® F127 and ExpertGel® 412. The vertical lines indicate the mean peak positions in cm^{-1}. The additional peaks of ExpertGel® as compared to Pluronics® are indicated in bold.

Table 3.2: Molecular weight characteristics of the precursor Pluronics® (F108 and F127) and the ExpertGel® copolymers (EG312 and EG412): number average molecular weight ($\overline{M}_n$), weight average molecular weight ($\overline{M}_w$) and dispersity ($Đ$).

Sample	$\overline{M}_n$ [kDa]	$\overline{M}_w$ [kDa]	$Đ$ [-]
F108	11	14	1.24
EG312	29	63	2.15
F127	9	11	1.25
EG412	23	44	1.88

was used as eluent at 25°C at a flow rate of 1 mL/min. Linear PEO standards were used for calibration. Figure 3.3 (a) and (b) show the molecular weight distributions for Pluronic® F108 and ExpertGel® 312, and for Pluronic® F127 and ExpertGel® 412, respectively. The bimodality in the Pluronic® molecular weight distributions (and as a consequence also in the ExpertGel molecular weight distributions) is induced by PEO-PPO impurities in commercial Pluronics® [266, 267]. The number and weight averages $\overline{M}_n$ and $\overline{M}_w$ are indicated by vertical lines. Table 3.2 summarizes the results. The dispersity ($Đ$) of ExpertGel molecules approaches 2, which is common for urethane chemistry.

^{1}H nuclear magnetic resonance spectroscopy ^{1}H-NMR spectra were recorded using a 500 MHz Avance Bruker and a 5mm BBO probe at 25°C and shifts are reported in ppm downfield from tetramethylsilane as the internal standard. Deuterated chloroform ($CDCl_3$, obtained from Eurisotop) was used as the solvent. Solutions were prepared at a concentration of approximately 10 mg of copolymer in 0.5 mL of $CDCl_3$. The data analysis was performed using cuteNMR© software. Figure 3.4 (a) and (b) show the ^{1}H-NMR spectra for Pluronic® F108 and ExpertGel® 312, and for Pluronic® F127 and ExpertGel® 412, respectively. A zero order phase shift of -14° around the main peak (3.64 ppm) as pivot and a baseline correction were applied. The peaks were (slightly) shifted to the deuterated chloroform peak at 7.26 ppm. The relevant peak positions corresponding to the protons of the EO and PO repeating units are summarized in Table 3.3. The additional peaks in the ExpertGel® spectra in the region from 2 to 1 ppm correspond to the protons of the SMDI linkers.

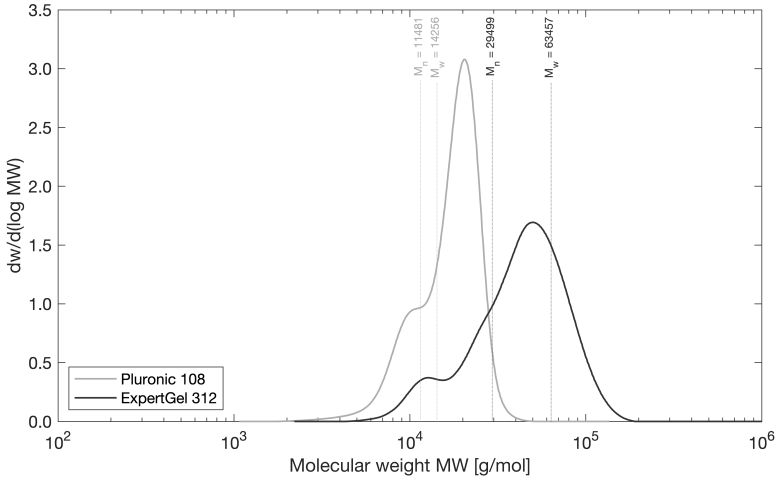

(a)

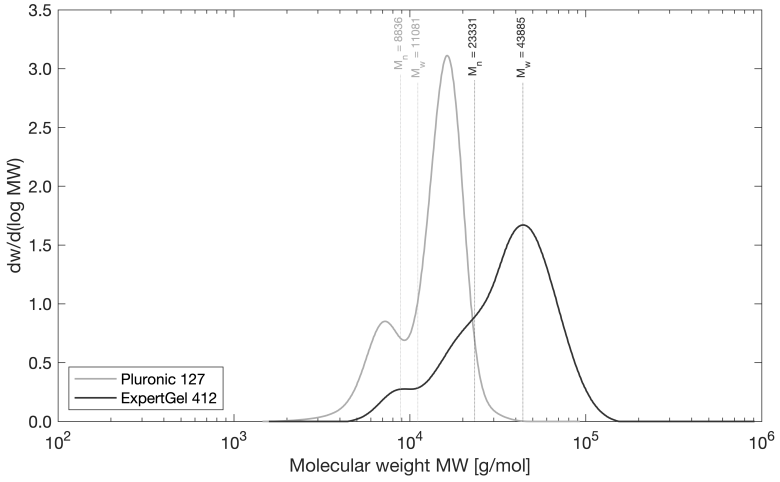

(b)

Figure 3.3: Molecular weight distribution of (a) Pluronic® F108 and ExpertGel® 312, and (b) Pluronic® F127 and ExpertGel® 412. The vertical lines indicate the number and weight average molecular weights $\overline{M}_n$ and $\overline{M}_w$ of Pluronics® (grey) and ExpertGel® (black).

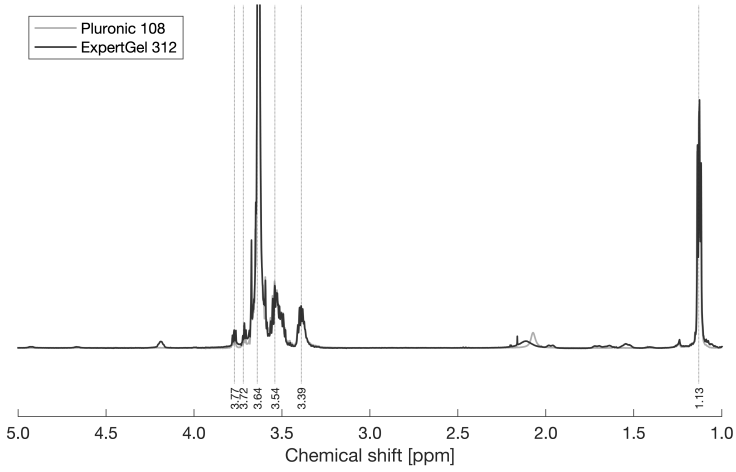

(a)

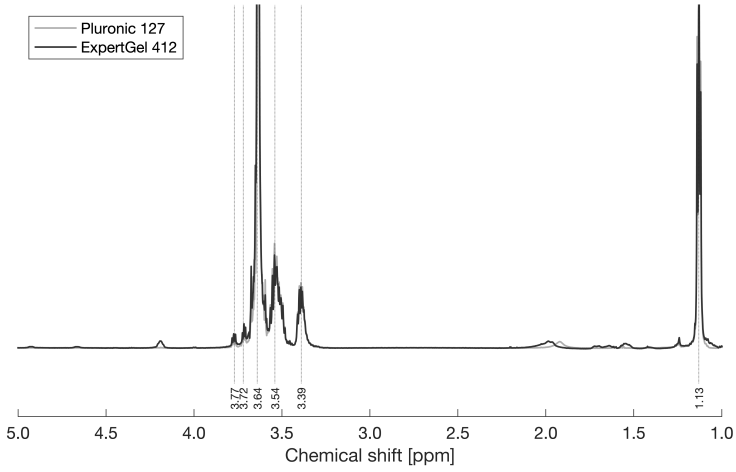

(b)

Figure 3.4: ^{1}H-NMR spectra of (a) Pluronic® F108 and ExpertGel® 312, and (b) Pluronic® F127 and ExpertGel® 412. The vertical lines indicate the main peak positions in ppm.

Table 3.3: ^{1}H-NMR peak positions and their origin in Pluronic® and ExpertGel® samples with *t* = triplet and *m* = multiplet.

Shift [ppm]	Multiplicity	Origin
3.77	t	EO: $OCH_2C\mathbf{H}_2$-OH
3.72	t	EO: $OC\mathbf{H}_2CH_2$-OH or -PPO
3.64	m	EO: -$OC\mathbf{H}_2C\mathbf{H}_2$-
3.54	m	PO: -$OCHCH_3C\mathbf{H}_2$-
3.39	m	PO: -$OC\mathbf{H}CH_3CH_2$-
1.13	t	PO: -$OCHC\mathbf{H}_3CH_2$-

Integration of the peaks corresponding to the H-atoms of PEO as compared to the integration of the peaks corresponding to the H-atoms of PEO and PPO, both corrected for the actual amount of H-atoms in the EO (4H) and PO (6H) monomer and their molar masses (44 g/mol for EO and 58 g/mol for PO), results in an approximate EO weight fraction f_{EO} of the molecules. Table 3.4 summarizes the characteristics, as inferred from ^{1}H-NMR, of both types of commercially available ExpertGel. The weight fraction of EO monomers relative to the weight of EO + PO monomers (f_{EO}) matches the values as specified by the manufacturer, and is very similar to the values of the Pluronic® precursors (for F108 f_{EO} = 0.83 on average and for F127 f_{EO} = 0.73 on average). This allows a comparison of the phase behavior of multiblock copolymers as compared to triblock copolymers based on architecture and overall molecular weight, rather than hydrophobicity. The similarity of the EO weight fraction of ExpertGel® and its precursor Pluronic®, is induced by the terminal PEO blocks in ExpertGel®, which are added to increase its stability (and act as dangling ends in the network). The a parameter, representing the average amount of hydrophobically associating blocks per chain, is approximated based on the following formula:

$$a = \frac{(1 - f_{EO}) \cdot \overline{M}_w}{\overline{M_{w,PPO}}}, \tag{3.1}$$

in which $\overline{M_{w,PPO}}$ represents the average molecular weight of the PPO blocks, i.e. the amount of repeating PO monomers in a PPO block times the molar mass of the PO monomer (58 g/mol). The amount of PO monomers (46 for EG312 and 52 for EG412) is calculated as an average between the y PO monomers of the precursor Pluronic® (y = 44 for EG312 and y = 56 for EG412) and the 4 repeating PPG-12 blocks, bearing in total 48 PO monomers in the PPG-12/SMDI copolymer linker. The use of $\overline{M_w}$ rather than $\overline{M_n}$ ensures a focus on the main, highest molecular weight peak of the

ExpertGel molecules (see Figures 3.3 (a) and (b) for EG312 and EG412, respectively) rather than the lower molecular weight peaks possibly induced by Pluronic® impurities. Note that for the use of the a parameter in the binomial distribution $P(\Psi)$ around the average value $\langle\Psi\rangle$ (see Section 5.1 for the derivation of the mechano-statistical transient network model), the calculated values in Table 3.2 should be rounded to their nearest natural number, which makes the value equal to 4 for both types of ExpertGel®. Based on this a value, the ExpertGel molecules consist of the following overall structure: poloxamer - PPG-12/SMDI - poloxamer - PPG-12/SMDI - PEO end cap, bearing in total approximately 4 hydrophobic blocks. Due to their overall alternating sequence, we refer to the polymers as 'alternating PEO-PPO multiblock copolymers', which abstracts the presence of the SMDI linkers.

Table 3.4: Characteristics of the two grades of ExpertGel® (EG312 and EG412) as determined by ^{1}H-NMR: weight fraction of EO monomers relative to the weight of EO + PO (f_{EO}) and the average number of hydrophobically associating blocks per chain (a).

Sample	f_{EO} [-][i]	a [-][ii]
EG312	0.83	3.95
EG412	0.75	3.60

[i] Determined by ^{1}H-NMR;
[ii] Calculated with Equation 3.1.

Polymer parameters

The transient network elasticity of the micellar networks formed by multiblock copolymers finds its origin in the presence of soluble, hydrophilic bridges in between micellar nodes. Such bridges will only form over length scales on the order of the radius of gyration of an intermediate hydrophilic block [268]. To theoretically predict the radii of gyration of the PEO and PPO blocks in our alternating multiblock copolymers, knowledge of the number of Kuhn segments N and the Kuhn length b of the equivalent freely jointed Kuhn chains with the same characteristics as the blocks, is required. This can be calculated according to Equations 3.2 and 3.3, respectively:

$$N = \frac{M_w \cdot \cos^2 \theta/2}{M_0 \cdot C_\infty}, \tag{3.2}$$

$$b = \frac{C_\infty \cdot l}{\cos \theta/2}, \tag{3.3}$$

in which M_w represents the molecular weight of the entire block, M_0 the molecular weight of the repeating monomer, C_∞ Flory's characteristic ratio, θ the tetrahedral

angle and l the bond length [153]. The tetrahedral angle θ for both PEO and PPO is 68° [153]. The bond length can be calculated as an arithmetic mean of the bonds present in the monomer of the polymer backbone, l(C-C) = 1.54 Å and l(C-O) = 1.43 Å [269–271], with the second one occurring twice. The mean bond length l thus equals 1.47 Å, which is similar for PEO and PPO. The molar mass M_0 of the monomers in PEO and PPO is 44 g/mol and 58 g/mol, respectively. Flory's characteristic ratio, which is a measure of the chain's local stiffness as an ideal chain, is experimentally determined by intrinsic viscosity $[\eta]$ measurements at θ-conditions: for PEO C_∞ = 4.1 ± 0.4 (H_2O + 0.45M K_2SO_4 at 35°C) [269] and for PPO C_∞ = 6.01 (iso-octane at 50°C) [272]. Similar values were obtained using mass spectrometry ($C_{\infty,PEO}$ = 3.96 and $C_{\infty,PPO}$ = 5.76) [271]. The number of monomers n, the molecular weight M_w and the resulting values for the number of Kuhn segments N and the Kuhn length b of the average PEO and PPO blocks are summarized in Table 3.5.

The theoretical calculation of the size of a polymer in solution does not only depend on the Kuhn characteristics N and b, but also on the solvent quality, which is reflected in the scaling exponent v in the Flory scaling relation $\sqrt{\langle R^2 \rangle} \sim bN^v$ [153]. It is well-known that low molecular weight polymer chains can be approximated as ideal chains ($v = 1/2$) in the so-called θ-region. Theoretically a chain can be treated as ideal as long as the number of Kuhn segments N is smaller than the number of monomers g_T in a thermal blob [153]. The latter can be calculated based on the Flory interaction parameter χ as

$$g_T = \frac{1}{(1-2\chi)^2}. \tag{3.4}$$

The value of χ for linear PEO polymers in milliQ water was experimentally determined by Merrill *et al.* using osmotic pressure measurements and equals 0.426 [273]. By equating N and g_T, a maximum molecular weight of 12 000 g/mol is obtained as the limiting PEO molecular weight for an ideal chain approximation, which justifies treating our relatively short PEO blocks (maximum 6 204 g/mol) as ideal chains. PPO chains with a M_w of 2000 g/mol are only soluble in water at low temperatures (< 18°C) [50] and hence, water is considered a non-solvent ($v = 1/3$) for higher molecular weight PPO at room temperature. In both cases, i.e. ideal θ-conditions with $v = 1/2$ and non-solvent conditions with $v = 1/3$, the radius of gyration R_g for linear flexible chains can be calculated according to Equation 3.5:

$$R_g = \frac{b \cdot N^v}{\sqrt{6}}. \tag{3.5}$$

The calculated sizes for the PEO and PPO blocks present in our alternating multiblock copolymers, according to this theoretical expression, are also included in Table 3.5.

Table 3.5: Polymer parameters of the PEO and PPO blocks present in the two grades of ExpertGel® (EG312 and EG412): the number of monomers n , the molecular weight of the block $M_{w,b}$, the number of Kuhn segments N, the Kuhn length b and the theoretically predicted radius of gyration R_g.

Sample	PEO block					PPO block				
	n^i	$M_{w,b}$ [Da]^i	N^{ii}	b [Å]^{iii}	R_g [nm]^{iv}	n^v	$M_{w,b}$ [Da]^v	N^{ii}	b [Å]^{iii}	R_g [nm]^{iv}
EG312	141	6 204	23.64	7.25	1.44	46	2 668	5.26	10.63	0.75
EG412	101	4 444	16.93	7.25	1.22	52	3 016	5.95	10.63	0.79

[i] Based on the length of the PEO block in the precursor Pluronics® F108 (EG312) and F127 (EG412);
[ii] Calculated with Equation 3.2;
[iii] Calculated with Equation 3.3;
[iv] Determined by Equation 3.5 using $\nu = 1/2$ for PEO and $\nu = 1/3$ for PPO;
[v] Calculated as an average between the PPO block of the precursor Pluronics® and that of the PPG-12/SMDI copolymer linker.

3.1.2 Terpyridine-functionalized 4-arm PEO stars

Materials

4-arm hydroxy-terminated poly(ethylene oxide) stars with a pentaerythritol core (OH-PEO) stars were acquired from Polymer Source. The total molecular weight ($\overline{M}_n$), as determined by size-exclusion chromatography by the manufacturer, was reported to be 41 500 g/mol, with a dispersity of 1.12 (and verified by GPC). It is assumed that each arm of OH-PEO has a $\overline{M}_n$ of 10 375 g/mol and hence 235 repeating EO monomers. The 4-arm OH-PEO stars were dried by two azeotropic cycles against toluene before use. All used solvents were of reagent grade and all materials (solvents and others) were used as received, unless stated otherwise. Toluene, dichloromethane (HPLC grade), tetrahydrofuran (THF), diethyl ether and sodium sulphate (anhydrous) were from VWR Chemicals. Methyl sulfoxide (99.7+%, extra dry over molecular sieve) was obtained from Acros Organics. Potassium hydroxide pellets (>- 85%, p.a.) were from Carl Roth and dried at 40°C under vacuum for at least one night prior to use. 4'-chloro-2,2':6',2"-terpyridine (95%) was obtained from FluoroChem. All water used in this study is ultrapure water, filtered by either a Puranity PU 15 + (VWR, 17.20 MΩcm at 23.3°C), an Arium pro system (Sartorius; 18 MΩcm) or an Arium 611 DI system (Sartorius; 18 MΩcm). Filtration paper MN615 with a diameter of 125 mm from Macherey-Nagel or filtration paper 413 with a diameter of 150 mm from VWR were used for regular filtration. For vacuum filtration, nylon Nylaflo™ filters with a pore size of 0.45 μm and a diameter of 47 mm from Pall were used. Dialysis was performed with Spectra/Por® molecular porous membranes with a molecular weight cutoff of 12-14 kDa, obtained from Spectrumlabs.com, which were soaked in water for at least 30 minutes and extensively rinsed with water before use.

Post-functionalization of 4-arm hydroxy-terminated PEO stars

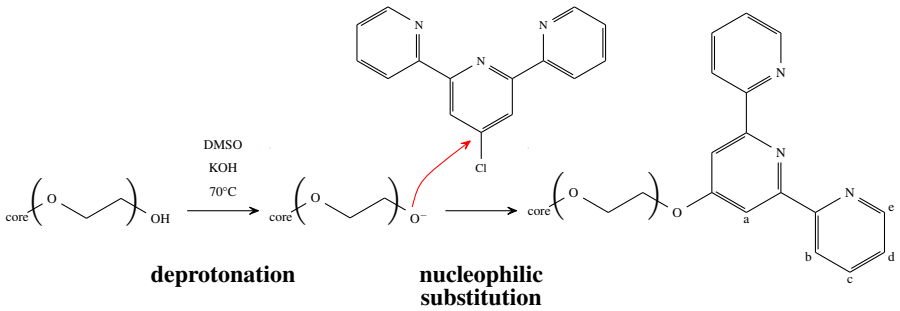

Figure 3.5: Post-functionalization reaction scheme

The post-functionalization of 4-arm OH-PEO stars with 4'-chloro-2,2':6',2"-terpyridine was performed according to the procedure reported by Schubert *et al.* [274] for linear PEO chains and adapted for 4-arm PEO stars. The reaction scheme of the post-functionalization procedure is shown in Figure 3.5. Potassium hydroxide (KOH) pellets were dried overnight in a vacuum oven at 40°C prior to use. 1 g of dried stars together with one dried KOH pellet (51.6 mg, 9.5 eq compared to OH groups) were brought in 20 mL of dry dimethyl sulfoxide (DMSO) under an argon atmosphere at 70°C and left to dissolve for 30 minutes under mild magnetic stirring. This allowed for the deprotonation of the terminal OH group of the 4-arm PEO stars. Subsequently, 84.2 mg (3.3 eq compared to OH groups) of 4'-chloro-2,2':6',2"-terpyridine was added to the reaction solution at 70°C and left to react by nucleophilic substitution. The nitrogen atom positioned para to the chloride leaving group of 4'-chloro-2,2':6',2"-terpyridine acts as an electron withdrawing group and activates the (otherwise nucleophilic) aromatic ring for nucleophilic attack. After 24 hours, one additional pellet of KOH was added to increase the availability of dissolved base for the reaction to proceed. Over the course of the reaction, the color changed from yellow, to dark red and finally, after 138 hours of total reaction time, bright orange. The reaction solution was then left to cool down to room temperature, mixed with 100 mL of milliQ water and washed three times with 50 mL of dichloromethane (DCM) in a separating funnel. The resulting water phase was mixed with sufficient amount of NaCl salt to create a brine solution and was washed once more with 50 mL of DCM. Afterwards, the combined DCM phases were extracted with 200 mL of fresh brine. An additional 50 mL of DCM was added to the brine phase to reduce the foam layer and recover all possible polymer present in the foam layer. The combined organic layers were then dried over sodium sulphate and filtered, before removing the DCM solvent in vacuo. The remaining polymer was redissolved in heated THF and precipitated in diethyl ether. After vacuum filtration,

the final 4-arm terpyridine-functionalized PEO stars (tpy-PEO) were dried overnight at 40°C under vacuum (yield: 81%). Additional purification of tpy-PEO was performed by dissolving the star polymers in water and performing 48 hours dialysis against water. The 4-arm tpy-PEO stars were recovered by lyophilization (yield: 84%), dried under vacuum at 40°C overnight and stored in a freezer.

Characterization of 4-arm tpy-PEO stars

To determine the amount of telechelic terpyridine functionalization of the 4-arm PEO stars, ^{1}H-NMR and Ultraviolet-Visible (UV-VIS) Spectroscopy measurements were performed.

^{1}H nuclear magnetic resonance spectroscopy The ^{1}H-NMR spectra, recorded as previously described, of the 4-arm tpy-PEO stars are shown in Figure 3.6. The assignment of the relevant peaks is summarized in Table 3.6, with the corresponding H atoms of terpyridine indicated in Figure 3.5. The main PEO polymer backbone peak at 3.64 ppm is fixed to 940 H-atoms per arm, i.e. 4H for 235 EO monomers per arm). The degree of functionalization can then be determined by the integration of the well-defined peak at 4.39 ppm (1.87419) corresponding to the H atoms of PEO linked to a terpyridine moiety, normalized by its ideal value of 2 H-atoms in case each PEO end would be functionalized by terpyridine. This results in a degree of functionalization of 94%.

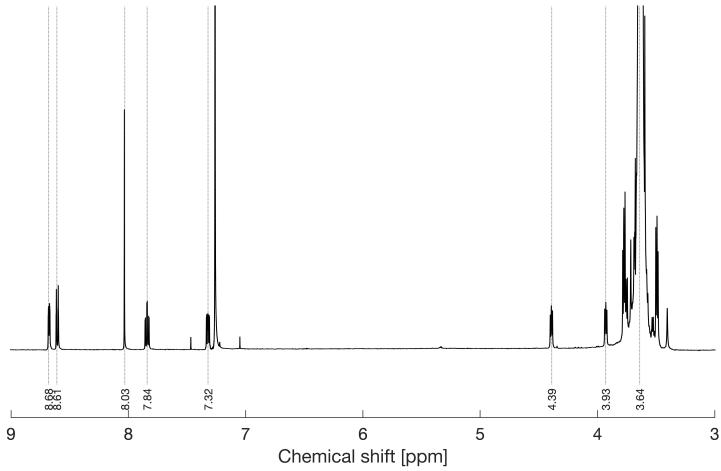

Figure 3.6: ^{1}H-NMR spectrum of 4-arm terpyridine-functionalized PEO stars. The vertical lines indicate the main peak positions in ppm.

Table 3.6: ^{1}H-NMR peak positions and their origin in 4-arm terpyridine-functionalized PEO stars with *s* = singlet, *d* = doublet, *t* = triplet and *m* = multiplet. The a, b, c, d and e H-atoms of terpyridine are indicated in Figure 3.5.

Shift [ppm]	Multiplicity	Origin
8.68	d	tpy: H (e)
8.61	d	tpy: H (b)
8.03	s	tpy: H (a)
7.84	m	tpy: H (c)
7.32	m	tpy: H (d)
4.39	t	EO: $OCH_2C\mathbf{H}_2$-tpy
3.93	t	EO: $OC\mathbf{H}_2CH_2$-tpy
3.64	m	EO: -$OC\mathbf{H}_2C\mathbf{H}_2$-

Ultraviolet-visible spectroscopy Additionally, the degree of functionalization was also determined by UV-VIS Spectroscopy (Jasco V630) at room temperature in the range of 700 to 200 nm with a resolution of 1 nm. Samples were prepared in 10 mm Quartz cuvettes. First, a calibration curve of 4'-chloro-2,2':6',2"-terpyridine in chloroform (>= 99%, Fluker Chemical) was constructed for terpyridine concentrations ranging from 0.02 to 0.1 mmol/L (see Figure 3.7 (a)). The molar extinction coefficient for terpyridine at 279 nm was found to be 21 483 mol/L cm (R^2 = 0.9979). Then, the absorbance of a 0.64 g/L tpy-PEO in chloroform solution at 279 nm was measured to be 1.23619. It was checked that OH-PEO stars in chloroform did not result in any significant absorbance signal at 279 nm, such that the absorbance could be linked to the concentration of terpyridine present. The UV-VIS spectra of the terpyridine solutions, the 4-arm OH-PEO stars and the 4-arm tpy-PEO stars are shown in Figure 3.7 (b).The absorbance corresponded to a concentration of terpyridine moieties of 0.057 mmol/L. If each of the 4 PEO arms in a 0.64 g/L tpy-PEO solution would be functionalized, a molar terpyridine concentration of 0.060 mmol/L would be present. For this calculation, the $\overline{M}_n$ as provided by the supplier (41 500 g/mol) minus 4 times the molar mass of a hydroxy (OH) group (18 g/mol) plus 4 times the molar mass of a terpyridine moiety (232.27 g/mol) was used. Hence, the degree of functionalization was determined to be 95% by UV-VIS. This in good agreement with the degree of functionalization as obtained from ^{1}H-NMR, and we can thus conclude that an average of 3.8 out of 4 arms is successfully functionalized with terpyidine.

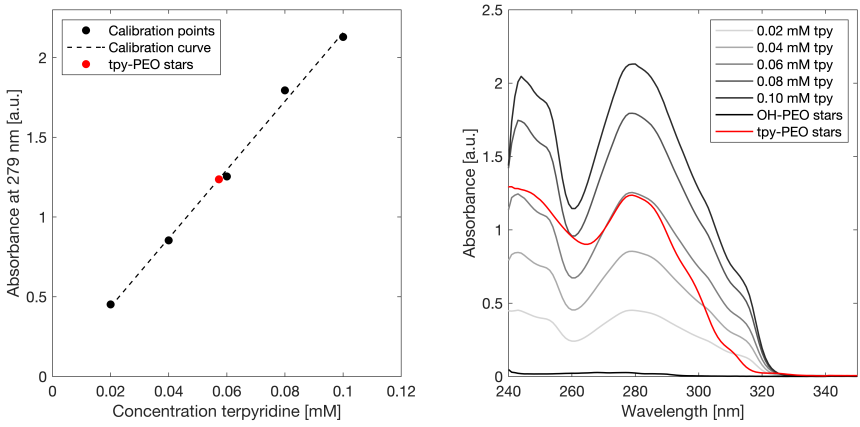

(a) **(b)**

Figure 3.7: (a) UV-VIS calibration curve of the absorbance at 279 nm as function of terpyridine concentration (black circles) and 4-arm tpy-PEO stars (red circle). (b) UV-VIS spectra of terpyridine solutions, OH-PEO stars and tpy-PEO stars.

3.1.3 Network preparation

Multiblock copolymer solution preparation

Aqueous solutions of alternating PEO-PPO multiblock copolymers were prepared by dissolving the required amount of ExpertGel® (weighing accuracy 0.01 mg) in milliQ water by magnetic stirring in an ice bath for at least 45 min. The cold samples were left in the fridge at 4°C for at least 12 hours, to completely eliminate the foam layer. The samples were used within one week after preparation.

Metal-ligand network preparation

Salt stock solutions were made by dissolving an exact amount of hydrated salts in ultrapure water by magnetic stirring, to yield an overall M^{2+} concentration of approximately 0.043 mol/L. Zinc(II) chloride (99.999% trace metals basis) was acquired from Sigma-Aldrich. After filtration, the exact concentration of transition metals was then determined by Inductively Coupled Plasma-Optical Emission Spectroscopy (ICP-OES, Optima 8300 from PerkinElmer) calibrated by 0, 1 and 10 ppm of a multi-element standard containing all required transition metals. A 1000 ppm multi-element standard (custom standard 19 elements: Al, As, B, Ba, Be, Cd,

Ce, Co, Cr, Cu, Fe, Li, Mn, Ni, Pb, Se, Sr, V and Zn) from SCP Science, a 1000 ppm Yttrium standard from Fluka and nitric acid (puriss. p.a.; >- 65%) from Honeywell were used. All samples for ICP-OES analysis contained 3 vol% HNO_3 to avoid precipitation and 5 ppm Yttrium as an internal standard. The salt stock solutions were always shaken prior to use, to ensure complete dissolution.

For preparation of the metal-ligand networks, an exact amount of telechelic terpyridine-functionalized 4-arm PEO stars was dissolved in milliQ water by magnetic stirring for at least 45 min. Subsequently, a precise volume of salt stock solution (accuracy of 0.1 μL) was added to yield a stoichiometric ratio of M^{2+} ions to terpyridine moieties of 1:2 and resulted in the immediate formation of a gel at the site of injection. Afterwards, the samples were homogenized by thorough vortex mixing during 10 minutes. Finally, the gels were left to stabilize overnight in a fridge at 4°C, after which a stable and bubble-free gel was obtained. The metal-ligand networks were characterized within one week after preparation.

Double network preparation

For double network preparation, after dissolution of an exact amount of tpy-PEO stars as described above, a precise quantity of ExpertGel multiblock copolymers was added to the solution and dissolved by magnetic stirring in an icebath. The solution was then left in the fridge at 4°C overnight, to get rid of the foam layer. Afterwards, the required volume of salt solution to yield a M^{2+}:tpy ratio of 1:2 was added and the sample was vortex mixed heavily for 10 minutes. Finally, the double network samples were left in the fridge (for minimum 1 night and maximum 2 days) until no air bubbles nor foam were present. Also the effect of the gel precursors of one network on the other network, prepared by the above described procedure, was checked. All double network samples were used within 3 days from the moment of preparation.

3.2 Characterization methods

3.2.1 Rheometry

Rheological measurements were performed using a stress-controlled rheometer (DHR3, TA Instruments) in strain-controlled mode. The temperature was controlled with an accuracy of 0.1°C by means of a Peltier system connected to a fluid bath.

Hydrophobically associating multiblock copolymers in aqueous solutions

For low viscous, dilute solutions of multiblock copolymers, an anodized aluminium double wall Couette (DWC) geometry with diameter dimensions $D_{c,i}$ = 40 mm, $D_{b,i}$ = 40,76 mm, $D_{b,o}$ = 43,92 mm, $D_{c,o}$ = 44,76 mm (c = cup, b = bob, i = inner, o = outer) and height H_b = 60 mm was used to ensure sufficient sample response with respect to the lower torque limit of the device (5 nNm in rotation as specified by the manufacturer). The measurements were conducted at a gap of 1 mm under the bob, but no significant influence of the gap was found in the range from 500 μm up to 1 mm. A solvent trap was used to prevent solvent evaporation. For each measurement, exactly 7.5 mL of sample, directly taken from the fridge at 4°C, was loaded in the DWC cup. The sample was kept at 15°C for a flow sweep from 1 to 100 s^{-1}, after which the sample was heated to the desired temperatures using a controlled heating rate of 0.1°C/min, while shearing at a constant shear rate of 100 s^{-1}. This relatively high shear rate was used to have enough sample response and was verified to not influence the (onset of) micellization. At intermediate temperatures in steps of 5°C from 20°C to 50°C, flow sweeps from 1 to 100 s^{-1} were recorded and proved Newtonian behavior, i.e. the viscosity was independent of the shear rate. This protocol was applied to all dilute copolymer solutions, as well as the milliQ water solvent.

For concentrated solutions, a stainless steel plate-plate (PP) geometry with a diameter of 40 mm was used at a gap of 250 μm. The gap was compensated for thermal expansion at a rate of 0.1°C/min by using a thermal gap compensation value of 0.82 μm/°C. No significant influence of wall slip was detected by comparing sample responses of measurements at different gap heights in the range of 150 μ to 750 μ. To avoid solvent evaporation at elevated temperatures, a peripheral pure mineral oil (Acros Organics) layer was placed around the sample after scraping the excess sample and reaching the measurement gap (at low temperatures). The oil layer was kept in place by means of a metal ring with an inner diameter of of 49 mm. No significant influence of the low viscosity mineral oil (viscosity of 0.14 Pas at 25°C) was found by comparing the rheological response with a peripheral oil layer at low temperatures, with the rheological response using a solvent trap to prevent solvent evaporation (which is insufficient for prolonged times at higher temperatures). Figure 3.8 compares the linear dynamic moduli G' and G'' as a function of temperature during a temperature ramp (heating rate of 0.1°C/min, 0.1% strain and 1Hz) using either a peripheral oil layer or a solvent trap. The measurement protocol was as follows: after carefully loading and scraping the samples coming from the fridge at 4°C, a thermal steady state at 15°C was ensured by monitoring the samples using a strain of 0.1% at a frequency of 1 Hz over a period of 10 minutes. Next, a frequency sweep from 100 Hz to 0.01 Hz at 0.1% strain was recorded, followed by the controlled heating of the samples to the desired temperature using a heating rate of 0.1°C/min, while applying a strain of 0.1% at a frequency of 1 Hz. At intermediate temperatures in the range from 16°C to 50°C in steps of 2°C, frequency sweeps from 100 Hz to 0.01 Hz with a strain of

0.1% were recorded, followed by a stress relaxation at a constant strain of 1% for 10 000s. The strain values of 0.1% (oscillatory measurements) and 1% (step-strain measurements) was verified to be in the linear regime for all samples and conditions. The thermoreversibility of the network formation by hydrophobic association was checked for a few reference samples by finishing the experiments with a cooling ramp from the highest temperature up to 15°C at 0.1°C/min, 0.1% strain and a frequency of 1 Hz. The rheological protocol performed on single networks formed by PEO-PPO multiblock copolymers in aqueous solutions is shown in Figure 3.9 (a). The rheological reproducibility of a few reference samples at low and high concentration was checked and found to be within the expectation for rheological measurements (usually between 5% and 10% deviation).

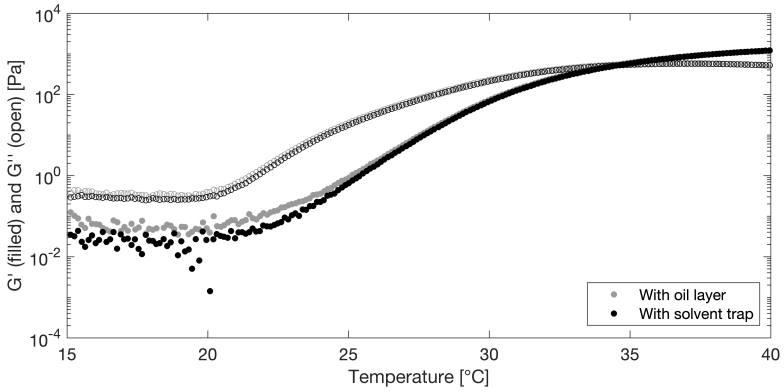

Figure 3.8: Comparison of the dynamic moduli G' (filled symbol) and G'' (open symbol) versus temperature for 92 g/L EG412 at a heating rate of 0.1°C/min, 0.1% strain and 1 Hz: gray is with peripheral oil layer, black is with solvent trap. Only 1 out of 15 consecutive points is shown for clarity.

Metal-ligand networks

The rheological set-up for measurements on metal-ligand (ML) networks formed by 4-arm tpy-PEO stars crosslinked with M^{2+} metal ions in aqueous solutions in a 1:2 $[M^{2+}]$:[tpy] ratio was the same as the one for the concentrated solutions of hydrophobically associating multiblock copolymers. The rheological protocol was very similar as well (see Figure 3.9 (a)): after carefully loading and scraping the samples when coming directly from the fridge at 4°C, the samples were monitored at 15°C using a strain of 0.1% (verified to be in the linear regime for all networks) at a frequency of 1 Hz over a period of minimum 10 minutes and maximum 24 hours, to eliminate all possible effect of loading and relax the normal force as well as to ensure a steady state.

The samples were probed with a strain of 0.1% and a frequency of 1 Hz when heating to the desired temperature using a controlled heating rate of 0.1°C/min. At the desired (intermediate) temperatures from 16°C to 40°C, mainly in steps of 2°C, frequency sweeps from 100 Hz to 0.01 Hz with a strain of 0.1% were recorded, followed by a stress relaxation at a constant strain of 1% (verified to be in the linear regime for the networks) for 1000s. Finally, the thermoreversibility of the gelation process was checked by performing a temperature sweep (0.1% strain, 1 Hz) from 40°C to 15°C at a controlled rate of 0.1°C/min. The rheological reproducibility of a 40 g/L samples was within experimental expectation.

Double networks

Rheological measurements on double networks (DNs) combining hydrophobically associating networks and metal-ligand networks were first performed with the exact same rheological setup as the single ML networks. However, prolonged DN measurements at elevated temperatures on stainless steel geometries resulted in a purple color due to possible metal ion contamination from the steel plates (see Section 7.3 in Chapter 7 for more details). Therefore, DN were also rheologically characterized by using a custom-made glass plate-plate geometry with a diameter of 20 mm. The use of a glass plate top geometry was combined with a very thin glass slide glued on the Peltier element in order to have both top and bottom surfaces of glass. The measurement gap was kept constant at 250 μm by using a thermal gap compensation (0.96 μ/°C for the PP20 glass geometry at a rate of 0.1°C/min). The effects of solvent evaporation were eliminated by adding a peripheral oil layer and keeping the oil in place using a Teflon ring (diameter of 33 mm for PP20). Finally, to avoid any other metal impurities in the samples, loading and scraping was performed with a Teflon spatula. The rheological test protocol was adapted to ensure complete steady state of the DNs at elevated temperatures. The double network samples, in which only the metal-ligand network was already present at low temperatures after preparation, were carefully loaded on the Peltier plate at 15°C. The temperature was steadily increased to 40°C at the lowest possible rate of 0.1°C/min, a strain of 0.1% (verified to be in the linear regime) and a frequency of 1 Hz, which allowed the formation of the second, hydrophobically associating network of PEO-PPO multiblock copolymers at elevated temperature. The double network was then kept at 40°C for a 60-hour time sweep using 0.1% strain and 1 Hz, to ensure the complete buildup and steady state of the double network structure. Afterwards, the double network structure was probed with an oscillatory frequency sweep from 100 to 0.1 Hz at a strain of 0.1% and a step-strain stress relaxation experiment using a strain of 1% for 10 000s. Finally, upon cooling down from 40°C to 15°C at a rate of 0.1°C/min, 0.1% strain and 1 Hz, the frequency sweep and stress relaxation were also performed at intermediate temperatures in steps of 2°C (38°C, 36°C, ...) up until 30°C, as well as at 15°C, to probe the (double) network structure at lower temperatures as well. The rheological protocol performed on double

networks combining hydrophobic association and metal-ligand complexation is shown in Figure 3.9 (b). Reproducibility of DN measurements was checked and discussed in Section 7.3 of Chapter 7.

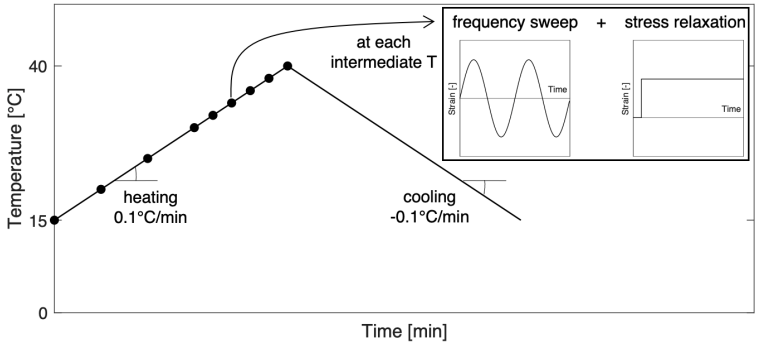

(a) Single network protocol

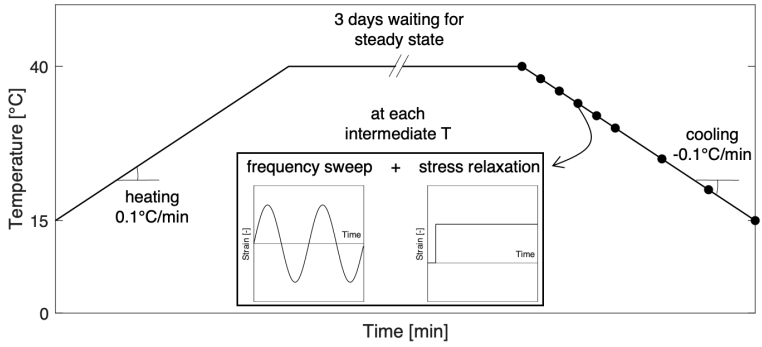

(b) Double network protocol

Figure 3.9: Rheological protocol performed on (a) single networks formed by either hydrophobic association or metal-ligand complexation and (b) double networks combining hydrophobic association and metal-ligand complexation.

3.2.2 Differential scanning calorimetry

Differential Scanning Calorimetry (DSC) measurements were performed using a DSC Q2000 (TA Instruments). Aluminium Tzero DSC pans were filled with approximately 20 mg of multiblock copolymer solution using a micropipette (1-10 μL Finnpipette, Thermo Scientific) when taking the sample from the fridge. An hermetic Tzero lid

was used to seal the samples. Samples were heated under an inert nitrogen atmosphere from 15°C to 50°C, followed by 5 minutes isothermal equilibration and subsequently cooled back down to 15°C at the same rate. Rates of 0.1°C/min and 1°C/min were applied. The first heating-and-cooling cycle at 0.1°C/min was repeated twice, in order to avoid possible thermal history effects as well as to check reproducibility. A milliQ water reference is used for temperature calibration and an Indium reference for heat flux and melting enthalpy calibration of the device, both at 0.1°C/min and 1°C/min.

3.2.3 Adiabatic scanning calorimetry

A home-built device was used for Adiabatic Scanning Calorimetry (ASC) measurements. The principles of ASC and the details of the Peltier-based set-up have been described elsewhere [275–277]. In short, a constant heating (or cooling) power is applied to the sample and allows the sample to undergo its phase transitions at its own pace, while recording the resulting temperature evolution. This is in contrast with DSC measurements, in which the sample is forced to follow the heating (or cooling) rate as dictated by the device, while the heat flux is being measured differentially as compared to that of the reference chamber. Therefore, ASC is believed to provide more representative and accurate measurements of phase transitions at true thermodynamic equilibrium [276]. Practically, the sample cell platform is equipped with an electrical heater for constant power supply and a sensitive Pt-resistor thermometer to measure the resulting temperature of the sample. The sample cell itself consists of an airtight, sealed DSC crucible filled with approximately 60 mg of sample. To ensure that all power is supplied to the sample (and its addenda), the sample platform is surrounded by an adiabatic shield and a very sensitive Peltier element is used as a differential thermometer to keep the temperature difference between sample and surroundings at zero. To this purpose, the top plate of the Peltier element is in good thermal contact with the sample cell platform, while the bottom plate of the Peltier element is in equally good thermal contact with the adiabatic shield. By PID-control, the necessary power is applied to the heater of the adiabatic shield, such that the temperature difference between sample platform and adiabatic shield, can be kept at zero. To achieve temperature stability at the μK level, the adiabatic shield itself is surrounded by an additional thermal shield and a heat bath, each maintained at a lower temperature and controlled by PID systems. In order to improve adiabatic conditions, the interior of the calorimeter is kept under vacuum and airtight sample crucibles are used. For all measurements, the multiblock copolymer solutions were subjected to a constant power supply of 300 μW, starting at 15° C and allowed to heat up until at least 55° C. Each thermometer used in the ASC setup is calibrated by comparing approximately 10 temperatures over the calorimeter's full measuring range, with the temperatures measured in situ using a Tinsley secondary Platinum reference thermometer, which is calibrated against the ITS-90 temperature scale by the National Physical Laboratory in the UK, resulting in an uncertainty of

< 0.2 K. In ASC, the temperature dependence of the specific heat capacity $c_p(T)$ is determined as

$$c_p = \frac{P}{m \cdot dT/dt} \tag{3.6}$$

in which P is the constant power input, m is the sample mass in the crucible and dT/dt the instantaneous heating rate. After baseline correction of c_p, which removes the large contribution of the milliQ water solvent (c_{p,H_2O} = 4.184 J/gK), the heat capacity can be converted to the enthalpy using the following integral

$$H = \int c_p dT. \tag{3.7}$$

3.2.4 Isothermal titration calorimetry

Isothermal Titration Calorimetry (ITC) measurements were performed with a TAM III isothermal calorimeter (TA Instruments). Prior to each ITC experiment, the multiblock copolymer solutions were degassed by mild sonication for 15 minutes using short ultrasound pulses under vacuum. The system was equilibrated at a constant temperature while stirring at 100 rpm until a stable baseline was obtained (baseline shift < 50 nW/h). Titrations were performed by injecting aliquots of 10 μL from the syringe containing an aqueous solution of multiblock copolymers into the sample cell with milliQ water. A waiting time of 30 minutes between injections allowed to reach a stable baseline after each injection. At least two independent titration experiments per case were performed to confirm consistency. For EG312 samples, isothermal conditions at 32° C and at 34° C were studied. For EG412 and F127 samples, isothermal conditions at 26° C and 30° C were studied, respectively.

3.2.5 Light transmittance

A Crystal16 (Technobis Crystallization Systems) device was used for light transmittance measurements, allowing 16 parallel measurements. The temperature was controlled by a combination of Peltier elements and a heater, with an accuracy of 0.1° C. The transmittivity of a red 645 nm laser through a glass HPLC microvial (11.5 mm diameter, flat bottomed, 1.5 mL volume) containing 1 mL of sample was monitored as a function of temperature in the range of 15° C to 90° C at a rate of 0.1° C/min. Despite possible negative effects on the homogenization of the sample, no stirring was applied in order to avoid foaming. Prior to all measurements, a calibration using milliQ water was performed, setting the transmittivity of the solvent background to 100%.

3.2.6 Light scattering

Dynamic Light Scattering (DLS) measurements were performed on a commercial 3D-DLS device (LS spectrometer, LS Instruments) to avoid possible influences of multiple scattering at the upper end of the dilute concentration range. The optical pathway comprises a 660 nm Cobalt laser, two Glan-Thompson polarizers and a beam splitter. The light travels through the sample chamber filled with filtered decalin as an index-matching fluid and is collected by two photon counting detectors mounted on a rotatable goniometer arm. The temperature of the sample chamber is controlled by a water-circulating fluid bath, and each sample was allowed to equilibrate for at least 30 minutes before starting a measurement. Scattering angles from 80 up to 140 were investigated in steps of 10° . Scattered intensities were measured for 50 seconds at each angle and the entire cycle (80° -90° -...-130° -140°) was repeated three times. The angular dependency was investigated by using the scattering vector

$$q = \frac{4\pi \cdot n_{sol} \cdot \sin(\theta/2)}{\lambda} \tag{3.8}$$

in which n_{sol} is the temperature-dependent refractive index of the milliQ water solvent, θ is the scattering angle and λ is the laser wavelength. As dust is detrimental for any light scattering measurement, the dilute solutions of multiblock copolymers were filtered at low temperatures (right after taking them from the fridge) using a hydrophilic PTFE filter with pore sizes of 0.2 μm. This allowed for effective filtering of possible dust particles, without altering the concentration of the polymers in solution. The CONTIN analysis [278] provided in the LS Instruments software was used to screen for possible multimodality and/or polydispersity.

Static Light Scattering (SLS) measurements were performed on the same commercial 3D-DLS device in 2D-mode, i.e. without the beam splitter in the optical pathway. Scattered intensities were measured for 5 seconds at each angle in between 80° and 140° in steps of 10° and the entire cycle was repeated ten times. Averaged values were used for further data analysis. The Excess Rayleigh ratio $R(q)$ was determined as

$$[I(q) - I_{sol}(q)] \cdot \left(\frac{n_{sol}}{n_{tol}}\right)^2 \cdot \frac{I_{tol,abs}}{I_{tol,meas}(q)} \tag{3.9}$$

with $I_{sol}(q)$ and $I_{tol,meas}(q)$ the measured and q-dependent scattering intensities of the milliQ water solvent and the toluene standard, respectively, and n_{tol} the temperature-dependent refractive index of the toluene standard . The absolute excess Rayleigh ratio and refractive index of toluene, both temperature and incident wavelength dependent, were calculated based on the empirical correlations of Sivokhin *et al.* [279]. The contrast factor K was calculated as

$$\frac{4\pi^2}{N_{Av} \cdot \lambda^4} \cdot n_{sol}^2 \cdot \left(\frac{dn}{dc}\right)^2 \tag{3.10}$$

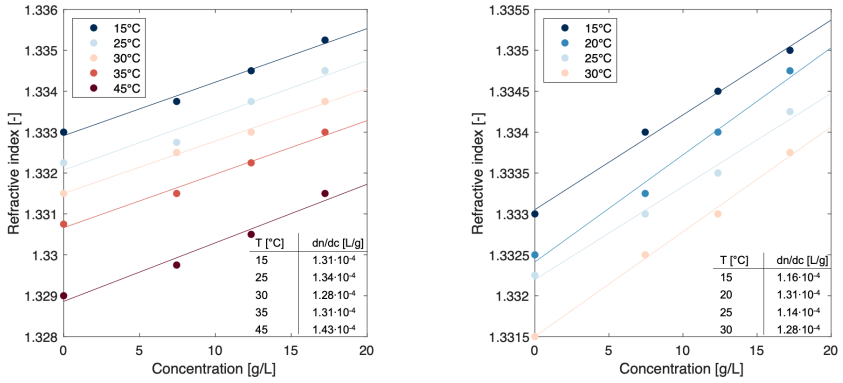

(a) EG312 **(b)** EG412

Figure 3.10: Determination of the refractive index increment dn/dc at different temperatures for (a) EG312 and (b) EG412. The data points represent the refractive index as a function of concentration. The solid line represents the linear fit with a slope equal to the increment dn/dc. The dn/dc values at different temperatures are summarized in the tables in the lower right corner.

in which dn/dc is the refractive index increment of the solution at a specific temperature and R is the excess Rayleigh ratio as defined above. An Abbe 2WAJ refractometer was used to determine the temperature-dependent refractive indices of the milliQ solvent and copolymer solutions for which the temperature was controlled by means of a water-circulating fluid bath. Figures 3.10 (a) and (b) display the dn/dc determination and results for EG312 and EG412 at different temperatures, respectively.

3.2.7 Small-angle X-ray scattering

Dilute samples forming micellar solutions

Synchrotron Small-Angle X-ray Scattering (SAXS) measurements were performed on the P62 beamline of the PETRA III storage ring (DESY, Hamburg, Germany) at 12keV, i.e. a wavelength of 1.03320 Å, with a Dectris EIGER2 X 9M detector in vacuum. A Linkam stage with a temperature accuracy < 0.1°C was used as a temperature-controlled sample holder. Calibration of the sample-to-detector distance (1.5 m) was performed using a silver(I) behenate standard. This setup allowed to investigate a q-range of 0.007 - 0.3 $Å^{-1}$, where q represents the scattering vector defined by $q = 4\pi \sin\theta/\lambda$ in which 2θ is the scattering angle. Multiblock copolymer solutions were injected in borosilicate glass capillaries with a diameter of 1 mm (Hilgenberg GmbH) at low temperatures, after

which the capillaries were sealed using glue from a glue gun and placed in the Linkam stage at 15°C. The samples were heated to the desired temperature (45°C for EG312 and 30°C for EG412) using a controlled heating rate of 1°C/min, while recording data every 10 s using an exposure time of 2 s. The 2D images were radially integrated to obtain 1D scattering intensity profiles I(q) using Python software. The measured intensities were corrected using the absolute intensity scale, taking into account the intensity of the transmitted direct beam, measured at the detector as an average prior to and post data collection. Subtraction of the milliQ water background was performed on the 1D intensity profiles prior to further data analysis.

The 1D data fitting was performed with SASview 5.0.3 software using the Levenberg-Marquardt fitting algorithm. A spherical form factor P(q) was fitted onto the data, according to Equation 3.11 with r the spherical radius and $\Delta\rho = \rho_s - \rho_{sol}$ the difference in scattering length densities for the sphere (s) and solvent (sol):

$$P(q) = 12\pi \cdot r^3 \cdot \Delta\rho^2 \cdot \left[\frac{\sin(qr) - qr\cos(qr)}{(qr)^3}\right]^2. \tag{3.11}$$

The scattering length density ρ_{sol} of the milliQ water solvent was fixed at $9.44 \cdot 10^{-6}$ Å^{-2}.

Concentrated samples forming micellar networks

SAXS measurements were performed on a commercial laboratory beamline (Xeuss 2.0C, Xenocs) consisting of a Cu K_α ultra-low dispersion X-ray source (50 kV, 0.6 mA) with wavelength 1.54189 Å and a Dectris EIGER 1M detector. The X-ray beam was collimated to a diameter of 0.5 mm at the sample position. A Linkam stage (HFSX350) with a temperature accuracy < 0.1°C was used as a temperature-controlled sample holder. The entire beam path was under vacuum (< 10 mbar) to reduce parasitic air scattering contributions during measurements. Calibration of the sample-to-detector distance (1.1929 m) was performed using a silver(I) behenate standard. This laboratory setup allowed to investigate a q-range of 0.006 - 0.255 Å^{-1}, corresponding to angles from 0.04° to 1.79°. Using Bragg's law ($q = 2\pi/d$), this q-range matches length scales from 2.5 to 105 nm. Multiblock copolymer solutions were injected in borosilicate glass capillaries with a diameter of 0.9 mm (WJM-Glas/Müller GmbH) at low temperatures, after which the capillaries were sealed using glue from a glue gun and placed in the Linkam stage at 30°C. The samples were heated to the desired temperatures using a controlled heating rate of 0.1°C/min. At intermediate temperatures in the range from 30°C to 50°C in steps of 2°C, three images of 1 hour acquisition time were collected at a constant temperature, after which the heating was continued to reach the next intermediate temperature. The three scattering images per sample and temperature were averaged to avoid large contributions from cosmic radiation at longer measurement

times. The 2D images were radially integrated to obtain 1D scattering intensity profiles I(q) using Foxtrot software (Xenocs/Synchrotron du Soleil). The measured intensities were corrected using the absolute intensity scale, taking into account the intensity of the transmitted direct beam, measured at the detector as an average prior to and post data collection. Subtraction of the milliQ water background was performed on the 1D intensity profiles prior to further data analysis.

The 1D data fitting was performed with SASview 5.0.3 software using the Levenberg-Marquardt fitting algorithm. A combination of a Porod power law $I_0 \cdot q^{-p}$, a spherical form factor P(q) and a hard sphere structure factor S(q) was fitted onto the data, according to Equation 3.12 in which I_0 and I_{bckg} represent scaling and background intensities, respectively:

$$I(q) = I_0 \cdot q^{-p} + P(q) \cdot S(q) + I_{bckg} \tag{3.12}$$

The expression for the spherical form factor is given in Equation 3.11. The hard sphere structure factor is determined by assuming a Percus-Yevick closure relation to solve the Ornstein-Zernike equation [280]. Possible polydispersity of the spherical radius was not taken into account in the fitting procedure. The scattering length density ρ_{sol} of the milliQ water solvent was fixed at $9.47 \cdot 10^{-6}$ Å^{-2}. The fitting was performed in the q-range from 0.006 - 0.01 Å^{-1} and weighed with the errors determined by the radial integration of the 2D-images. The q-range > 0.01 Å^{-1} was not taken into account due to large errors after milliQ solvent subtraction.

3.2.8 Data analysis

All data analyses were performed using MATLAB® 2021b.

Part I

SINGLE NETWORKS
by hydrophobic association

Chapter 4

Mapping their phase behavior by a multitude of techniques

Even though the discovery of Pluronics® and seminal studies thereon date back several decades, their excellent biocompatibility and non-toxicity, together with their ability of forming a thermoreversible elastic gel phase at temperatures around human body temperature, currently make poloxamers attractive as injectable matrices in (bio)medical applications [41, 281, 282]. They are also used for advanced drug encapsulation and delivery such as in anticancer therapeutic applications [283–285] and for stem cell-assisted tissue engineering [286]. Nonetheless, Pluronic® solutions and hydrogels have shortcomings such as limited viscosity increase, poor stability, short residence times and unacceptably high permeability, which could potentially be addressed by using PEO-PPO multiblock copolymers instead [80]. For such multiblocks to replace Pluronics® in pharmaceutical applications, fundamental knowledge on their micellization is crucial. A recent review by Naharros-Molinero *et al.* points out that in this regard reverse Pluronics® are currently underreported [282], let alone PEO-PPO multiblock copolymers. Therefore, we intend to study the phase behavior, i.e. micellization and clouding, and the ensuing rheological properties of commercially available PEO-PPO multiblock copolymers in dilute as well as concentrated solutions, as such systems can then serve as attractive alternatives to Pluronics®.

In this chapter, the phase behavior of medium-length PEO-PPO alternating multiblock copolymers with approximately 4 repeating units in aqueous solutions will be investigated. This will allow us to gain a view on the relevant temperature and concentration ranges in which either a polymer solution, a solution of isolated micelles, a micellar network or even a phase separated structure are obtained. By studying

two grades of multiblock copolymers with different PEO and PPO block lengths, the differences arising from an altered overall hydrophobicity are elucidated. Comparing the behavior of these multiblock copolymers with that of their precursor Pluronic® triblock copolymers with similar EO weight fractions allows pinpointing the distinct behavior driven by copolymer architecture. Hereto, a unique combination of multiple techniques is employed, including rheometry, calorimetry, light and X-ray scattering and light transmittance. Not only do these techniques allow us to determine the relevant phase boundaries, they also provide insights in the related mechanical properties of the phases (rheology), the energetic driving forces for phase transitions (calorimetry) and the phase microstructures (scattering). This in turn facilitates identifying potential benefits of these novel medium-length alternating block copolymers as compared to triblock copolymers, as well as compared to longer alternating multiblock copolymers that have been studied before. Moreover, an in-depth understanding of the phase behavior and the related properties is a crucial first step in the further investigation of the network structure in the next chapters.

The main part of this chapter was previously published and adapted for this dissertation:

An-Sofie Huysecom, Christ Glorieux, Jan Thoen, Wim Thielemans, Charles-André Fustin, Paula Moldenaers and Ruth Cardinaels, "Phase behavior of medium-length hydrophobically associating PEO-PPO multiblock copolymers in aqueous media", *Journal of Colloid and Interface Science*, 641:521-538, 2023

4.1 Phase boundaries

4.1.1 Micellization temperature

In the past few decades, multiple studies on Pluronic® triblock copolymers (PEO_x-PPO_y-PEO_x) have pointed out that the increase of their amphiphilic character with increasing temperature is responsible for their thermoreversible micellization in aqueous solutions [44]. The dehydration of the central hydrophobic PPO block at elevated temperatures causes clustering of PPO blocks into hydrophobic micellar cores. The critical temperature (CMT) and concentration (CMC) for this thermoreversible micellization process are 1-to-1 correlated since the CMT is a function of concentration and the CMC is a function of temperature. Aqueous solutions of medium-length alternating multiblock copolymers of PEO and PPO with similar block lengths as Pluronics®, also undergo micellization above a certain critical temperature [79, 88].

Figure 4.1 (a) shows the evolution of the viscosity of a 30 g/L EG312 solution with increasing temperature probed at a slow heating rate of 0.1°C/min certifying

thermal equilibrium. The evolution of viscosity exhibits an abrupt change at a certain transition temperature (indicated with a circle). Below this critical temperature, the viscosity decreases due to enhanced thermal mobility, as expected for a viscous polymer solution. Above the critical temperature, on the other hand, the viscosity increases. This macroscopic effect indicates a change in the microstructure that restricts the (thermal) mobility of the polymer chains. Similar to Pluronics®, it is expected that the amphiphilic multiblock copolymers spontaneously self-assemble by clustering their hydrophobic PPO blocks into aggregates. Obviously, such configuration changes the free motion of individual polymer chains, and is reflected in the viscosity evolution with temperature. Hence, the transition temperature, inferred from the temperature dependent viscosity evolution as the crossover between the tangents of the viscosity curve (in a semi-log plot) over a range of at least 5°C at low temperatures sufficiently below the CMT and at higher temperatures above the CMT but below the cloud point, is used to detect the micellization. Such identification of the CMT is comparable to the minimum of the viscosity as a function of temperature, which has been adopted by other authors [287, 288]. In contrast to triblock copolymers containing one single PPO block and hence forming 'hairy' micelles (see Figure 4.3 (a)), the micelles formed by multiblock copolymers contain multiple PPO blocks of the same polymer chain and are expected to have both PEO 'hairs' and 'loops' in the hydrophilic corona surrounding the PPO core (see Figure 4.3 (b)).

In order to further investigate this phase transition, calorimetric measurements have been performed. Figure 4.1 (b) shows the baseline-corrected heat flow of a 30 g/L EG312 solution as measured in a differential scanning calorimeter (DSC) using a heating rate of 0.1° C/min. The baseline correction is illustrated in Figure A.1 in Appendix A. An endothermic peak is observed, for which the peak maximum as well as the on- and endset temperatures can be determined. The latter two were determined using the tangent lines at the inflection points as indicated in Figure A.1 in Appendix A, and represent the start and end of the micellization process, respectively. For such a low heating rate, the heat flow curve is significantly scattered at low copolymer concentrations, which makes an accurate determination of the endothermic peak troublesome. Therefore, the better resolution obtained by adiabatic scanning calorimetry (ASC) [276] renders ASC more suitable for low concentrations of multiblock copolymers. The ASC data analysis procedure is illustrated in Figure A.2 in Appendix A. In Figure 4.1 (c), the enthalpy evolution with temperature using a constant heating power of 300 μW is displayed for a 30 g/L EG312 solution. The increase in enthalpy is indicative of the endothermic micellization process. The critical transition temperatures, i.e. the inflection point and on- and endset temperatures determined by the tangent line at the inflection point, are also indicated.

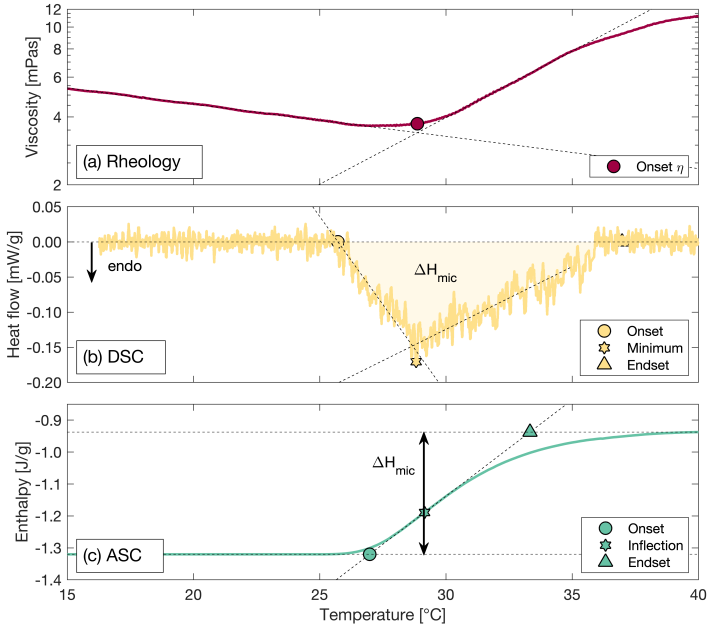

Figure 4.1: Temperature evolution of (a) the viscosity at a shear rate of 100 s^{-1} and a heating rate of 0.1° C/min, (b) the DSC heat flow at a heating rate of 0.1° C/min and (c) the ASC enthalpy at a constant power supply of 300 μW for a dilute solution of 30 g/L EG312. The DSC heat flow and ASC c_p data are baseline corrected. The critical transition temperatures are also indicated.

As inferred from the difference in on- and endset temperatures of both calorimetric methods, the micellization process of the multiblock copolymers spans over a rather wide temperature range of at least 5° C, indicating a progressive conversion of individual copolymers into larger scale micellar assemblies [45, 49, 55] (also see Section 3.2.2). This gradual increase of the amount of micelles explains why the viscosity gradually increases over an extended temperature range in Figure 4.1 (a). Such a broad micellization process was also observed by Wanka *et al.* for Pluronics®, and associated with significant polydispersity in the commercially available poloxamer range [27]. Note that the micellization onset temperatures, as determined by rheometry, DSC and ASC, are slightly different due to the distinct probing principles. Whereas the calorimetric techniques immediately pick up the onset of micellization through changes in the heat flow (DSC) or temperature evolution (ASC), the influence of the micelles on the viscosity does not appear until a certain conversion from unimers into micelles is attained. Nonetheless, for most concentrations there seems to be

good agreement between the transition temperature determined from the viscosity evolution and the peak temperature from DSC or the inflection temperature of ASC thermograms. The latter two represent an 'average micellization temperature' at which most of the micelle formation is being observed. At this temperature, enough micelles are formed to also alter the rheological response. Notably, the ASC onset temperatures seem to lag behind that determined by DSC. The latter is quite surprising, as other studies comparing mainly first-order phase transitions using DSC and ASC have consistently found that the transition temperatures inferred from DSC reflect the need for superheating or -cooling [276, 277]. This is a direct consequence of the application of a fixed heating rate in a differential calorimeter, which does not allow slow kinetic processes to happen at their equilibrium temperatures. Therefore, first-order transitions are shifted and broadened in DSC thermograms as compared to ASC [289]. The ASC thermograms of multiblock copolymer solutions, however, clearly reveal the broadness of the micellization transition at equilibrium conditions. The absolute difference in onset temperatures as probed by DSC and ASC might be a consequence of the temperature uncertainty of the DSC device, which is usually on the order of 1°C.

Similar conclusions about the broad phase transition and the critical transition temperatures as inferred from calorimetric techniques, can be drawn for concentrated multiblock copolymers, as can be seen in the (b) (DSC) and (c) (ASC) graphs of a 132 g/L EG312 solution in Figure 4.2. Additionally, linear oscillatory shear rheology measurements reveal an additional elastic contribution upon micellization in concentrated solutions of multiblock copolymers. In Figure 4.2 (a) the temperature dependence of the dynamic moduli of a 132 g/L EG312 solution are shown, as measured during a temperature sweep at a heating rate of 0.1°C/min, 1 Hz and 0.1% strain using a plate-plate (PP) geometry. At low temperatures, the behavior is similar to that of a dilute copolymer solution, with a decreasing trend in the viscous modulus G'' or the viscosity η with increasing temperature. Note that for purely viscous solutions with a phase angle close to 90°, the viscosity can be calculated from G'' and the angular frequency ω using the relationships $\eta' = G''/\omega$ and $\eta' = \eta$ (at low frequencies) [290]. A clear transition is again observed in the evolution of G'' (or viscosity), corresponding to the micellization of the multiblock copolymers. At the very limited contact surface between sample and peripheral oil layer, the micellization might locally be influenced by the presence of the oil, but this is not detected in the dynamic moduli and hence can be considered to be negligible. Not only a progressive increase in the viscous modulus G'' over multiple decades is observed, but an elastic modulus G' appears that steadily increases with temperature above the CMT and even starts to dominate over the viscous contribution at higher temperatures indicative of an elastic gel-like network structure. Multiple characteristic transition temperatures can be determined from this temperature evolution of the dynamic moduli (see Figure 4.2 (a)). Figure A.3 in Appendix A illustrates the determination of these transition temperatures. As the onset temperature of G'' (circle symbol, determined based on the most significant slope change over a

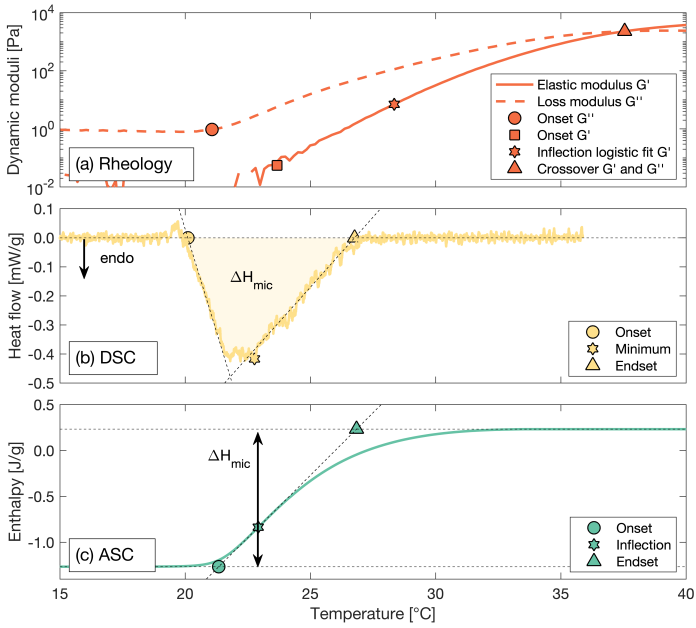

Figure 4.2: Temperature evolution of (a) the dynamic moduli G' and G'' at a frequency of 1 Hz, 0.1% strain and a heating rate of 0.1° C/min, (b) the DSC heat flow at a heating rate of 0.1° C/min and (c) the ASC enthalpy at a constant power supply of 300 μW for a concentrated solution of 132 g/L EG312. The DSC heat flow and ASC c_p data are baseline corrected. The critical transition temperatures are also indicated.

range of 3°C below and above the transition in a semi-log plot) is the equivalent of the onset temperature of the viscosity increase for dilute solutions (see Figure 4.1 (a)), it will further be considered as an indicator for the onset of micellization as inferred from oscillatory rheology. Compared to dilute solutions, its value does not differ as significantly from the onsets as determined by DSC and ASC, thereby indicating that for more concentrated solutions, rheology is more sensitive to micellization. At the onset of the G' increase (square symbol, determined based on the most significant slope change over a range of 3°C below and above the transition in a semi-log plot and taking into account the lower torque noise limit of 0.04 Pa), the micellar solution acquires elasticity, which occurs approximately at the same temperature as the peak and inflection temperatures in DSC and ASC thermograms, respectively, thereby reflecting the need for sufficient micelles to be present to enhance elasticity. The 'inflection point' of the $G'(T)$ curve is determined based on a logistic function fit of the $G'(T)$ data (see Appendix A) and represents the maximum elasticity increase per temperature increment. It is observed at the end of the micellization process, whereafter elasticity still increases

with temperature, but less pronounced. The crossover temperature between G' and G'' is frequently used as an approximation of the gel formation temperature T_{gel}, but has been shown to be more strongly dependent on the applied frequency [52]. The fact that elastic networks (or gels) seem to only be observed at temperatures well above the calorimetric endset temperatures (see Figures 4.2 (b) and (c)), finds its origin in the effect of temperature on the dynamics of the hydrophobic association, combined with the frequency dependency of the rheological results. Therefore, at temperatures above the calorimetric endset temperature of concentrated solutions, an elastic network might already exist, but it is a dynamic network that is rheologically not detected at a frequency of 1 Hz due to the very labile hydrophobic interaction at that temperature (i.e. the time it takes for a hydrophobic block to detach from a micellar core is significantly shorter than 1 s). Finally, it is important to mention that the increase in G' and G'' with increasing temperature is thermoreversible, without any hysteresis at a rate of 0.1°C/min, as can be inferred from rheological heating and cooling ramps (see Figure A.4 in Appendix A for temperature ramps of a 147 g/L EG412 solution at 0.1°C/min). As a consequence, the rheological properties at all individual, intermediate temperatures are stable, i.e. they do not further evolve upon long isothermal annealing.

The gradual G' and G'' evolution spanning over a temperature range of $\pm$ 15° C is in strong contrast with the rheological response of concentrated Pluronic® solutions exhibiting a very abrupt and drastic increase in dynamic moduli over a limited temperature region of < 5° C above the CMT [52]. Figure A.5 in Appendix A shows the dynamic moduli G' and G'' as a function of temperature for a 92 g/L EG412 solution and a 169 g/L F127 solution, both having a similar onset temperature for the increase in G'' but a very different profile with the increase spanning over 10°C for EG412 and over 0.5°C for F127. Moreover, frequency sweep experiments of concentrated Pluronic® solutions at temperatures above this abrupt sol-to-gel transition, manifest a typical fingerprint of an elastic solid, i.e. $G' > G''$ for the entire frequency range [52], whereas our concentrated solutions of multiblock copolymers have a viscoelastic network response with a crossover between G' and G'' at a certain frequency (see Figures 5.9 (a) and (b) for EG312 at 46°C and EG412 at 40°C). Therefore, the microscopic picture giving rise to elasticity at more elevated concentrations must be significantly different for ExpertGel multiblock copolymers as compared to Pluronic® triblock copolymers. It is well-known that the micelles formed by Pluronics® jam into a lyotropic liquid crystalline lattice at a certain critical volume fraction (ϕ_{crit}). A schematic representation of this micellar packing is shown in Figure 4.3 (a). This liquid crystalline behavior has been the subject of many studies investing the microstructural evolution of concentrated Pluronic® solutions as a function of concentration and temperature by light and neutron scattering [27, 50, 55, 291], as well as polarized microscopy [27].

The higher hierarchical packing of micelles in a crystalline lattice structure is also observed in the DSC thermogram of concentrated Pluronic® solutions as an additional first-order phase transition and corresponds nicely with the vast increase in the shear

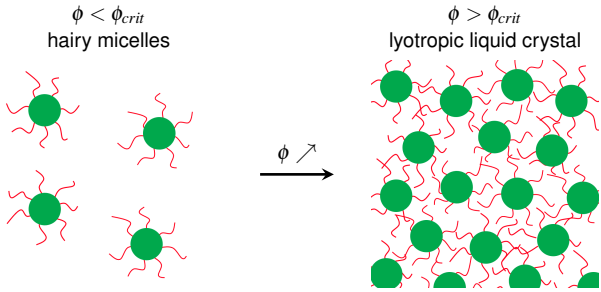

(a) ABA triblock copolymers (Pluronics®)

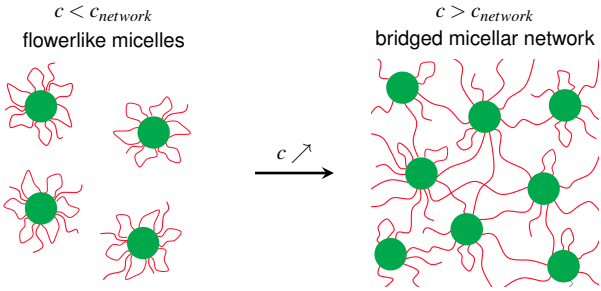

(b) AB multiblock copolymers (ExpertGel®)

Figure 4.3: Transition from a dilute solution of isolated micelles to a gel-like network at volume fractions or concentrations above the critical volume fraction (ϕ_{crit}) or the critical network concentration ($c_{network}$), respectively.

moduli [27, 45, 52, 291]. For alternating multiblock copolymers, on the other hand, both the DSC and ASC thermograms of concentrated solutions (see (b) and (c) graphs in Figure 4.2) do not reveal an additional phase transition other than the endothermic micellization. Hence, their elastic network properties do not originate from crystalline micellar jamming. In this regard, the presence of soluble PEO blocks, capped by hydrophobic PPO blocks at both ends, allows the formation of a PEO 'bridge' in between two different hydrophobic cores instead of looping back to the same micellar core. With increasing concentration, the closer proximity of other micellar cores allows such bridges to form more easily, which transforms the material from a viscous solution of isolated micelles at low concentrations to a sample-spanning, three-dimensional network at higher concentrations. A schematic overview of the network formation by multiblock copolymers can be seen in Figure 4.3 (b). This is similar to the network formation of BAB triblock copolymers bearing their hydrophobic blocks (B) as end groups, but with the additional possibility of forming multiple hydrophilic bridges per

multiblock copolymer (as compared to only one for triblock copolymers). Note that such elastic bridges are impossible in Pluronic® triblock copolymers, in which PEO blocks are only present as dangling ends (ABA configuration).

4.1.2 Cloud point

For aqueous solutions of Pluronic® triblock copolymers, turbidity measurements have clearly indicated clouding and phase separation at higher temperatures (far) above the CMT [63, 292]. Pluronics® thus exhibit lower critical solution temperature (LCST) behavior in water, meaning they are soluble at temperatures below the LCST and phase separate above a certain concentration-dependent temperature. For investigating the solubility of multiblock copolymers in water, the transmittance of laser light through a solution of multiblock copolymers was monitored as a function of temperature upon controlled heating. Figure 4.4 shows the transmissivity of 645 nm laser light as a function of temperature at a heating rate of 0.1° C/min for different dilute and more concentrated solutions of EG312. As can be seen, there exists a rather sharp transition over a span of < 3.5 ° C at which the solution transforms from transparant (100% transmittivity) to cloudy (0% transmittivity). The characteristic temperature corresponding to this transition is referred to as the cloud point. It is determined as the inflection point of the sharp transition. The region between the CMT (as a lower limit) and the cloud point (as an upper limit) determines the relevant temperature range of the multiblock copolymers in applications requiring micelles. Above the CMT, micelles

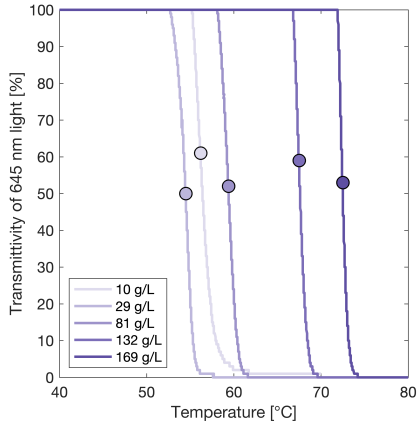

Figure 4.4: Transmittivity of 645 nm laser light as a function of temperature for different concentrations of EG312. The cloud point is determined as the inflection point and indicated with circles.

are (progressively) being formed, whereas above the cloud point these micelles cluster together, form large aggregates and eventually phase separate.

4.1.3 Phase diagram

The determination of the onset temperature of micellization (CMT) and cloud point for each concentration of multiblock copolymer allows us to construct a phase diagram. Figures 4.5 (a) and (b) show the phase diagram of EG312 and EG412, respectively. The onset temperature for micellization, as determined by different techniques, as well as the cloud point are indicated in the graph and define distinct areas corresponding to different states. The phase diagrams clearly reveal LCST behavior of the multiblock copolymer solutions, with the LCST corresponding to the minimum cloud point as indicated in the graphs (54.2°C for 15 g/L EG312 and 34.9 °C for 5 g/L EG412) [88]. At temperatures below the CMT, a purely viscous polymer solution is obtained. Visual inspection of the samples by tube inversion, after reaching thermal equilibrium in a temperature-controlled water bath for at least 15 minutes per temperature, indeed shows a transparant, flowable sol. Above the CMT and at dilute concentrations, micellization results in a viscous and transparant solution of isolated micelles. Via tube inversion, no clear distinction between the polymer and micellar solutions is possible, whereas calorimetric techniques, as well as the evolution of viscosity with temperature, indicate a pronounced change in the state of the sample. On the other hand, at higher concentrations, inversion of the sample tubes undoubtedly reveals the formation of a gel-like phase upon micellization, which does not flow under the influence of gravity. As explained before, the gel phase formed by multiblock copolymers is believed to arise from soluble PEO bridges in between adjacent micellar cores, which are in close proximity only at elevated concentrations. The experimentally determined critical temperatures marking the onset of rheological gel formation (T_{gel}) as a function of concentration (see Figures 4.4 (a) and Figure A.6 in Appendix A for the determination of T_{gel} at different concentrations of EG312) have also been added to the phase diagram in Figure 4.5. For the phase behavior of EG312 shown in Figure 4.5 (a), the transition between micellar solution and micellar network is indicated as a gradual transition zone. At concentrations around this critical transition, fluctuations and inhomogeneity in the microstructure induce unstable and irreproducible behavior [101, 194], which hampers the determination of a well-defined transition temperature (see also Section 5.2 in Chapter 5). Finally, by increasing the temperature to temperatures above the cloud point, both the micellar solution and micellar network turn white and cloudy, indicative of the formation of large scale aggregates. These eventually phase separate in the sol-state at low concentrations (see 20 g/L EG412 at 75° C in Figure 4.5 (b)), but remain stabilized in the gel structure at elevated concentrations (see 124 g/L EG412 at 75° C in Figure 4.5 (b)). The phase diagrams reveal large similarity between the differently assessed onsets of micellization. Nonetheless, it is important to highlight

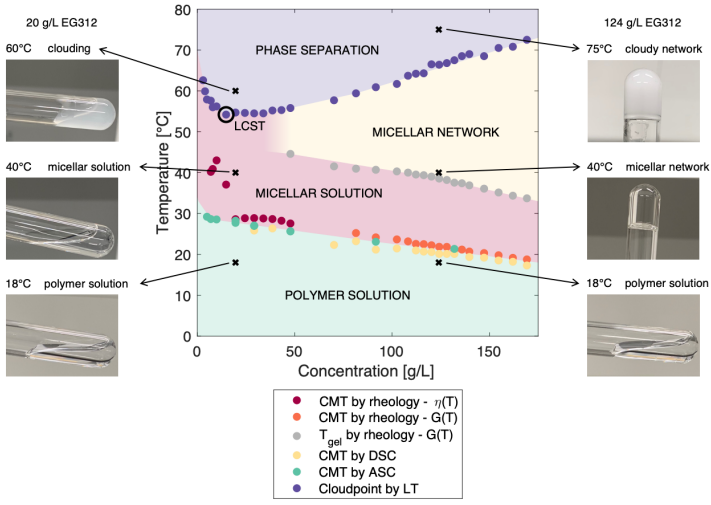

(a) EG312

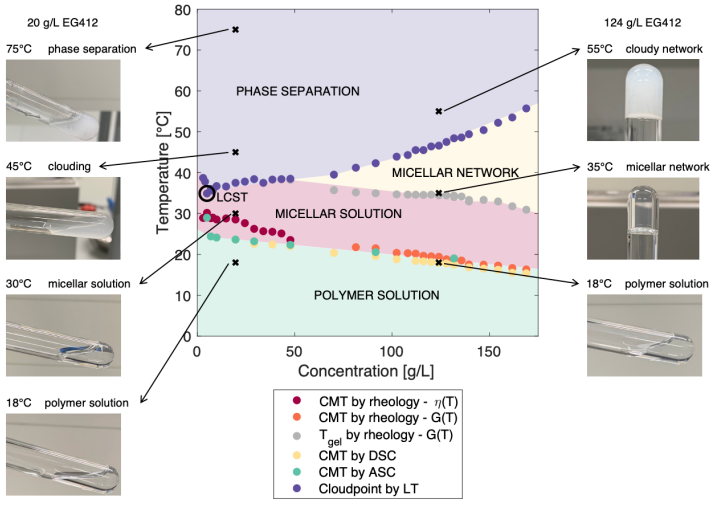

(b) EG412

Figure 4.5: Phase diagram indicating the different sample states as a function of temperature and concentration. The micellization temperatures are determined by rheology, i.e. based on the temperature evolution of viscosity for dilute solutions and based on the temperature evolution of the dynamic moduli for concentrated solutions, as well as by calorimetric techniques, i.e. differential (DSC) and adiabatic (ASC) scanning calorimetry. The cloud point is determined by light transmittance (LT). The T_{gel} values, as determined from rheological temperature ramps on concentrated solutions at 1 Hz, are also shown. Pictures are taken for visual inspection of the sample upon tube inversion at thermal equilibrium, and clearly show the transition from transparent to cloudy sample states.

that differences in CMT determined by the temperature-dependent viscosity evolution as compared to the CMT from DSC and ASC are more pronounced at very dilute concentrations of multiblock copolymers (< 25 g/L).

Comparing the phase diagram obtained for EG312 with that of EG412 allows us to pinpoint two main differences in the phase behavior of the multiblock copolymers with different EO weight fraction (see Table 3.4). The critical micellization temperatures of EG312 are located 3 to 4° C above those of EG412, which can be attributed to the slightly lower hydrophobicity and smaller PPO block length of EG312 as compared to that of EG412, similar to the trends observed for Pluronics® [27, 43]. Remarkably, the cloud point curve of EG312 is shifted by approximately 18° C as compared to that of EG412, due to which the interesting micellar regions span over a wider range of temperatures for EG312. The LCST behavior of Pluronics® has been previously attributed to the increasing hydrophobicity of the PEO block at high temperatures above the CMT [88, 292], and is therefore governed by the length of both the PPO and PEO blocks. Regarding the PPO block length, it seems unlikely that only the limited decrease in PPO block lengths and overall hydrophobicity causes such a large increase in the cloud point of EG312 as compared to EG412. Moreover, the progressive dehydration of PEO at elevated temperatures above CMT would induce an opposite effect, i.e. the higher PEO fraction in EG312 would lower the cloud point. Combining these two effects, one would expect that the cloud points of EG312 and EG412 would not differ much. Therefore, the cloud point seems to be more sensitive to a difference in molecular multiblock copolymer architecture as compared to the CMT.

Besides the difference in gelation mechanism and the absence of crystalline stacking of micelles formed by multiblock copolymers, the CMC of the EG312 and EG412 is lower as compared to that of their precursor Pluronics® F108 and F127, respectively. Table 4.1 summarizes the CMC at 25° C for EG312 and its precursor F108, and at 20° C for EG412 and its precursor F127. The values for ExpertGel® are obtained by interpolation of the CMT data as an average between DSC and PP rheology data, and expressed as a molar concentration. The values for the precursor Pluronics® are taken from literature [43]. Note that at these temperatures, the CMCs of both Pluronics®, expressed as a molar concentration, are approximately equal and indicate the need for a lower thermal driving force in the more hydrophobic component F127. The lower CMC values of multiblock copolymers as compared to that of Pluronics® with similar EO weight fractions, find their origin in the increased length of the multiblock copolymers. In this regard, Alexandridis *et al.* found that also for Pluronic® triblock copolymers with similar EO weight fraction and a molecular weight ranging from 2900 g/mol to 14600 g/mol, an increase in the molecular weight lowers the observed CMC (or CMT) in a linear fashion [43, 44]. A similar reasoning also explains the difference in the cloud points of the multiblock copolymers as compared to that of Pluronics®, for which phase separation was found to occur only above 100° C for F108 and F127 [63]. It should also be highlighted that the reduction in CMC by a factor

of 3.1 (EG312) or 1.5 (EG412) for our medium-length multiblock copolymers with 4 repeating PEO-PPO units, is very limited as compared to the 100-fold reduction obtained by employing long multiblock copolymers with 6 to 10 repeating PEO-PPO units, as studied by Rikiyama *et al.* [79] and compared to their triblock copolymer counterparts with similar EO content. Since the molecular weight of their multiblocks was not vastly increased as compared to that of our multiblocks at similar f_{EO} values, this implies that also the copolymer architecture, and more specifically the amount of repeating units, plays a crucial role in the final CMC reduction of multiblocks as compared to triblocks. Similarly, also the concentration and temperature at which the LCST is reached seems to be greatly reduced if more hydrophobic blocks are present (54.2°C at 15 g/L for EG312 multiblock copolymers with 4 repeating units as used this study, 58°C at 3 g/L for alternating multiblock copolymers having 8 repeating units but similar hydrophobicity as studied by Horiuchi *et al.* [88]).

Table 4.1: Comparison of the CMC values for ExpertGel® (EG312 and EG412) as determined in the current study, as well as for Pluronics® (F108 and F127) as found in literature.

Sample	Temperature [K]	CMC [mM]
EG312	298	0.90
F108[i]	298	3.08
EG412	293	2.58
F127[i]	293	3.17

[i] Based on the data of Alexandridis *et al.* [43].

4.2 Thermodynamics of micellization

The thermodynamic driving forces behind the self-assembly process of multiblock copolymers can provide interesting insights and help pinpointing differences as compared to triblock or longer multiblock copolymers. Micellization is often considered as a closed-association equilibrium reaction

$$n \cdot \mathrm{U} \rightleftharpoons \mathrm{M}_n$$

between a unimer (U) and an n-mer (M_n), i.e. a multimer in which n unimers are combined [43, 293]. Polydispersity in micellar assemblies is thus considered negligible. The standard Gibbs free energy for this equilibrium reaction, i.e. the micellization

Gibbs free energy per copolymer ΔG_{mic}, is defined as

$$\Delta G_{mic} = -\frac{RT}{n} \ln K = -\frac{RT}{n} \ln \frac{[M_n]}{[U]^n}, \tag{4.1}$$

in which R is the universal gas constant (8.3145 J/molK), T the absolute temperature and K the equilibrium constant. The latter is defined as the ratio of the equilibrium concentrations of micelles $[M_n]$ and unimers $[U]$ taking into account the stoichiometry of the reaction in their exponent. Note that the stoichiometric factor n is closely related to the micellar aggregation number N_{agg}, defined in this work as the amount of hydrophobic blocks per micellar core. In the case of multiblock copolymers containing more than 1 hydrophobic block per chain, N_{agg} and n are related through the relationship $N_{agg} = a \cdot n$, in which a represents the amount of hydrophobic blocks per chain. Making use of the law of mass action, together with the fact that n is usually significantly larger than 10, the well-known simplified expression

$$\Delta G_{mic} = RT \ln x_{CMC}(T) \tag{4.2}$$

for the Gibbs free energy of micellization is obtained, in which $x_{CMC}(T)$ represents the mole fraction of copolymers at the CMC [44]. A similar expression for ΔG_{mic} can be derived using the more controversial pseudo-phase separation model for micellization by assuming a constant concentration of free unimers equal to the CMC [44]. In Section 5.2, the dependence of the onset temperature for micelle formation on concentration, i.e. CMT(c), was determined by rheometry, DSC and ASC. The interchangeability between the temperature dependence of the CMC and the concentration dependence of the CMT allows us to determine the Gibbs free energy of micellization from our experimentally determined CMT(c) values.

In Figures 4.6 (a) and (b), the ΔG_{mic} values (circles, left y-axis) based on the CMT(c) as inferred from rheology (in orange and red), DSC (in yellow) and ASC (in green) by using Equation 4.2, are shown as a function of temperature for both EG312 (a) and EG412 (b). Note that not the concentration, but the temperature is used as independent variable, by using CMT(c) as the relation between concentration and temperature. As expected, the negative Gibbs-free energy implies an exothermic, spontaneous self-assembly process. The values of the Gibbs free energy at the CMT of a 1wt% solution and a comparison with the values obtained for Pluronics® F108 and F127 as obtained by Alexandridis *et al.* [43] for 1% w/v solutions are given in Table 4.2. Note that the CMTs are rather similar, while the molar concentration is significantly reduced in the multiblock copolymer solutions due to their higher molecular weight. The Gibbs free energy of micellization for multiblock copolymers is more exothermic (more negative with approximately 12-13%) than that of Pluronics®. Since the multiblock copolymers contain 4 hydrophobic blocks per chain and the Pluronic® triblock copolymers solely contain 1 hydrophobic PPO block per chain, the micellar aggregation of multiblock copolymers is energetically more beneficial (per mol) as compared to that of Pluronics®,

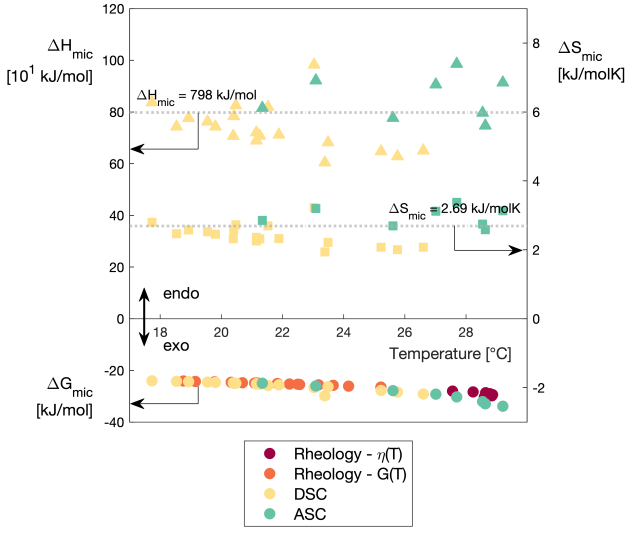

(a) EG312

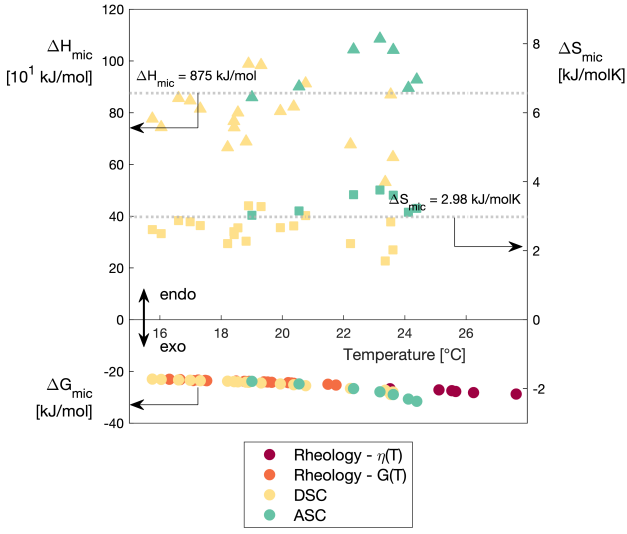

(b) EG412

Figure 4.6: Thermodynamic quantities of micellization ΔG_{mic} (exothermic, lower left y-axis), ΔH_{mic} (endothermic, upper left y-axis) and ΔS_{mic} (right y-axis) for (a) EG312 and (b) EG412 as a function of temperature. ΔG_{mic} is calculated from the CMT as determined by rheology (η(T) in red and G(T) in orange), by DSC at 1°C/min (yellow) and by ASC (green), ΔH_{mic} is measured by calorimetric techniques (DSC at 1°C/min in yellow and ASC in green) and ΔS_{mic} is calculated using ΔG_{mic}, ΔH_{mic} and CMT. Horizontal dotted lines represent the average values for ΔH_{mic} and ΔS_{mic} from DSC and ASC.

even though the overall hydrophobicity is similar. In this regard, it is important to mention that Alexandridis *et al.* [43] obtained comparable ΔG_{mic} values (deviations of less than 4%) for Pluronics® having similar f_{EO} but twice the molecular weight. Moreover, they found an increase in absolute ΔG_{mic} of 12% for triblock copolymers with a doubled f_{EO} from 0.4 to 0.8. Therefore, we can conclude that the increase in ΔG_{mic} of multiblock copolymers compared to triblock copolymers with equal EO content, is significant and induced by its multiblock nature, rather than the increased molecular weight.

Table 4.2: Thermodynamic quantities of micellization ΔG_{mic}, ΔH_{mic} and ΔS_{mic} for ExpertGel® (EG312 and EG412) as determined in the current study, as well as for Pluronics® (F108 and F127) as found in literature, all evaluated at the CMT.

Sample	CMT [K]	Concentration [mM]	ΔG_{mic} [kJ/mol]	ΔH_{mic} [kJ/mol]	ΔS_{mic} [kJ/molK]
EG312[i]	301.5	0.16	-32.06	797	2.8
F108[ii]	302.5	0.69	-28.4	266	1.0
EG412[i]	297.1	0.23	-30.68	896	3.1
F127[ii]	297	0.79	-27.5	253	0.9

[i] Determined based on ASC results of a 1wt% multiblock copolymer solution;
[ii] Determined by Alexandridis *et al.* [43] for a 1% w/v solution.

It is well-known that spontaneous processes happen due to a reduction in the Gibbs-free energy $\Delta G = \Delta H - T\Delta S$, which consists of both an enthalpic (ΔH) and an entropic (ΔS) contribution. Calorimetric techniques such as DSC, ASC and ITC, besides providing insights in the critical transition temperatures, also allow the determination of the enthalpy related to phase transitions. Hence, combining our knowledge of $\Delta G_{mic}(T)$ from CMT(c) with the experimentally determined ΔH_{mic} from calorimetric techniques, will help pinpointing the exact energetic driving forces for the spontaneous micellization of multiblock copolymers in aqueous solutions in the following two paragraphs.

4.2.1 Scanning calorimetry

The heat flow curve obtained by applying a DSC heating cycle at 0.1° C/min to a concentrated solution of 30 g/L EG312 in Figure 4.1 (b) revealed a clear endothermic and broad transition from unimers into micellar assemblies. The enthalpy ΔH_{mic}, expressed per mol copolymer, can be determined by integrating the specific heat flux curve (see area indicated in Figure 4.1 (b)), dividing the integrated enthalpy by the

applied heating rate as well as the weight percentage of copolymer in the solution and converting to a molar basis using the molecular mass of the multiblock copolymers. Since the data at a very low heating rate of 0.1° C/min are significantly scattered and compromise a correct integration, the heat flow results upon application of a heating rate of 1° C/min were also investigated. Figures A.7 and A.8 in Appendix A clearly indicate less scatter on the DSC data using a higher heating rate. Figure 4.6 shows the obtained ΔH_{mic} values from DSC thermograms at 1° C/min (yellow triangles, left y-axis) as a function of temperature for (a) EG312 and (b) EG412. The values do not change much with temperature (and hence concentration) with an average of 0.76 $\pm$ 0.09 MJ/mol and 0.8 $\pm$ 0.1 MJ/mol for EG312 and EG412, respectively. The enthalpy values obtained for 0.1° C/min thermograms are notably more scattered around average values of 0.9 $\pm$ 0.7 MJ/mol for EG312 and 0.8 $\pm$ 0.2 MJ/mol for EG412 (see Figure A.8 in Appendix A), which are not unlike the ΔH_{mic} values obtained at 1° C/min but with much higher standard deviation. Due to the low signal-to-noise ratio of DSC measurements on dilute copolymer solutions, ASC was used to resolve the phase transition and its associating enthalpy in dilute solutions. As can be seen in Figure 4.1 (c) for 30 g/L EG312, the endothermic ΔH_{mic} can be calculated as the difference in overall enthalpy at temperatures sufficiently above and below the smooth and broad micellization process. The ΔH_{mic} values divided by the weight percentage of copolymer in the solution, are also shown in Figures 4.6 (a) and (b) (green triangles, left y-axis). The average values of 0.86 $\pm$ 0.09 MJ/mol and 0.97 $\pm$ 0.09 MJ/mol for EG312 and EG412, respectively, are in agreement with the ones obtained from DSC.

The values of ΔH_{mic} of EG312 and EG412 micellization are significantly larger than those of their precursor Pluronics® (see Table 4.2). Moreover, the enthalpy values normalized by the amount of EO and PO monomers, $\Delta H_{mic}/(N_{EO}+N_{PO})$ were found to be similar to those of Pluronics® with similar hydrophobicity. The ExpertGel® EG312 and EG412 multiblock copolymers have normalized enthalpy values of 0.6 $\pm$ 0.1 kJ/mol and 0.9 $\pm$ 0.1 kJ/mol, whereas those of Pluronic® F108 and F127 equal 0.85 kJ/mol and 0.95 kJ/mol [43], respectively. The scaling relation as generally observed for a wide set of Pluronics® by Alexandridis *et al.* [43] states that the normalized enthalpy values solely depend on the weight fraction of PO to EO and are thus similar for Pluronics® of equal hydrophobicity and different molecular weight. Interestingly, the ΔH_{mic} values obtained for our medium-length multiblock copolymers with 4 repeating PEO-PPO units are significantly larger than the ones obtained by Rikiyama *et al.* [79] for longer alternating PEO-PPO multiblock copolymers, which contain 6 or more repeating units per chain. The normalized enthalpies of their longer multiblock copolymers were also found to be significantly lower (reduced by a factor 3 to 9) as compared to that of Pluronics with similar EO fraction [79]. A possible explanation for this counterintuitive difference as compared to our medium-length multiblock copolymers can be found in the core-corona unimer assemblies formed by long multiblock copolymers. Since such unimer assemblies are already present below the CMT, their PPO blocks are already efficiently screened from the aqueous medium and no drastic change in the

chain configuration upon multimer micellization is anticipated, resulting in rather low ΔH_{mic} and normalized ΔH_{mic} values. In contrast, for medium-length multiblocks with only 4 hydrophobic PPO blocks, the entropic hydrophobic driving force for a collapsed, core-corona configuration of unimers in which the PPO blocks cluster together, is lower as compared to that of long multiblocks with at least 6 PPO blocks. Therefore, ExpertGel multiblocks® do not exhibit any significant unimer aggregation and have their PPO blocks fully exposed to the surrounding water solvent below the CMT [79]. The clustering of these PPO blocks into a micellar core is thus enthalpically more expensive.

The positive, endothermic micellization enthalpy indicates that upon micellization, energy is consumed for breaking the interactions between PPO and the surrounding water. The spontaneous micellar self-assembly of the multiblock copolymers must thus be driven by entropic gains. The entropy loss correlated with the clustering of multiple PPO blocks into one micellar core, is widely overcome by the gain in entropy of the surrounding water molecules upon collapsing their cage-like clathrate structure formed around individual hydrophobic PPO blocks [43]. This so-called hydrophobic effect has been observed for Pluronics® as well [27, 43], and is the common driving force for amphiphilic self-assembly. The temperature-dependent entropy of micellization ΔS_{mic} (squares, right y-axis), as calculated from ΔG_{mic} and ΔH_{mic} by DSC (yellow) and ASC (green), is also shown in Figures 4.6 (a) and (b) for EG312 and EG412, respectively. The horizontal line shows the average ΔS_{mic}. A comparison of the ΔS_{mic} values for 1wt% solutions is added to Table 4.2. Analogous to the enthalpic cost of micellization, the entropic gain upon micellization is also governed by the amount of clustering PPO blocks in one chain, thereby resulting in a significantly increased micellization entropy of ExpertGel® as compared to that of Pluronics®) as well as compared to that of longer multiblocks already forming unimer micelles below CMT.

4.2.2 Titration calorimetry

Scanning calorimetry studies phase transitions in materials of constant composition as a function of temperature, albeit by different driving principles such as the application of a thermal protocol in DSC or the application of a heat power protocol in ASC. Isothermal titration calorimetry (ITC), on the other hand, allows measuring enthalpic interactions upon a step-wise increase of concentration at isothermal conditions to extract critical transition concentrations and energies. As an example, Figure 4.7 (a) shows the exothermic heat releases as a function of time upon consecutive injections of a concentrated micellar solution of EG312, sufficiently above the CMC of the multiblock copolymers, into (initially) water at isothermal conditions of 34° C. After integration of the released heat, a so-called enthalpogram of the heat as a function of the multiblock copolymer concentration is obtained (see Figure 4.7 (b)). For amphiphilic molecules, the enthalpogram often exhibits a sigmoidal shape, indicating that the

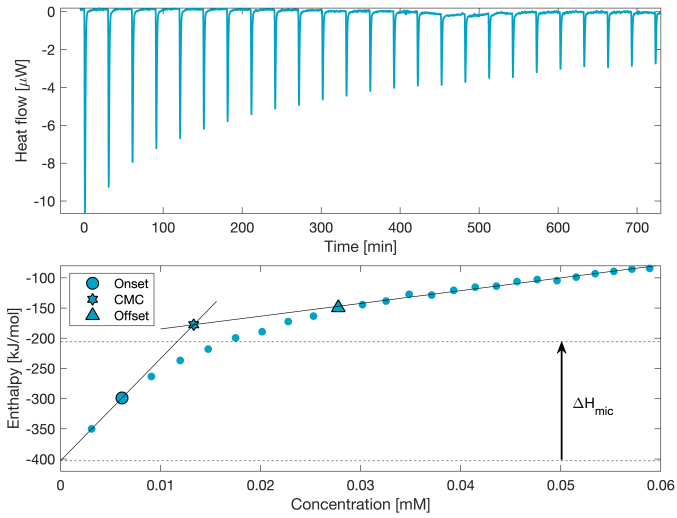

Figure 4.7: ITC data analysis of EG312 at 34° C: (a) time evolution of the heat flow upon consecutive injections of a concentrated (0.11 mM) micellar solution and (b) integrated heat data after baseline subtraction as a function of multiblock copolymer concentration in the cell. The full lines represent the linear fits at the lowest and highest concentrations. The critical transition concentrations (onset of transition, CMC and end of transition) are also indicated.

CMC is progressively reached and exceeded [293]. From such sigmoidal shapes, three enthalpic contributions are usually discerned in the enthalpogram [293]. At low concentrations, the injected micelles dissociate into unimers and the detected heat is related to the dilution of unimers. At intermediate concentrations around the CMC, an equilibrium between the dissociation of micelles to cover the surface of the cell and the formation of the first micelles exists, resulting in an endothermic (sharp) increase in the released heat, which corresponds to the enthalpy of micellization (ΔH_{mic}). The CMC is usually determined based on the inflection point of this increase. At high concentrations, above the CMC, the injected micelles are diluted in the cell and micelle dilution enthalpy is detected.

However, in many cases, the shape of the enthalpogram is non-sigmoidal and a sharper and more abrupt increase of the released heat as a function of concentration at the start of the enthalpogram is observed. This indicates the absence of the micelle dissociation process into unimers, and is usually an implication of a rather low CMC [67, 293–296]. In that case, the determination of the CMC and ΔH_{mic} is less obvious. Following the procedure by Bouchemal et al. [61, 293], the start and end of the micellization process can be determined as the concentrations at which the data deviate from the

linear fits at the lowest and highest concentrations, respectively. This procedure is shown in Figure 4.7 (b). To obtain a single CMC value for comparison, the crossover between both linear fits was taken as the CMC [296]. The enthalpy of micellization (ΔH_{mic}) was defined as the difference between the intercepts of the linear fits [61, 293], and corrected by a factor $c_{syr}/(c_{syr} - CMC)$ to account for the micelles present in the syringe with concentration c_{syr} (> CMC). Table 4.3 summarizes the as such obtained values of the CMC and ΔH_{mic} for EG312, EG412 and F127 at different isothermal conditions. Interestingly, as can be seen in the phase diagrams of EG312 and EG412 in Figures 4.8 (a) and (b), respectively, the CMCs at a constant temperature, as determined by ITC, are in line with the CMT values determined by other techniques at higher multiblock copolymer concentrations. It should be mentioned that the unexpected increase in CMC (of 0.002 mM) with increasing temperature from 32° C to 34° C for EG312, falls within the standard deviation (of 0.0015 mM at 32° C and 0.002 mM at 34° C) around the mean values of independent measurements, and is therefore not further interpreted. Notably, such analysis procedure is more arbitrary than in case of a sigmoidal enthalpogram. As a matter of comparison, for some measurements for which the enthalpogram had a more sigmoidal shape, the analysis procedure as described by Bouchemal *et al.* for sigmoids [293], was also adopted and compared to the procedure as described above (see Figure A.9 in Appendix A for a measurement of EG412 at 26° C). The CMC, determined as the inflection point of the sigmoid, was significantly lower, whereas the enthalpy ΔH_{mic} was in good agreement with the value obtained by the non-sigmoidal analysis, thereby confirming that the non-sigmoidal ITC analysis results in reliable enthalpy values.

The enthalpy of micellization as determined by ITC summarized in Table 4.3 was found to differ quite substantially from the ΔH_{mic} values previously determined by scanning calorimetry (see Figure 4.6 and Table 4.2). It is well-known that the enthalpy of micellization from ITC can differ from that obtained by other techniques such as DSC due to the very different probing principles [293]. Indeed, for Pluronic® F127 Bouchemal *et al.* found ΔH_{mic} values between 80 and 177 kJ/mol upon increasing temperatures from 28 to 31° C using ITC [61], whereas Pham-Trong *et al.* obtained 321 kJ/mol for ΔH_{mic} of F127 by micro-DSC [45]. However, there also exist examples in literature for which only slight differences between the enthalpy of micellization, as probed by ITC and other techniques, were detected [61, 297]. Therefore, it is believed that the discrepancy between ΔH_{mic} from different techniques depends on the type of amphiphiles [293]. For our PEO-PPO multiblock copolymers, it seems plausible that similar behavior as for their precursor Pluronics® is observed. Note that also for our multiblock copolymers, an increasing trend in ΔH_{mic} with temperature is evident (see Table 4.3), similar to Pluronics® [61]. Moreover, the CMC and ΔH_{mic} obtained for Pluronic F127 at 30° C correspond quite nicely with the ones obtained by Bouchemal *et al.* (CMC = 0.085 $\pm$ 0.001 mM, ΔH_{mic} = 141 $\pm$ 1 kJ/mol) [61]. In Table 4.3, the other calculated thermodynamic quantities $\Delta G_{mic}$and ΔS_{mic} are also given. Whereas the values of the overal exothermic Gibbs free energy ΔG_{mic} comply well with the ones

obtained by DSC and ASC, the entropy deviates quite significantly due to the great discrepancy in ΔH_{mic}. Besides the determination of the CMC and the corresponding thermodynamic quantities, ITC measurements also allow to determine the aggregation number N_{agg}, which is closely linked to the slope of the increase in enthalpy around the CMC [298] and can be determined by the regression method of Olesen *et al.* [299]. Nonetheless, such procedure requires a sigmoidal enthalpogram and is thus not further considered.

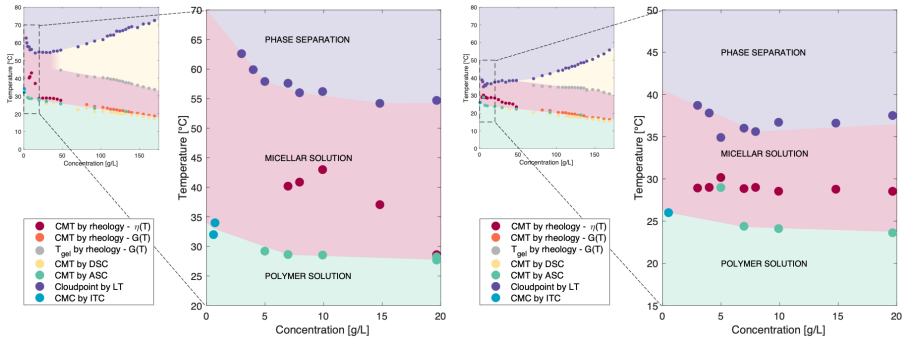

(a) EG312 **(b)** EG412

Figure 4.8: Phase diagram indicating the different sample states as a function of temperature and concentration. The micellization temperatures (CMT) are determined by rheology, DSC and ASC. The micellization concentrations (CMC) as determined by isothermal titration calorimetry (ITC) fall in line with the CMTs. The cloud point is determined by light transmittance (LT).

Table 4.3: Critical micellar concentration (CMC) and thermodynamic quantities of micellization ΔG_{mic}, ΔH_{mic} and ΔS_{mic} for ExpertGel® (EG312 and EG412) and Pluronic® F127 as determined by ITC at a constant temperature.

Sample	Temperature [K]	CMC [mM]	ΔG_{mic} [kJ/mol]	ΔH_{mic} [kJ/mol]	ΔS_{mic} [kJ/molK]
EG312	305	0.009±0.001	-39.6	120±20	0.5
EG312	307	0.011±0.002	-39.3	180±40	0.7
EG412	299	0.012±0.004	-38.2	30±10	0.2
F127	303	0.074	-34.1	100	0.4

4.3 Micellar sizes and topology

4.3.1 Dynamic light scattering

The phase behavior of medium-length alternating PEO-PPO multiblock copolymers as a function of temperature and concentration goes hand in hand with morphological changes. The individual unimers of a dilute polymer solution at low temperatures, aggregate into relatively small and hence transparant, non-scattering micellar assemblies at temperatures above their CMT. Dynamic Light Scattering (DLS) allows to estimate the size and topology of the assemblies present in dilute solution based on the interaction with visible light. Studying different temperatures (below and above the CMT) and concentrations in the dilute regime reveals their evolution with temperature and concentration. As an example, Figure 4.9 (a) shows the normalized intensity autocorrelation function $g^{(2)}(\tau) - 1$ at different scattering angles for 17 g/L EG312 at 35° C, which is above the CMT of 27.9° C. Since no clear multimodality is detected in the autocorrelation function, nor in the CONTIN fitting performed in the LS Instruments software, the normalized intensity autocorrelation function was fitted with a single stretched exponential decay $\exp[-2(\Gamma\tau)^{\beta}]$ in which Γ represents the decay rate and β the broadness. The latter was found to be higher than 0.8 for all measurements (and usually even close to 0.9) without a systematic trend as function of concentration and/or temperature. This value is close to unity (i.e. the broadness value of a single exponential) and is indicative of a rather monodisperse population, despite the significant polydispersity in the molecular weight of the polymers (see Table 3.2). In Figure 4.9 (b) the decay rate Γ is shown as a function of the squared scattering vector q^2 for 17 g/L EG312 at different temperatures. A linear evolution, especially far above CMT (35° C and 45° C), is observed, indicating Brownian diffusion for which the translational diffusion coefficient can be calculated from the slope as $D = \Gamma/q^2$. The absence of any angular dependency of Γ/q^2 thus suggests that no significant anisotropy is present [300]. Hence, the micellar assemblies formed by medium-length alternating PEO-PPO multiblock copolymers above their CMT must be spherical. Similar conclusions about the micellar monodispersity and shape as for EG312 were made for dilute solutions of EG412 at temperatures above their CMT (see Figure A.10 in Appendix A). Micelles formed by the precursor Pluronics®, F108 and F127, in aqueous solutions, were also found to be spherical [27, 50]. Moreover, the studies by Horiuchi and Rikiyama *et al.* on a longer alternating multiblock copolymer of PEO and PPO with similar hydrophobicity ($(EO_{220}PO_{33})_6$ with $f_{EO} = 0.83$), also provide evidence of spherical micelles both by DLS and synchrotron small-angle X-ray scattering (SAXS) on dilute solutions of isolated micelles [79, 88]. Nonetheless, the DLS studies on their longer multiblock copolymers in aqueous solutions showed a clear multimodality in the autocorrelation function. The authors attributed the larger sized structures of approximately 100 nm, which were present both below and above

the CMT, to non-structured aggregates for which the dye solubilization method did not reveal a clear hydrophobic core [79]. Such aggregation could be the result of the longer overall length of their molecules, combined with the peculiar behavior of PEO in water [79]. Owing to the smaller molecular weight of our alternating PEO-PPO block copolymers with similar hydrophobicity ($6.3 \cdot 10^4$ g/mol versus $13 \cdot 10^4$ g/mol), no aggregates with dimensions smaller than 200 nm were observed for our dilute copolymer solutions after filtration.

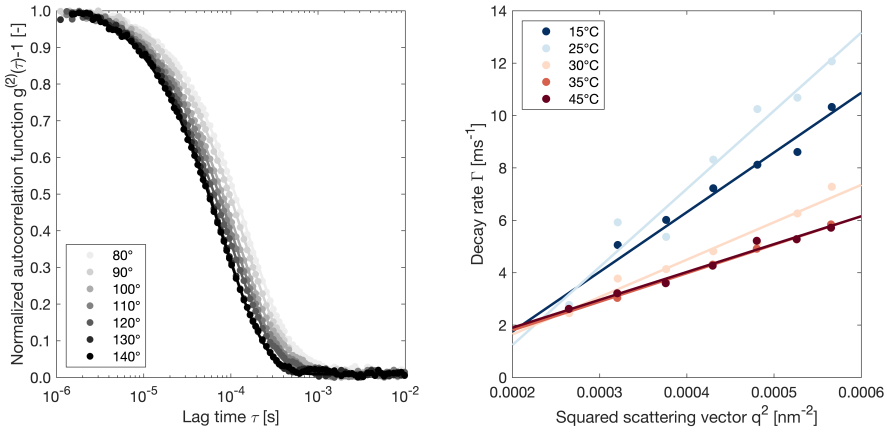

(a) **(b)**

Figure 4.9: Dynamic light scattering measurements on 17 g/L EG312: (a) normalized intensity autocorrelation function $g^{(2)}(\tau) - 1$ at different scattering angles at 35° C. Solid lines represent stretched exponential fits $\exp[-2(\Gamma\tau)^{\beta}]$. (b) Decay rate Γ versus squared scattering vector q^2 at different temperatures above and below the CMT (27.9° C for 17 g/L EG312). The solid line represents the linear fit with a slope equal to the translational diffusion coefficient D.

Using the Stokes-Einstein relation for spherical particles, the hydrodynamic radius R_H can be determined using

$$D = \frac{k_b \cdot T}{6\pi \cdot \eta_{sol} \cdot R_H} \tag{4.3}$$

with k_b the Boltzmann constant, T the absolute temperature and η_{sol} the temperature dependent viscosity of the surrounding milliQ water solvent. Figure 4.10 displays the evolution of the average hydrodynamic radius as a function of concentration at different temperatures for EG312 (a) and EG412 (b). The error bars are determined by performing the size analysis on three consecutive runs from 80° to 140° scattering angle on the same sample. At low temperatures below the CMT (15° C and 25° C for EG312 and 15° C and 20° C for EG412), individual polymer chains with hydrodynamic radii

between 6.8 and 9.5 nm are obtained with a decreasing trend as function of temperature, which can be attributed to the dehydration of the molecules and hence a more collapsed chain configuration at elevated temperatures [64]. Interestingly, SAXS measurements performed by Rikiyama *et al.* on dilute solutions of long alternating $(EO_{220}PO_{33})_6$ multiblock copolymers below the CMT, reveal a core-corona topology rather than a random coil configuration of single unimers ($R_g/R_H \sim 0.77$ as for spheres). Hence, the authors concluded that the unimers form single-molecule micelles below the CMT [79]. Based on thermodynamic considerations, we previously concluded that our medium-length multiblock copolymers do not form unimer micelles.

At temperatures around or just above the CMT (e.g. 30° C for 12 and 17 g/L EG312 in Figure 4.10 (a)), which are located in the broad temperature range where micellization happens, slightly larger sizes than below the CMT are observed demonstrating the onset of micelle formation. Note that during the broad micellization process, a progressive evolution from unimers to micelles happens and the solution exists of a mixture of unimers and micelles. The radius probed by DLS thus presumably represents an average size, since no clear bimodality indicative of two different populations, is observed in the autocorrelation functions. In this regard, it must be noted that the Rayleigh scattering intensity scales with $\sim R^6$, making the contribution of a small fraction of smaller particles to the DLS signal very limited. At temperatures sufficiently above the CMT (35° C and 45° C for EG312 and 25° C and 30° C for EG412), on the other hand, the detected hydrodynamic radii are at least 2 to 3 times larger as compared to that of the single polymer chains, indicative of the multimer micellar assemblies formed above the micellization temperature. The micelles of Pluronic® molecules were proven to be of smaller dimensions (5-8 nm) by using DLS and small-angle neutron scattering (SANS) [27, 55, 291]. The trend of hydrodynamic radius with concentration in Figure 4.10 changes from more or less constant below the CMT to increasing above the CMT. This trend, however, asks for a careful interpretation with respect to microstructural changes of individual micelles as function of concentration. In this regard, it is important to point out that the hydrodynamic radius, as probed by DLS, also takes into account the solvent layer surrounding the micelles and following their movement. Therefore, an increase in the hydrodynamic radius is not necessarily linked to the micellar assembly on its own, such as for example an increase in the aggregation number, but can also be the result of increased hydration of the hydrophilic corona. For Pluronic® molecules, for example, SLS and SANS experiments indeed revealed no significant change in the aggregation numbers with concentration, nor with temperature sufficiently above the CMT [27, 50]. Note that for the multiblock copolymers in Figure 4.10, besides a trend with concentration, no significant difference in hydrodynamic radius is observed at both temperatures (35° C and 45° C) above the CMT. This is quite striking and implies that there is no significant growth of the micellar assemblies with temperature above the CMT. Nonetheless, the presence of a clear and abrupt clouding behavior of the micellar solutions (see Section 3.1.2) proves that upon reaching the cloud point, a rapid increase in the size of the micellar assemblies and/or

other aggregates in general causes phase separation. These temperature independent micellar sizes sufficiently above the CMT and below the LCST were also observed for Pluronics® [27].

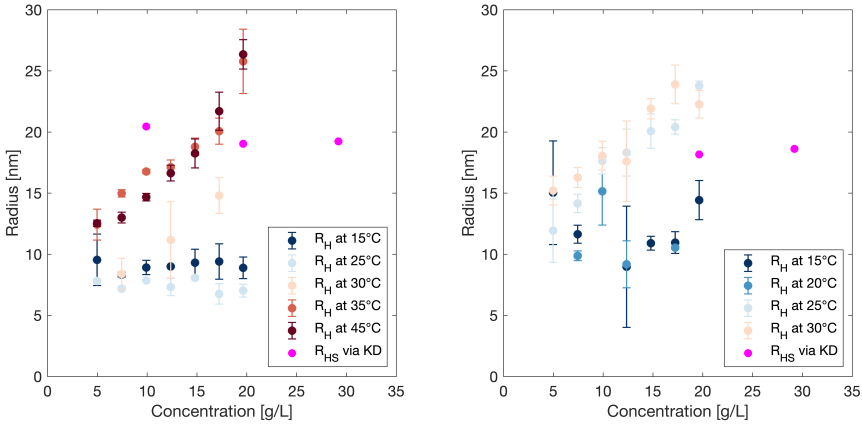

Figure 4.10: Evolution of the hydrodynamic radius R_H with concentration at different temperatures below and above the CMT for (a) EG312 and (b) EG412. The hard sphere radius R_{HS} as determined via the Krieger-Dougherty viscosity scaling is also indicated in the graphs.

4.3.2 Static light scattering

Additional information about the micellar assemblies can be obtained by Static Light Scattering (SLS), during which the interaction with the surrounding solvent does not play such a prominent role. SLS measurements were performed on multiple dilute copolymer concentrations at different temperatures below and above the CMT, detecting an average intensity I(q) at different scattering vectors. However, the Excess Rayleigh ratio $R(q)$ did not show any eminent angular dependency, rendering the determination of the radii of gyration by SLS impossible [301]. Based on the hydrodynamic radii determined by DLS and the fact that the radii of gyration are usually of similar size, i.e. 0.5 to 1.5 times R_H depending on the shape and topology, R_g is expected to be smaller than $\lambda/20$ (= 33 nm), thereby giving rise to pure Rayleigh point scattering without any destructive interference and hence also no size information. Nonetheless, SLS can still be useful for the detection of the weight average molecular weight $\overline{M}_w$ and second virial coefficient A_2, accounting for non-idealities, for both polymer and micellar solutions [301]. In a Debye plot of Kc/R versus concentration c (ideally at $q \to 0$), the

intercept and slope of the linear fit are equal to $1/\overline{M}_w$ and $2A_2$, respectively [301]. The Debye plots for both EG312 (a) and EG412 (b) at different temperatures below and above the CMT and the resulting evolution of $\overline{M}_w$ and A_2 as a function of temperature for EG312 (c) and EG412 (f) are shown in Figure 4.11. For the EG312 polymer solution without any micellar aggregation below the CMT, the molecular weight determined by SLS remains rather constant (average value of 78 869 g/mol) and corresponds quite nicely with the $\overline{M}_w$ value of 63 457 g/mol as determined by GPC (see Table 3.2). The positive A_2 values below the CMT indicate that water acts as a good solvent, with repulsive excluded-volume interactions between individual multiblock copolymer chains. At temperatures below the CMT, the multiblock copolymers are thus considered to be hydrophilic and completely soluble. Above the micellization temperature, on the other hand, the molecular weight significantly increases as compared to that of the individual chains, thereby proving that the multiblock copolymers assemble into micelle-like aggregates. Of particular interest is the fact that the molecular weight of a micellar assembly sufficiently above the CMT can be used to estimate of the aggregation number N_{agg}, i.e. the number of hydrophobic blocks in a micellar core, by using the following relationship:

$$N_{agg} = a \cdot \frac{\overline{M_{w,mic}}}{\overline{M_{w,copol}}}, \tag{4.4}$$

in which a represents the amount of hydrophobic blocks per multiblock copolymer chain (see Table 3.2). For this calculation, it is assumed that all multiblock copolymers are segregated in micellar assemblies sufficiently above the CMT, i.e. above the offset temperatures as determined by DSC and ASC (see Figures 4.1 and 4.2). Using the maximum detected molecular weight of EG312 micelles formed at 45° C (see Figure 4.11 (c)), an aggregation number of 57 is obtained. This value is in line with common aggregation numbers between 50 and 100 for Pluronic® molecules [55] and complies nicely with the constant aggregation number of 62, as determined by SAXS (see Section 5.3 in Chapter 5). For EG412, an approximation of N_{agg} based on SLS is not performed, as the molecular weight of individual polymer chains below the CMT (153 990 g/mol) was found to greatly differ from the value as obtained by GPC (43 885 g/mol). However, using the copolymer molecular weight $M_{w,copol}$ from GPC and the $M_{w,mic}$ value from SLS at 30°C (see Figure 4.11 (d)) in the calculation, results in an aggregation number of 79, which corresponds well with the aggregation number of 87 as determined by SAXS (see Section 5.3 in Chapter 5). The second virial coefficient A_2 decreases upon exceeding the onset temperature of micellization, due to an increasing attractive interaction between the multiblock copolymer molecules. This attractive interaction results in the aggregation of multiple copolymers into a micelle. As can be seen in Figures 4.11c and 4.11c, A_2 eventually reaches negative values sufficiently above the CMT. The temperature at which A_2 reaches 0 is a good indication of the θ-temperature of the multiblock copolymers in water. As expected, this θ-temperature is higher for the more hydrophilic EG312 copolymers as compared to EG412.

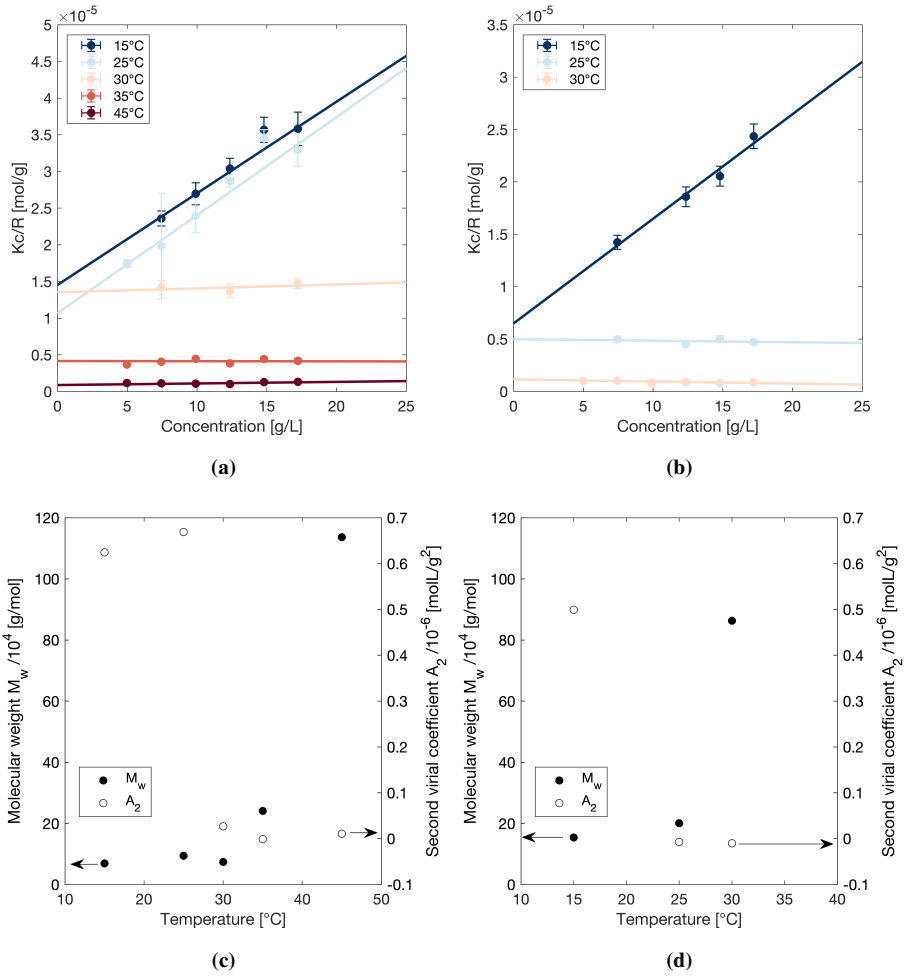

Figure 4.11: Debye plots of Kc/R versus concentration for the aqueous solutions of (a) EG312 and (b) EG412 at different temperatures below and above the CMT. The solid lines represent the linear fitting results. The temperature dependence of $\overline{M_w}$ (left axis) and A_2 (right axis) estimated from the intercept and slope of the Debye fitting results for (c) EG312 and (d) EG412.

4.3.3 Small-angle X-ray scattering

Besides visible light, the interaction between the molecules and other sources of radiation, such as X-rays and neutrons, can reveal additional information about the morphological changes upon micellization. However, the low electron density contrast between the molecules and the solvent, as well as the limited number of molecules in dilute solutions mandate the use of high intensity synchrotron X-ray radiation. As a preliminary study, small angle X-ray scattering (SAXS) measurements on dilute 35 g/L solutions of both types of multiblock copolymers were performed at the DESY facilities in Hamburg (Germany). Figures 4.12 (a) and (b) show the scattering intensity profiles $I(q)$ at various temperatures for 35 g/L EG312 and EG412 solutions, respectively. The different temperatures were reached during a continuous temperature ramp at a heating rate of 1°C/min and investigated by a 2 s exposure time. Although the data contain a considerable amount of scatter, a clear and progressive change with increasing temperature is observed for both types of multiblocks. At low temperatures, the intensities are highly scattered (or negative) after subtraction of the milliQ water solvent response at the same temperature, indicative of a very dilute polymer solution. In the wide temperature interval of micellization, a transition towards a well-resolved region with a characteristic slope of -4 (in a log-log plot) reveals the presence of spherical structures, as also previously inferred from the absence of anisotropy in DLS

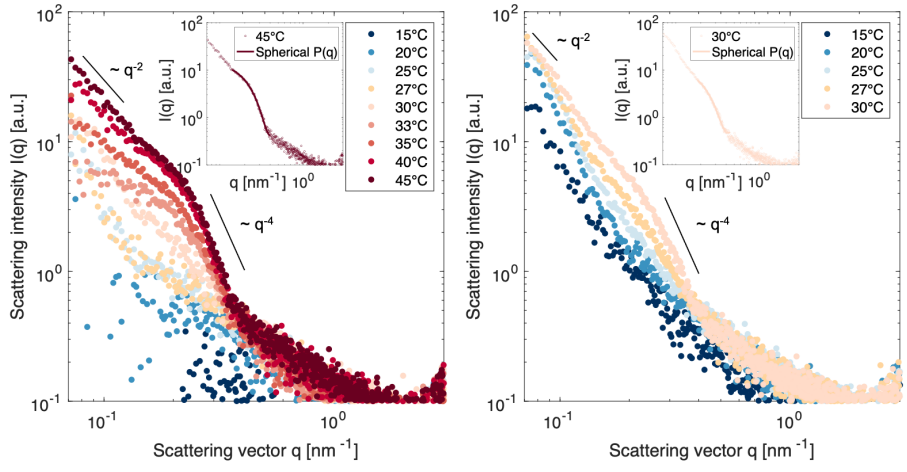

Figure 4.12: Synchrotron small-angle X-ray scattering intensity profiles $I(q)$ of (a) a 35 g/L EG312 solution and (b) a 35 g/L EG412 solution at different temperatures. The insets show the fitting of part of the intensity profiles at 45°C (EG412) and at 30°C (EG412) with a spherical form factor.

measurements. Figure 4.12 (a) also proves that at temperatures far above the CMT (40°C and 45°C) at which the micellization process is complete, the structures do not change much as a function of temperature, similar to the hydrodynamic radii in Figures 4.10 (a) and (b). The slope of -2 that seems to be observed at low q may be due to larger aggregates ($R_g = 182$ nm according to Guinier analysis of the EG312 sample at 45°C), although these were not detected in DLS measurements. The insets of Figures 4.12 (a) and (b) show the fitting of part of the intensity profiles at the highest temperatures of 45°C for EG312 and 30°C for EG412 with a spherical form factor $P(q)$ (see Equation 3.11). The use of a regular spherical form factor, rather than a more complex core-shell spherical form factor often used for micellar assemblies, can be justified by the absence of a significant secondary peak at a high scattering vector, which would be indicative of a core-shell structure. In addition, SAXS studies on micellar assemblies with a PEO-based corona in aqueous solutions reveal that X-rays do not significantly interact with the PEO corona [302]. Hence, only the PPO cores are detected by X-ray scattering and fitting the intensity profiles with a spherical core-shell form factor would imply that the PPO centre of the micellar assemblies consists of a core and a shell with significantly different scattering length densities, other than the PEO corona. Lemmers *et al.* [302] used both a spherical and a core-shell form factor to describe SAXS intensity profiles of dilute micelles with a polyelectrolyte complex core and a neutral PEO corona. They found that the spherical radius obtained by using a spherical form factor equals the radius of the core plus the thickness of the shell obtained by using a core-shell approach, which indicates that a spherical radius also correctly describes the size of the overall micellar core. Since a core-shell approach would increase the amount of fitting parameters, combined with the absence of a clear fingerprint of a core-shell structure, a simple spherical form factor seems appropriate for our multiblock copolymers. The spherical radius obtained by these fits equals 11 nm for both EG312 and EG412. This is significantly smaller than the hydrodynamic radii in Figures 4.10 (a) and (b), and provides additional proof that the PEO corona is not detected using X-rays.

4.3.4 Viscosity scaling

The Newtonian behavior and increase in viscosity as a function of temperature during micellization of dilute solutions without any elasticity (see Figure 4.1) resembles the behavior of a suspension of hard spheres with only repulsive interactions [45]. For such suspensions, the relation between the relative viscosity η_{rel}, i.e. the ratio between the viscosity of the suspension η and that of the surrounding medium η_{sol}, and the volume fraction of spheres ϕ is often described based on the Krieger-Dougherty (KD) equation [303]:

$$\eta_{rel} = \frac{\eta}{\eta_{sol}} = \left(1 - \frac{\phi}{\phi_{max}}\right)^{[\eta]\phi_{max}} \tag{4.5}$$

in which ϕ_{max} is the maximum packing fraction (0.637 for randomly packed spheres) and $[\eta]$ the intrinsic viscosity (2.5 for rigid spheres). It is anticipated that the Krieger-Dougherty relation also correctly describes the viscosity of micellar solutions formed by multiblock copolymers [45]. In that case, the micellar volume fraction can be determined based on the following equation:

$$\phi_{mic} = n_{mic} \cdot \frac{4\pi}{3} \cdot R_{HS}^3 = \frac{a \cdot c_{mic} \cdot N_{Av}}{N_{agg} \cdot M_w} \cdot \frac{4\pi}{3} \cdot R_{HS}^3 \tag{4.6}$$

in which n_{mic} is the number density of micelles, a the amount of hydrophobic blocks per multiblock copolymer chain (4 for both types of multiblock copolymers), N_{agg} the aggregation number, i.e. the amount of hydrophobic blocks per micellar core, c_{mic} is the concentration of multiblock copolymers segregated in micelles and R_{HS} the hard sphere radius of the micelle. Note that c_{mic} progressively evolves from 0 to the total concentration c during the broad micellization process, due to which c_{mic} and hence also ϕ_{mic} is temperature dependent at a fixed total copolymer concentration. The hard sphere radius R_{HS} gives a size indication of the micelles if they would be considered to be rigid spheres, and is usually smaller than the hydrodynamic radius R_H determined by DLS [304]. The evolution of c_{mic} during the micellization process can be determined based on the ratio of the enthalpy, for example as determined by ASC, to the total enthalpy of micellization ΔH_{mic} according to

$$c_{mic} = \frac{H(T)}{\Delta H_{mic}} \tag{4.7}$$

by assuming a density of 1000 g/L (cfr. water) for these dilute suspensions. The concentration of remaining unimers is then determined as $c_{uni} = c - c_{mic}$. In Figure 4.13 (a) the evolution of c_{mic} and c_{uni} as a function of temperature during the micellization process of a 30 g/L EG312 solution, as determined based on ASC data, is shown.

Using c_{mic} as inferred from ASC and the constant aggregation numbers of 62 and 87 for EG312 and EG412, respectively, as obtained from SAXS (see Section 5.3.1 in Chapter 5) and imposing a KD viscosity scaling of η_{rel} versus ϕ_{mic} allows to determine R_{HS} as another size indication of the spherical micelles. The relative viscosity η_{rel} can be obtained by using the temperature evolution of the viscosity η as obtained from rotational rheological measurements (see Figure 4.1 (a)) and dividing it by the temperature dependent viscosity of the surrounding fluid η_{sol} consisting of not only water, but also a progressively decreasing fraction of unimers. This temperature and unimer concentration dependent η_{sol} can be obtained by fitting the solution viscosity at different low temperatures below the CMT and at different concentrations using a surface fit (see Figures A.11 (a), (b) and (c) in Appendix A for EG312) and by extrapolating it to higher temperatures above the CMT and interpolating it to intermediate concentrations covering the continuous evolution of c_{uni} during micellization. The relative viscosity η_{rel} is then linked to the micellar volume fraction

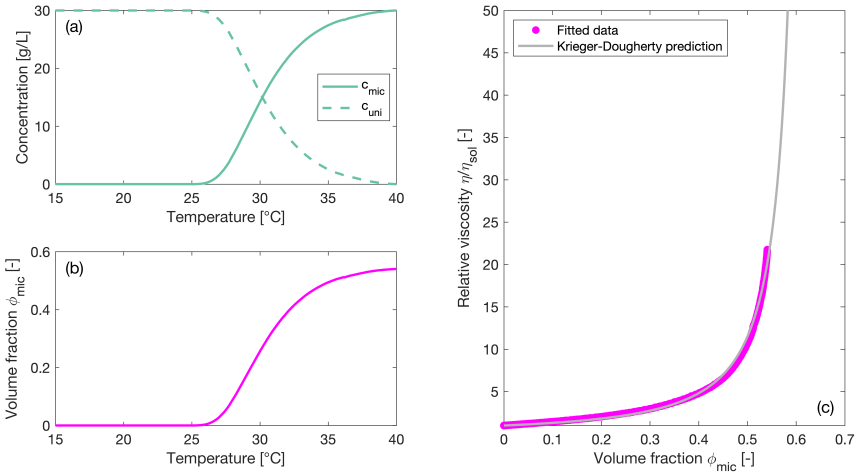

Figure 4.13: Analysis for determination of the hard sphere radius R_{HS} of 30 g/L EG312: (a) evolution of c_{mic} and c_{un} as function of temperature determined based on the enthalpy H(T) evolution probed by ASC, (b) volume fraction of micelles ϕ_{mic} based on c_{mic} using N_{agg} = 62 and R_{HS} = 19.23 nm and (c) fitting of the evolution of relative viscosity $\eta_{rel} = \eta/\eta_{sol}$ versus ϕ_{mic} to the Krieger-Dougherty prediction using R_{HS} as the fitting parameter.

ϕ_{mic} based on temperature. The procedure is shown for 30 g/L EG312 in Figures 4.13 (b) and (c) displaying respectively the temperature dependent ϕ_{mic} and the KD viscosity scaling of η_{rel} versus ϕ_{mic} for the optimal fitting parameter, i.e. a hard sphere radius R_{HS} = 19.23 nm. In Figure 4.10, the hard sphere radii obtained by the KD viscosity scaling are shown for the concentrations for which ASC measurements were performed. Only concentrations for which the micellar volume fraction ϕ_{mic} exceeds 0.2 upon micellization are shown, as to ensure enough deviation from the linear Einstein prediction of η_{rel} versus ϕ. The R_{HS} radii remain rather constant around 20 nm as a function of concentration. As expected, the hard sphere radii are smaller than the hydrodynamic radii R_H (except for 10 g/L EG312, which has a maximum ϕ_{mic} value only slightly above 0.2) and larger than the PPO core radius of approximately 10 nm, as obtained by SAXS (see Section 4.3.3 and Section 5.3.1 in Chapter 5). For a 20wt% micellar solution of Pluronic® F127, Pham Trong *et al.* determined a temperature dependent R_{HS} based on the KD viscosity scaling and a constant N_{agg} of 50, and found a 20% decrease in size from 11 to 9.2 nm upon increasing temperature during micellization [45]. Nonetheless, it should be mentioned that they studied a more concentrated micellar solution for which a compression of the 'hairy' corona might be responsible for the decrease of the hard sphere radius [305].

4.4 Conclusions

In this chapter, we mapped the phase behavior of PEO-PPO alternating multiblock copolymers with 4 repeating PEO-PPO units as a function of temperature and copolymer concentration using shear rheology, calorimetry, light and X-ray scattering and light transmittance. Comparing their behavior to that described in literature for Pluronic® PEO-PPO-PEO triblock copolymers with similar hydrophobicity [43] as well as longer PEO-PPO alternating multiblocks with 6 to 10 repeating units [79, 88], revealed some important similarities as well as differences and demonstrated the influence of copolymer composition and molecular weight.

Similar to triblocks and long multiblocks, the PPO blocks cluster together into microphase-separated domains and form micellar assemblies at elevated temperatures, driven by the entropy-dominated hydrophobic effect. The investigation of two different types of PEO-PPO multiblock copolymers with different overall hydrophobicity (EG312 with f_{EO} = 0.83 and EG412 with f_{EO} = 0.75) showed that the critical micellization temperature and the cloud point are governed by the hydrophobicity, analogous to other PEO-PPO based copolymers. Nonetheless, the copolymer architecture, i.e. the amount of PPO blocks in one copolymer chain, and the molecular weight play a vital role in the location of the phase boundaries, the thermodynamic driving forces and the micellar sizes. Very different as compared to Pluronics® [45], is the rheological behavior of concentrated multiblock copolymer solutions due to distinct network formation principles. The evolution of the dynamic shear moduli G' and G'' as a function of temperature demonstrated a gradual increase spanning over about 10° C from a micellar solution into a viscoelastic transient network. Contrary to Pluronics®, the network formed by multiblocks is not induced by crystalline ordering of micelles, as verified by the absence of another enthalpic process in calorimetric thermograms, but is formed by elastic PEO bridges connecting micellar PPO cores.

Comparing the aggregation behavior of medium-length PEO-PPO alternating multiblock copolymers with that of longer PEO-PPO alternating multiblocks [79], revealed that shorter multiblocks do not form single-molecule micelles below the CMT, thereby exhibiting a more drastic morphological change upon micellization and possibly allowing more efficient and homogeneous encapsulation of therapeutic agents using temperature as an external stimulus. This chapter has thus shown the potential of alternating block copolymers for the development of micellar systems with tailored (mechanical) properties depending on temperature, concentration and molecular architecture. Moreover, the construction of the phase diagrams is crucial for the determination of the relevant temperature and concentration ranges for network formation, studied in the coming chapters.

Chapter 5

Unravelling their network topology and elasticity using a novel transient network model

In the previous chapter, PEO-PPO multiblock copolymers were found to self-assembly into an elastic, transient micellar network at elevated concentrations and temperatures. In this chapter we focus on these network structures and aim to explain the concentration-dependent elasticity in such networks by means of a transient network model. As discussed in Section 2.3 of Chapter 2, a multitude of different transient network models predicting the rheological behavior of telechelic or multisticker networks has been developed in the last few decades. Nonetheless, explaining the behavior of networks consisting of large, micellar crosslinking nodes formed by multisticker polymers still remains rather challenging, especially since there are very few examples in the literature. The lack of quantitative agreement between theoretical frameworks and experimental data, as well as the lack of a qualitative agreement between different model approaches, indicates that a thorough understanding of their rheological behavior and its physical origin remains an open question.

For unentangled, telechelic stickers, the constitutive modeling approaches of Tanaka-Edwards and others failed to predict the strong concentration dependence of the elasticity [147]. To address this, Annable *et al.* used a statistical approach, in which the rheological properties could be linked to the probabilities of loop and bridge formation, and succeeded in making a correct concentration dependent prediction of the network

elasticity [147, 148]. The aim of this chapter is to extend Annable's mechano-statistical approach, developed for linear elasticity of telechelic unentangled associative polymers, to multisticker unentangled associative polymers using combinatorics. This approach might open up a different perspective on transient networks with large crosslinking nodes formed by non-telechelic associative polymer, as it will allow us to gain insights in the probabilities of soluble blocks to form loops or bridges, in the functionalities of the crosslinking nodes as well as in the evolution of the number of elastically active bridges, all as a function of concentration. Besides the molecular characteristics of the multisticker polymer chains, in-depth knowledge of the microstructure of the transient network is crucial for understanding the final mechanical properties of physical gels formed by micellar aggregation. Hereto, we will use small-angle X-ray scattering to determine the relevant length scales, aggregation numbers and the overall spatial distribution of the micellar nodes in thermoreversible transient networks formed by alternating PEO-PPO multiblock copolymers in aqueous solutions. By combining knowledge about the network topology with our mechano-statistical model, we can detect microstructural changes as a function of concentration and how they translate into macroscopic behavior. The performance of the transient network model is verified by comparing the model results with the evolution of the number density of elastically active chains with concentration as inferred from linear shear rheology. By establishing the link between the building block architecture, the network microstructure and its final macroscopic properties, we can contribute to the rational design of physical hydrogels and transient networks with tunable mechanical properties.

The main part of this chapter was previously published and adapted for this dissertation:

An-Sofie Huysecom, Wim Thielemans, Paula Moldenaers and Ruth Cardinaels, "A generalized mechano-statistical transient network model for unravelling the network topology and elasticity of hydrophobically associating multiblock copolymers in aqueous solutions", *Macromolecules*, 56(2):612-633, 2023

5.1 Generalized mechano-statistical transient network model

In this section, the mechano-statistical transient network model originally developed by T. Annable and coworkers for HEUR copolymers bearing their associating groups as telechelic end groups [147, 148], is extended and generalized for alternating multiblock copolymers. The presence of more than two associating blocks along the chain significantly increases the amount of possible configurations of the chain as compared to those of telechelic polymers, and hence also the complexity of the model. Here,

the Annable model is extended by adopting a combinatorics approach for all possible configurations of the multiblock copolymers. In what follows, this approach and the derivation of the expression predicting the amount of elastically active chains as a function of concentration is discussed. The simplest case of our model framework, i.e. that of triblock copolymers having telechelic associating groups, is treated in Appendix B (Section B.1) and results in the original expressions as derived by Annable *et al.* [147, 148].

Consider a linear block copolymer chain with a associating blocks, of which 2 are telechelic and the other $a-2$ are evenly distributed along the chain. As a consequence, the chain contains $a-1$ soluble blocks which are capped by associating blocks. In fact, it can be noted that the assumption of associating end blocks is not a limitation of the model, since soluble end blocks form dangling ends that do not contribute to the network's elasticity. In this regard, it is also important to stress that entanglements are not taken into account in this transient network model, which aims at unentangled polymers. The absence of entanglements in the relevant concentration range used in this study will be experimentally confirmed for our multiblock copolymers in Section 5.2. Since block copolymers form micellar assemblies with large aggregation numbers N_{agg} (often $N_{agg} \gg 10$ for self-assembly of non-ionic block copolymers [26]), the association interaction between the associating blocks is assumed to be multifunctional ($f > 2$) in the following framework. The model is thus expected to apply not only to systems interacting through micellar aggregation, but also to polymer chains bearing smaller associating groups along their backbone or as a side group, which form multifunctional interaction nodes. In this regard, an interesting review by Seiffert and co-workers reveals the importance of such junction clustering in polymer networks constructed through physical, supramolecular interactions [104]. Since transient micellar networks are only formed at concentrations well above the CMC, the concentration of free unimers is assumed to be negligible in our model derivations.

5.1.1 Configuration probabilities

Each of the $a-1$ capped soluble blocks is presumed to have only two possible configurations. It either forms a bridge in between two different association nodes, or it forms a loop connected to just one association node. This assumption can be justified by the large binding energy between the associating blocks [147], resulting in a negligible fraction of associating blocks being present as either free dangling ends or as entire freely soluble chains, both configurations not contributing to an association node. The amount of possible configurations for a chain with $a-1$ capped soluble blocks thus equals 2^{a-1}. As an example, the second column in Table 5.1 shows the 8 possible configurations for a chain with $a = 4$ associating blocks and $a-1 = 3$ capped soluble blocks. Importantly, it is assumed that once a chain leaves a certain association node to form a bridge towards another node, it eventually does not come

back to that same node. Chain configurations with so-called redundant bridges in between the same association nodes, might be possible for chains with $a \geq 3$ and for configurations having $i \geq 2$ bridges, and are expected to be more significantly present in long multiblock copolymers with $a \gg 3$. Therefore, the performance of our model is anticipated to be insufficient for systems in which such configurations are predominant, and adjustments might be needed.

Following the terminology from the original work by Annable [147], the probability of a capped soluble block to from a bridge is denoted as F_1. Assuming a negligible fraction of 'open' stickers, the probability of forming a loop F_2 is equal to $1 - F_1$. The probability of a specific configuration with i bridges and hence $a - 1 - i$ loops thus equals $F_1^i \cdot F_2^{a-1-i}$. Note that multiple configurations having i bridges exist due to the possibility of a different order of occurrence of the bridges and loops, as shown in Table 5.1. The total amount of configurations with i bridges can be calculated from the binomial coefficient

$$\binom{a-1}{i} = \frac{a-1!}{i!\,(a-1-i)!}. \tag{5.1}$$

Hence, the overall probability of all configurations with i bridges and $a - 1 - i$ loops is

$$\binom{a-1}{i} \cdot F_1^i \cdot F_2^{a-1-i}, \tag{5.2}$$

as illustrated in the 4th column in Table 5.1.

In micellar networks formed by soluble polymer bridges, there usually exists a critical onset concentration for network formation $c_{network}$. This was illustrated in Figure 4.1 in Chapter 4. At dilute concentrations below this $c_{network}$, the nearest neighboring micellar cores are all too far away for an intermediate hydrophilic block to span the distance between them and hence to form a bridge. The resulting structure at concentrations below $c_{network}$ is thus a purely viscous solution of isolated micelles, as can be seen in Figure 4.3 (a) in Chapter 4. Therefore, the probability of forming a loop F_2 should equal 1 below $c_{network}$. At concentrations above $c_{network}$, other micellar cores appear within the volume spanned by a soluble block, such that bridges towards other micellar cores can arise (see Figure 4.3 (b)). These bridges provide the network with its elasticity, while the dynamic, reversible character of the association interaction gives rise to so-called transient crosslinking nodes by continuous association and dissociation events. In our model, we will replicate Annable's crucial approximation that the probability of forming a loop F_2 is inversely proportional to the average amount of association (micellar) nodes n_m, present in the volume defined by the span of a soluble block [147, 148]. This n_m thus represents the amount of micellar nodes in such close proximity that a soluble block can possibly form a bridge in between these nodes. Note that below $c_{network}$, only one micellar core is present within the volume defined by the soluble blocks (n_m = 1) and the probability of forming a loop $F_2 = 1/n_m$ thus equals 1. Therefore, $c_{network}$ is an important, indirect parameter influencing the

performance of the transient network model (via n_m and hence F_2), as it dictates where the onset of network formation is located. In Section 5.2, a hypothetical and theoretical approximation of $c_{network}$ based on the overlap concentration c^*, is proposed. In Section 5.3, n_m at concentrations above $c_{network}$ will be determined based on microstructural information of the micellar network topology.

5.1.2 Node functionality

Since the amount of bridges is crucial for the network elasticity, we define an average node functionality $\langle\Psi\rangle$ as the average amount of bridges that originate from an association node. This average functionality can be calculated as the product of N_b, the average amount of bridges one chain contributes to a crosslinking node [bridges/chain], and N_c, the average amount of chains contributing to one crosslinking node [chains/node]. The latter can be approximated as N_{agg}/N_a, in which N_{agg} is the aggregation number of the micellar node, i.e. the amount of hydrophobic blocks per micellar core [associating blocks/node] and N_a the average amount of associating blocks one chain contributes to a crosslinking node [associating blocks/chain]. Both N_b and N_a can be calculated from a summation over all possible configurations, resulting in the following expressions:

$$N_b = \sum_{i=0}^{a-1} \underbrace{\boxed{\frac{2(i+1)-2}{i+1}}}_{\substack{\text{average \# of bridges}\\ \text{a chain with i bridges}\\ \text{contributes to a node}}} \cdot \underbrace{\boxed{\binom{a-1}{i} \cdot F_1^i \cdot F_2^{a-1-i}}}_{\substack{\text{overall probability of}\\ \text{having a chain}\\ \text{with i bridges}}} \tag{5.3}$$

$$N_a = \sum_{i=0}^{a-1} \underbrace{\boxed{\frac{a}{i+1}}}_{\substack{\text{average \# of}\\ \text{associating blocks}\\ \text{a chain with i bridges}\\ \text{contributes to a node}}} \cdot \underbrace{\boxed{\binom{a-1}{i} \cdot F_1^i \cdot F_2^{a-1-i}}}_{\substack{\text{overall probability of}\\ \text{having a chain}\\ \text{with i bridges}}} \tag{5.4}$$

An illustrative example of the calculation of the factors in the expressions for N_b and N_a is shown in the last two columns of Table 5.1 for a multiblock copolymer with 4 associating blocks. The final expression of $\langle\Psi\rangle$ is shown in Equation 5.5:

$$\langle \Psi \rangle = N_b \cdot N_c = N_b \cdot \frac{N_{agg}}{N_a} = N_{agg} \cdot \frac{\sum_{i=0}^{a-1} \frac{2(i+1)-2}{i+1} \cdot \binom{a-1}{i} \cdot F_1^i \cdot F_2^{a-1-i}}{\sum_{i=0}^{a-1} \binom{a}{i+1} \cdot F_1^i \cdot F_2^{a-1-i}}. \quad (5.5)$$

The association nodes exhibit a distribution of functionalities defined by the probability distribution function $P(\Psi)$, i.e. the probability P of finding a node with a certain functionality Ψ. This distribution does not only arise from fluctuations in the functionality itself at a constant aggregation number, but can also be partly attributed to micellar polydispersity (at a constant temperature and concentration) resulting in fluctuations in aggregation number [147]. The functionality distribution is assumed to be binomial around the average value $\langle \Psi \rangle$ determined in Equation 5.5, with the maximum functionality Ψ_{max} attained when all $a-1$ capped soluble blocks form bridges ($F_1 = 1$). The expression for $P(\Psi)$ and Ψ_{max} are given in Equations 5.6 and 5.7, respectively:

$$P(\Psi) = \binom{\Psi_{max}}{\Psi} \cdot \left(\frac{\langle \Psi \rangle}{\Psi_{max}} \right)^{\Psi} \cdot \left(1 - \frac{\langle \Psi \rangle}{\Psi_{max}} \right)^{\Psi_{max} - \Psi} \quad (5.6)$$

$$\Psi_{max} = \langle \Psi \rangle \big|_{F_1=1} = N_{agg} \cdot \frac{2a-2}{a}. \quad (5.7)$$

Even though no fundamental basis for assuming a binomial distribution of node functionalities exists, two physical limitations justify our choice of the distribution function: (1) the function should be discrete and (2) the function should be delimited in nature as $\Psi \in \{0, 1, 2, ..., \Psi_{max}\}$. It can be noted that the definition of Ψ_{max} in Equation 5.7 does not necessarily result in a discrete number and therefore, it is approximated as its nearest natural number. As expected, for multiblock copolymers with $a > 2$, the Ψ_{max} value will exceed N_{agg} due to the fact that when F_1 =1, each non-telechelic associating block will create 2 bridges leaving the same node.

5.1.3 Elastically active bridges

Since loops are assumed to be elastically inactive, the number density of elastically active chains (ν) can be calculated from the amount of bridges connected to a node multiplied by the number density of nodes (n_{mic}). For this calculation, a few considerations must be made. First, a bridge connects two crosslinking nodes and hence, each bridge included in the node functionality Ψ only counts as half of an elastically active chain. Therefore, the amount of elastically active chains involves

	Configuration	Configuration probability	Overall configuration probability for i bridges	Average amount of bridges from a node	Average amount of associating blocks in a node
i = 0		$F_1^0 \cdot F_2^3$	$\binom{3}{0} \cdot F_1^0 \cdot F_2^3$	0	4
			$\binom{3}{0} = \frac{3!}{0!(3-0)!} = 1$	$= 0/1$	$= 4/1$
i = 1		$F_1^1 \cdot F_2^2$	$\binom{3}{1} \cdot F_1^1 \cdot F_2^2$	$\frac{1}{2} \cdot 1 + \frac{1}{2} \cdot 1$	$\frac{1}{2} \cdot 2 + \frac{1}{2} \cdot 2$
		$F_1^1 \cdot F_2^2$		$\frac{1}{2} \cdot 1 + \frac{1}{2} \cdot 1$	$\frac{1}{2} \cdot 3 + \frac{1}{2} \cdot 1$
		$F_1^1 \cdot F_2^2$		$\frac{1}{2} \cdot 1 + \frac{1}{2} \cdot 1$	$\frac{1}{2} \cdot 1 + \frac{1}{2} \cdot 3$
			$\binom{3}{1} = \frac{3!}{1!(3-1)!} = 3$	$= 2/2$	$= 4/2$
i = 2		$F_1^2 \cdot F_2^1$	$\binom{3}{2} \cdot F_1^2 \cdot F_2^1$	$\frac{1}{3} \cdot 1 + \frac{1}{3} \cdot 2 + \frac{1}{3} \cdot 1$	$\frac{1}{3} \cdot 1 + \frac{1}{3} \cdot 2 + \frac{1}{3} \cdot 1$
		$F_1^2 \cdot F_2^1$		$\frac{1}{3} \cdot 1 + \frac{1}{3} \cdot 2 + \frac{1}{3} \cdot 1$	$\frac{1}{3} \cdot 2 + \frac{1}{3} \cdot 1 + \frac{1}{3} \cdot 1$
		$F_1^2 \cdot F_2^1$		$\frac{1}{3} \cdot 1 + \frac{1}{3} \cdot 2 + \frac{1}{3} \cdot 1$	$\frac{1}{3} \cdot 1 + \frac{1}{3} \cdot 1 + \frac{1}{3} \cdot 2$
			$\binom{3}{2} = \frac{3!}{2!(3-2)!} = 3$	$= 4/3$	$= 4/3$
i = 3		$F_1^3 \cdot F_2^0$	$\binom{3}{3} \cdot F_1^3 \cdot F_2^0$	$\frac{2}{4} \cdot 1 + \frac{2}{4} \cdot 2$	1
			$\binom{3}{3} = \frac{3!}{3!(3-3)!} = 1$	$= 6/4$	$= 4/4$
$\sum_{i=0}^{a-1}$	2^{a-1}	$F_1^i \cdot F_2^{a-1-i}$	$\binom{a-1}{i} \cdot F_1^i \cdot F_2^{a-1-i}$	$\frac{2(i+1)-2}{i+1}$	$\frac{a}{i+1}$

Table 5.1: Example of the combinatorics approach for a chain with a = 4 associating blocks (green) and a-1 = 3 soluble blocks (red): possible configurations and the resulting probabilities, the average number of associating blocks in one crosslinking node (dotted circle) and the average number of bridges connected to one crosslinking node. The last row in grey shows the symbolic expressions.

the summation of the node functionalities divided by 2 ($\Psi/2$), weighted with their occurance probability ($P(\Psi)$). Second, only node functionalities $\Psi \geq 3$ should be taken into account in the calculation of unique elastically active chains, since nodes with $\Psi = 1$ are dangling ends not contributing to a sample-spanning connectivity, while nodes with $\Psi = 2$ act as additional, redundant steps in dangling ends, and in superloops or superbridges consisting of multiple connected nodes. Schematic illustrations of a dangling end, a superloop and a superbridge can be found in Figure 5.1. Lastly, the fraction of bridges originating from a node with $\Psi \geq 3$, which are linked to a unifunctional node, should also be eliminated in the expression for the number density of elastically active chains. Accordingly, only a fraction $\frac{1-P(0)-P(1)}{1-P(0)}$ of the summation is included in Equation 5.8. The denominator contains $1-P(0)$ instead of 1 because each bridge must connect to a node with a functionality of 1 or more (zero-functional nodes ($\Psi = 0$) only have loops).

$$\nu = n_{mic} \cdot \left(\frac{1-P(0)-P(1)}{1-P(0)} \right) \cdot \sum_{\Psi=3}^{\Psi_{max}} \left(\frac{\Psi}{2} \right) \cdot P(\Psi) \tag{5.8}$$

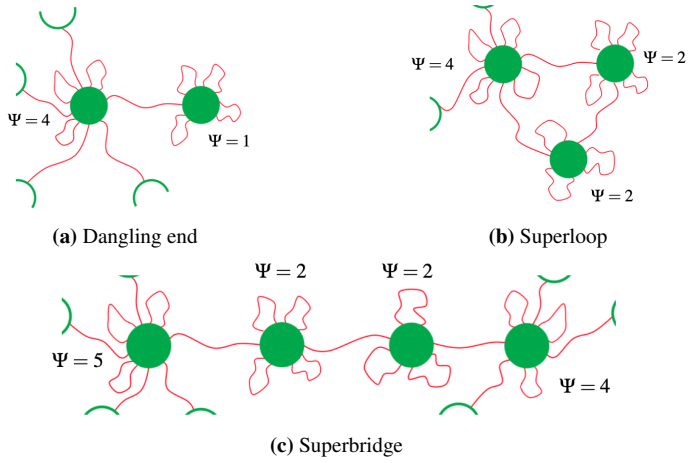

(a) Dangling end **(b)** Superloop **(c)** Superbridge

Figure 5.1: Schematic illustrations of (a) a dangling end, (b) a superloop and (c) a superbridge. For simplicity, the micellar cores are represented as filled green circles. The node functionalities of the involved cores are indicated on the figures.

The number density of micelles n_{mic} can be calculated from the number density of chains n, the aggregation number N_{agg} and the number of associating blocks a, as

shown in Equation 5.9:

$$n_{mic} = \frac{n \cdot a}{N_{agg}}. \tag{5.9}$$

The number density of chains n can be linked to the mass concentration c of multiblock copolymer in solution by making use of its molecular weight M_w and Avogadro's number N_{Av} ($6.02 \cdot 10^{-23}$ mol^{-1}). Equation 5.10 thus represents the evolution of the number density of elastically active chains as a function of concentration:

$$\nu = \left(\frac{c \cdot N_{Av}}{M_w} \cdot \frac{a}{N_{agg}}\right) \cdot \left(\frac{1 - P(0) - P(1)}{1 - P(0)}\right) \cdot \sum_{\Psi=3}^{\Psi_{max}} \left(\frac{\Psi}{2}\right) \cdot P(\Psi). \tag{5.10}$$

Note that this equation can be fully evaluated, without the need for parameter fitting, by knowledge of a, M_w, N_{agg} and n_m. The latter reveals its importance in the calculation of the bridge and loop probabilities F_1 and F_2, respectively, and is eventually reflected in the node functionality distribution function $P(\Psi)$ around the average value $\langle\Psi\rangle$. Equation 5.10 allows to calculate the fraction of all $(a-1) \cdot n$ available soluble blocks which are effectively active as unique elastic bridges according to Equation 5.11:

$$\frac{\nu}{(a-1) \cdot n} = \left(\frac{a}{(a-1) \cdot N_{agg}}\right) \cdot \left(\frac{1 - P(0) - P(1)}{1 - P(0)}\right) \cdot \sum_{\Psi=3}^{\Psi_{max}} \left(\frac{\Psi}{2}\right) \cdot P(\Psi). \tag{5.11}$$

The performance of this model prediction can be verified by comparing the model expression of the number density of elastically active chains with the information as extracted from rheological measurements in the linear viscoelastic region (see Section 5.2). Analogous to the affine network theory of rubber elasticity [153], ν can be estimated from the plateau modulus G_0, i.e. the constant elastic modulus G' usually detected at high frequencies for viscoelastic networks, as

$$\nu = \frac{G_0}{k_b \cdot T}, \tag{5.12}$$

in which k_b is the Boltzmann constant ($1.38 \cdot 10^{-23} m^2 kg/s^2 K$) and T the absolute temperature. The prediction of the plateau modulus as inferred from the more accurate phantom network theory ($G_0 = \nu k_b T \cdot (f-2)/f$), which does take into account fluctuations of the crosslinking nodes and the resulting reduction of cumulative stretching of the network strands, approaches the affine network prediction in the limit of high crosslinking functionalities f [153]. The real elastic network theory (RENT), developed by Olsen and Johnson [154, 155] as an extension of the phantom network theory, takes into account different orders of cyclic topological defects (loops), but again approximates the affine network theory at higher functionalities. Since the functionalities of micellar crosslinking nodes with aggregation numbers in the order of 50-100 [26], are a priori assumed to be relatively large even if a significant fraction of loops is present, this provides a justification for the use of the affine network approach.

The fraction of the available soluble blocks that are elastically active can thus also be calculated from the plateau modulus as

$$\frac{\nu}{(a-1)\cdot n} = \frac{G_0}{(a-1)\cdot n\cdot k_b T}. \tag{5.13}$$

Besides the generalization of the transient network model of Annable *et al.* [147, 148] for multiblock copolymers, another novelty of our work is he fact that n_m will be experimentally determined, rather than approximated via a theoretical balance. In contrast with Annable's assumption of a randomly close-packed lattice of micellar cores [147], our approach using SAXS will provide information about the exact spatial distribution of the micellar cores, as specified by the radial distribution function $g(r)$ and will hence facilitate a better representation of the network's microstructure (see Section 5.2). Additionally, Annable and co-authors [148] argue that their assumption of a random arrangement ($g(r) = 1$) of micellar cores throughout the sample might be violated at least at concentrations close to the critical network concentration $c_{network}$, as the analysis of NMR data [306, 307] showed that the structure might be fractal up until some length scale at these concentrations [308]. The approach of using experimental information about the exact radial distribution was previously suggested by Annable and coworkers [148] to improve the performance of their model, but to the best of our knowledge, has never been implemented. Therefore, the current study combines insights from the experimentally probed network topology, resulting in n_m

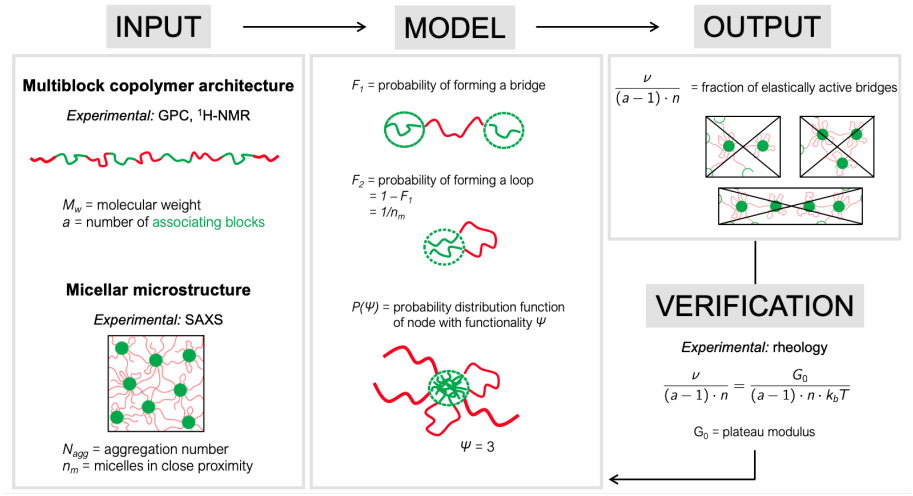

Figure 5.2: Schematic overview of the mechano-statistical transient network model: input, model principles, output and model verification. The experimental methods are also included.

and N_{agg} values, of multiblock copolymers with known values of a and M_w, with a generalization of a mechano-statistical network model, to predict the evolution of the network elasticity as a function of concentration. In Figure 5.2 a schematic overview of the transient network model is given, i.e. the input, main principles, output and verification, as well as where experimental methods come into play.

5.2 Critical network concentration

In the previous chapter, we extensively investigated the entropy-driven micellization and related phase transitions as a function of temperature and concentration for both types of ExpertGel® using a multitude of techniques including rheometry, calorimetry, light scattering and light transmittance, and compared the characteristics to that of their precursor Pluronics®. Linear oscillatory shear rheology measurements on concentrated multiblock copolymer solutions revealed an elastic contribution upon micellization, indicative of the formation of a solid-like network as a function of temperature. However, the absence of a calorimetric process other than that of the micellization, shows that no higher hierarchical, crystalline structuring takes place, as is the case for Pluronics® [45]. Alternatively, the alternating sequences of soluble PEO blocks capped by hydrophobic PPO blocks, allow the formation of elastic PEO bridges between two different hydrophobic cores. Figure B.1 in Appendix B shows rheological heating and cooling ramps of a 140 g/L EG312 solution at a rate of 0.1°C/min and a frequency of 100 rad/s in the linear viscoelastic regime. Note that at this frequency, the elastic modulus G' and hence the elasticity saturates to a constant value at high temperatures (with an increase $< 4\%$ in the relevant temperature range from 40 to 46°C).

Undoubtedly, the capability of a soluble PEO block to form an elastic bridge greatly depends on the proximity of other micellar cores. Besides a critical concentration for micelle formation at a certain temperature (CMC in the previous chapter), there thus also exists a critical temperature dependent concentration $c_{network}$ at which micellization results in the formation of bridges between micellar cores and hence a network, rather than fully isolated micelles (see Figure 4.3 in Chapter 4). This concentration represents a theoretical boundary at which at least one other micellar core is close enough such that an intermediate soluble PEO block can span the distance between these two neighboring micellar cores. Upon increasing the concentration above the critical network concentration, continuously more micellar cores are in close proximity and the material transforms from a viscous Newtonian solution of isolated micelles to a viscoelastic network of bridged micellar cores. At concentrations around this critical network concentration, large fluctuations in the microstructure usually induce unstable and irreproducible behavior [101,194] and render a macroscopic, experimental assessment of $c_{network}$ in real systems very challenging. As an alternative, $c_{network}$ can be approximated from the overlap concentration c^* of the entire multiblock copolymer.

This overlap concentration c^* represents the transition from the dilute to semi-dilute concentration regime, and is defined as the concentration at which there is exactly one polymer chain present in the volume defined by its radius of gyration R_g

$$c^* = \frac{M_w}{(4\pi/3) \cdot R_g^3 \cdot N_{Av}}. \tag{5.14}$$

Using c^* as an approximation for $c_{network}$ would underestimate the actual value of $c_{network}$ as it does not necessarily allow hydrophobic blocks of different polymer chains to aggregate and form a micellar core. In this regard, it is important to point out that the PEO-PPO multiblock copolymers used in this study are not end-capped by hydrophobic PPO blocks, but contain soluble PEO blocks as dangling ends. Therefore, $c_{network}$ is defined as the concentration at which one full chain plus one repeating PEO-PPO unit are present in the volume defined by the radius of gyration of the entire multiblock copolymer

$$c_{network} = \frac{M_w + (M_w/a)}{(4\pi/3) \cdot R_g^3 \cdot N_{Av}}. \tag{5.15}$$

It is relevant to mention that the hydrophobic association between PPO blocks cannot be viewed as point 'interactions' due to the significant size of the PPO blocks. This definition of $c_{network}$ thus ensures that two PPO blocks from different multiblock copolymer chains can find each other and can fully overlap at the critical network concentration. Note that to determine the molecular weight of the repeating unit we have simply divided the molecular weight of the entire multiblock copolymer by the amount of repeating PEO-PPO sequences. The latter can be approximated by using the a parameter defined as the average amount of PPO blocks per multiblock copolymer. Since the critical network concentration can thus be calculated from the overlap concentration c^* of the entire chain as

$$c_{network} = \frac{a+1}{a} \cdot c^*, \tag{5.16}$$

an experimental assessment of c^* at multiple low temperatures below the CMT, where no micellar aggregation takes place, will enable determination of a temperature dependent $c_{network}$. Finally, it is important to stress that such definition of $c_{network}$ is hypothetical, as it decouples micellization and network formation by omitting the microstructural changes upon micellization and assuming random chain configurations upon network formation.

The critical transition from the dilute to the semi-dilute concentration regime at the overlap concentration c^*, is often inferred from the scaling of viscosity with concentration. Figure 5.3 (a) shows the specific viscosity $\eta_{sp} = (\eta - \eta_{sol})/(\eta_{sol})$ as a function of the dimensionless concentration $c[\eta]$ for EG312 at multiple low temperatures below the CMT. The temperature dependent intrinsic viscosity $[\eta]$ is determined according to the Huggins's method, i.e. $\lim_{c \to 0} \eta_{sp}/c$. The obtained values for

the intrinsic viscosities of EG312 and EG412 at 20°C are 67.63 mL/g and 54.15 mL/g, respectively. These values are in line with the value of 67.78 mL/g obtained for linear PEG chains of 35 000 g/mol in water at 20°C [309] and 53.3 mL/g at 25°C [310], and follow the trend of increasing intrinsic viscosity with increasing molecular weight and decreasing temperature [309]. The viscosities at low concentrations, represented by the circle symbols in Figure 4.5 (a), were determined from the temperature sweeps at 100 s^{-1} using the double wall couette geometry. Flow sweeps from 0.1 s^{-1} up to 100 s^{-1} at these temperatures show Newtonian behavior for these dilute polymer solutions. The viscosities at higher concentrations, represented by the triangle symbols, were determined from oscillatory temperature sweeps at a frequency of 1 Hz and 0.1% strain using the plate-plate geometry. Note that for purely viscous solutions with a phase angle close to 90°, which is the case at low temperatures below the CMT, the viscosity can be calculated from the loss modulus G'' and the angular frequency ω using the relationship $\eta' = G''/\omega$ and $\lim_{\omega\to 0}\eta' = \lim_{\dot{\gamma}\to 0}\eta_0$.

Changes in the slope of η_{sp} versus $c[\eta]$ in a log-log plot are linked to the critical transitions from dilute to semi-dilute solutions (at c^*), from semi-dilute unentangled to semi-dilute entangled (at c_e) and to concentrated solutions (at c^{**}) [311]. Only one clear transition is observed in Figure 5.3 (a), with the slope changing from 1.07 to 2.86. The viscosity scaling of EG412 at multiple low temperatures below the CMT can be found in Appendix B (see Figure B.2) and shows similar behavior with the slope changing from 1.12 at low concentrations to 3 at higher concentrations. The crossover, as an average of all probed temperatures, happens at $c^* = 2.68/[\eta]$ for EG312 and at $c^* = 2.24/[\eta]$ for EG412. The slope of 1.07 in the first region in Figure 5.3 (a) is very close to 1 and corresponds to the dilute regime according to the Zimm model [311]. The slope of 2.86 in the second region is rather high as compared to the slope of $1/(3\nu - 1) = 1.3$ usually obtained for semi-dilute unentangled (homo)polymer solutions in good solvents ($\nu = 0.588$) and relatively low as compared to the usually obtained slope of $3/(3\nu - 1) = 3.9$ for semi-dilute entangled solutions in good solvents [153]. For linear PEO (with a minimum molecular weight of 100 000 g/mol) in water at 20°C indeed a slope of 3.85 was obtained in the semi-dilute entangled regime [312]. We hypothesize that this intermediate slope obtained for our multiblock copolymers above c^* finds its origin in the possible weak associative interactions between PPO blocks below the CMT, which do not result in true micellar self-assembly. These short-lived interactions restrict the flow of the polymers and induce a more pronounced concentration dependence of the viscosity as compared to that of simple homopolymers. However, these interactions are less effective as the restrictions imposed by physical entanglements. Higher scaling exponents than theoretically predicted by the Rouse-Zimm model for semi-dilute unentangled polymers were also observed by Zhang *et al.* for polyimide solutions containing associative dipole-dipole interactions [313]. Finally, the c^* transition of our multiblock copolymers happens at $\eta_{sp} = 4$, meaning that the solution viscosity is roughly 5 times that of the solvent, whereas the critical transition to the semi-dilute entangled regime at c_e usually happens at viscosities of 10 to 300

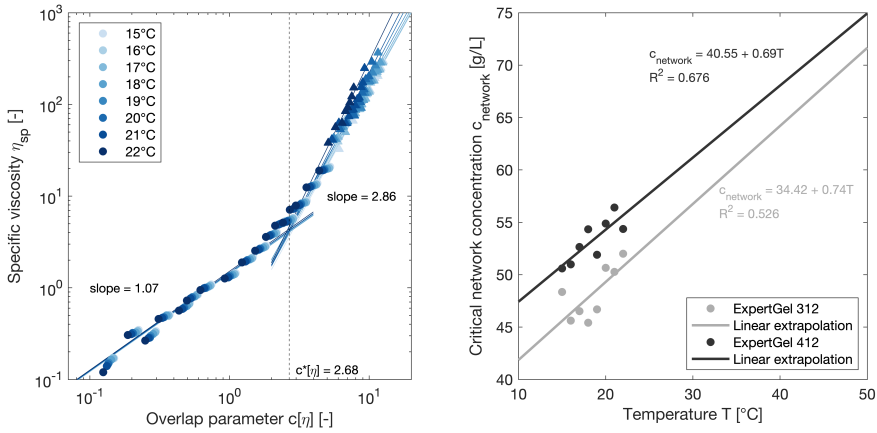

(a) **(b)**

Figure 5.3: Viscosity scaling and determination of temperature dependent $c_{network}$: (a) specific viscosity η_{sp} versus overlap parameter $c[\eta]$ for EG312 at different low temperatures (< CMT). The lines represent the power law scalings in the dilute and semi-dilute regions. The overlap concentration c^* is determined at the crossover of both scaling regimes. The value of $c^*[\eta]$ and the slopes indicated in the graph are average values. (b) Critical network concentration $c_{network}$ versus temperature for EG312 and EG412. The lines represent the linear extrapolation to higher temperatures with the R^2 indicated.

times the solvent viscosity [311]. Therefore, the transition observed for our multiblock copolymers is believed to correspond to the transition from a dilute to a semi-dilute unentangled polymer solution at the overlap concentration c^*. The absence of another transition at concentrations above c^*, indicates that our study operates in a concentration range with no entanglements between entire multiblock copolymer chains, and hence also not between soluble blocks. This justifies our assumption that entanglements are not significant in the micellar networks and therefore are also not taken into account in the transient network model in Section 5.1. From the experimentally determined c^*, we can also get an indication of the radius of gyration R_g of the multiblock copolymer chains, resulting in 8.67 nm for EG312 at 15°C and 7.60 nm for EG412 at 15°C. Using the theoretically calculated radii of gyration of the separate PEO and PPO blocks (see Table 3.5), another approximation of the number of repeating PEO-PPO sequences in the entire multiblock copolymer can be determined. The as such calculated values of 3.97 and 3.74 for EG312 and EG412 respectively, comply quite nicely with the calculated a values in Table 3.4.

Figure 5.3 (b) displays the calculated values of $c_{network}$ as a function of (low)

temperature for EG312 and EG412. At these temperatures, the molecules are completely soluble without micellar aggregation. An increasing trend of $c_{network}$ with temperature is evident, indicative of a more collapsed chain configuration at elevated temperatures due to an increased dehydration of the molecules [64]. The trend as observed for these low temperatures, is linearly extrapolated to obtain an estimate of $c_{network}$ at higher temperatures for which the viscosity scaling approach is compromised by micellization and network formation. Such linear extrapolation, i.e. $c^* \sim T$, is justified by the temperature evolution of the radius of gyration of a single PEO molecule as obtained by coarse-grain modelling [314,315], which appears to follow a $R_g \sim T^{-1/3}$ trend. The fits have R^2 values of 0.526 for EG312 and 0.676 for EG412. Since our definition of $c_{network}$ does not take into account the drastic morphological changes upon micellization, it does not comply with experimental indicators for true gel formation, such as the concentration dependent T_{gel}, determined as the crossover between G' and G'' in temperature ramps in Chapter 4. Moreover, as $c_{network}$ is not governed by hydrophobic driving forces, its temperature dependence is also opposite to that of the CMC or the evolution of T_{gel} with concentration (see phase diagrams in Figures 4.5 (a) and (b) in Chapter 4).

5.3 Micellar network topology

The microstructure of the networks formed by alternating PEO-PPO multiblock copolymers in concentrated aqueous solutions consists of small-sized micellar cores connected by hydrophilic PEO bridges. The interaction between these structures and X-ray radiation used in SAXS, allows to study the shape and size of the cores based on the angular dependency of the scattering intensity. Moreover, SAXS measurements also provide insights into the interactions between neighboring micellar cores and the overall network topology of the connected structure. In this regard, the structure factor $S(q)$ will appear to be of crucial importance for revealing the spatial distribution of the micellar cores and to determine the amount of micellar cores n_m close enough to allow bridging.

5.3.1 SAXS intensity profile

Figure 5.4 (a) shows the scattered intensity I as a function of scattering vector q at 46°C for multiple concentrated solutions of EG312 (92, 108, 124, 140 and 155 g/L). For clarity, the curves are shifted by the factor indicated in the graph. The error bars are determined by the radial integration of the 2D scattering images, and do not represent independent measurements on different sample batches. Upon increasing the concentration, the structure peak, indicative of a reccurring length scale d in the microstructure, becomes more pronounced and shifts to higher q values, due to a more

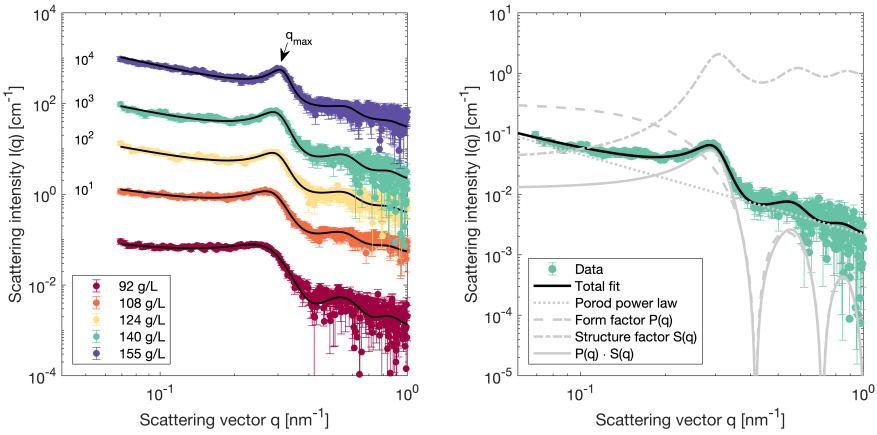

Figure 5.4: Small-Angle X-ray scattering measurements on EG312 at 46°C: (a) background corrected scattering intensities $I(q)$ at different concentrations ($> c_{network}$). Shift factors are indicated on the graph. Solid lines represent curve fittings. (b) Separate fitting contributions for 140 g/L EG312 including a Porod power law, a spherical form factor P(q) and a hard sphere structure factor S(q).

dense spatial arrangement. Using the empirically modified Bragg's law $d = 2.2\pi/q$ as determined for fluid-like ordered suspensions [316], the average center-to-center intermicellar distance d corresponding to the maximum peak position q_{max}, decreases from 26.2 to 22.9 nm upon increasing the concentration from 92 to 155 g/L EG312. The data are fitted with a combination of a Porod power law, a spherical form factor $P(q)$ and a hard sphere structure factor $S(q)$ (see Section 5.3.1). These separate contributions are shown in Figure 5.4 (b) for a solution of 140 g/L EG312 at 46°C. The resulting fit is in good agreement with the experimental data. Similar graphs for EG412 can be found in Figure B.3 in Appendix B.

The spherical form factor was previously inferred from synchrotron SAXS measurements on dilute solutions of multiblock copolymers (only probing the form factor $P(q)$) and revealed PPO cores with a radius of approximately 11 nm (see Section 4.3.3 in Chapter 4). The inability to clearly detect the PEO corona with X-rays [302] supports our additional fitting assumption that the spherical radius used in the form factor ($r_{P(q)}$) and the one used in the hard sphere structure factor ($r_{S(q)}$) must be identical and equal to the PPO core size. Releasing this size constraint, i.e. $r_{P(q)} \neq r_{S(q)}$, on a selection of representative samples resulted in a difference in radius of maximum 10% between $r_{P(q)}$ and $r_{S(q)}$, with the inconsistency that for some fits $r_{P(q)} > r_{S(q)}$ was obtained, while in others the physically more plausible [302] inequality $r_{P(q)} < r_{S(q)}$ was realized.

Based on these arguments, constraining the spherical radii in the form and structure factor to be equal appears reasonable. The structure factor is determined based on the Percus-Yevick closure relationship assuming no significant attractive well between individual micellar PPO cores. Only excluded volume repulsive interactions are taken into account, giving rise to a simple hard sphere approach with a micellar core radius r_c and a micellar volume fraction ϕ. For some representative samples, the use of a sticky hard sphere structure factor, to account for possible attractive interactions between the micelles, did not result in a significant attractive interaction (well depth less than kT), nor in greatly different values for r_c and ϕ, and was therefore not further considered.

As DLS indicated no significant micelle polydispersity, nor an anisotropic micellar shape (see Section 4.3.1 in Chapter 4), the Porod power law might be induced by larger scale heterogeneities present in concentrated solutions forming networks. Such heterogeneities and the corresponding Porod law were also observed in SAXS studies on concentrated solutions of other amphiphilic molecules forming hydrophobic network nodes [317]. The obtained exponents of 1.1-1.3 for EG312 and 3.4-3.5 can be linked to mass and surface fractality, respectively, of larger scale aggregates and further discussion hereof is beyond the scope of this work. For the curve fitting, a few other assumptions are made to reduce the amount of fitting parameters and fitting time. Firstly, the scattering length density of the scatterer (PPO core) was forced to be larger than that of the solvent ($9.47 \cdot 10^{-6}$ Å^{-2}), as the scattering length densities of PEO and PPO were determined in the SASview software to be $10.4 \cdot 10^{-6}$ Å^{-2} and $9.95 \cdot 10^{-6}$ Å^{-2}, respectively. Secondly, with varying temperature at a specific concentration of ExpertGel, it was found that the absolute intensity scale (I_0) and Porod power exponent (p) did not vary much and hence, those were kept constant per concentration.

Figures 5.5 (a) and 5.5 (b) show the hard sphere fitting parameters, i.e. the radius r_c and volume fraction ϕ respectively, as function of EG312 concentration at different elevated temperatures above the CMT. The core radius as probed in concentrated micellar networks (10.7 nm on average), corresponds well with the radius obtained by synchrotron SAXS of dilute multiblock copolymer micelles (11 nm) and is significantly smaller than the hydrodynamic radii (26.1 nm on average at 19 g/L EG312) obtained for dilute micelles using DLS (see Section 4.3). Upon increasing concentration, the core radius does not vary significantly, which is in contrast with the increasing hydrodynamic radius as a function of concentration for dilute solutions (see Section 4.3.1 in Chapter 4). Nonetheless, for Pluronic® PEO-PPO-PEO triblock copolymers it was also found by SLS and SANS studies [27, 50] that the micellar size and aggregation number did not vary significantly upon increasing the concentration substantially above their CMT. The volume fraction ϕ of the micelles, on the other hand, seems to increase linearly as a function of concentration, as could be expected. Similar conclusions can be drawn for EG412 in Figures B.4 (c) and (d) in Appendix B.

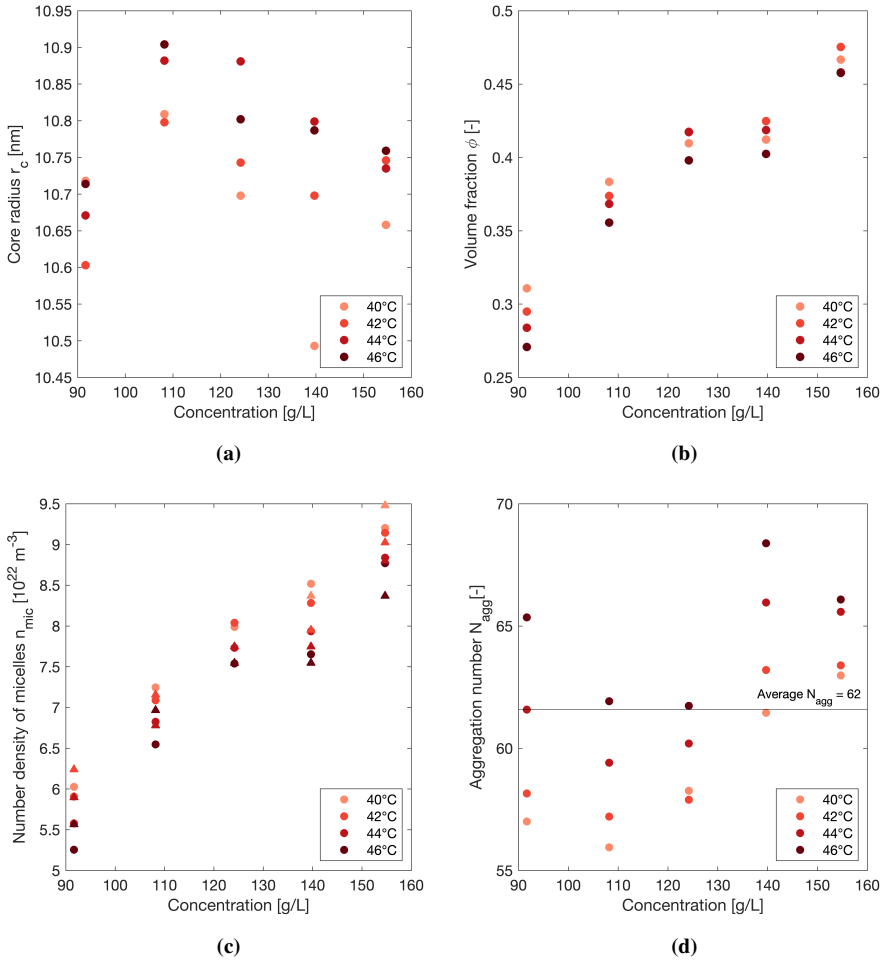

Figure 5.5: Evolution of the hard sphere fitting parameters (a) core radius r_c and (b) micellar volume fraction ϕ with concentration for EG312 at different temperatures (> CMT). Evolution of the calculated values (c) number density of micelles n_{mic} as calculated from SAXS fitting parameters (circles) and as calculated from $d = 2.2\pi/q_{max}$ (triangles) and (d) aggregation number N_{agg} with concentration for EG312 at different temperatures (> CMT).

From the fitting parameters r_c and ϕ, the concentration dependent number density of micelles n_{mic} can be calculated as

$$n_{mic} = \frac{\phi}{(4\pi/3) \cdot r_c^3}. \tag{5.17}$$

Since the micellar assembly itself does not change significantly with concentration at elevated concentrations, additional copolymers are assumed to form more micelles resulting in a linearly increasing number density of micelles as a function of concentration (see circles in Figure 5.5 (c) for EG312 and Figure B.4 (c) in Appendix B for EG412). When considering simple packing arguments, another estimate of the micellar density can be made based on the intermicellar distance d, derived from the peak maximum q_{max}, as $n_{mic} = 1/d^3$, and is in good agreement with the values calculated from the fitting parameters (see triangles in Figure 5.5 (c) for EG312 and Figure B.4 (d) in Appendix B for EG412). Based on the assumption that all multiblock copolymers are segregated in micellar assemblies at concentrations c above the CMC(T), an estimation of the aggregation number N_{agg} can be made according to

$$N_{agg} = \frac{a \cdot c \cdot N_{av}}{n_{mic} \cdot M_w}, \tag{5.18}$$

in which a represents the amount of hydrophobic blocks in the multiblock copolymer and M_w the molecular weight of the multiblock copolymer. As can be seen in Figure 5.5 (d) for EG312 (and Figure B.4 (d) in Appendix B for EG412), the aggregation number does not change substantially with concentration nor temperature. Therefore, it will be assumed that the aggregation number, at least at these elevated concentrations can be approximated as constant and has average values of 62 and 87 for EG312 and EG412, respectively. The maximum deviation from this values is approximately 11% for EG312 and 24% for EG412. Interestingly, by comparing the weight-average molecular weight of dilute EG312 chains at 15°C (below CMT) with that of micelles at 45°C (above CMT) as obtained by SLS, the aggregation number of EG312 is estimated to be 57 (see Section 4.3 in Chapter 4). This nicely agrees with the value of 62 calculated from SAXS measurements on EG312 micellar networks, and justifies our calculation. Moreover, the good agreement between the aggregation numbers as determined by SLS for isolated micelles in dilute solutions and as determined by SAXS for bridged micelles in networks formed at elevated concentrations, confirms that no significant change in the micellar morphology takes place as a function of concentration. Since the scattering length density of the spherical scatterers proves that the PPO core is not completely dehydrated, an approximation of the aggregation number by simple division of the core volume ($4\pi/3 \cdot r_c^3$) by the volume of the PPO block ($4\pi/3 \cdot R_{g,PPO}^3$, see Table 3.5) represents an overestimation by approximately an order of magnitude. Instead, by taking into account a correction factor for the core volume, which accounts for the true volume of PPO in the core based on the scattering length density differences of scatterer and solvent as compared to that of PPO and solvent, the obtained average

aggregation numbers (143 for EG312 and 90 for EG412, see detailed calculations in Appendix B, Section B.2) are at least of the same order as the ones obtained from n_{mic}. Since the fitting error on the scattering length density of the core is rather small (on the order of 10^{-11} Å^{-2}), the difference between N_{agg} obtained from n_{mic} and the one obtained from r_c might be related to the oversimplification of a linear mixing rule between the scattering length densities of PPO and water in the core.

The SAXS fitting parameters r_c and ϕ, allow us to calculate the average intermicellar 'gallery' spacing h, which is the distance in between the surfaces of two neighbouring micellar cores by assuming a maximum separation, i.e. $d-2r_c$, according to Equation 5.19.

$$h = d - 2r_c = \left(\frac{1}{n_{mic}}\right)^{1/3} - 2r_c = \left(\frac{4\pi r_c^3}{3\phi}\right)^{1/3} - 2r_c = 2r_c\left[\left(\frac{\pi}{6\phi}\right)^{1/3} - 1\right] \quad (5.19)$$

Using the expression with r_c and ϕ, the average spacing decreases from 5.27 nm to 0.98 nm upon increasing the concentration from 92 to 155 g/L EG312 (at 46°C). As compared to the radius of gyration of an intermediate soluble PEO block (in the order of 1.44 to 1.22 nm, see Table 3.5), this implies that the PEO blocks should, on average, stretch over approximately 3.65 times their R_g at the lowest concentration (92 g/L) to form a bridge in between two neighbouring micellar cores. As this seems rather unlikely, it is anticipated that at the lowest concentration almost no bridges are formed. At the highest concentration (155 g/L), on the other hand, the average spacing is smaller than the R_g of a PEO block, thereby allowing the formation of bridges between different micellar cores. Similar conclusions can be drawn by using the distance d directly, as inferred from the maximum peak position q_{max} of the SAXS profiles in Figure 5.4 (a), resulting in an average spacing h ranging from 4.76 nm to 1.34 nm upon increasing the concentration from 92 to 155 g/L EG312 (at 46°C). However, these calculations only represent an average view on the micellar spacing, and do not provide information about the local micellar distribution needed for the calculation of the crucial n_m parameter (i.e. the amount of micellar cores in such close proximity that an intermediate PEO block can form a bridge).

5.3.2 Radial distribution function

Fortunately, the hard sphere structure factor $S(q)$, fully defined by r_c and ϕ, can also provide detailed information about the spatial distribution of micelles through its Fourier relation with the radial distribution function $g(r)$. The latter describes normalized micellar density variations around a central micellar core and reveals information about the proximity of other micelles. It can thus be used to calculate the amount of micellar cores n_m which are close enough such that an intermediate PEO block can connect to this core by forming a bridge.

The relation between the structure factor $S(q)$ and the radial distribution function $g(r)$ [318] is

$$S(q) = 1 + 4\pi \cdot n_{mic} \int_0^\infty r^2 \cdot [g(r) - 1] \cdot \frac{sin(qr)}{qr} dr. \tag{5.20}$$

Taking the inverse sine-Fourier transform gives the following expressing for $g(r)$ [318]:

$$g(r) = 1 + \frac{1}{2\pi^2 \cdot r \cdot n_{mic}} \int_0^\infty q \cdot [S(q) - 1] \cdot sin(qr) dq. \tag{5.21}$$

It is well-known that Fourier calculations might induce artefacts and therefore, an additional Verlet-Weis correction in the analytical Percus-Yevick solution [319] is introduced in our calculation of $g(r)$. This correction compensates the overestimation of the principal peak height in dense micellar solutions with a micellar volume fraction $\phi > 0.4$ [320]. Figures 5.6 (a) and (b) show the hard sphere structure factor $S(q)$ and the radial distribution function $g(r)$ calculated using the Verlet-Weis correction, respectively, for a concentrated solution of 140 g/L EG312 at 46°C.

For the calculation of the crucial n_m parameter, a similar approach as for the calculation of the coordination number is adopted. The coordination number describes the amount

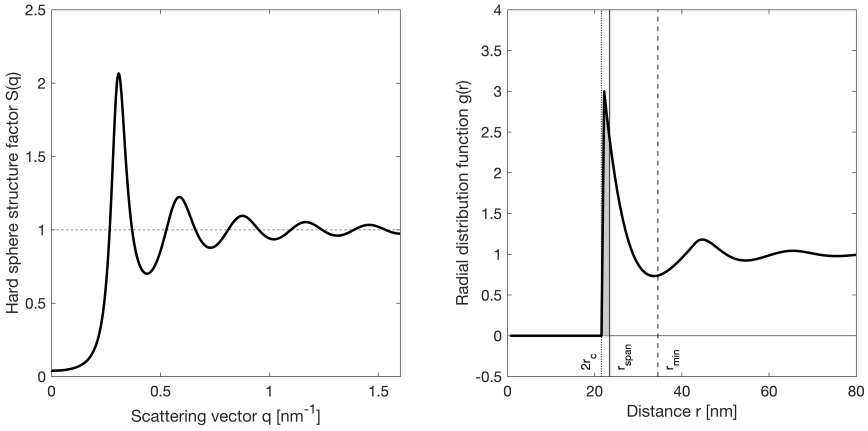

(a) **(b)**

Figure 5.6: Determination of the amount of micellar cores n_m for 140 g/L EG312 at 46°C: (a) the hard sphere structure factor $S(q)$ defined by r_c and ϕ, (b) the radial distribution function $g(r)$ defined by the inverse sine-Fourier transform (see Equation 5.21) with a Verlet-Weis correction. The spherical integration of $g(r)$ up to r_{span} to determine n_m (see Equation 5.22), is also indicated as the grey area under the $g(r)$ curve.

of nearest neighbors and is calculated by spherical integration up until the first minimum r_{min} in the radial distribution function, thereby taking into account the first 'dense' layer of micellar cores around the central core, as illustrated in the schematic in Figure 5.7 (a). Importantly, for the calculation of n_m integrating up to r_{min} would be an overestimation as intermediate PEO blocks will not necessarily be able to span the distance to all of the nearest neighbors. Therefore, the number of micellar cores in close proximity such that a PEO block can effectively form a bridge, is calculated by integration up until a length r_{span}. The span length r_{span} is defined as twice the core radius r_c plus the radius of gyration of an intermediate PEO block $R_{g,PEO}$, which can be calculated with a theoretical ideal chain approximation (see Table 3.5). Figure 5.6 (b) depicts the area under the radial distribution function $g(r)$ by integration up until r_{span}, needed for the calculation of n_m. The principle of a PEO bridge over r_{span} is illustrated in Figure 5.7 (b). The assumption that a bridge is likely to occur over a distance of R_g can be justified by the Monte Carlo simulations of Testard *et al.* [268], who found that the pair potential between two colloidal particles, induced by telechelic polymer chains bridging the particles, reaches its minimum around R_g. As an approximation, we will thus assume that the main fraction of capped PEO blocks can only form a bridge towards another micellar core, instead of looping back to its own micellar core, when the other core is within an average distance of $R_{g,PEO}$. Equation 5.22 displays the final expression to

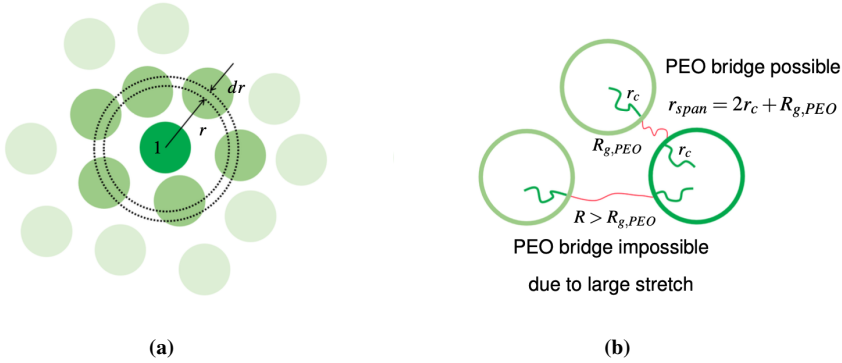

Figure 5.7: Schematic illustrations of (a) the radial distribution function $g(r)$ describing the normalized micellar density around a central core, represented by the green core indicated with 1. The 6 nearest neighboring cores are shown as slightly lighter green. (b) Upper right: PEO bridge between the central core (green) and a neighboring core (lighter green) over a length of $R_{g,PEO}$ with the span length defined as $r_{span} = 2r_c + R_{g,PEO}$. Lower centre: impossible PEO bridge due to too large stretch of the intermediate PEO block over a length $R > R_{g,PEO}$.

calculate the n_m parameter:

$$n_m = 1 + 4\pi \cdot n_{mic} \int_0^{r_{span}} r^2 g(r) dr. \tag{5.22}$$

Since the central micellar core (indicated as 1 in Figure 5.7 (a)) is not included in the integration, one additional core is included in the calculation of n_m. Note that this central core should be reflected in n_m to ensure that without any micellar cores in close proximity, solely loops are formed with a probability $F_2 = 1/n_m = 1$.

Systematically applying this formalism of converting the structure factor $S(q)$ to the radial distribution function $g(r)$, followed by a spherical integration of $g(r)$ up to r_{span}, to the SAXS fitting results of micellar networks formed by EG312 or EG412 multiblock copolymers, allows to identify a trend of n_m as a function of concentration. Figure 5.8 (a) shows the evolution of the experimentally determined n_m data as a function of concentration at different temperatures for EG312, for which a clear linear trend is observed. As the probability of forming a loop F_2 is inversely related to n_m, the value of n_m is expected to be 1 (only the central core) for all concentrations below $c_{network}$. Therefore, the n_m evolution with concentration is fitted with a linear trend with the additional constraint that the linear fit should reach $n_m = 1$ at $c_{network}$. The latter was earlier determined by extrapolation of $c_{network}$ as a function of temperature (see Figure 5.3 (b) in Section 5.2) and is also indicated in Figure 5.8 (a). The final continuous evolution of n_m as a function of concentration is a combination of $n_m = 1$ at $c < c_{network}$ and the linear fit of n_m versus concentration for $c > c_{network}$, with a smooth, logistic-like transition at $c_{network}$ indicated as a solid line in Figure 5.8 (a).

The obtained concentration dependent microstructural fingerprint can directly be translated to statistical information about the micellar network topology. More specifically, the amount of micellar cores within the span length of a PEO block is linked to the probabilities F_1 and F_2 of a PEO block for either forming a bridge or a loop, respectively, through the relationships $F_2 = 1/n_m$ and $F_1 = 1 - F_2$. Figure 5.8 (b) displays F_1 (solid line) and F_2 (dotted line) as a function of concentration. As expected, upon increasing concentration, the probability of forming a loop gradually decreases from 1 sufficiently below $c_{network}$ to asymptotically reaching 0 at very high concentrations (concentration $\rightarrow \infty$), while the opposite trend from 0 to 1 is observed for the probability of forming a bridge. Nonetheless, phase separation and insolubility practically limit the relevant concentration range for ExpertGel multiblock copolymers up to 200 g/L, at which F_1 and F_2 reach values of about 0.8 and 0.2, respectively. A similar, but less steep evolution was observed in the n_m values of EG412 solutions (see Figure B.5 (a) in Appendix B), resulting in lower probabilities for forming a bridge (B.5 (b)). This can be explained by the shorter PEO block lengths and hence a smaller span width of soluble PEO blocks in networks formed by EG412. The continuous evolutions of F_1 and F_2 as a function of concentration will be used as an input for our generalized transient network model, which will be verified against experimental rheological data in the next section.

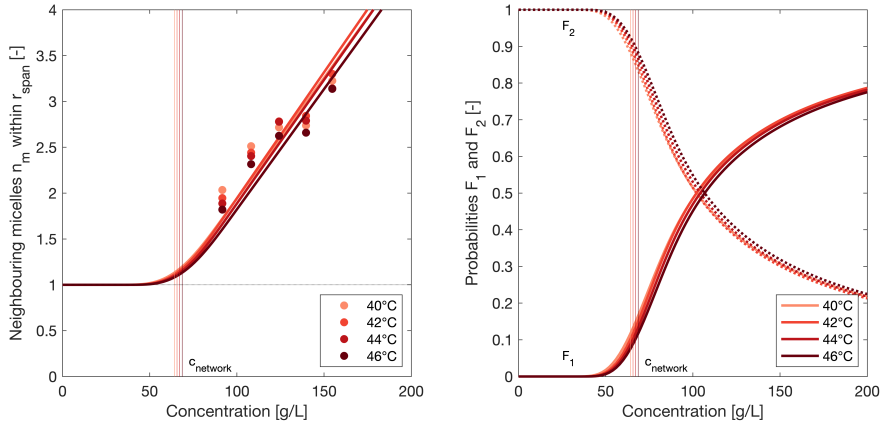

Figure 5.8: (a) Evolution of the experimentally determined amount of micellar cores n_m with EG312 concentration at different temperatures (> CMT). Solid lines represent fits with the additional constraint that $n_m = 1$ at $c < c_{network}$. (b) The evolution of the probabilities $F_1 = 1 - F_2$ (full line) and $F_2 = 1/n_m$ (dotted line) as a function of EG312 concentration at different temperatures (> CMT). The vertical lines on (a) and (b) indicate the extrapolated values of $c_{network}$ at the different temperatures.

5.4 Network elasticity and model performance

Dynamic rheological measurements in the linear regime, i.e. not disturbing the structure, probe the material properties at different time scales and thus provide insights in the material's overall structure. Figure 5.9 (a) shows the elastic (G') and loss (G'') modulus as a function of angular frequency for different concentrations (92, 108, 124, 140 and 155 g/L) of EG312 at 46°C. The presence of a high-frequency elastic plateau is indicative of the elastic, solid-like nature of the micellar network at short time scales. The plateau modulus G_0, defined in this work as the value of G' at the frequency at which G'' reaches its minimum [321] and indicated with black stars in Figure 5.9, is often used as a measure of the elasticity. Analogous to the affine network model for rubber elasticity, each elastically active strand accounts for k_bT of the elastic plateau modulus G_0 (see Equation 5.12) [153]. The terminal flow behavior ($G' \sim \omega^2$ and $G'' \sim \omega^1$) at low frequencies is proof of viscous, liquid-like behavior at longer time scales and reveals the transient character of the micellar association nodes. When given sufficient time, hydrophobic blocks detach from their micellar cores and cause the elastic bridges to relax their stored energy. The elastic plateau, relaxation process and terminal flow were also observed in the frequency sweep data of networks formed

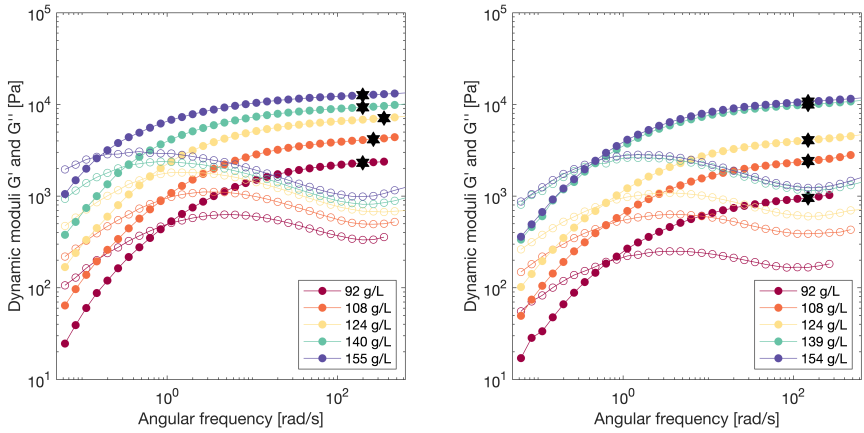

Figure 5.9: Dynamic moduli G' (filled symbol) and G'' (unfilled symbol) as a function of angular frequency for different concentrations ($> c_{network}$) of (a) EG312 at 46°C and (b) EG412 at 40°C at 0.1% strain. The black star symbols indicate the plateau modulus G_0.

by EG412, as can be seen in Figure 5.9 (b) for different concentrations of EG412 at 40°C. Clearly, increasing the multiblock copolymer concentration results in a higher elastic modulus and a slower relaxation process, both of which can be attributed to the formation of a denser micellar network at elevated concentrations. In such a dense structure, the proximity of other micellar cores implies the formation of more elastic bridges contributing to elasticity and thereby influencing the amount of relaxation stages needed for terminal relaxation (see Chapter 6).

5.4.1 Model performance

By performing systematic rheological measurements on networks formed by multiblock copolymers at different concentrations and temperatures, the concentration evolution of the plateau modulus G_0 can be studied (see Figures B.6 (a) and B.6 (b) in Appendix B for EG312 and EG412, respectively). The linear evolution in the log-log plots of plateau modulus versus concentration suggests a power law scaling. Neither of the obtained exponents of 3.16 for EG312 and 4.67 for EG412 comply with the theoretically predicted power law scalings as provided by the Sticky-Rouse model for unentangled, semi-dilute networks, e.g. $G_0 \sim \phi^{2.60}$ at low volume fractions ϕ of the polymers and $G_0 \sim \phi$ at high volume fractions in good solvents ($\nu = 0.588$ and $z =$

0.225) [207]. Moreover, the concentration dependence of the plateau modulus in our micellar networks also does not obey the power law scaling relation ($G_0 \sim \phi^{0.56}$) as predicted by Semenov and Rubinstein for an unentangled micellar phase above the overlap concentration of micelles [210].

Due to the deviations from the existing model predictions for unentangled transient networks, the concentration evolution of $\nu/(a-1)n$ as determined by the plateau modulus (see Equation 5.13) is compared to the prediction based on our generalized mechano-statistical transient network model (see Equation 5.11) in Figure 5.10 (a) for EG312 and (b) for EG412. The model prediction succeeds in describing the rheological data well and captures both the sharp increase at lower concentrations and the asymptotic leveling at higher concentrations. Hence, the generalization of the mechano-statistical transient network model has proven to correctly predict the amount of elastically active chains as inferred from rheology. Moreover, the mechano-statistical nature of the model also enables to determine the evolution of the bridge and loop probabilities (see Figure 5.8 (b)), as well as to gain insights in the node functionality probability distribution $P(\Psi)$ according to Equation 5.6. In Figure 5.10 (c) and (d), the binomial probability distribution functions of the node functionality Ψ around its average value $\langle\Psi\rangle$ (see Equation 5.5) are shown for different concentrations of EG312 at 46°C and EG412 at 40°C, respectively. The average node functionality is more than doubled when increasing the concentration from 92 to 155 g/L EG312. Interestingly, the values of the average node functionality $\langle\Psi\rangle$ indeed show high node functionalities, even at low concentrations ($\langle\Psi\rangle$ = 24 at 92 g/L EG312), which proofs our a priori assumption of high node functionalities in micellar networks and the resulting use of the affine network approach (see Section 5.1). This, together with our insights from the trends of F_1 and F_2, helps to draw a microscopic picture of the network's evolution as a function of concentration above the critical network concentration. At low concentrations, the network predominantly contains PEO loops, as $F_2 > F_1$, and the association nodes have a low functionality as compared to the overall aggregation number and the maximum number of bridges Ψ_{max}. Upon increasing the concentration, the micellar cores gradually transition into bridge-dominated, highly functional network nodes. This topological change goes hand in hand with a change in mechanical properties, reflected in both the elasticity and relaxation behavior. Similar conclusions can be drawn for EG412 networks (see model results and node probability distributions in Figure 5.10 (b) and (d), respectively). To provide an idea about the sensitivity of the model to the SAXS fitting parameters, a sensitivity analysis by inducing a 10% variation in the core radius r_c (see Figure B.7 in Appendix B) and in the micellar volume fraction ϕ (see Figure B.8) is performed for different concentrations of EG312 at 46°C. The effects on the quality of the SAXS intensity profile fits (subfigure a), the crucial n_m evolution as a function of concentration (subfigure b) and the final model performance to predict the network's elasticity (subfigure c) are shown. Note that a variation in r_c and ϕ is also reflected in the aggregation number N_{agg} needed for model evaluation. A variation in the core radius r_c at constant volume fraction, on the

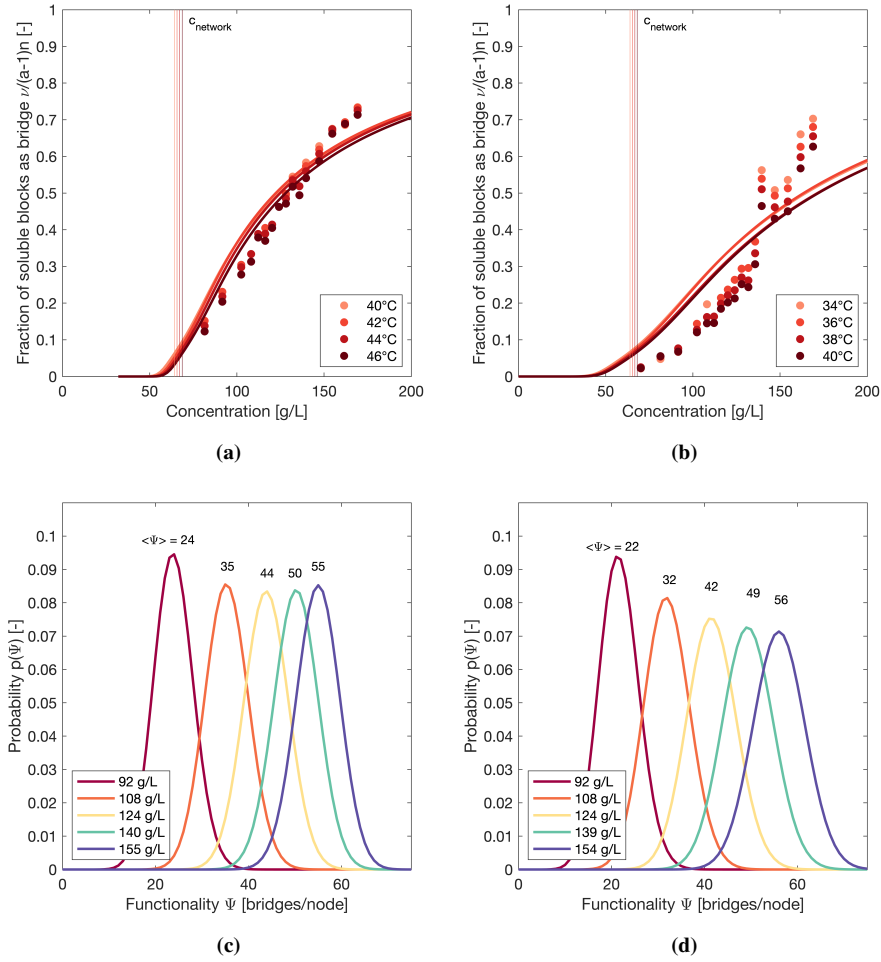

Figure 5.10: Fraction of soluble blocks active as a unique elastic bridge $\frac{\nu}{(a-1)n}$ as a function of (a) EG312 and (b) EG412 concentration at different temperatures (> CMT). The data symbols are calculated from the rheologically determined plateau modulus using Equation 5.13. The solid lines represent the model predictions according to Equation 5.11. The vertical lines indicate the extrapolated values of $c_{network} = \frac{a+1}{a} \cdot c^*$ at the different temperatures. Probability distribution function of nodes with functionality Ψ for different concentrations ($> c_{network}$) of (c) EG312 at 46°C and (d) EG412 at 40°C. The distribution functions are binomial around the average $\langle\Psi\rangle$ (see Equation 5.6) as indicated on the graph.

one hand, has a pronounced effect on the quality of the SAXS profile fits, but does not affect the n_m values as well as the model prediction significantly. A variation in the micellar volume fraction ϕ at constant core size, on the other hand, has a rather limited impact on the SAXS intensity profiles, but does influence the n_m evolution and model predictions more severely. It can thus be concluded that the adopted approach is significantly more sensitive to the micellar volume fraction than to the micellar core size. Nonetheless, the actual elasticity data as inferred from rheology, are located within the model boundaries induced by a 10% variation in volume fraction.

5.4.2 Critical assessment

It must be pointed out that the model predictions for EG412 in Figure 5.10 (b), are less successful in describing the concentration dependent fraction of PEO blocks active as an elastic bridge. Even though the model predicts a correct evolution of the fraction of elastically active PEO blocks, its absolute values present an overprediction at low concentrations and an underprediction at high concentrations. These over- and underpredictions of the elasticity data are also present for EG312 samples in Figure 5.10 (a), albeit to a lesser extent. Therefore, a critical assessment of the physics included in the model allows pinpointing some mechanisms not accounted for in the presented generalized mechano-statistical transient network model.

Firstly, the presence of some odd chain configurations, which are not taken into account in the model derivation, might result in both the over- and underprediction of the elasticity. In this regard, it was previously indicated that so-called redundant bridges (see Figure 5.11 (a) for a schematic representation) are not expected to be formed for our multiblock copolymers with relatively low a values. Nevertheless, the network structure at low concentrations close to $c_{network}$, is potentially fractal [308] and prone to fluctuations, thereby sometimes resulting in no other possibility for a chain than to revisit an old core and hence to form a redundant PEO bridge within the same chain, with a 'shared' PPO block between both bridges. The presence of such redundant bridges at lower concentrations could thus possibly explain the overprediction of the elasticity. Moreover, at low concentrations close to $c_{network}$, the presence of large, unconnected clusters is also not fully accounted for in our model derivations. In this regard, an extension and generalization of the mean field approach [322], as adopted by Skrzeszewska *et al.* [323] for telechelic stickers undergoing trifunctional associative interactions, to multiblock copolymers with functionalities (much) higher than 3, could also possibly correct the overprediction at low concentrations. At high concentrations, on the other hand, a dense micellar structure is formed in which the chances of finding another micellar core are greatly increased. This crowded structure in turn might lead to possible 'entanglements' between loops of different micellar cores (loop-loop entanglement in 5.11 (b)), between non-redundant bridges (bridge-bridge entanglement in Figure 5.11 (c)) or between a loop and a bridge of different micellar

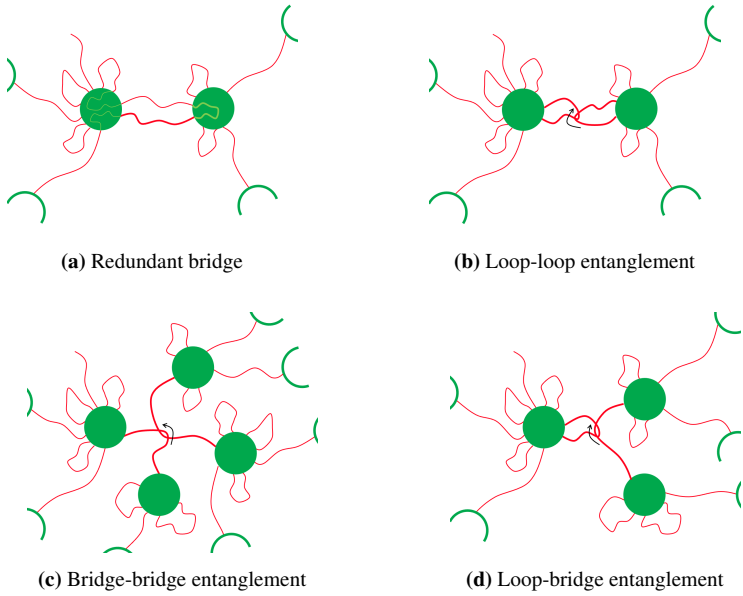

(a) Redundant bridge

(b) Loop-loop entanglement

(c) Bridge-bridge entanglement

(d) Loop-bridge entanglement

Figure 5.11: Schematic illustrations of (a) a redundant bridge, (b) a loop-loop entanglement, (c) a bridge-bridge entanglement and (d) a loop-bridge entanglement. For simplicity, the micellar cores are represented as filled green circles. The arrows indicate the entangled structure.

cores (loop-bridge entanglement in 5.11 (d)). Note that such 'entangled' configurations are solely induced by the drastic microstructural changes upon micellization at high concentrations and cannot be treated according to the classic interpretation of entanglements in polymer solutions. Nonetheless, just like conventional entanglements they do contribute to the elasticity of the network as crosslinking nodes creating additional bridges (1 extra bridge for each loop-loop entanglement and 2 extra bridges for each bridge-bridge or loop-bridge entanglement). These additional bridges are not considered in the model derivation and could provide an explanation for the underprediction of the model at elevated concentrations. The overprediction due to redundant bridges at low concentration as well as the underprediction due to entanglements at higher concentration, could both be captured in a factor α. By dividing the elasticity data as inferred from the plateau modulus (Equation 5.13) by the model prediction (Equation 5.11), a concentration dependent α can be obtained. Note that such ratio should be smaller than 1 at low concentrations above $c_{network}$ and larger than 1 at higher concentrations. The evolution of α as a function of concentration is shown in Figures B.9 (a) and (b) in the Appendix B for EG312 and EG412, respectively. The ratio

shows that indeed the model prediction approaches the actual elasticity data for EG312 (α = 0.80 - 1.15), while for EG412 α ranges from 0.30 at the lowest concentration up to 1.40 at the highest concentrations. Provided that the above mentioned configurations are the sole contributors to the over- and underprediction, it implies that at the lowest concentration of EG412 for each effective elastic bridge, there are about 2 redundant bridges, while at the highest concentration for each 5 bridges between crosslinking nodes, 2 additional bridges are created via entanglements (either as 1 bridge-bridge or loop-bridge entanglement, or as 2 loop-loop entanglements).

Secondly, a rather crucial parameter in the indirect evaluation of the model is the critical concentration for network formation $c_{network}$. As already mentioned, experimentally assessing this onset of network formation is often troublesome [101, 194] and rheological measurements indeed showed irreproducibility and unstable behavior of multiblock copolymer solutions at concentrations close to $c_{network}$. Therefore, we opted for an approximation of $c_{network}$ based on the overlap concentration c^* obtained from viscosity measurements (at low temperatures) in which entire multiblock copolymer chains were allowed to overlap with $1/a^{th}$ of another chain (see Section 5.2). The $(a+1)/a$ factor serves as a correction factor, as the presence of PEO end blocks in ExpertGel® molecules is also reflected in the overlap concentration c^*, thereby hindering PPO blocks of different chains to find each other at c^*. More importantly, such an approximation of $c_{network}$ assumes no microstructural change of the polymer solution upon network formation. The entropy-driven clustering of the PPO blocks, however, causes the formation of a compact hydrophobic core and hence a significantly different and more collapsed chain configuration. It is thus plausible that the theoretical approximation of $c_{network}$ from c^* represents an absolute lower limit for the critical onset concentration of networks formed by micellar aggregation. Additionally, the linear fits of $c_{network}$ at low temperatures showed relatively poor R^2 values (see Figure 5.3 (b) in Section 5.2) over a limited temperature range. Upon extrapolation of this fit to higher temperatures, more uncertainty is likely to be induced. Therefore, a sensitivity analysis of the influence of $c_{network}$ on the transient network model by considering a confidence interval on the regression parameters of the linear fit seems appropriate.

Lastly, it is important to point out that the current verification is performed using commercially available systems. As a result, some polydispersity in terms of the total molecular weight as well as the length of the individual PEO and PPO blocks cannot be excluded. The overall architecture of the molecules as alternating, linear block copolymer can also be disturbed due to potential local branching induced by a very minor fraction of biuret or allophalate bonding units. However, these were not observed in the FT-IR spectra of the ExpertGel molecules (see Section 3.1.1). In addition, possible impurities such as PEO-PPO diblock fractions were found to be present in the precursor Pluronics® [267] and affect ExpertGel® as well (see GPC characterization in Section 3.1.1). All of these effects have their consequences on the correct determination of M_w, a, N_{agg} and n_m, which all need to be known a priori

for model evaluation. Therefore, in the future the model should be validated with more well-defined and carefully synthesized multiblock copolymers with hydrophobic blocks distributed along the chain, or even for transient polymer networks formed by multifunctional association interactions other than micellar self-assembly.

5.5 Conclusions

In this chapter, we report an extension and generalization of the mechano-statistical transient network model originally developed by Annable *et al.* [147,148] for telechelic, hydrophobically associating triblock copolymers to more general alternating multiblock copolymers bearing multiple hydrophobic blocks along their polymer backbone. This was achieved by adopting a combinatorics approach thereby taking into account the different configurations of loops and bridges in multiblock copolymers with multiple association blocks per chain. Herein, the probabilities of individual soluble blocks to form either a bridge (F_1) between two different association nodes or a loop (F_2 = 1-F_1) towards the same association node, were closely linked to the micellar network's microstructure. The loop probability F_2 was approximated as the inverse of the amount of micellar nodes n_m present within the span volume defined by a soluble, hydrophilic block. The average node functionality, defined as the average amount of bridges starting from one association node, was then determined by assessing both the average amount of bridges and the average amount of associating blocks that a certain chain configuration contributes to an association node. Through the construction of a probability distribution function around this average functionality, the model enabled to translate microstructural changes (via n_m) to statistical changes in the chain configurations (via F_1 and F_2) and eventually to macroscopic elasticity fully governed by the amount of bridges. As such, unifunctional dangling ends as well as redundant bifunctional nodes contributing to superloops and superbridges, were eliminated in the determination of the network's elasticity. By a priori knowledge of the multiblock copolymer architecture (number of hydrophobic blocks a and M_w), as well as the micellar network structure (n_m and aggregation number N_{agg}), a complete model evaluation is possible.

For the verification of our model's performance, alternating PEO-PPO multiblock copolymers forming transient micellar networks at elevated temperatures, were investigated. Rather than theoretically approaching the crucial microstructural parameters n_m and N_{agg}, they were experimentally determined by Small-Angle X-ray scattering (SAXS) measurements. To unravel the exact spatial arrangement of the micellar nodes throughout the network, the structure factor as inferred from SAXS on concentrated solutions, was converted to the radial distribution function by its inverse Fourier relation. This allowed the determination of n_m by spherical integration of the radial distribution function up to some length scale r_{span}, defined by the radius

of gyration of a soluble, hydrophilic PEO block. By combining the evolution of the experimentally determined n_m values as a function of concentration with the additional constraint that n_m equals 1 below the critical network concentration $c_{network}$, a smooth evolution of n_m with concentration could be used as an input for our mechano-statistical transient network model.

The model predictions of the fraction of PEO blocks active as a unique elastic bridge were verified with the results inferred from linear oscillatory rheological measurements. The agreement between the model and the experimental data was within reasonable accuracy. Possible explanations of the under- and overpredictions of the network's elasticity could be found in the presence of redundant bridges at low concentrations and entangled loops and/or bridges at higher concentrations, respectively, which were not considered in the model. Nonetheless, with the help of our model a microscopic picture of the evolution of the network's topology as a function of concentration, could be derived. Below $c_{network}$, only isolated flowerlike micelles are formed without any connecting bridges, resulting in a viscous micellar solution. At concentrations slightly above $c_{network}$, loops are still predominant and the micellar nodes have rather low functionalities, leading to limited network elasticity. Upon increasing concentrations, a denser micellar arrangement induces progressively more bridges, such that bridge-dominated and highly functional network nodes are obtained. The elasticity of the ensuing network is greatly increased as compared to networks formed by lower concentrations of multiblock copolymers. This thorough understanding of the network topology, the related statistical probabilities of bridge or loop formation and their effect on the macroscopic rheological properties of the networks, are believed to contribute to a more controlled development of physical hydrogels and transient networks in general with tailor-made mechanical properties. Moreover, our generalized mechano-statistical transient network model is believed to be useful for other equally spaced, multisticker associating polymers forming networks by multifunctional interactions.

Chapter 6

Understanding their sticky Rouse-like relaxation dynamics

The previous chapter focused on correlating the macroscopic elasticity and the microscopic network topology in micellar networks of PEO-PPO multiblock copolymers with the use of a generalized mechano-statistical network model. Besides elasticity, many of the conventional theoretical frameworks also discuss and predict the relaxation behavior in transient networks. Compared to telechelic networks in which the dissociation of one sticker is sufficient for full chain relaxation, multisticker polymers relax via a step-by-step process in which all of their many stickers have to be released. This often results in broad relaxation behavior that cannot be described by a single Maxwell element with one relaxation time. An additional difficulty in networks constructed by hydrophobic association is the presence of micellar crosslinks of significant size possibly contributing to the relaxation mechanism(s). As a result, contrasting assumptions are often made in different models such as for example a single chain versus a collective dynamics approach and whether or not bond life renormalization should be considered. To date, there thus appears to be no broad consensus on the exact relaxation mechanism in such networks, particularly since very few experimental studies examine this relaxation behavior.

This chapter sheds light on the relaxation behavior of the micellar networks formed by PEO-PPO multiblock copolymers by thorough investigation of their rheological time-dependent fingerprint at various temperatures and concentrations. The temperature dependence of the characteristic relaxation times allows highlighting the origin of

the dynamics in the micellar networks. The underlying microscopic processes during relaxation are elucidated by studying the scaling relations of the relaxation times with concentration. The latter do not conform to the typical scaling laws determined by existing transient network models and require a careful reinterpretation of the relaxation behavior in networks formed by multisticker polymers with large scale crosslinking nodes. To this end, we propose a hybrid model, in which we combine different concepts from other models with the insights from our previously developed mechano-statistical network model to explain the relaxation behavior.

6.1 Identification of characteristic relaxation times

A rheological frequency sweep allows studying the frequency and hence time dependent properties of (viscoelastic) materials and as such provides a fingerprint of the material's structure. The typical dynamic response of the micellar networks formed by ExpertGel 312 and 412 at elevated temperatures and concentrations as shown in Figures 5.9 (a) and (b), respectively, in Chapter 5, reveals the characteristics of a transient network. At short timescales (or high frequencies), an elastic network with energy storing capabilities is probed, whereas at long timescales (or low frequencies) terminal flow behavior is obtained. A transition zone characteristic of the relaxation process is present at intermediate timescales. In Chapter 2, networks based on telechelic dynamic crosslink interactions, whether being hydrophobic association of triblock copolymers or metal-ligand complexation, were found to be universally described by a single Maxwell element that includes both storage and dissipative properties. In a rheological frequency sweep, this results in the presence of a clear single relaxation time, usually defined as the crossover between G' and G''. Other determination methods of the single relaxation time, including the (extrapolated) crossover of the terminal slopes ($G' \sim \omega^2$ and $G'' \sim \omega^1$ at low frequencies) [324], the maximum of the loss modulus G'' [19] or the peak in the relaxation time spectrum $H(\tau)$ as calculated from the dynamic moduli [325], all result in the same relaxation time for ideal Maxwellian behavior. This rather simple relaxation behavior is dominated by the sticker dissociation time τ_S, possibly renormalized due to re-associations of the sticker with its old partner on very short time scales (usually referred to as τ_S^*). Once a sticker effectively detached from its partner, the solvable polymer chain attached to it can release its stored energy and relax. Note that for effective stress relaxation as measured by rheology, only the relaxation of intermolecular, elastic bridges matters, while intra-molecular loops contribute little to the rheological response.

In multisticker networks, on the other hand, a much broader relaxation process is often observed and a Maxwellian model fails to correctly describe the rheological fingerprint. In Figure 6.1 (a) the response of a 140 g/L EG312 network at 40°C is shown, together with a Maxwell model fit with its relaxation time determined by the crossover between

G' and G'', and the very limited agreement between the model and the data is evident. For an entire multisticker polymer chain to be able to dissipate all of its stored energy at the network or longest relaxation time τ_N, all hydrophobic stickers along the chain must detach form their partners, thus causing the complete network relaxation to take considerably more time than in telechelic networks. Hence, two characteristic relaxation times, i.e. the (renormalized) sticker dissociation time τ_S and the network relaxation time τ_N, should be considered (see also Figure 2.15 (b) in Chapter 2). These relaxation times are determined based on the intersection of the characteristic slopes in the G' response, which correspond to the different structure regimes. As discussed in Chapter 5, the elastic network structure probed at high frequencies results in an elastic plateau ($G' \sim \omega^0$). Once the sticker dissociation time is reached at τ_S, the relaxation process kicks in according to a stepwise Rouse process referred to as the Sticky rouse regime with a characteristic slope of $G' \sim \omega^{0.5}$. Therefore, τ_S can be approximated as the crossover between the plateau and the best $\omega^{0.5}$ fit of at least 3 consecutive G' data points at lower frequencies deviating from the elastic plateau. Importantly, the assumption of a sticky Rouse regime is justified by the absence of conventional entanglements in the polymer solutions of the PEO-PPO multiblock copolymers, as inferred from the viscosity scaling with concentration in Section 5.2 of Chapter 5. The presence of entanglements between loops and/or bridges in the micellar networks, on the other hand, cannot be fully excluded, especially at very high network concentrations. Interestingly, the rheological fingerprints of the micellar networks do not reveal a second 'Leibler' plateau and hence do not follow a sticky reptation relaxation mechanism of multisticker chains with occasional entanglements ($M_S < M_E$, see Figure 2.16). Instead, it does resemble the typical response as displayed in Figure 2.15 (b) in Chapter 2, due to which we confidently assume a sticky Rouse-like relaxation mechanism in the micellar networks of PEO-PPO multiblock copolymers. The final network relaxation time τ_N is determined as the crossover between the characteristic sticky Rouse region with slope of 0.5 and the terminal flow regime $G' \sim \omega^2$ at the lowest frequencies. Figure 6.1 (b) shows the determination of both relaxation times τ_S and τ_N for a 140 g/L EG312 network at 40°C according to this formalism.

The two characteristic relaxation times τ_S and τ_N can also be determined by fitting a sticky Rouse model onto the dynamic moduli. Such model accounts for the stepwise relaxation of N Rouse modes, corresponding to the N elastic bridges within one polymer chain. The fitting equations for the storage modulus G' and loss modulus G'' are

$$G' = \frac{G_0}{N} \sum_{p=1}^{N} \frac{(\omega \tau_S (N/p)^2)^2}{1 + (\omega \tau_S (N/p)^2)^2} \tag{6.1}$$

$$G'' = \frac{G_0}{N} \sum_{p=1}^{N} \frac{\omega \tau_S (N/p)^2}{1 + (\omega \tau_S (N/p)^2)^2} \tag{6.2}$$

in which G_0 is the plateau modulus, τ_S the sticker dissociation time and N the positive integer number of elastic bridges per chain. The characteristic network relaxation time

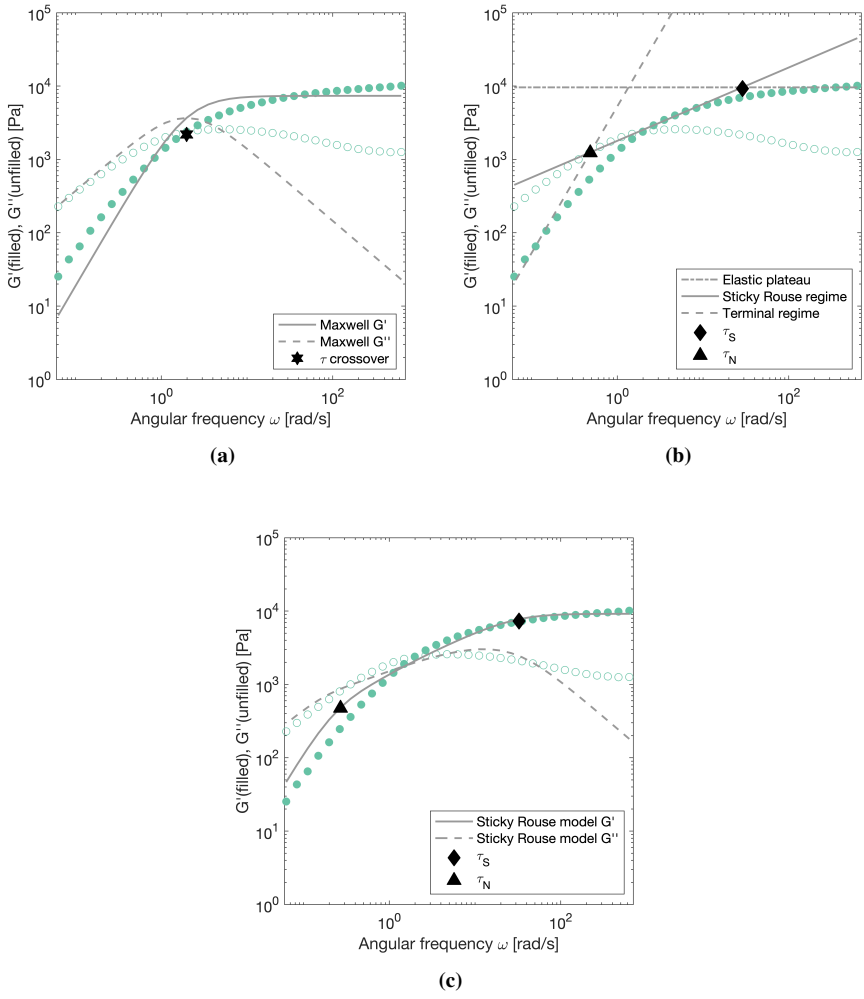

Figure 6.1: Identification of the characteristic relaxation times τ_S and τ_N from a rheological frequency sweep in the linear viscoelastic regime of a 140 g/L EG312 network at 40°C: (a) Maxwell model fit using the crossover between G' and G'' as single relaxation time shows bad agreement, (b) crossovers between characteristic G' versus ω slopes of 0 (elastic plateau), 0.5 (sticky Rouse regime) and 2 (terminal flow) as indicators of τ_S and τ_N and (c) sticky Rouse model fit with $\tau_N = N^2\tau_S$ and $N = 11$.

τ_N then equals $N^2\tau_S$. Note that for our multiblock copolymers with approximately 4 hydrophobic stickers per chain, N can in principle have a maximum value of 3 according to the sticky Rouse model. However, to optimize the fitting results and to release the constraint that the networks formed by multiblock copolymers should comply with the sticky Rouse model assumptions, we allow N to be larger than 3. Figure 6.1 (c) shows the sticky Rouse model fitting of the dynamic response of a 140 g/L EG312 network at 40°C, together with the as such determined relaxation times τ_S and τ_N. The N value for the optimized fit equals 11 and is thus significantly larger than 3. This, together with the fact that the agreement between experimental data and model fit is still not great, provides evidence that the sticky Rouse model is not sufficient as an exact description of the true underlying microscopic relaxation process(es). Moreover, the fact that τ_S and τ_N are linked via N, which is constrained to be a positive integer, results in limited degrees of freedom to fit the data accurately for other concentrations and temperatures. Therefore, the sticky Rouse model is not further considered for the extraction of the characteristic relaxation times. However, it should be mentioned that possible incorporation of molecular weight distribution information, i.e. dispersity in the amount and length of the PEO and PPO blocks, might allow more accurate sticky Rouse fitting [239], but does not fall within the scope of the present dissertation (see also the outlook in Section 8.2 of Chapter 8).

6.2 Temperature and concentration dependence

6.2.1 Temperature dependence

Besides the concentration, as shown in Figure 5.9 in Chapter 5, temperature also has a significant effect on the rheological behavior of the micellar networks formed by alternating PEO-PPO multiblock copolymers. Figures 6.2 (a) and (b) show the dynamic responses of a 140 g/L EG312 network and a 154 g/L EG412 network, respectively, at different network temperatures. Whereas the high-frequency elastic plateau and thus also the network topology (i.e. the bridge-to-loop ratio) is barely influenced by temperature, there is a significant delay of the relaxation at higher temperatures. This is in contrast with conventional thermally activated behavior and hints at the fact that the relaxation is dominated by the dissociation of the hydrophobic clusters. At higher temperatures, the PPO hydrophobicity and thus the strength of the hydrophobic clusters increases, which is reflected in the sticker dissociation time τ_S as well as in the longest relaxation time of the network τ_N.

Figures 6.3 (a) and (b) show the temperature dependencies of τ_S and τ_N in an Arrhenius plot of $\ln(\tau)$ versus the inverse temperature for a 140 g/L EG312 network and a 154 g/L EG412 network, respectively. Note that not for each temperature, both relaxation times can be determined due to the absence of 3 consecutive G' data points that have slopes of

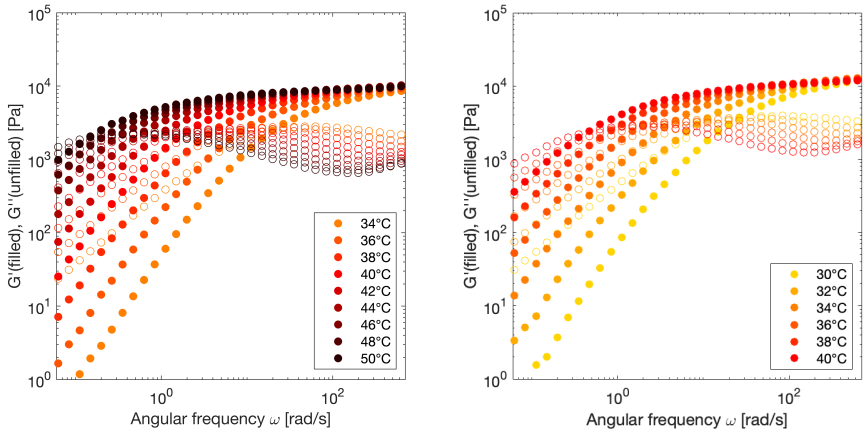

Figure 6.2: Linear dynamic moduli G' (filled symbol) and G'' (open symbol) as function of angular frequency at various elevated network temperatures for (a) 140 g/L EG312 and (b) 154 g/L EG412 at 0.1% strain.

0 (plateau), 0.5 (sticky Rouse) or 2 (terminal flow) as a function of frequency. The linear dependencies in Figures 6.2 prove that for each relaxation time, a single mechanism governs the rheological relaxation process upon increasing temperature [45]. These linear dependencies suggest an Arrhenius-like dependency

$$\tau = A \exp\left(\frac{E_{a,relax}}{RT}\right) \text{ or } \ln(\tau) = \ln(A) + \frac{E_{a,relax}}{RT} \tag{6.3}$$

in which A is a pre-exponential factor, $E_{a,relax}$ the relaxation activation energy and R the universal gas constant. Figures 6.4 (a) and (b) display the as such obtained absolute values of the activation energies for both τ_S and τ_N as a function of concentration for EG312 and EG412 networks, respectively. It is important to bear in mind the following two points of attention when interpreting this activation energy: firstly, the relaxation processes as probed in networks formed by PEO-PPO multiblock copolymers are not thermally activated as is conventionally the case for Arrhenius-like processes, and secondly, only a limited temperature range spanning maximum 16°C is considered for determination of the activation energy. Additionally, linking the activation energy for sticker dissociation to the enthalpy of micellization as determined in Chapter 4 by various calorimetric techniques [198], is not straightforward due to the different underlying processes. Whereas the sticker dissociation represents the detachment of a single hydrophobic block from a micellar core, the calorimetric techniques probe the gradual but entire micellization process in which multiple copolymers cluster together

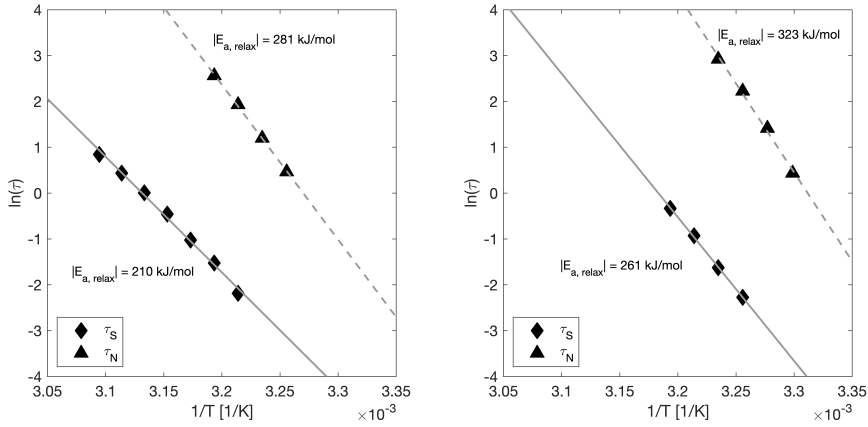

(a) **(b)**

Figure 6.3: Arrhenius plot of $\ln(\tau)$ versus 1/T using the relaxation times as obtained from the crossovers of the characteristic G' slopes for (a) 140 g/L EG312 and (b) 154 g/L EG312. The lines represents the linear Arrhenius fits with the absolute values of the activation energies indicated.

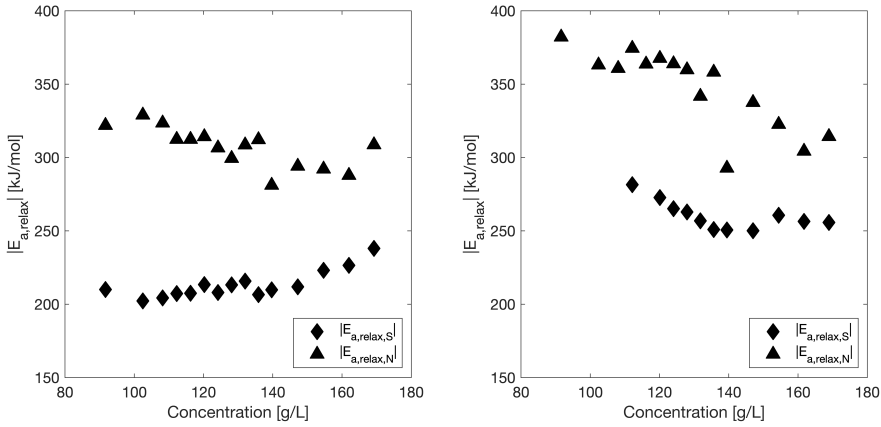

(a) **(b)**

Figure 6.4: Absolute values of the activation energies as a function of concentration, as inferred from Arrhenius fitting of the temperature dependence of the relaxation times τ_S and τ_N for (a) EG312 and (b) EG412.

to form micelles. Therefore, it also seems plausible that the enthalpic contributions of micellization (see Table 4.2 in Chapter 4) are significantly larger than the activation energy needed for a single PPO block to dissociate and to allow the stepwise relaxation to proceed. Nonetheless, similar to the enthalpy of micellization, the activation energies of EG312 sticker dissociation and network relaxation are lower than the ones obtained for EG412, and must thus be governed by the lower hydrophobicity of EG312.

Moreover, the sticker dissociation process has a lower activation energy as compared to that of the complete network relaxation, which is consistent for all network concentrations (see Figures 6.4 (a) and (b)). This is not surprising as the activation energy for network relaxation does not only reflect the need for sticker dissociation events, but also reflects the activation energy for pure polymer flow [198]. However, an estimate of the latter from the Arrhenius-like evolution of the viscosity (or G''/ω) versus inverse temperature at temperatures sufficiently below the CMT results in $E_{a,flow}$ values on the order of 20-25 kJ/mol for both dilute and concentrated solutions of multiblock copolymers and thus seems insufficient to account for polymer flow in the networks. In this regard, the complex network microstructure, i.e. crowded micelles as compared to individual polymer chains below the CMT, together with the stepwise relaxation mechanism could possibly explain this mismatch.

6.2.2 Concentration dependence

Whereas the temperature dependence of the relaxation times allows to study the driving force behind network relaxation, the concentration dependence helps to unravel the underlying processes taking place during relaxation by comparison with the characteristic scaling laws as derived in different theoretical model frameworks. Figures 6.5 (a) and (b) show the concentration dependence of both characteristic relaxation times τ_S and τ_N in a log-log plot for (a) EG312 at 40°C and (b) EG412 at 34°C, together with their power law fitting and exponents. Good agreement between the experimental data and the power law fits is achieved, except maybe at the highest concentrations for which deviations from the power law exist (in τ_N of EG312 in Figure 6.5 (a)). As expected, the absolute values of τ_N are at least one order of magnitude higher than the ones of τ_S and reflect the need for multiple sticker dissociations. Interestingly, the exponent of the τ_N concentration dependence is significantly lower than that of the τ_S concentration dependence. Figures 6.6 (a) and (b) displaying the obtained power law exponents at different temperatures for EG312 and EG412, respectively, illustrate that this observation is consistent for all network temperatures. Moreover, Figures 6.6 (a) and (b) reveal a decreasing trend in both power law exponents as a function of temperature. It is noteworthy that other indicators of the relaxation times, such as the crossover between the terminal slopes as an indication for the longest relaxation time [324], or the maximum in the loss modulus G'' [19] have a similar concentration

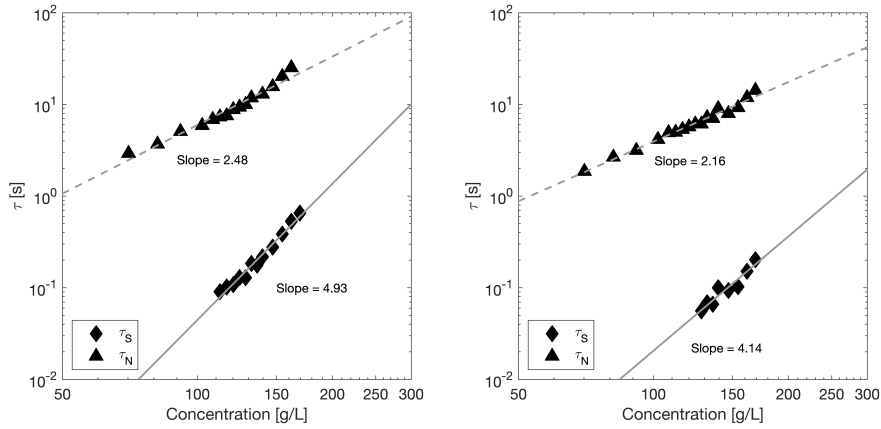

(a) **(b)**

Figure 6.5: Relaxation times τ_S and τ_N versus concentration in a log-log plot for (a) EG312 at 40°C and (b) EG412 at 34°C. The lines represents the power law fits with the power law exponents indicated.

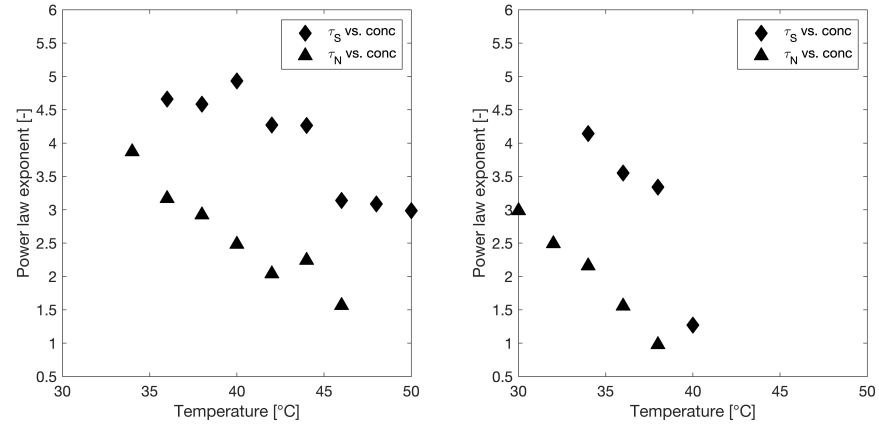

(a) **(b)**

Figure 6.6: Power law exponents as a function of temperature, as inferred from fitting of the concentration dependence of the relaxation times τ_S and τ_N for (a) EG312 and (b) EG412.

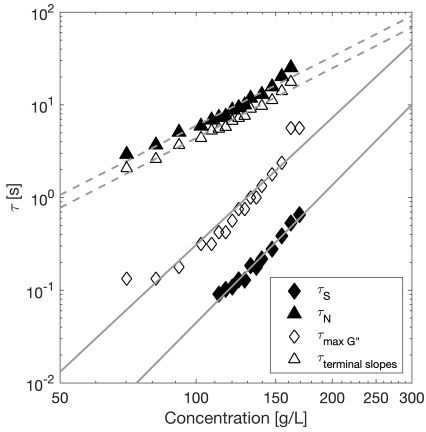

Figure 6.7: Relaxation times determined by different methods versus concentration in a log-log plot for EG312 at 40°C. The lines represent the power law fits.

dependence as τ_N and τ_S, respectively, as can be seen in Figure 6.7 comparing the different relaxation times for EG312 at 40°C.

6.3 Comparison with theoretical frameworks

The combination of these peculiar concentration dependent trends of the relaxation times in networks based on micellar crosslinking nodes between multisticker polymers demands a careful comparison with the existing theoretical frameworks as discussed in Section 2.3 of Chapter 2 (see also Table 2.2 for characteristic concentration dependencies).

6.3.1 Existing models

Semenov's multisticker micellar network model

The multisticker micellar network model as developed by Semenov *et al.* for multisticker polymer networks with large scale aggregates as crosslinking nodes predicts the relaxation behavior based on a collective dynamics approach in which micellar debridging and/or hopping is crucial [210]. Additionally, they suggest to ignore bond lifetime renormalization in networks with multifunctional interaction nodes, hence considering τ_S to be independent of concentration. The resulting longest

(or network) relaxation time τ_N scales with concentration according to a $\tau \sim \exp(c^n)$ relation in which n typically has values of 0.14, -0.43 or 0.87 depending on the dominant relaxation pathway and mechanism (see Figure 2.17). Such exponential scaling relations of τ_N are not observed in our systems. Moreover, as shown by the strong concentration dependence of τ_S, there seems to be a severe renormalization effect for the PPO block stickers in our networks. Therefore, we conclude that the multisticker micellar network model does not provide an accurate description of the relaxation dynamics in networks formed by PEO-PPO multiblock copolymers. Moreover, the recent results by Mordvinkin *et al.* support this conclusion as they proved using multiple-quantum NMR that for networks formed by telechelic micellar crosslinking nodes, the terminal relaxation is governed by single chain relaxation principles rather than micellar reorganization [225, 226].

Rubinstein's sticky Rouse relaxation model

The rheological fingerprints of the networks formed by multiblock copolymers reveal sticky Rouse-like relaxation dynamics. In the sticky Rouse model as developed by Rubinstein *et al.* for multisticker polymers undergoing pairwise associations, the sticker dissociation time τ_S and the network relaxation time τ_N are linked by the number of elastically active bridges per multisticker chain N as $\tau_N = N^2\tau_S$. Network relaxation is thus achieved upon relaxation of all N Rouse-like steps within one single polymer chain. Using a mean field approach and significant correlation effects between sticker dissociation and association, they derived the concentration dependencies of τ_S representing significant bond lifetime renormalization, and of N accounting for the concentration dependent conversion from intramolecular inelastic loops to intermolecular elastic bridges (see Table 2.2) [206, 207]. However, the characteristic scaling exponents in Figures 6.5 (a) and (b) do not comply with the predicted values of Rubinstein's sticky Rouse model for pairwise association, i.e. $\tau_S \sim c^{1.81}$ and $\tau_N \sim c^{4.96}$ or $\tau_S \sim \tau_N \sim c^{0.17}$ at higher concentrations at which only bridges are present.

Nonetheless, the basic principles of a sticky Rouse-like relaxation process can be combined with the insights from the generalized mechano-statistical transient network model as derived earlier (see Section 5.1 in Chapter 5) to get a more accurate indication of N in networks formed by large scale hydrophobic associations. Assuming τ_S to be the time it takes for one PPO block to detach from a micellar core (possibly normalized due to many re-associations), the time it takes for one multiblock copolymer chain to abandon one specific micellar core τ_C can be calculated as:

$$\tau_C = N_a^2 \cdot \tau_S \tag{6.4}$$

in which N_a represents the average amount of PPO blocks one chain contributes to one micellar core (see Equation 5.4 in the previous chapter). For this calculation, the dissociations of all N_a PPO blocks are considered to be independent, random and

Rouse-like, as reflected in the quadratic dependence. Moreover, as already mentioned in Chapter 5, it is assumed that once a chain leaves a certain micellar node to form a bridge towards another node, it does not come back to that same node. Hence, different PPO blocks of one polymer chain only contribute to the same micellar node through loops. The overall network relaxation time τ_N then represents the time it takes for a chain to abandon all of the micellar cores it is bridging to. Again assuming a Rouse-like process, it can be calculated as:

$$\tau_N = N_d^2 \cdot \tau_C \tag{6.5}$$

in which N_d represents the average amount of bridges per multiblock copolymer chain. Using our combinatorics approach, N_d can be determined as:

$$N_d = \sum_{i=0}^{a-1} i \cdot \binom{a-1}{i} \cdot F_1^i \cdot F_2^{a-1-i}. \tag{6.6}$$

The resulting relation between τ_S and τ_N is the following:

$$\frac{\tau_N}{\tau_S} = (N_a \cdot N_d)^2. \tag{6.7}$$

and is shown as a full line in Figures 6.8 (a) and (b) for EG312 networks at 40°C and EG412 at 34°C, respectively. For the calculation of N_a and N_d, the concentration dependent evolutions of F_1 and F_2 as determined earlier are used. The τ_N/τ_S evolution shows an additional, positive concentration dependence of τ_N as compared to τ_S at low network concentrations, but saturates rapidly at more elevated concentrations to a constant factor of 9 ($= (a-1)^2$ with a = 4 in our multiblock copolymers). However, due to the lack of such saturation, as well as the weaker concentration dependence of τ_N as compared to that of τ_S, such approach also does not correctly describe the true relaxation dynamics in multiblock copolymer networks as inferred from the true experimental τ_N/τ_S values shown as dots in Figures 6.8 (a) and (b).

Annable's mechano-statistical transient network model

Networks formed by telechelic crosslinks usually exhibit ideal Maxwellian rheological behavior with one single relaxation time ($\tau_S = \tau_N$). Nevertheless, (strong) concentration dependencies of this relaxation time are often observed. In their original mechano-statistical transient network model for telechelic triblock copolymers, Annable *et al.* attribute this concentration dependence to the presence of superbridges and do not consider the possibility of bond lifetime renormalization. Such superstructures relax faster as compared to separate single bridges due to their larger probability of 'breakage' per unit time [146, 147] and are accounted for using the following concentration dependent correction factor

$$\frac{\tau_N}{\tau_S} = \frac{1 - P(0) - P(1) - P(2)}{1 - P(0) - P(1)}. \tag{6.8}$$

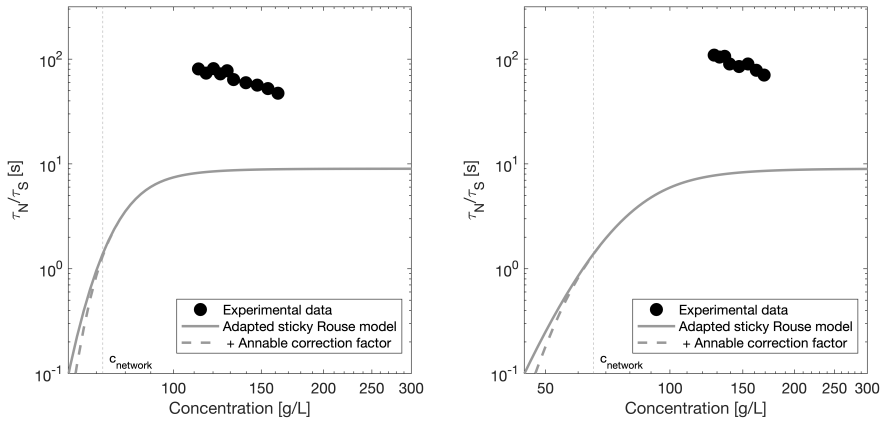

Figure 6.8: Comparison of τ_N/τ_S experimental data with the adapted sticky Rouse model prediction (see Equation 6.7) without and with additional Annable correction factor (see Equation 6.8), both making use of the generalized mechano-statistical transient network model as developed earlier for (a) EG312 at 40°C and (b) EG412 at 34°C.

Herein, $P(0)$, $P(1)$ and $P(2)$ represent the occurrence probabilities of non-functional, uni- and bifunctional crosslinking nodes, respectively, and Equation 6.8 eliminates the fraction of nodes involved in superstructures with $P(2)$, i.e. superloops and -bridges, which speed up the relaxation. Another approach was taken by West *et al.* [326], who linked the single Maxwellian relaxation time τ_N to the sticker dissociation time τ_S for unentangled, telechelic transient networks using the following concentration dependent expression

$$\frac{\tau_N}{\tau_S} = \frac{G_0/c_T}{dG_0/dc_T} \tag{6.9}$$

in which G_0 is the plateau modulus and c_T the number concentration of telechelic chains. Such expression assumes that a sticker dissociation event (τ_S) contributes to the network stress relaxation (τ_N) as predicted by the fractional decrease in shear stress (reflected in the plateau modulus G_0) upon removal of that sticker (reflected in the concentration c_T). West *et al.* showed that Equation 6.9 is consistent with the 'superbridge' explanation as proposed by Annable *et al.* for telechelic systems [326]. An implicit assumption of West's approach is that the network relaxation process can be captured by a single relaxation time, which is the case for telechelic systems exhibiting a universal Maxwellian response. For multiblock copolymers, however, the

relaxation process is broad and the identification of only a single relaxation time is impossible, thus making the calculation of West *et al.* inaccurate. It is therefore not further considered here.

The correction factor as proposed by Annable *et al.* in Equation 6.8 does not necessarily impose the constraint of a single relaxation process, and can thus also be applied to Equation 6.7 for transient networks formed by multiblocks. The resulting τ_N/τ_S prediction is added to Figures 6.8 (a) and (b) as dashed lines. However, due to the significant aggregation number of the micellar cores in our networks, the correction factor has a negligible effect on the evolution of τ_N/τ_S as superstructures are only significantly present below and very close to $c_{network}$. Even though concepts of both Rubinstein's and Annable's transient network models might be applicable to the networks formed by PEO-PPO multiblock copolymers, most features of the relaxation dynamics thus remain unexplained in the existing network frameworks and therefore, we propose a hybrid approach in the following section.

6.3.2 Hybrid model

The above mentioned transient network models all consider the chain dynamics to occur much faster as compared to the sticker dissociation, the latter thus being the bottleneck for the relaxation process. Hence, upon release of a PPO block from a micellar core, the elastic chain attached to it has sufficient time to fully relax before the PPO block re-associates with another partner. The sticker dissociation time τ_S is thus actually a representation of how long a sticker remains 'open' before it finds a new partner. We question the assumption that $\tau_{chain} \ll \tau_S$ as often made in other model frameworks, and we therefore propose a hybrid model which takes into account the intrinsic chain dynamics, similar to the Cates model developed for 'living' polymers [203]. Instead of only considering the sticker dissociation time τ_S for the calculation of τ_N, we propose a geometric mean $\sqrt{\tau_S \cdot \tau_{chain}}$ of both τ_S and the chain dynamics τ_{chain} in the following way:

$$\tau_N = \underbrace{\frac{1-P(0)-P(1)-P(2)}{1-P(0)-P(1)}}_{\text{Annable's correction factor}} \cdot \underbrace{(N_a \cdot N_d)^2}_{\text{sticky Rouse contribution}} \cdot \underbrace{\sqrt{\tau_S \cdot \tau_{chain}}}_{\text{Cates geometric mean } \tau} \tag{6.10}$$

Owing to the possible concentration dependence of τ_{chain}, this approach allows the power law exponent of τ_N versus concentration to be different than that of τ_S. Assuming Equation 6.10 to be correct, the concentration dependent evolution of τ_{chain} can be calculated and is shown in Figures 6.9 (a) and (b) for EG312 at 40°C and EG412 at

34°C, respectively, together with the previously determined τ_N and τ_S. Interestingly, the as such calculated τ_{chain} values are indeed non-negligible as compared to τ_S, and are even as large as the overall network relaxation time τ_N. We hypothesize that the crowded and complex microstructure of the micellar network might be responsible for this very slow chain dynamics. The concentration dependence of τ_{chain} has a varying power law exponent depending on the temperature, with values of 1.36 and -0.39 for EG312 at 40°C and 42°C, and values of 0.47 and -1.13 for EG412 at 34°C and 36°C. Note that only a limited set of data allows this calculation, as at other more elevated network temperatures the simultaneous determination of both τ_S and τ_N in a rheological frequency sweep is impossible, i.e. either only τ_S is detected for the lower concentrations or only τ_N is detected for the higher concentrations. Hence, an assessment of the temperature dependence of τ_{chain} based on only two different network temperatures, is not performed. Due to this limited data set, it is thus difficult to draw exact conclusions about the origin of τ_{chain} and its concentration and temperature dependence. Nonetheless, our hybrid model has shown that by combining insights from the sticky-Rouse model and the Cates model for 'living' polymers, and using input from our mechano-statistical transient network model, a more accurate view on the relaxation in micellar, multisticker networks can be obtained. However, further verification of this hybrid model still remains future work and does not fall within the

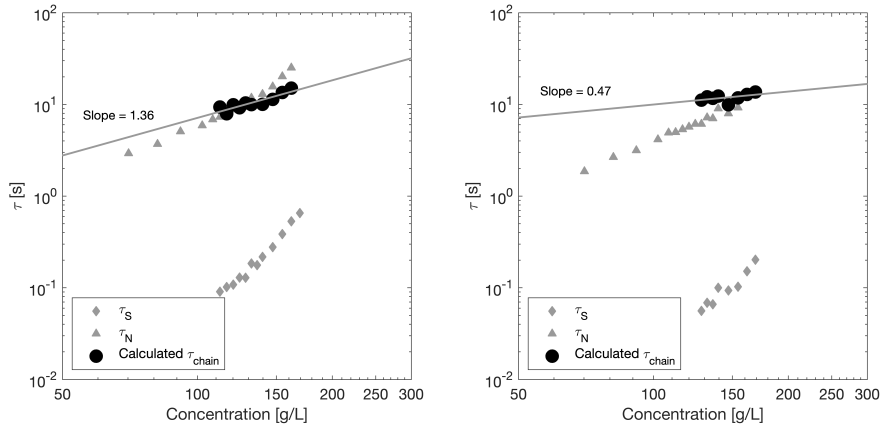

Figure 6.9: τ_{chain} versus concentration as calculated using Equation 6.10 which combines the experimental τ_N and τ_S data (also shown) with a hybrid model having elements from the sticky Rouse model, the mechano-statistical transient network model and the Cates model for (a) EG312 at 40°C and (b) EG412 at 34°C.

scope of this PhD dissertation.

6.4 Conclusions

This last chapter of part I elucidates the relaxation behavior of micellar networks formed by PEO-PPO multiblock copolymers in aqueous solutions at different elevated temperatures and concentrations. In absence of chain entanglements, such networks are theoretically predicted by Rubinstein and Semenov [206, 207] to relax according to a sticky Rouse mechanism, which requires a stepwise dissociation of all stickers along the chain and results in a much broader relaxation as compared to that of networks with telechelic stickers. By investigation of the linear oscillatory rheological fingerprint, two characteristic relaxation times were identified for networks formed by multiblock copolymers, i.e. the sticker dissociation time τ_S and the (longest) network relaxation time τ_N. At timescales $< \tau_S$, the elastic plateau ($G' \sim \omega^0$) is indicative of an elastic network structure. At timescales $> \tau_N$, the terminal behavior ($G' \sim \omega^2$, $G'' \sim \omega^1$) proves viscous flow and complete stress relaxation. At intermediate timescales $\tau_S < t < \tau_N$ the broadness of the relaxation hints towards a $G' \sim G'' \sim \omega^{0.5}$ scaling characteristic of a Rouse-like relaxation process and thus acts in favor of sticky Rouse-like relaxation dynamics. The characteristic relaxation times were determined based on the crossovers of the characteristic G' slopes of 0, 0.5 and 2.

The temperature dependence of the relaxation times was found to be opposite to that of conventional thermally activated processes, thereby revealing that the release of a PPO block from its hydrophobic micellar core initiates the relaxation process. Interestingly, the power law concentration dependencies of τ_S and τ_N do not obey the scaling relationships as predicted by Rubinstein and Semenov for sticky Rouse-like relaxation, and surprisingly show a stronger concentration dependence of τ_S as compared to that of τ_N. Moreover, the comparison of the scaling exponents with those predicted by the existing transient network relaxation frameworks, shows that there is in fact no agreement with any of the conventional transient network models. Therefore, we constructed a hybrid model which combines concepts from the sticky Rouse model and the Cates model for 'living' polymers, and uses input from our previously developed mechano-statistical transient network model. In contrast to most transient network models for multisticker polymers, we herein assume the intrinsic chain dynamics of the polymers to be non-negligible, thus affecting the network relaxation time τ_N. With the help of our hybrid model, we could successfully explain the peculiar concentration dependencies of the characteristic relaxation times, but an exact microscopic interpretation thereof still remains future work.

Part II

DOUBLE NETWORKS
combining hydrophobic association and metal-ligand complexation

Chapter 7

Identifying the multiple dynamics and synergy in double networks

Double networks (DNs) or interpenetrating polymer networks (IPNs) in which both networks are constructed through supramolecular crosslink interactions, are currently underreported in the literature. Instead, the focus is usually on the combination of supramolecular interactions with dynamic covalent bonds due to the significant dynamic difference between networks based on these interactions. Although promising stimuli-responsive properties are often obtained in such systems, the dynamic covalent bonds behave as either static covalent bonds with no relaxation or as very labile dynamic interactions whose relaxation is too fast to be probed, depending on their external stimulus. The wide range of possible physical, supramolecular interactions span the full spectrum of bond strengths (see Figure 2.1 in Chapter 2) and allow the selection of compatible, but significantly different dynamic networks for which true 'double dynamics' are achieved. Smart design of such supramolecular DNs or IPNs can thus result in complete but multi-dynamic relaxation behavior on reasonable time scales accessible by experimental techniques. Therefore, DNs or IPNs exclusively based on physical crosslinking interactions with different binding strengths hold a promising potential as model systems to gain fundamental insights in the synergistic properties of DNs. However, the current characterization techniques are often limited to studying the mechanical performance of these materials as soft, deformable solids and their resulting self-healing or shape memory properties, while their viscoelastic nature as well as their microstructure often remain unexplored.

In this chapter, DN hydrogels combining hydrophobic association of PEO-PPO multiblock copolymers in aqueous solutions with metal-ligand complexation of terpyridine-functionalized PEO stars will be discussed. Owing to the broad tunability of the metal-ligand interaction strength, networks with true dual dynamic behavior can be obtained by appropriate selection of the metal ion. The viscoelastic nature of the single networks and their different relaxation time scales promote rheology as an ideal tool for probing the distinct dynamic modes and elastic contributions to the double network. Moreover, the combination of a thermoreversible network formed by hydrophobic association at elevated temperatures, with a metal-ligand network exhibiting the regular thermal behavior, allows the use of temperature as an external stimulus to differentiate between the different network contributions. In the next sections, we elaborate on the selection and formation of the double network model system, its temperature dependent behavior, the synergistic rheological properties and finally its reproducibility and highlight important features as well as shortcomings of these fully supramolecular double networks.

7.1 Double network model system

For a correct assessment of the elasticity and relaxation processes in the double network structure and isolation of the contributions of the single networks, it is of utmost importance that both networks have significantly different transient dynamics. This allows to probe not only the difference in the relaxation time scales of both networks, but also their effect on the overall elasticity of the double network structure. In the previous chapters, the phase behavior (Chapter 4), the network formation, topology and related elasticity (Chapter 5) as well as the relaxation dynamics (Chapter 6) of medium-length alternating PEO-PPO multiblock copolymers with different block lengths in aqueous solutions were extensively investigated. As a logical consequence, the transient networks formed by hydrophobic clustering (HC) of the PPO blocks at elevated temperatures and concentrations, will be used as one of the networks in the double network structure. The thermoreversibility of the hydrophobic crosslinking nodes adds an interesting feature to this network, as it allows to exclusively form the network structure at elevated temperatures and to selectively weaken and destroy the network structure upon decreasing the temperature.

7.1.1 Characterization of the relaxation process

As a starting point, consider the linear rheological properties of a 92 g/L EG412 solution at different temperatures in Figure 7.1 as obtained by an oscillatory frequency sweep (a), as well as a stress relaxation (b). The latter can probe the linear rheological response at longer times scales as compared to a frequency sweep experiment, since it

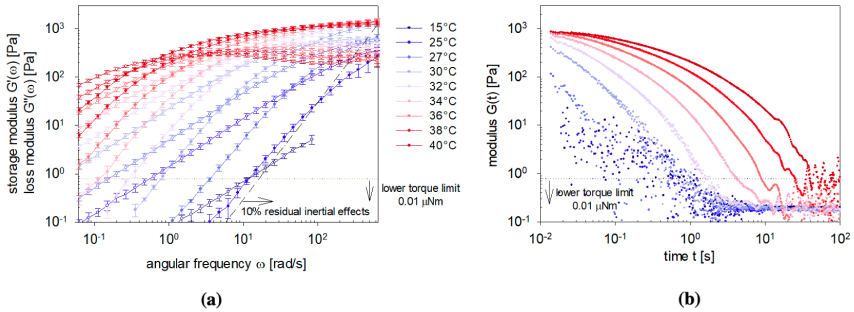

Figure 7.1: Linear rheological response of a 92 g/L EG412 solution at different temperatures: (a) dynamic moduli G' (filled symbol) and G'' (open symbol) as function of angular frequency at 0.1% strain, (b) shear modulus G as function of time upon application of 1% strain. Modulus contribution from 10% residual inertial effects in oscillatory measurements and the rheometer's lower torque limit are also indicated.

is not hindered by experimental (time) limitations. As already discussed in Chapter 6, the broad relaxation process is indicative of the multistep chain relaxation of polymers containing multiple hydrophobic stickers along the chain. However, in contrast to our previous approach in which we thoroughly dissected the relaxation dynamics according to a sticky Rouse framework, for the analysis of their contribution to the double network dynamics and in view of simplicity, the broad relaxation process will be described as a stretched exponential decay of the shear modulus versus time

$$G(t) = G_0 \exp\left(-(t/\tau)^{\beta}\right) \tag{7.1}$$

in which G_0 is the plateau modulus, τ the relaxation time and β the broadness. Even though this is an oversimplification of the relaxation processes in the single network, it does allow to capture the dynamic response of the network in one single relaxation time which facilitates the comparison with its dynamics in the double network structure. The stretched exponential fit for a 92 g/L EG412 network at the highest temperature of 40°C is displayed in Figure 7.2 and complies well with the experimental rheological data. The 'stretching exponent' β was found to be close to 1/3, which was also observed by Erk *et al.* for thermally reversible, physically associating triblock copolymer solutions and was linked to structural relaxation in a wide range of disordered viscoelastic materials [327]. The Fourier transformation of a stretched exponential stress relaxation response in the time domain to the dynamic moduli in the frequency domain is ill-posed and usually relies on series expansions in the limit of either low or high frequencies [328]. It is therefore not further considered here and only the results from the stress relaxation stretched exponential fitting are used.

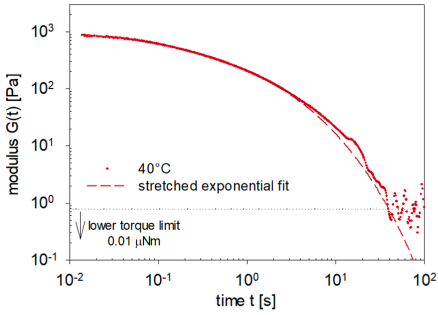

Figure 7.2: Shear modulus G as a function of time upon application of 1% strain for a 92 g/L EG412 solution at 40°C. Dashed line represents a stretched exponential fit according to Equation 7.1.

As extensively discussed in Chapter 5, the plateau modulus G_0 is an indication of the network's elasticity and is strongly dependent on concentration. As previously shown, the elasticity in HC networks is due to PEO bridges between micellar cores, which have the ability to store elastic energy. The presence of more hydrophobic micellar cores upon increasing concentration favors the formation of PEO bridges over loops and transforms the network form loop-dominated to bridge-dominated. At a relatively low concentration of 92 g/L EG412, Figure 5.10 (b) in Chapter 5 shows that only a limited fraction (less than 10%) of all available PEO blocks forms elastically active bridges. One might argue that the presence of defects (e.g. loops) is not ideal for the formation of a double network with optimal rheological properties. However, from a fundamental point of view, allowing a significant fraction of defects to be present in the single network also facilitates identifying potential benefits of the double network structure on the amount of bridges and the resulting elasticity. In this regard, Klymenko *et al.* [259] concluded in their study on IPN hydrogels formed by two different hydrophobically associating triblock copolymers that the presence of another network favors bridge formation over loop formation and lowers the percolation threshold for network formation [259]. Moreover, our choice for a relatively low concentration of the HC network ensures that the broad relaxation remains within an experimentally accessible frequency window and that possible entanglements between bridges and/or loops are non-existent. The latter were previously hypothesized to only happen at higher network concentrations (see Section 5.4.2 in Chapter 5).

In Figure 7.3 (a), the temperature dependence of the fraction of elastically active PEO blocks in 92 g/L EG412 solutions is displayed, as calculated from the plateau modulus G_0 of the stretched exponential fit to the stress relaxation data at sufficiently high temperatures ($\geq$ 34 °C) according to Equation 5.13. Good agreement with

the elastically active fractions inferred from the plateau modulus of the rheological frequency sweep data in Chapter 5 (see Figure 5.10 (b)), is achieved. Interestingly, an increase in temperature reduces the network's elasticity. The increased thermal energy seems to slightly promote the formation of inelastic structures such as loops or dangling ends. Nonetheless, as evident from Figures 7.1 (a) and (b) the effect of thermal energy is rather small and it is therefore safe to assume that the loop-to-bridge ratio of the micellar network at a certain concentration does not change significantly with temperature. Contrary and as already discussed in Chapter 6, temperature has a significant influence on the frequency-dependent rheological behavior through a shift in relaxation dynamics. The temperature dependence of the single relaxation time τ obtained from stretched exponential fits, can be investigated in a plot of $\ln(\tau)$ versus $1/T$ in Figure 7.3 and shows a linear dependence that can be fitted with an Arrhenius-like dependency (see Equation 6.3 in Chapter 6). Unlike thermally activated processes, the apparent activation energy is negative $E_{a,relax} = -415$ kJ/mol and indicates that the sticky interactions, i.e. the hydrophobic clustering, slows down the relaxation at more elevated temperatures. As compared to the activation energy of the network relaxation time τ_N as determined in Chapter 6, the absolute value obtained from a single indicator of the relaxation dynamics as considered here, is higher ($E_{a,\tau_N} = -363$ kJ/mol for 92 g/L EG412 in Figure 6.4 (b)). As previously discussed in Chapter 6, linking the activation energy for relaxation to the thermodynamic quantities of micellization is not straightforward since the dissociation of one hydrophobic block from a micellar core is not one-to-one correlated to the energetic contributions of the entire and gradual micellization process in which multiple copolymers cluster together. Moreover, for multiblock copolymers with multiple elastic bridges per chain, the contribution of

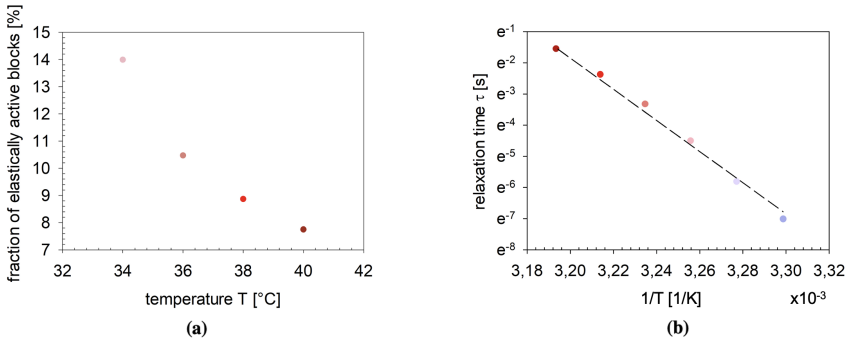

Figure 7.3: (a) Fraction of elastically active PEO blocks versus temperature as calculated from the plateau modulus obtained from fitting the stress relaxation data of a 92 g/L EG412 network with a stretched exponential. (b) Arrhenius plot of $\ln(\tau)$ versus 1/T as obtained from fitting the stress relaxation data of a 92 g/L EG412 network with a stretched exponential. The dashed line represents the linear Arrhenius-like fit.

the pure polymer flow is not easily accounted for due to the step-wise sticky Rouse-like relaxation pattern. Therefore, we will here use the single relaxation time and its temperature dependence mainly for comparison with the properties of the double network.

7.1.2 Selection of metal-ligand network

It is well-known that the (rheological) properties of networks formed by coordination complexes strongly depend on the type of metal ion [101, 329, 330]. The interaction strength is linked to the stability of the complex. For divalent first-row transition metals in aqueous solutions, this stability can be tuned according to the Irving-Williams series, which predicts Mn(II) < Fe(II) < Co(II) < Ni(II) < Cu(II) > Zn(II) [98]. Other influencing factors are the temperature [99], pH [100], the solvent [101] and the presence of competing counterions [102]. Hence, networks formed by metal-ligand complexation are highly tunable and represent ideal candidates to be used in double network structures. A selection of the divalent transition metal ion for the bifunctional crosslinking of the 4-arm telechelic terpyridine-functionalized PEO stars (tpy-PEO) in this study is made by ensuring enough difference in relaxation time as compared to the network formed by PEO-PPO multiblock copolymers. As the latter show rather slow relaxation dynamics at elevated temperatures, we opt for the use of metal ions resulting in weakly crosslinked and more ductile networks that relax relatively fast such as Mn(II), Fe(II) or Zn(II). Since some authors have pointed out that Fe ions are prone to the formation of precipitating ferric hydroxides ($Fe(OH)_2$) [195], Fe(II) is not further considered as a potential candidate for the construction of metal-ligand networks. Rossow *et al.* compared Mn(II), Zn(II) and Co(II) as crosslinkers for aqueous solutions of four-arm PEO star polymers with an arm length of 2.5 kDa and telechelic terpyridine functionalization. They found that Mn(II) was not effective as a crosslinker, whereas Zn(II) and Co(II) significantly decelerated the relaxation as compared to the uncrosslinked polymer solution [101, 198]. For hydrogels crosslinked by the stronger Co(II)-tpy complexes, the relaxation time was shifted by more than five decades and fell outside of the rheologically detected frequency domain. For Zn(II)-tpy networks, on the other hand, a viscoelastic response with a clear relaxation at intermediate frequencies was obtained (see also Figure 2.13 in Chapter 2). Rossow *et al.* also microstructurally investigated their hydrogels by static light scattering, and found significant heterogeneity in networks with Co(II) ions, whereas networks crosslinked with Zn(II) ions showed a homogeneous topology [198]. Therefore, they concluded that their metallosupramolecular hydrogels based on tetra-PEO stars of 10 kDa, combined with Zn(II) ions had a potential model-network structure. This network homogeneity combined with the fact that the relaxation of Zn(II)-tpy networks occurs in an ideal dynamic timescale, naturally brings our attention to Zn(II) as the ideal candidate for metal-ligand (ML) complexation in DN structures.

Importantly, for the 4-arm PEO stars to be able to form a network through terpyridine bis-complexes with Zn(II) metal ions, the telechelic terpyridine moieties should be able to find each other. Hence, similar to the hydrophobically associating networks, there exists a certain 'critical network concentration' ($c_{network}$) for the metal-ligand network. Due to the fact that the 'stickers' in such networks are telechelically present on each PEO arm, $c_{network}$ can simply be approximated as the overlap concentration c^* of the stars

$$c^* = \frac{M_w}{(4\pi/3) \cdot R_g^3 \cdot N_{Av}}. \tag{7.2}$$

As an approximation of the radius of gyration R_g of their PEO stars in water, Rossow *et al.* calculated R_g based on their experimentally obtained hydrodynamic radius R_H of 2 nm (obtained by DLS) using the correlation between R_g and R_H for uniform star polymers in a good solvent ($R_g = 1.58R_H$). They obtained a c^* of 133 g/L [198]. Our commercially obtained 4-arm PEO stars have longer arms of 10.4 kDa (total M_w of 41.5 kDa) instead of 2.5 kDa and therefore c^* will be lower. By adopting a simple scaling relation for monodisperse star polymers predicting that $R_g \sim M_w^v$ in good solvents ($v = 0.588$) [331] and using the R_g value obtained by Rossow *et al.*, an overlap concentration of 45 g/L is estimated for our PEO-stars. This overlap concentration abstracts the presence of the rather bulky telechelic terpyridine units and therefore, represents an overestimation of the true overlap concentration. Due to the very limited sample amounts, a first trial for the formation of the Zn(II) metal-ligand network is made with only 40 g/L. Just as for the HC network, the many defects present in the single ML network close to the overlap concentration might be converted to effective elastic bridges in the double network structure due to the topological constraints of the HC network [261]. Moreover, at such a low concentration the absence of entanglements between polymer arms can also be guaranteed.

Figure 7.4 (a) and 7.4 (b) show the linear rheological frequency sweep and stress relaxation results at different temperatures, respectively, of a reference metal-ligand network of 40 g/L tpy-PEO star solution crosslinked by a 1:2 [Zn(II)]:[tpy] ratio. A clear viscoelastic network with an elastic plateau at high frequencies (short times) and terminal flow at low frequencies (long times) is obtained in which an increase in the temperature leads to an acceleration of the relaxation. This rheological fingerprint thus proves that a concentration of 40 g/L, below but very close to c^* is sufficient for the formation of a ML network. In this regard, it is important to mention that Rossow *et al.* also observed viscoelastic networks at 100 g/L below the c^* of 133 g/L for their 10 kDa stars and attribute this to the existence of transient nanogel clusters. In our case, however, a concentration of 40 g/L is certainly closer to the calculated overlap concentration of 45 g/L and we therefore believe it is safe to assume almost complete percolation and more homogeneity in our ML networks.

Unsurprisingly, the rheological frequency-dependent behavior of these telechelic ML networks can be captured with the Maxwell model (see Equations 2.3 and 2.4 in

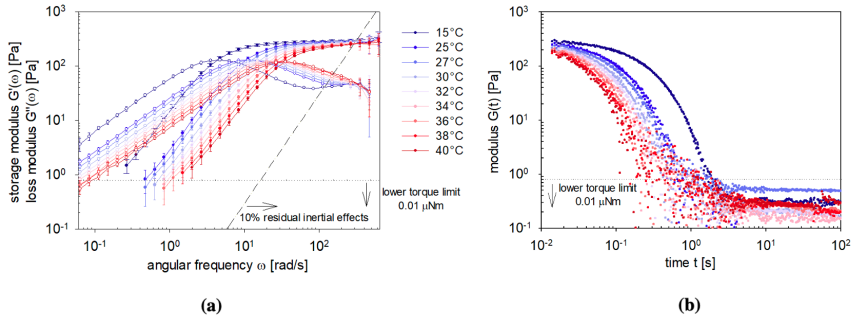

Figure 7.4: Linear rheological response of a 40 g/L 4-arm tpy-PEO star network crosslinked by 1:2 [Zn(II)]:[tpy] ratio at different temperatures: (a) dynamic moduli G' (filled symbol) and G'' (open symbol) as function of angular frequency at 0.1% strain, (b) shear modulus G as function of time upon application of 1% strain. Modulus contribution from 10% residual inertial effects in oscillatory measurements and the rheometer's lower torque limit are also indicated.

Chapter 2) or its equivalent for a stress relaxation experiment, i.e. a simple exponential decay

$$G(t) = G_0 \exp(-t/\tau). \tag{7.3}$$

Figure 7.5 shows the good agreement between the Maxwell model fitting and the rheological data of an oscillatory frequency sweep experiment (a) and a stress relaxation experiment (b) of the 40 g/L tpy-PEO networks crosslinked by Zn(II) at 15°C. Similar to the HC network, the plateau modulus of the ML network is an indication of the network's elasticity and can be converted to a fraction of elastically active arms by adopting the simple affine network theory (see Equation 5.12 in Chapter 5).

Figure 7.6 (a) displays the obtained fractions from both the frequency sweep Maxwell model fit as well as the stress relaxation single exponential decay fits at different temperatures and proves the good agreement between the two fitting methods. At the highest temperatures (above 36°C), however, the fast dynamics of the more labile networks make the stress relaxation experiments more scattered, resulting in a larger discrepancy between both methods. Since we are probing the network slightly below its critical network concentration, many loop defects are present resulting in an extremely low fraction of elastically active chains of about 2-3 %. Note that this low elastically active fraction can not be attributed to insufficient telechelic terpyridine functionalization, as both ^{1}H-NMR and UV-VIS have independently shown 94-95% of functionalization (see Chapter 3). Similar to the HC network, the decreasing trend with increasing temperature is a result of thermal mobility and the possible slight favoring of loops and/or dangling chains over bridges at elevated temperatures.

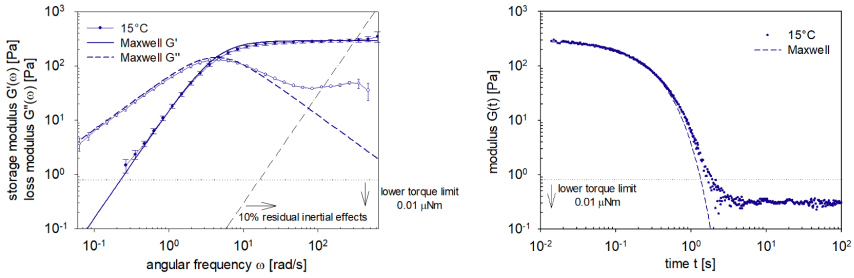

Figure 7.5: Maxwell model fitting of the linear rheological response of a 40 g/L 4-arm tpy-PEO star network crosslinked by a 1:2 [Zn(II)]:[tpy] ratio at 15°C: (a) dynamic moduli G' (filled symbol) and G'' (open symbol) as function of angular frequency at 0.1% strain. Full line is the G' fit, dashed line is the G'' fit. (b) Shear modulus G as a function of time upon application of 1% strain. Dashed line represents a single exponential decay fit.

As shown by the Arrhenius fit (see Equation 6.3) of the relaxation time as obtained from the Maxwell model fits, versus inverse temperature in Figure 7.6 (b), the activation energy for rheological relaxation of the ML network is positive as expected for conventional thermally activated processes. From the fitting of the frequency sweep data, an activation energy of 63 kJ/mol is obtained, whereas fitting of the stress relaxation data results in a slightly lower activation energy of 58 kJ/mol. Both values are significantly lower than the value of 415 kJ/mol obtained for 92 g/L HC networks, thereby indicating the more labile character of the ML bond as compared to the hydrophobic cluster in the HC micellar networks. It is important to note that the activation energy for relaxation $E_{a,relax}$ does not only contain a contribution from the dissociation of the Zn(II)-tpy complexes ($E_{a,diss}$), but also reflects the activation energy for subsequent pure polymer relaxation and flow without crosslinks ($E_{a,flow}$). Rossow *et al.* approximated $E_{a,diss}$ as the heat of metal-ligand complex formation from isothermal titration calorimetry measurements at 25°C, and obtained a value of $\Delta H_{ass} = 50.5$ kJ/mol for Zn(II)-tpy bis-complexes [198]. As an approximation of $E_{a,flow}$ in the networks, they obtained $E_{a,relax,pol} = 12.6$ kJ/mol for the polymers without supramolecular linking (their relaxation time was not experimentally detected, but extrapolated from pure terminal behavior in rheological frequency sweeps). The good agreement between $\Delta H_{ass} + E_{a,relax,pol}$ and their value of $E_{a,relax} = 64.8$ kJ/mol in Zn(II)-tpy networks justified the simple additive operation [101]. Hence, $E_{a,flow}$ of our longer PEO stars of 41.5 kDa can be estimated to be on the order of 8-13 kJ/mol by assuming a similar $\Delta H_{ass} = 50.5$ kJ/mol for Zn(II)-tpy bis-complexes as Rossow *et al.* [198]. Note that this fairly simple approach is rationalized by the less complex structure of the ML network as compared to the HC network, since each star arm can

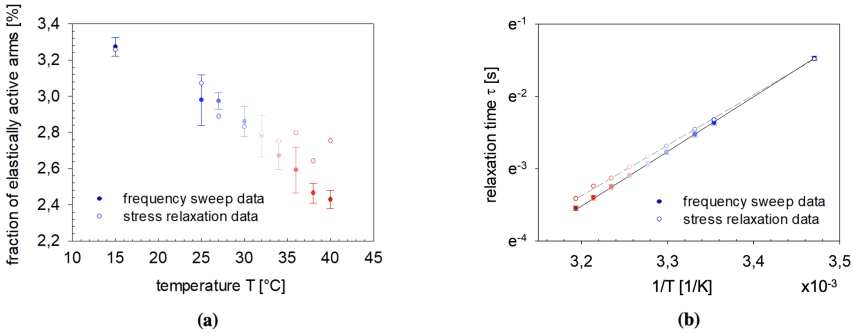

Figure 7.6: (a) Fraction of elastically active PEO arms versus temperature as calculated from the plateau modulus in either linear frequency sweeps or stress relaxations of a 40 g/L 4-arm tpy-PEO star network crosslinked by a 1:2 [Zn(II)]:[tpy] ratio. (b) Arrhenius plot of ln(τ) versus 1/T as obtained from fitting either the dynamic response or the stress relaxation data of a 40 g/L 4-arm tpy-PEO star network crosslinked by a 1:2 [Zn(II)]:[tpy] ratio with the Maxwell model. The lines in (b) represent the linear Arrhenius-like fits.

only form one elastic bridge with a telechelic, bifunctional ML crosslink.

7.1.3 Time-dependent network formation

The different dynamic behavior and contrasting temperature dependencies make HC and ML networks an interesting combination to be exploited in fully supramolecular DNs. Since the molecular weight of the PEO blocks in the HC network is 4.5 kDa and that of the PEO arms in the ML network is 10 kDa, the potential double network is anticipated to consist of a more sparsely and weakly crosslinked ML minority network of only 40 g/L and a more densely and strongly crosslinked HC majority network of 92 g/L. This is in contrast with the conventional picture of a double network, as originally discussed by Gong *et al.* [254], in which a sacrificial minority network of weak but densely crosslinked polymers is combined with a strongly but loosely crosslinked majority network.

Whereas the ML crosslinks rapidly form at room temperature, the PEO-PPO multiblock copolymers in aqueous solutions still behave as polymer solutions at low temperatures and only form micellar networks upon increasing the temperature (see also Figures 4.2 in Chapter 4). Hence, the buildup of a potential double network can be probed by a rheological temperature ramp. Figure 7.7 shows the evolution of G' and G'' (left y-axis) versus time for a combination of a 92 g/L HC network of PEO-PPO multiblock

copolymers with a 40 g/L tpy-PEO star solution crosslinked by a 1:2 [Zn(II)]:[tpy] ratio, as measured with a PP40 stainless steel geometry. On the right y-axis the temperature evolution versus time is shown. The first part of the curve is obtained during a temperature ramp from 15°C to 40°C and the second part during a time sweep at 40°C, both performed at 0.1% strain (in the linear regime) and 1 Hz frequency (see protocol in Figure 3.9 in Chapter 3). At 15°C the elastic modulus G' dominates over the viscous modulus G'' and indicates that the single ML network is already present. Its elastic modulus is slightly higher ($G' = 199$ Pa) than the one obtained at 15°C and 1 Hz for a single ML network ($G' = 174$ Pa, see Figure 7.5), which might be attributed to a possible enhancing effect of the uncrosslinked PEO-PPO multiblock copolymers on the formation of ML crosslinks by topological constraints [261]. The subsequent temperature ramp from 15°C to 40°C at a relatively low heating rate of 0.1°C/min clearly reveals the buildup of an additional elastic contribution upon increasing temperature, which can be attributed to the formation of the thermoreversible HC network. As compared to the buildup of a single HC network of 92 g/L (see Figure 3.8 in Chapter 3), the increase in G' and G'' happens around the same temperature of 20 °C in the DN and in the single network, thus showing little influence of the presence of the ML network on the initial formation of the HC network. Upon reaching 40°C, the increasing loss modulus G'' in the DN has exceeded the elastic modulus G'. This is in contrast to a single 92 g/L EG412 HC network, in which the elastic contribution dominates over the viscous contribution at elevated temperatures. However,

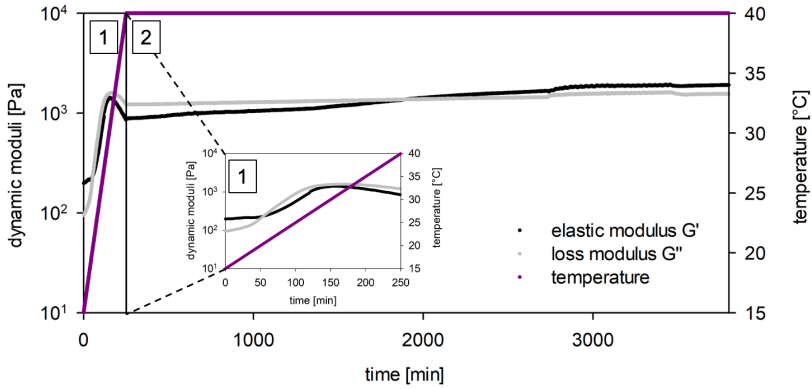

Figure 7.7: Linear dynamic moduli G' (black) and G'' (grey) (left y-axis) versus time at 1 Hz and 0.1% strain for a DN of 100 g/L PEO-PPO multiblock copolymers and 40 g/L tpy-PEO star solution crosslinked by a 1:2 [Zn(II)]:[tpy] ratio. The corresponding temperature evolution is shown in purple (right y-axis). Part 1 is obtained during an oscillatory temperature ramp from 15°C to 40°C at 0.1°C/min and part 2 during an oscillatory 60 hrs time sweep. A zoom of the temperature ramp is also shown in the inset.

the single networks, after being subjected to a 0.1°C/min heating ramp, immediately reach rheological steady state. For the DN structures, on the other hand, the dynamic moduli increase for very prolonged times until after approximately 60 hrs a steady state is obtained, as inferred from the second part of Figure 7.7. Hence, the formation of the hydrophobically associating micellar network in the DN structure takes substantially more time as compared to the single network and this is believed to be induced by the presence of the ML network as a spatial constraint. Fortunately, the dynamic nature of both networks allows for efficient redistribution and -formation such that the most energetically favorable and stable structure can eventually be attained. In this process, the slower dynamics of the HC network at 40°C seem to be the bottleneck. The resulting very long buildup time is a major drawback of this supramolecular DN, which might possibly be circumvented by allowing network buildup at slightly lower temperatures with faster HC dynamics. Nonetheless, the results in Figure 7.7 prove the successful formation of a thermoresponsive, elastic polymeric DN hydrogel formed by two different supramolecular crosslink interactions.

In Figure 7.8, the dynamic response of the steady state DN at 40°C is shown, together with the single network HC and ML networks of similar concentration. Based on the frequency dependency of the dynamic moduli, a pronounced dual dynamic behavior is present in the DN. At high frequencies, a first elastic plateau is probed with a plateau value approximately one decade above that of the single HC network. Its value is significantly larger ($G_{0,1} = 5.75$ kPa) than a mere addition of the plateau moduli of the single networks ($G_{0,sup} = 1.46$ kPa) and reflects a synergistic elasticity in the DN. At intermediate frequencies, a partial relaxation takes place, which seems to correspond well with the Maxwellian relaxation of the single ML network. At low

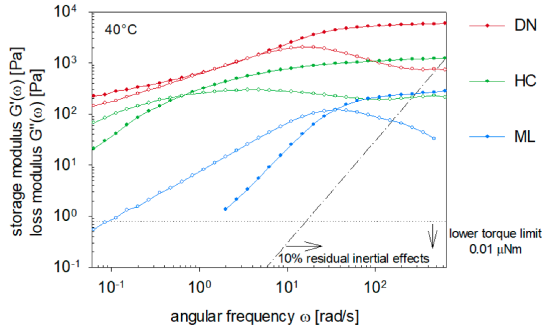

Figure 7.8: Linear dynamic moduli G' (filled symbol) and G'' (open symbol) versus angular frequency at 0.1% strain for a DN of 92 g/L PEO-PPO multiblock copolymers (HC network) and 40 g/L tpy-PEO star solution crosslinked by a 1:2 [Zn(II)]:[tpy] ratio (ML network) at 40°C. The corresponding single network responses are also shown.

frequencies, the dynamic response of the DN has not fully relaxed and appears to reach a secondary elastic plateau. This plateau is possibly due to the persistence of the HC network, despite the fact that the single HC network already reaches viscous flow at these frequencies. Figure 7.8 thus shows that our selection of zinc(II) as a suitable metal-ion has been successful for the development of DNs containing hydrophobically associating PEO-PPO multiblock copolymers and exhibiting a clear multi-dynamic and synergistic character. To fully pinpoint whether this two-step dynamic behavior indeed originates from the single network contributions, temperature can be used as an ideal external stimulus and the temperature dependency of both processes can be investigated.

7.2 Multiple dynamics and synergy

Since stress relaxation experiments enable to follow the relaxation behavior of materials over (much) longer time scales as compared to oscillatory frequency sweeps, it is relevant to study the DNs with such measurements as well. Figure 7.9 reveals the results of 1% step strain experiments on the DN at decreasing temperatures starting at 40°C. In between temperatures, the sample was cooled using a slow cooling rate of 0.1°C/min (see protocol in Figure 3.9). In contrast to the long buildup time of the DN during heating, the sample was found to be in a steady state at the intermediate temperatures during cooling. For the measurement at 40°C, the initial fingerprint of the stress relaxation curve upon increasing time is very similar to the G' response upon decreasing frequency in Figure 7.8. However, at prolonged times (up until 10 000 s) it

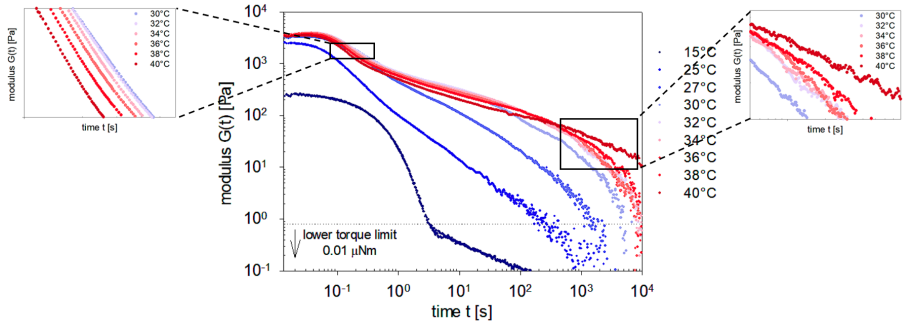

Figure 7.9: Shear modulus G as a function of time upon application of 1% strain on a DN of 92 g/L PEO-PPO multiblock copolymers and 40 g/L tpy-PEO star solution crosslinked by a 1:2 [Zn(II)]:[tpy] ratio at different decreasing temperatures. The insets are zooms of the temperature dependency of both the fast and the slow relaxation processes.

becomes evident that the DN will eventually relax. The network thus has a fast and a very slow relaxation process with the latter not accessible by rheological frequency sweeps. The presence of two clearly separated relaxation processes hints at the fact that each of these might be linked to one of the two network contributions in the DN structure. More convincingly, both relaxation processes have a different temperature dependence, as shown in the insets of Figure 7.9. The fast relaxation speeds up as a function of temperature, i.e. shifts to shorter time scales, while the slow relaxation process slows down. These opposite temperature trends, which were also observed in the ML and HC single networks (cfr. supra), make us more confidently conclude that the fast relaxation corresponds to the stress relaxation in the ML network and the slow relaxation indicates that also the HC network eventually relaxes in the DN structure.

To further unravel both relaxation processes, the stress relaxation response at different temperatures can be fitted with a single exponential Maxwellian decay at short time scales (with a relaxation time τ_1 and a total plateau modulus $G_{0,1}$), and a broad stretched exponential decay (with a relaxation time τ_2) at long time scales. Such fits allow us to extract a fast relaxation time τ_1 and a slow relaxation time τ_2 from the DN response. The latter is an indication of the DN longest relaxation time. Both fits are performed separately, since the gradual transition zone at intermediate timescales makes the fitting of a combined model considerably more difficult. The physical origin of the gradual response in this transition zone is not entirely clear, but might be linked to the complex 'intertwined' and possibly entangled nature of the polymer strands. Hence, upon dissociation of the Zn(II)-tpy complexes, the flow of the uncrosslinked PEO stars might be hindered by the presence of the unrelaxed HC network. In Figure 7.10,

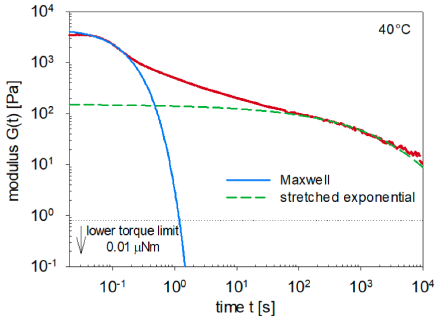

Figure 7.10: Shear modulus G as a function of time upon application of 1% strain on a DN of 92 g/L PEO-PPO multiblock copolymers and 40 g/L tpy-PEO star solution crosslinked by Zn(II) in a 1:2 [Zn(II)]:[tpy] ratio at 40°C. The fast relaxation is fitted with a Maxwellian single exponential decay (full blue line) and the slow relaxation is fitted with a stretched exponential decay (dashed green line).

the Maxwell model fit of the fast relaxation and the stretched exponential fit of the slow relaxation are displayed for the 92 g/L HC and 40 g/L ML DN at 40°C. The fact that the fast relaxation can be fully and correctly described by a Maxwellian response provides additional evidence that this is controlled by the stress relaxation in the ML network. Note that the stretched exponential fit indeed captures the longest relaxation time of the DNs, which is assumed to be fully governed by the HC network based on its temperature dependency, and leaves the intermediate modes of relaxation out of the fitting regions.

7.2.1 Synergistic elasticity

The plateau modulus of the fast relaxation process $G_{0,1}$ is a representation of the elasticity in the double network structure, determined by elastically active strands in both the ML and the HC network. As previously mentioned, its value is higher than the additive superposition of the plateau moduli of the single networks. Figure 7.11 displays the number density of elastically active chains in the DN (calculated according to Equation 5.12) as well as the calculated summation of the number densities of elastically active chains in the single networks as a function of temperature. In the DN structure, a 5-fold increase in the amount of elastic bridges per volume is observed as compared to the superposition of the single networks. Such impressive synergistic elasticity was also observed by other authors [259–261] and is often attributed to the presence of entanglements between the two networks, which are trapped by crosslinks,

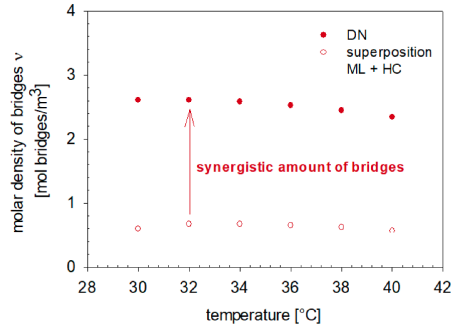

Figure 7.11: Number density of elastically active chains, as calculated from the plateau modulus $G_{0,1}$, versus temperature for a DN of 92 g/L PEO-PPO multiblock copolymers and 40 g/L tpy-PEO star solution crosslinked by a 1:2 [Zn(II)]:[tpy] ratio. The summation of the number density of elastically active chains in the separate single networks is also shown.

thereby creating additional elastic bridges. The contribution of these 'inter-network' entanglements to the DN elasticity is relaxed upon relaxation of one of the two networks. Moreover, as both Klymenko *et al.* [259] and Yang *et al.* [261] independently found that a DN or IPN structure promotes the formation of elastically active bridges over loops as compared to single HC or ML networks, such topological favoring mechanisms are probably mutually present in our DN structure as well. Especially for our single networks containing a large number of inelastic defects, we suspect that these effects are significantly reflected in the synergistic DN elasticity.

7.2.2 Relaxation delay

The fitting of the DN stress relaxations also facilitates the comparison of the relaxation times τ_1 and τ_2 with the relaxation times obtained in single ML and HC networks (see Figures 7.12 (a) and (b)). For both DN relaxation processes, it is evident that the DN structure imposes a delay on the relaxation dynamics of the contributing ML and HC networks, albeit to a different extent. The comparison between the fast relaxation time τ_1 and the ML single network relaxation time (both from Maxwell model fits) in Figure 7.12 (a) shows a limited delay of less than a decade. Interestingly, at the lowest temperatures of 15°C and 20°C, the difference between τ_1 and the single network τ is almost negligible, since at these temperatures, the multiblock copolymers do not yet form a hydrophobically crosslinked network (see also Figure 7.7). We can therefore confidently conclude that the relaxation delay is induced by the true DN structure, and not just by the presence of other polymer chains. The origin of this delayed relaxation might lie in the concept of the bond lifetime renormalization, as introduced by Rubinstein and Semenov in their sticky frameworks [206, 207, 209]. This renormalization takes into account that stickers may reassociate with the same 'partner' several times on very short time scales before they finally really dissociate and allow full chain relaxation. We hypothesize that in a DN structure, a stronger renormalization effect for the dissociation of Zn(II)-tpy bis-complexes is present as compared to that in the single ML network. In this regard, the presence of a second elastic network consisting of hydrophobic crosslinking nodes with a non-negligible size, imposes topological constraints that prevent a terpyridine sticker from exploring its environment and engaging in a ML bis-complex with a new partner. The sticker thus has no other choice but to re-engage with its old, close partner. The Arrhenius fit of the evolution of $\ln(\tau_1)$ versus 1/T at elevated temperatures above 30°C (see Equation 6.3) shows that the fast relaxation process is thermally activated, with an activation energy of 31 kJ/mol. The lower activation energy as compared to the single ML network (58 kJ/mol) is quite surprising. Possibly, the complex DN structure facilitates the dissociation of ML complexes, resulting in a shorter true bond life time. However, the DN structure also imposes much more frequent reassociations with the same partner,

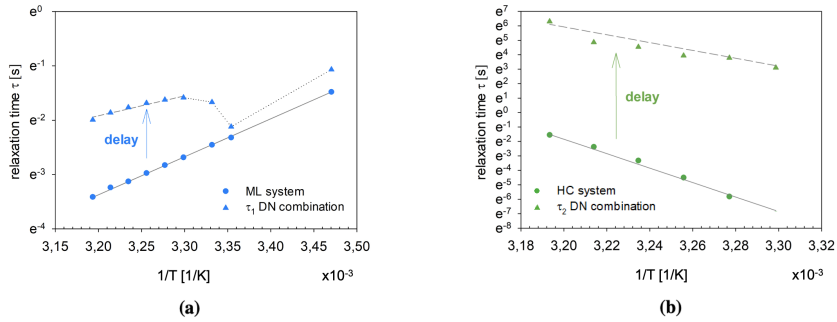

Figure 7.12: Arrhenius plot of ln(τ) versus 1/T as obtained in a DN of 92 g/L PEO-PPO multiblock copolymers and 40 g/L tpy-PEO star solution crosslinked by a 1:2 [Zn(II)]:[tpy] ratio, and its corresponding single networks: (a) DN fast relaxation time τ_1 and ML single network relaxation time and (b) DN slow relaxation time τ_2 and HC single network relaxation time. All relaxation times are extracted from stress relaxation fittings. The dashed lines are the linear Arrhenius fits in the DN, the full lines are the Arrhenius fits in the single networks.

as reflected in the renormalized bond lifetime, thereby still considerably increasing the absolute stress relaxation time τ_1 as compared to that of the single ML network.

The delay in the longest relaxation time τ_2 as compared to that of single HC networks spans over more than two decades, as inferred from Figure 7.12 (b). The linear evolution of ln(τ_2) versus 1/T in the Arrhenius-like plot indicates that the temperature dependence of the longest relaxation process in the DN structure is governed by a single mechanism. It slows down at elevated temperatures, as evidenced by the negative activation energy of -225 kJ/mol, and is thus most likely dominated by the dissociation of hydrophobic blocks from their micellar cores. The absolute value of the activation energy is again notably lower than that obtained for the single HC network relaxation (-415 kJ/mol), even though the absolute relaxation time is greatly increased. We suspect that the same mechanisms as for the ML relaxation could explain this. In the DN structure, a PPO block can more easily disengage from its micellar core as compared to a PPO block in a single HC network, which ensures a lower activation energy for the relaxation process. Nonetheless, a considerably stronger bond renormalization effect in the complex DN structure accounts for the large difference in absolute relaxation times between DN and single networks. We also speculate that these effects might be more pronounced in the HC network, due to the presence of non-telechelic stickers and hence multiple elastic bridges per polymer chain, as well as due to the multifunctionality of the hydrophobic crosslink interactions.

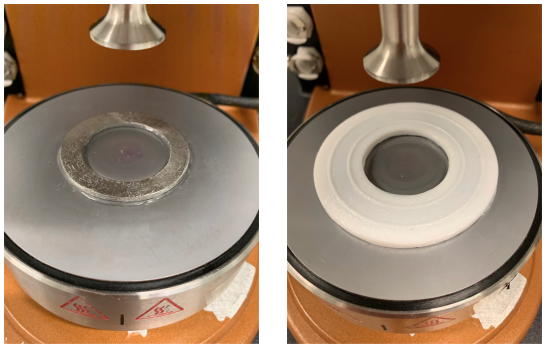

(a) (b)

Figure 7.13: Picture of the purple sample color obtained after long overnight measurements at elevated temperatures using PP20 stainless steel plates for samples containing 92 g/L PEO-PPO multiblock copolymers and 40 g/L uncrosslinked tpy-PEO star solution. The purple color was observed when using a metal ring (a), but also when using a Teflon ring (b).

7.3 Reproducibility issues

To gain more insights into the synergistic elasticity and delayed relaxation behavior in DNs, a systematic variation of the network concentrations might allow us to study whether characteristic scaling relations of the plateau moduli and/or relaxation times as a function of concentration could be established. Due to the limited amounts of tpy-functionalized PEO stars, the PP40 stainless steel geometry is replaced by a smaller PP20 stainless steel geometry. However, prolonged DN measurements at elevated temperatures on a PP20 stainless steel geometry result in a purple color of the final sample. In Figure 7.14, photographs of the DN sample (without Zn(II) ions) after an overnight measurement on stainless steel (SS) plates of 20 mm using both a metal (a) and a Teflon ring (b) to contain the peripheral oil layer around the sample, are shown. The evident purple color is assumed to be induced by a very small fraction of iron ion depositions, which can also form complexes with terpyridine in the ML network and thereby compete with zinc ions. This, in turn, could alter the rheological response. It is important to mention that this purple color was absent for the (shorter) measurement protocol on single ML networks using a SS PP40 geometry, nor did we clearly observe it during our first set of measurements on DNs using a SS PP40 geometry as well (discussed above). In this regard, it might be of relevance that the SS PP20 geometry was newly acquired and therefore possibly more prone to releasing small contaminants.

By comparing the results of the initial temperature ramp of a DN combining 92 g/L HC

network and 40 g/L ML network as measured on a SS PP40 geometry (transparant final sample - black/grey symbol color) with the results obtained on a SS PP20 geometry (purple final sample - dark and light purple symbol color) in Figure 7.14 (a), it is evident that with the PP20 geometry both G' and G'' increase more strongly. Moreover, the stress relaxation data obtained after subsequent 60 hrs waiting at 40°C, as shown in Figure 7.14 (b), reveal rather different relaxation dynamics. Whether this large rheological discrepancy is solely related to the possible presence of stronger iron(II)-tpy bis-complexes in the purple sample (PP20), can be checked by eliminating possible iron impurities and their ensuing complexes using a custom-made glass plate-plate geometry. Two independent measurements performed using a glass PP20 geometry and a glass bottom plate and hence no purple color, are also shown in Figures 7.14 (a) and (b). Surprisingly, these measurements also exhibit an unacceptably large rheological discrepancy. Hence, the large variability between the measurements on stainless steel geometries is not exclusively caused by metal impurities. After being subjected to the exact same sample preparation protocol and being manually loaded onto the rheometer in the same way, the moduli at 15°C in Figure 7.14 (a) are significantly different in all cases and indicate that a large variability in the initial state of the sample is already present. Even after long waiting times at 40°C, during which the dynamic character of the sample might induce some homogenization, the stress relaxations in Figure 7.14 (b) show that the large differences between the rheological behavior of the samples persist. Since the samples were given the same macroscopic history (to the best of our ability), we hypothesize that the origin of this large variability must lie in the complex microstructure of the DN sample. In this regard, Katashima *et al.* pointed out in a recent

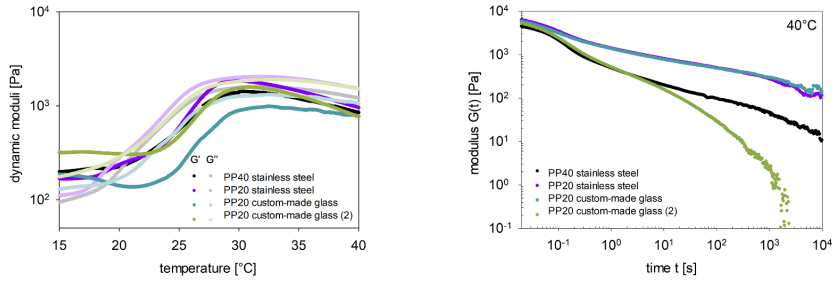

Figure 7.14: Linear rheological measurements on a DN of 100 g/L PEO-PPO multiblock copolymers and 40 g/L tpy-PEO star solution crosslinked by a 1:2 [Zn(II)]:[tpy] ratio, using different plate-plate geometries: (a) linear dynamic moduli G' and G'' versus temperature during an oscillatory temperature ramp from 15°C to 40°C at 0.1°C/min, 1 Hz and 0.1% strain and (b) shear modulus G as a function of time upon application of 1% strain after prolonged waiting times at 40°C.

review paper that unexpected structures such as spatial and connective heterogeneities are inevitable in polymer networks and the detection and precise control thereof is almost impossible [332]. The combination of two polymer networks might promote heterogeneities and thereby further complicate the characterization and controlled development of polymeric DNs. In our DNs, relatively simple and model-like ML networks [198] are combined with considerably complex single networks formed by PEO-PPO multiblock copolymers. It is therefore the latter that, in our view, have the largest contribution to this variability. The stress relaxation experiments in Figure 7.14 (b) indeed show that mainly the slowest relaxation process, linked to the HC networks, induces unacceptable reproducibility issues. Finally, to end on a positive note, we would like to emphasize that, despite the great variability, the interesting and promising features of our DNs combining hydrophobic association and metal-ligand complexation still remain present in all cases.

7.4 Conclusions

In this chapter, we present a synergistic double network (DN) hydrogel that combines thermoreversible hydrophobically clustering (HC) PEO-PPO multiblock copolymers with 4-arm PEO stars crosslinked by telechelic zinc(II)-terpyridine metal-ligand (ML) complexes. The viscoelastic nature of both networks allows us to study both the elastic behavior and the complete relaxation dynamics of the DN using linear shear rheology. The single ML networks show ideal Maxwellian rheological behavior whose stress relaxation response could be described by a single exponential decay. This is in contrast to the very broad relaxation behavior of HC networks captured by a stretched exponential decay. Even more contrasting are the temperature-dependent relaxation dynamics of both networks as dominated by the dissociation of their crosslinks. While the dissociation of ML complexes is thermally activated and thus faster at elevated temperatures, the clustering of hydrophobic blocks further reinforces at elevated temperature leading to slower stress relaxation. Both networks are examined close to their critical concentration for network formation, resulting in a very significant fraction of loop defects in their network structures.

Owing to the thermo-responsiveness of the HC network, temperature is used as an external stimulus to probe the effective buildup of the HC network in the DN structure. However, reaching a steady state DN at high temperature takes a considerable amount of time, for which we consider the slow dynamics of the HC network as the bottleneck. Nonetheless, the final rheological fingerprint of the steady state DN reveals the desired behavior of a synergistic elastic network with a clear two-step dynamic process. The reason behind the synergistic elasticity is twofold: firstly, the topological constraints imposed by the presence of a second network might have favored the formation of elastic bridges over inelastic loop defects and secondly, the in-situ formation of the

DN structure might have caused inter-network, trapped entanglements. Interestingly, the opposite temperature dependence of both relaxation processes, combined with the fact that both processes could be described by either a single or a stretched exponential decay, provide evidence that the faster relaxation of the DN structure could be attributed to the ML network dissociation, whereas the slow relaxation could be associated with the HC network. In addition, both network stress relaxations are significantly decelerated in the DN as compared to that of the single networks. We hypothesize that this delay is induced by an enhanced renormalization effect for effective dissociation of an ML or HC sticker, i.e. the stickers possibly reassociate more frequently with their old partner due to more spatial constraints in the DN as compared to their single networks.

Despite these very promising features of the DNs combining hydrophobic association and metal-ligand complexation, a systematic investigation reveals unacceptably large variability in the rheological response, especially regarding the slowest HC relaxation process. We speculate this irreproducibility finds its origin in the complex microstructure of the HC network, constructed through large hydrophobic crosslinking nodes of multisticker polymer chains. We therefore hope that our preliminary work can provide inspiration for further research into such DNs.

Chapter 8

Conclusions and outlook

8.1 Conclusions

During the last few decades, scientists have been exploiting non-covalent interactions in synthetic polymer systems for the creation of materials with unique self-assembled microstructures. In particular for pharmaceutical applications, the spontaneous and entropy-driven self-assembly of amphiphilic molecules in selective solvents has been considered a valuable tool. In dilute solutions, the presence of hydrophobic 'pockets' makes these structures promising microcarriers for poorly soluble drugs and other therapeutic agents and aids targeted delivery. At higher concentrations, elastic gel phases are often formed in which the hydrophobic, microphase-separated zones for efficient encapsulation persist, thereby promoting these materials as multifunctional biomatrices in tissue engineering applications. In this regard, the often stimuli-responsiveness of the hydrophobic association proves to be of great value in guaranteeing efficient formation and degradation of the structures, and release of possible cargo.

In the quest for hydrophobically associating polymers suitable for biomedical applications, block copolymers comprising of poly(ethylene oxide) (PEO) and poly(propylene oxide) (PPO) are widely researched due to their excellent biocompatibility and thermoreversible micellization. The latter allows the self-assembly and ensuing network formation to occur at elevated temperatures around human body temperature. Whereas there is extensive literature on PEO-PPO-PEO triblock copolymer model systems (commercially available as Pluronics®), both in terms of fundamental insights and applications, various other copolymer architectures are currently underreported. Nonetheless, Pluronic solutions and hydrogels face issues such as low viscosity increase,

poor stability, short residence times and high permeability, which could potentially be addressed by using longer PEO-PPO multiblock copolymers having more than one hydrophobic PPO block. However, for such systems to be an attractive alternative to Pluronics®, a fundamental understanding of their behavior, microstructure and ensuing rheological properties as function of concentration and temperature is crucial, which is the ultimate aim of part I of this dissertation. Hereto, two grades of commercially available alternating PEO-PPO block copolymers with 4 repeating PEO-PPO units of different PEO and PPO block lengths (ExpertGel®), were studied.

Chapter 4 focuses on the phase behavior, the energetic driving forces and the micellar microstructure by using a combination of techniques, including rheometry, scanning and titration calorimetry, light and X-ray scattering and light transmittance. Analogous to other PEO-PPO based copolymers, the phase boundaries are governed by hydrophobicity. However, the copolymer architecture, i.e. the amount of PPO blocks in one copolymer chain, and the molecular weight also play a vital role in the location of the phase boundaries, the thermodynamic driving forces and the micellar sizes. **As compared to Pluronic® triblock copolymers with similar hydrophobicity, the longer multiblock copolymers with more than one hydrophobic PPO block per chain revealed lower phase boundaries in terms of temperature and concentration, stronger energetic contributions and larger spherical micellar sizes.** By using the different characterization techniques, solutions of unimers, micellar solutions, micellar networks (or 'gels') and macroscopically phase-separated phases can be distinguished as a function of temperature and concentration. The single-molecule micellar aggregates as detected by other authors below the CMT for longer PEO-PPO alternating multiblock copolymers with 6 to 10 repeating units and similar hydrophobicity [79] are not observed in our systems. This causes more drastic morphological changes and greater energetic contributions upon micellization of medium-length multiblock copolymers as compared to longer multiblocks. Rheological investigation of more concentrated solutions reveals a significantly different network formation principle as compared to PEO-PPO-PEO triblock copolymers. **Whereas Pluronic® micelles jam into lyotropic liquid crystalline phases with the rheological fingerprint of an elastic colloidal glass, multiblock copolymers assemble into viscoelastic, transient networks by forming PEO polymer bridges between hydrophobic micellar PPO nodes.**

In Chapter 5, we correlate the macroscopic elasticity of these transient networks with their microscopic network topology using a mechano-statistical transient network model. Such a model has previously been developed for unentangled telechelic triblock copolymers bearing their hydrophobic stickers as end groups [147,148], but the increased molecular complexity of multiblock copolymers having more than one PPO 'sticker' per chain, mandates a novel approach. **Combinatorics allow us to develop a generalized mechano-statistical network model which considers the different configurational possibilities of inelastic loop and elastic bridge formation within**

one multisticker polymer chain. By assigning statistical probabilities to the formation of loops and bridges, an average node functionality is constructed, around which a binomial distribution is assumed. This functionality distribution facilitates the elimination of uni- and bifunctional nodes, contributing to inelastic dangling ends or superstructures (superloops and -bridges), respectively, in the determination of effective elastic bridges. **The link with the microstructure is established by assuming the probability for loop formation to be inversely proportional to the amount of nearby micellar nodes (n_m) whose distance can be overcome by a soluble PEO block in its equilibrium configuration.** This n_m is experimentally determined from small-angle X-ray measurements by converting the hard sphere structure factor to the radial distribution function, and spherically integrating the radial distribution function up to a length scale on the order of the radius of gyration of a PEO block. By a priori knowledge of the multiblock copolymer architecture, i.e. the amount of hydrophobic blocks as well as the PEO block length, the model enables the translation from microstructural parameters such as n_m or the micellar aggregation number, to statistical changes in the chain configurations and eventually to network elasticity. The model predictions show good agreement with elasticity data as probed by linear shear rheology, and provide a microscopic explanation for the concentration-dependent rheological properties of transient networks. **Above the critical network concentration, the network evolves from a poorly elastic and sparse distribution of loop-dominated micellar crosslinking nodes with inelastic superstructures and dangling ends, to a denser distribution of bridge-dominated micellar crosslinking nodes with high functionality and an enhanced elasticity upon increasing concentration.**

Chapter 6, the last chapter of part I, examines the relaxation dynamics of the transient networks formed by multiblock copolymers at various elevated temperatures and concentrations. **The linear rheological fingerprints reveal sticky Rouse-like relaxation dynamics, which require stepwise dissociation of all stickers along the multisticker polymer chain and result in a much broader relaxation as compared to that of networks with telechelic stickers.** Two characteristic relaxation times are distinguished, i.e. the sticker dissociation time τ_S determined as the crossover between the elastic plateau and the sticky Rouse regime, and the longest network relaxation time τ_N determined as the crossover between the sticky Rouse regime and the terminal flow behavior. The Arrhenius-like temperature dependencies of both relaxation times indicate that the dynamic origin of the networks lies in the dissociation of hydrophobic blocks from their micellar cores. **Since the stronger power law concentration dependence of τ_S as compared to that of τ_N cannot be predicted with any of the existing transient network relaxation frameworks, we employ a hybrid model that also accounts for intrinsic chain dynamics.** Such hybrid relaxation model combines concepts from our previously developed mechano-statistical transient network model, the sticky Rouse model and the Cates model for 'living' polymers. **It does succeed in explaining the distinct concentration dependencies of τ_S and τ_N by considering very slow chain dynamics, but requires**

further (microscopic) verification of the latter.

In part II of this dissertation, the complexity is further increased by combining networks of hydrophobically associating multiblock copolymers with a second supramolecular network in an interpenetrating or double network structure. Smart design of such fully supramolecular double networks can induce distinct dynamic modes with complementing features, thereby promoting synergistic final properties. Owing to the wide tunability of their interaction strength and related dynamic timescales, metal-ligand complexes are ideal candidates to be exploited as reversible crosslinks in supramolecular double networks. In Chapter 7, networks of 4-arm PEO stars functionalized with telechelic terpyridine and crosslinked by zinc(II)-terpyridine biscomplexes are introduced due to their rather labile dynamics, simple Maxwellian response and model network structure. **In combination with a metal-ligand network, the thermoresponsive nature of the multiblock copolymers allows temperature to be used as an external stimulus for the formation of a double network. In addition, the opposite temperature dependence of the dynamics in both networks makes temperature an ideal variable to pinpoint the separate network contributions.** The rheological fingerprint of the double network reveals a thermally activated, Maxwellian relaxation at short time scales and a broad relaxation which slows down as a function of temperature at (very) long time scales, governed by the dissociation of metal-ligand complexes and hydrophobic clusters, respectively. **Compared to the single network responses, a synergistic elasticity is obtained and both processes in the two-step relaxation of double networks are significantly delayed.** An explanation can be found in the topological constraints imposed by the presence of a second network. Such constraints may favor the formation of elastic bridges over inelastic loops in the separate networks as well as the in-situ creation of inter-network entanglements, both increasing the elasticity. Moreover, they cause crosslinks to frequently reassociate with their old partner, thereby delaying stress relaxation. **Despite the promising features of double networks, the rheological reproducibility is poor and assumed to be governed by the microstructural complexity of the hydrophobically associating network formed by multiblock copolymers.**

This dissertation has attempted to provide a comprehensive overview of the behavior of PEO-PPO alternating multiblock copolymers in aqueous media with increasing complexity: from dilute solutions to concentrated networks and finally in complex double network structures. Throughout, the relationships between the building block architecture, the formed microstructure and the final rheological properties were highlighted. We hope that we have demonstrated the broad tunability and great potential of hydrophobically associating multiblock copolymers, and that with our work we can contribute to further progress in the rational design of such promising systems. Naturally, this also encourages us to critically provide our future perspectives.

8.2 Outlook

Whereas our study examines two grades of commercially available PEO-PPO multiblock copolymers, lab-scale chemical synthesis of such systems would allow greater control over important molecular parameters such as the PEO and PPO block lengths and the amount and configuration of these blocks in an alternating or random sequence, as well as to reduce the dispersity and presence of impurities as observed in commercial systems. As such, more systematic studies can elucidate the importance of the overall hydrophobicity, the amount of repeating blocks and the total molecular weight on the micellization temperatures, thermodynamic driving forces and ensuing self-assembled morphologies as discussed in Chapter 4. Moreover, by varying important molecular design parameters (a, $M_{w,PEO\ block}$) and the resulting structural characteristics (N_{agg}, n_m), the final rheological properties of micellar transient networks formed by multiblocks as discussed in Chapters 5 and 6, can be tuned. For the chemical synthesis of such PEO-PPO multiblocks, inspiration can be drawn from the works of Cohn *et al.* [80, 83–85], Wang *et al.* [86, 87], Sun *et al.* [78], and Horiuchi and Rikiyama *et al.* [79, 88, 89] in which different binding moieties between the PPO and PEO block, such as phosgene and diisocyanates, were exploited.

In Chapter 5, the commercial alternating PEO-PPO multiblock copolymers were used for the experimental verification of a novel and generalized mechano-statistical transient network model predicting the elasticity of networks formed by large micellar crosslinking nodes of multisticker polymer chains. Further experimental verification of this model is recommended, both for more well-defined and carefully synthesized hydrophobically associating multiblock copolymer systems with varying molecular design, as well as for other equally spaced, multisticker associating polymers that form networks through large scale multifunctional interactions other than micellar assembly [104]. Despite our effort to account for non-trivial network structures such as superloops and -bridges, as well as dangling end network nodes, our model can be further refined by considering network entanglements between loops and/or bridges, as possibly induced by the drastic morphological changes upon micellization. Nonetheless, a theoretical framework for such entanglements is currently unreported in literature and offers opportunities for further research. Such ‘entanglements’ act as additional physical junctions and reduce the mesh size of the micellar network to length scales smaller than that of a PEO bridge. Therefore, they might experimentally be revealed by studying the rheological response of the networks upon addition of a small fraction of short, unentangled PEO chains of similar lengths as the PEO bridges. These chains are trapped if the mesh size is smaller than their size, resulting in a contribution to the network elasticity as well as a delay in their relaxation dynamics [333]. More insights into the mesh size of the network can also be obtained by dynamic light scattering using the partial heterodyne method [333, 334]. Such approach has been successfully adopted for networks with point-like associations of negligible size [101, 335], but also

for bulky micellar cores as crosslink interactions [336]. In addition, further extension of the model using the information present in the molecular weight distribution (see Section 3.1.1 in Chapter 3) could potentially result in a more accurate description of the network properties. In this regard, a decomposition of the molecular weight distribution into fractions with different amounts of PPO blocks allows these fractions to be considered separately in the mechano-statistical network model rather than being captured in an average a value. The fraction with one PPO block, whether present in a diblock PEO-PPO or triblock PEO-PPO-PEO configuration, should be eliminated as it does not contribute to the network properties. Finally, it is important to mention that the dispersity in the molecular weight distribution is caused not only by a distribution in the number of blocks, but also by a distribution in the block lengths themselves. The latter affects the radius of gyration of the capped PEO block, an important model parameter for the determination of n_m that must also be taken into account. A true dissection of the molecular weight distribution without a priori assumptions is thus not straightforward, and fractionation of the ExpertGel samples combined with ^{1}H-NMR analysis of the separate fractions possibly results in more accurate information. Also in this respect, the use of synthesized and hence more controlled multiblock copolymers instead of commercial systems, is recommended.

Chapter 6 sheds light on the transient and sticky Rouse-like dynamics of networks formed by PEO-PPO multiblock copolymers by using linear shear rheology. Even though conventional transient network models usually focus on predicting the rheologically detected relaxation time(s), we do recognize the need for other experimental techniques to probe the dynamics in such systems. In dynamic light scattering, the partial heterodyne approach accounting for the network's non-ergodicity has been adopted by other authors to unravel distinct diffusional dynamics [334, 337]. Another valuable tool relies on probing the diffusion of fluorescently labeled tracer polymer throughout the network by optical techniques such as forced Rayleigh scattering [337–340] and temporally and spatially resolved fluorescence recovery after photobleaching [101, 238, 341]. Hereto, nitrobenzofurazan fluorophores can telechelically be incorporated in PEO-based polymers by post-functionalization [337, 340]. Importantly, not only PEO-PPO multiblock copolymers are relevant tracer molecules, but also plain 'uncrosslinked' PEO chains of equal molecular weight as the entire chain may be insightful for an indication of τ_{chain}.

An open question thereafter remains the relation between the (network) dynamics as probed by rheology or other dynamic techniques (probing timescales from milliseconds onwards) with the micellar dissociation kinetics. It is well-known that there are two relaxation processes involved in micellar solutions: a fast relaxation on the order of microseconds corresponding to the exchange of a molecule from a micellar core to its surrounding bulk, and a slower relaxation process on the order of milliseconds (or longer) associated with complete dissolution of the micelle. The former gives an indication of the residence time of a molecule in the micelle, whereas the latter

is a representation of the lifetime or stability of the entire micelle. Both time scales are accessible in dilute solution by experimental techniques such as stopped-flow, temperature-jump or pressure-jump techniques, and ultrasonic absorption [342]. However, such studies usually focus on 'simple' molecules with only one hydrophobic block in which the dissociation of one block implies the dissociation of an entire molecule from its micellar core, whereas experimental studies on the kinetics of multiblock copolymers with multiple hydrophobic blocks per chain remain elusive in current literature. Therefore, an interesting follow-up fundamental study on multiblock copolymers in aqueous solutions could be an experimental assessment of the micellar kinetics at various temperatures and concentrations. Potentially, three different dynamic processes can be discerned: the exchange of a single hydrophobic block from micelle to bulk, the exchange of a multiblock copolymer with multiple hydrophobic blocks from micelle to bulk and the full dissociation of a micelle. The comparison with the timescales obtained from rheology or other dynamic techniques, and their temperature and concentration dependencies might reveal relevant insights. In this regard, the temperature dependence of the micellar relaxation times possibly allows the determination of activation energies, which in turn could be compared with the thermodynamic quantities of micellization as inferred from calorimetric techniques on dilute solutions (see Chapter 4), as well as with the activation energies as determined from rheology on concentrated solutions (see Chapter 6).

The peculiar thermal behavior of PEO-PPO block copolymers was exploited in proof-of-concept thermoresponsive double networks combining hydrophobic association and metal-ligand complexation in Chapter 7. Unfortunately, the structural complexity of the networks formed by the PEO-PPO multiblock copolymers resulted in poor rheological reproducibility of such double networks. Hence, for fundamental insights into the synergistic behavior and relaxation dynamics in double networks combining thermoreversible hydrophobic association with metal-ligand complexation, we suggest to start from more simple single network designs. As the network formed by 4-arm PEO stars crosslinked by telechelic terpyridine-zinc(II) complexes exhibited model network characteristics described by a single Maxwell element, it seems appropriate to also opt for a telechelic hydrophobically associating network. Such PPO-PEO-PPO triblock copolymers are limitedly available as commercial systems (inverse Pluronics®) and often lack an optimal balance between the PEO and PPO blocks needed for stable transient network formation. Therefore, chemical synthesis of such systems is again crucial and would additionally allow the development of less dense hydrophobic associating networks by increasing the length of the soluble PEO block. This, together with the less complex, often Maxwellian universal rheological fingerprint of telechic systems, may benefit the reproducibility of the double networks and advance research into such systems. Subsequent systematic rheological investigation of varying individual network concentrations could elucidate their contributions to the synergistic double network elasticity and delayed relaxation times. Furthermore, the results as obtained by rheology should be verified by making use of other experimental

characterization techniques such as the dynamic methods mentioned above. The fluorescent techniques provide the additional benefit of studying selectively labelled molecules of one of the two networks in the double network structure [343]. Static structural characterization techniques such as static light, X-ray or neutron scattering that rely on contrasting properties other than dynamics, on the other hand, might be more challenging as the main constituent of both networks is PEO and distinguishing between the two networks may be difficult. Nevertheless, they can give an indication of the homogeneity of the double networks, a parameter that is possibly of pivotal importance for the reproducibility of the systems. For effective differentiation between both networks, selective deuteration of one of the networks can be a useful feature to study a single network in its double network structure by neutron scattering [344].

Appendix A

Appendix to Chapter 4

A.1 Additional figures discussed in Chapter 4

This section contains additional figures which are discussed and referred to in the main text of Chapter 4.

For the analysis of the DSC and ASC data, the baseline was determined to be linear between two consecutive data points. In the transition temperature range where the peak is located, the consecutive points, i.e. the start and end point of the peak, where determined as these temperatures where the heat flow data point deviated with more than 0.5% as compared to the linear fit of the heat flow data using a combination of a low temperature interval of at least 2°C before micellization and a high temperature interval of at least 2°C after micellization. Outside of the transition temperature range, each out of 10 data points was taken into account to reduce the scatter on the baseline, corresponding to a temperature interval of 0.1°C between consecutive data point for DSC and of approximately 0.02°C for ASC.

For the analysis of the oscillatory rheological data, the $G'(T)$ data was fitted using a logistic function

$$f(x) = a + \frac{b}{1 + \exp(-c(x-d))}$$

in which d represents the inflection point. The onset temperatures were determine based on the most significant slope change over a range of 3°C below and above the transition in a semi-log plot. For $G'(T)$ data, only data points above the lower torque noise limit of 0.04 Pa were taken into account.

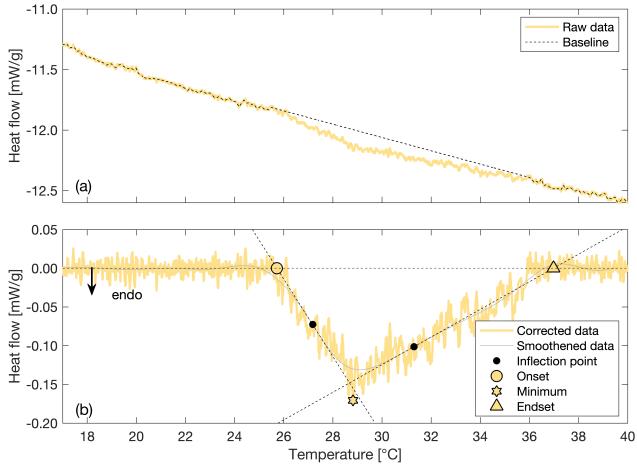

Figure A.1: DSC data analysis of a 30 g/L EG312 solution: (a) temperature evolution of the raw heat flow data and baseline and (b) baseline-corrected heat flow data and smoothened data fit as a function of temperature. The inflection points of the smoothened fit together with the tangent lines are indicated in order to determine the critical transition temperatures, which are also shown in the graph.

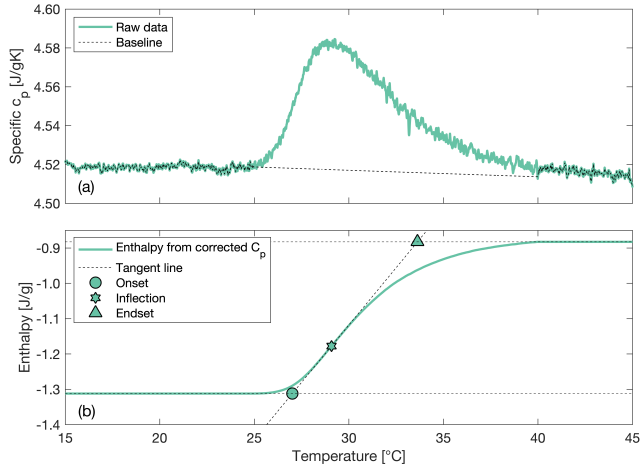

Figure A.2: ASC data analysis of a 30 g/L EG312 solution: (a) temperature evolution of the specific heat capacity data and baseline and (b) specific enthalpy as a function of temperature as calculated from c_p. The inflection point and tangent line are indicated in order to determine the critical transition temperatures, which are also shown in the graph.

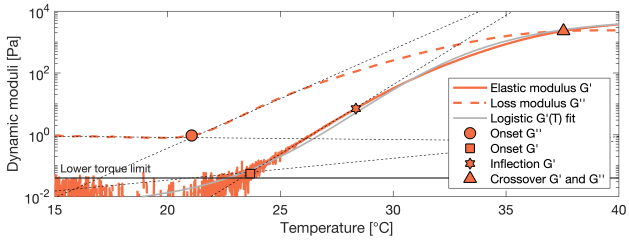

Figure A.3: Rheological oscillatory temperature ramp data analysis of a 132 g/L EG312 solution: temperature evolution of the dynamic moduli G' and G'' at a frequency of 1 Hz, 0.1% strain and a heating rate of 0.1°C/min. The logistic $G'(T)$ fit for determination of the inflection point temperature, as well as the slopes for the determination of the onset temperatures in G' and G'' are indicated in the graph. All G' data points are shown.

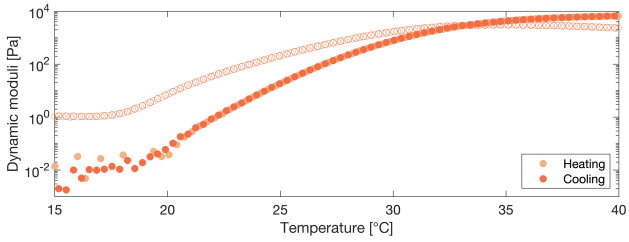

Figure A.4: Dynamic moduli G' (filled symbol) and G'' (unfilled symbol) as a function of temperature for a 147 g/L EG412 solution during heating and cooling ramps at a rate of 0.1°C/min, a frequency of 1 Hz and 0.1% strain. For clarity, only 1 out of 40 consecutive data points are shown.

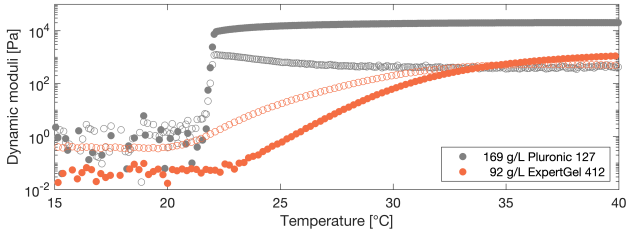

Figure A.5: Dynamic moduli G' (filled symbol) and G'' (unfilled symbol) as a function of temperature for a 92 g/L EG412 solution and a 169 g/L F127 solution during heating at a rate of 0.1°C/min, a frequency of 1 Hz and 0.1% strain. For clarity, only 1 out of 40 consecutive data points are shown.

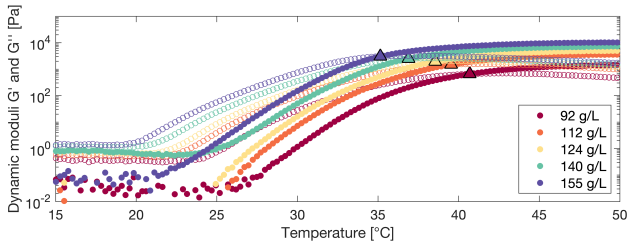

Figure A.6: Dynamic moduli G' (filled symbol) and G" (unfilled symbol) as a function of temperature for different concentrations of EG312. The crossover between G' and G" as an indication of the gel temperature T_{gel} is also shown in the graph for the different concentrations.

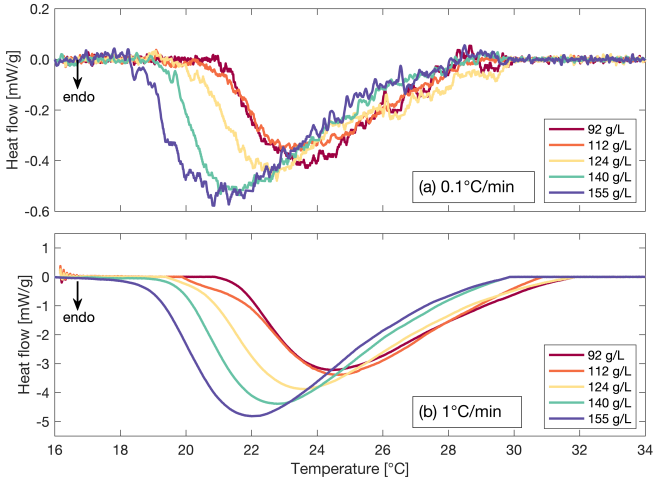

Figure A.7: Comparison baseline corrected heat flow as a function of temperature for different concentrations of EG312 using a heating rate of (a) 0.1°C/min and (b) 1°C/min.

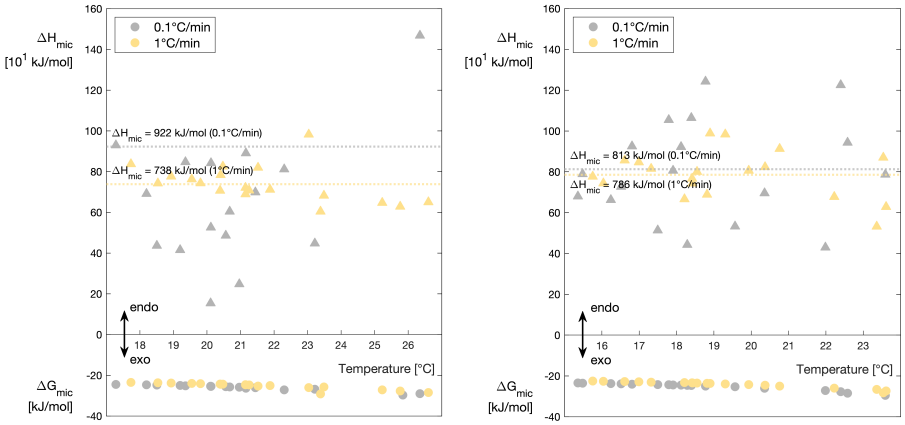

(a) EG312 **(b)** EG412

Figure A.8: Thermodynamic quantities of micellization ΔG_{mic} (exothermic, lower left y-axis) and ΔH_{mic} (endothermic, upper left y-axis) for (a) EG312 and (b) EG412 as a function of temperature determined by DSC at two different heating rates of 0.1°C/min (grey) and 1°C/min (yellow). ΔG_{mic} is calculated from the CMT, whereas ΔH_{mic} is determined by integration of the heat flux peak. Horizontal dotted lines represent the average values for ΔH_{mic} for both rates.

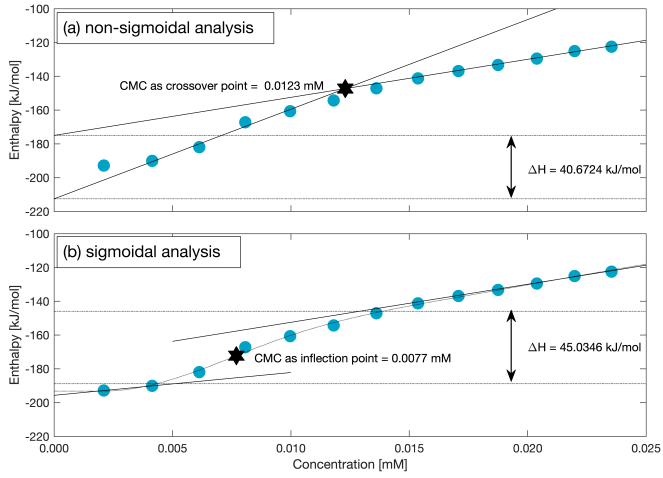

Figure A.9: Comparison of (a) non-sigmoidal analysis and (b) sigmoidal analysis of ITC enthalpogram, i.e. enthalpy versus molar concentration, for one measurement of EG412 at 26°C. The CMC is indicated with a black star and the enthalpy of micellization ΔH_{mic} is given in the graph.

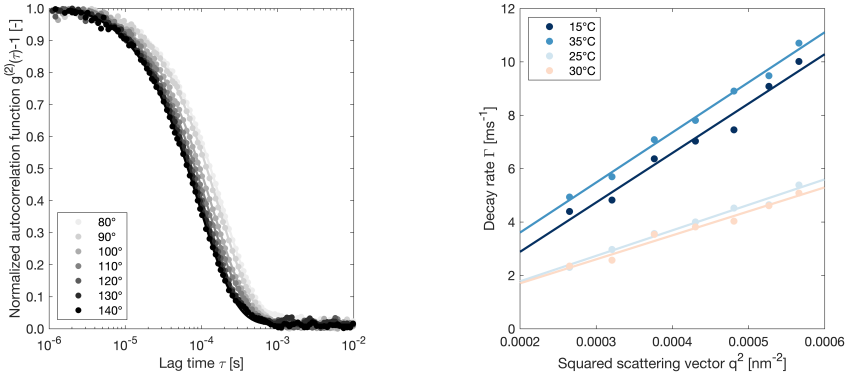

(a) **(b)**

Figure A.10: Dynamic light scattering measurements: (a) normalized intensity autocorrelation function $g^{(2)}(\tau) - 1$ of 17 g/L EG412 solutions at different scattering angles at 30°C. Solid lines represent stretched exponential fits $\exp[-2(\Gamma\tau)^{\beta}]$ and (b) decay rate Γ versus squared scattering vector q^2 of 17 g/L EG412 at different temperatures above and below the CMT (23.8°C for 17 g/L EG412). The solid line represents the linear fit with a slope equal to the translational diffusion coefficient D.

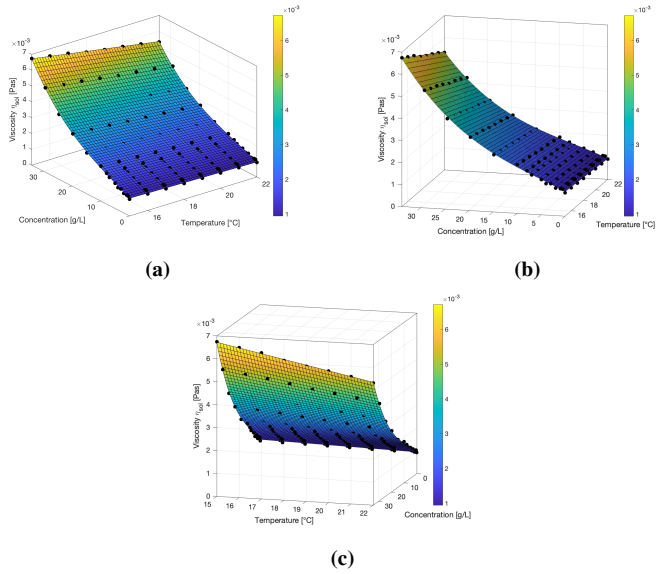

Figure A.11: Viscosity of a unimer solution η_{sol} sufficiently below CMT as a function of temperature and concentration for EG312. Graphs (a), (b) and (c) are different views. Data points represent real data as measured by rotational rheological experiments using a DWC geometry. Surface fit using a 'poly13' MATLAB function is shown using the colorbar. The fit is used for extrapolation of η_{sol} to higher temperatures above CMT and interpolation to intermediate concentrations.

Appendix B

Appendix to Chapter 5

B.1 Transient network model for telechelic triblock copolymers

This section contains the expressions of the generalized mechano-statistical transient network model for the simplest case of telechelic triblock copolymers ($a = 2, a-1 = 1$), resulting in the original equations derived by T. Annable and coworkers [147, 148] for HEUR copolymers. Table B.1 shows the $2^{a-1} = 2$ possible configurations for triblock copolymers, together with the calculation of each configuration probability, the average amount of bridges connected to one crosslinking node and the average number of associating blocks in one crosslinking node. The calculations of N_b, the overall average amount of bridges one chain contributes to a crosslinking node [bridges/chain], and N_a, the overall average amount of associating blocks one chain contributes to a crosslinking node [associating blocks/chain] are shown in Equations B.1 and B.2.

$$\begin{aligned} N_b &= \sum_{i=0}^{a-1} \frac{2(i+1)-2}{i+1} \cdot \binom{a-1}{i} \cdot F_1^i \cdot F_2^{a-1-i} \\ &= \frac{0}{1} \cdot \binom{1}{0} \cdot F_2 + \frac{2}{2} \cdot \binom{1}{1} \cdot F_1 \\ &= F_1 \end{aligned} \tag{B.1}$$

$$
\begin{aligned}
N_a &= \sum_{i=0}^{a-1} \frac{a}{i+1} \cdot \binom{a-1}{i} \cdot F_1^i \cdot F_2^{a-1-i} \\
&= \frac{2}{1} \cdot \binom{1}{0} \cdot F_2 + \frac{2}{2} \cdot \binom{1}{1} \cdot F_1 \\
&= 2 \cdot F_2 + F_1 = 2 \cdot (1 - F_1) + F_1 \\
&= 2 - F_1
\end{aligned}
\tag{B.2}
$$

The final expression of the average node functionality $\langle \Psi \rangle$ is derived in Equation B.3. This equation is similar to the expression obtained by T. Annable and co-authors (expression (30) in reference S1). Note that $\Psi_{max} = \langle \Psi \rangle \big|_{F_1=1}$ is equal to the aggregation number N_{agg}.

$$
\begin{aligned}
\langle \Psi \rangle &= N_b \cdot \frac{N_{agg}}{N_a} \\
&= \frac{F_1 \cdot N_{agg}}{2 - F_1}
\end{aligned}
\tag{B.3}
$$

B.2 Approximation of the aggregation number based on the core volume

A well-known approximation of the aggregation number of micelles formed by PEO-PPO-PEO Pluronic® triblock copolymers [50] is

$$
N_{agg} = \frac{V_{core}}{V_{PPO}} = \frac{4\pi/3 \cdot r_c^3}{4\pi/3 \cdot R_{g,PPO}^3} = \left(\frac{r_c}{R_{g,PPO}} \right)^3, \tag{B.4}
$$

in which r_c represents the core radius and $R_{g,PPO}$ the radius of gyration of the PPO block in the multiblock copolymers. The latter can be theoretically approximated, as discussed in Section 3.3 and summarized in Table 3 in the main text. This approximation assumes the micellar PPO core to be completely dehydrated. However, the obtained scattering length densities (SLD) of the spherical core of the micelles formed by PEO-PPO multiblock copolymers are on the order of $9.49 - 9.50 \cdot 10^{-6} \text{Å}^{-2}$. As compared to the SLD of pure PPO ($9.95 \cdot 10^{-6} \text{Å}^{-2}$) and that of the water solvent ($9.47 \cdot 10^{-6} \text{Å}^{-2}$), the values proof that the core contains a very significant fraction of solvent. Therefore, using Equation B.4 with the average core radii of 10.7 nm for EG312 and 9.6 nm for EG412 results in very large and incorrect average aggregation numbers of 2904 and 1794 for EG312 and EG412 respectively.

	Configuration	Configuration probability	Overall configuration probability for i bridges	Average amount of bridges from a node	Average amount of associating blocks in a node
i = 0		$F_1^0 \cdot F_2^1 = F_2$	$\binom{1}{0} \cdot F_1^0 \cdot F_2^1$	0	2
			$\binom{1}{0} = \frac{1!}{0!(1-0)!} = 1$	$= 0/1$	$= 2/1$
i = 1		$F_1^1 \cdot F_2^0 = F_1$	$\binom{1}{1} \cdot F_1^1 \cdot F_2^0$	1	1
			$\binom{1}{1} = \frac{1!}{1!(1-1)!} = 1$	$= 2/2$	$= 2/2$
$\sum_{i=0}^{a-1}$	2^{a-1}	$F_1^i \cdot F_2^{a-1-i}$	$\binom{a-1}{i} \cdot F_1^i \cdot F_2^{a-1-i}$	$\frac{2(i+1)-2}{i+1}$	$\frac{a}{i+1}$

Table B.1: Example of the combinatorics approach for a triblock copolymers with a = 2 telechelic associating blocks (green) and a-1 = 1 soluble blocks (red): possible configurations and the resulting probabilities, the average number of bridges connected to one crosslinking node (dotted circle) and the average number of associating blocks in one crosslinking node. The last row in grey shows the symbolic expressions.

A more accurate approximation takes into account the real core volume taken up by PPO, by making use of a correction factor x_{PPO}:

$$N_{agg} = \frac{x_{PPO} \cdot V_{core}}{V_{PPO}} = x_{PPO} \left(\frac{r_c}{R_{g,PPO}} \right)^3 \tag{B.5}$$

The PPO fraction in the scattering core (x_{PPO}) is calculated based on the SLD values of the scatterer (sc), PPO and solvent (sol), as

$$x_{PPO} = \frac{SLD_{sc} - SLD_{sol}}{SLD_{PPO} - SLD_{sol}} \tag{B.6}$$

Using Equation B.4 with the average core radii and SLDs of the scatterers ($9.4936 \cdot 10^{-6}$ Å^{-2} for EG312 and $9.4940 \cdot 10^{-6}$ Å^{-2} for EG412) results average aggregation numbers of 143 and 90 for EG312 and EG412 respectively.

B.3 Additional figures discussed in Chapter 5

This section contains additional figures which are discussed and referred to in the main text of Chapter 5.

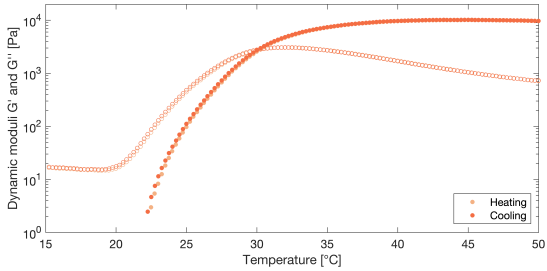

Figure B.1: Dynamic moduli G' (filled circle) and G'' (unfilled circle) as a function of temperature for a 140 g/L EG312 solution during heating and cooling ramps at a rate of 0.1°C/min, a frequency of 100 rad/s and 0.1% strain. For clarity, only 1 out of 40 consecutive data points are shown.

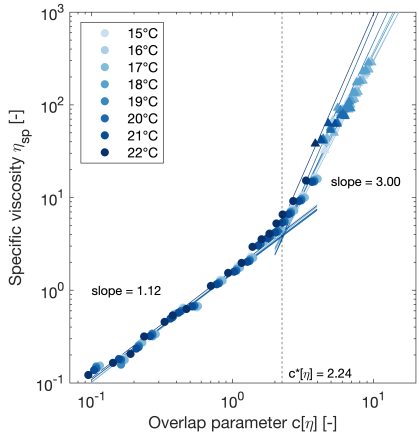

Figure B.2: Specific viscosity η_{sp} versus overlap parameter $c[\eta]$ for EG412 at different low temperatures (< CMT). The lines represent the power law scalings in the dilute and semi-dilute regions. The overlap concentration c^* is determined at the crossover of both scaling regimes. The value of $c^*[\eta]$ and the slopes indicated in the graph are average values.

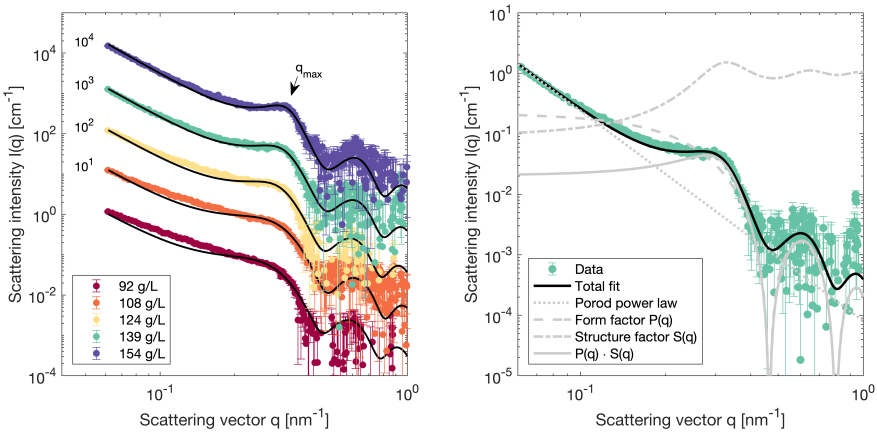

Figure B.3: Small-Angle X-ray scattering measurements of EG412 at 40°C: (a) background corrected scattering intensities $I(q)$ at different concentrations ($> c_{network}$) in aqueous solutions. Shift factors are indicated on the graph. Solid lines represent curve fittings. (b) Separate fitting contributions for 139 g/L EG412 including a Porod power law, a spherical form factor P(q) and a hard-sphere structure factor S(q).

The procedure of fitting a combined Porod power law, a spherical form factor $P(q)$ and a hard sphere structure factor $S(q)$ to the SAXS intensity profiles of EG412 samples was slightly adjusted as compared to the EG312 samples. To correctly fit the structure peak of EG412 samples, the fitting was not weighed with the actual error determined by the 2D image to 1D profile integration in the Foxtrot software, but the error in the peak region was artificially induced to be lowered by a factor of 0.1 in the q-region from 0.02 to .0.07 Å^{-1}. This forced the SASview fitting procedure to shift its focus to the peak area instead of the Porod slope area.

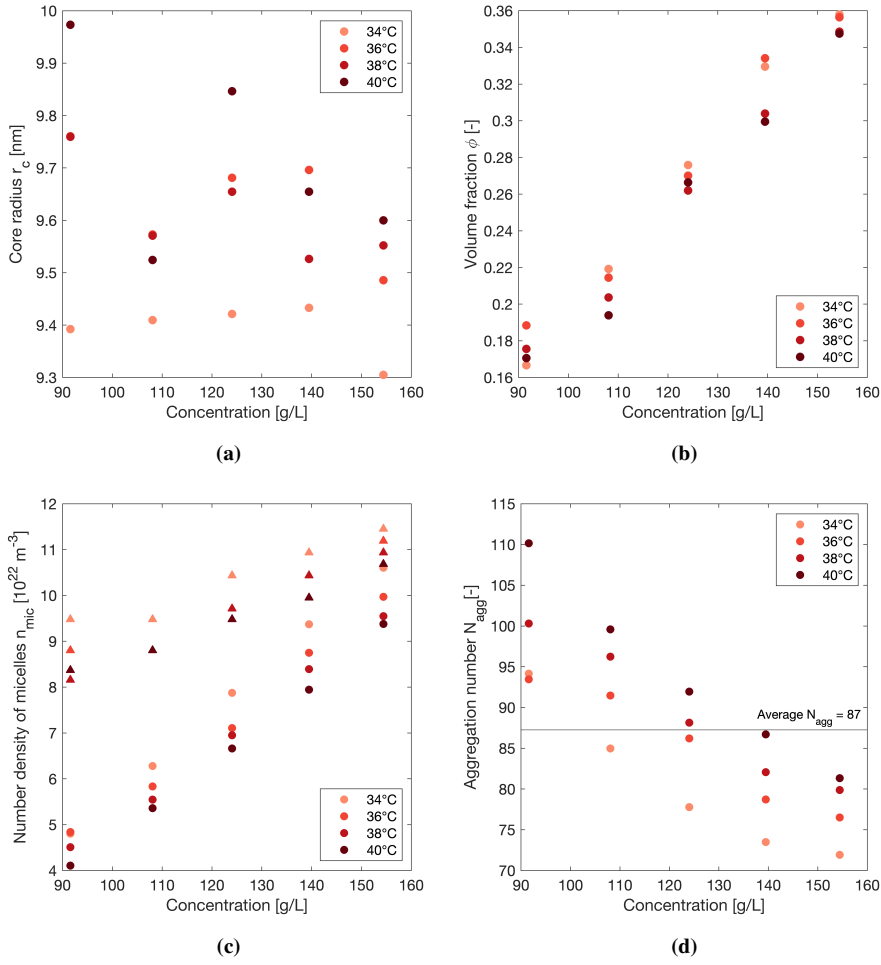

Figure B.4: Evolution of the hard sphere fitting parameters (a) core radius r_c and (b) micellar volume fraction ϕ with concentration for EG412 at different temperatures (> CMT). Evolution of the calculated values (c) number density of micelles n_{mic} as calculated from SAXS fitting parameters (circles) and as calculated from $d = 2.2\pi/q_{max}$ (triangles) and (d) aggregation number N_{agg} with concentration for EG412 at different temperatures (> CMT).

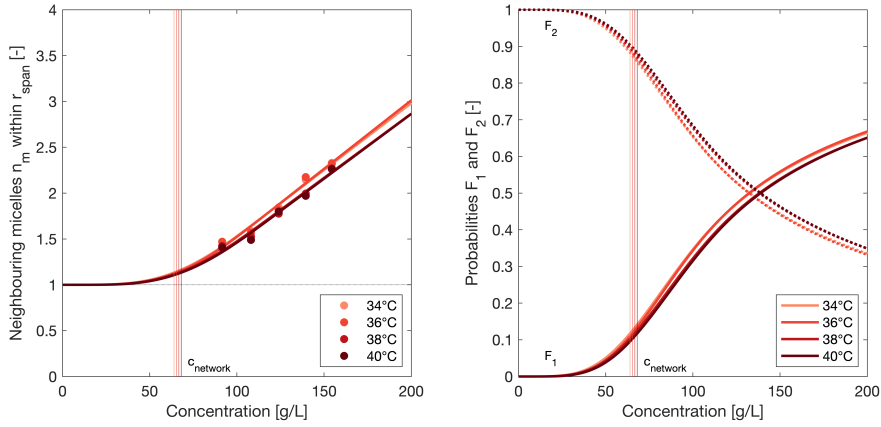

Figure B.5: (a) Evolution of the experimentally determined amount of micellar cores n_m with EG412 concentration at different temperatures (> CMT). Solid lines represent fits with the additional constraint that $n_m = 1$ at $c < c_{network}$. (b) The evolution of the probabilities $F_1 = 1 - F_2$ (full line) and $F_2 = 1/n_m$ (dotted line) as a function of EG412 concentration at different temperatures (> CMT). The vertical lines indicate the extrapolated values of $c_{network}$ at the different temperatures.

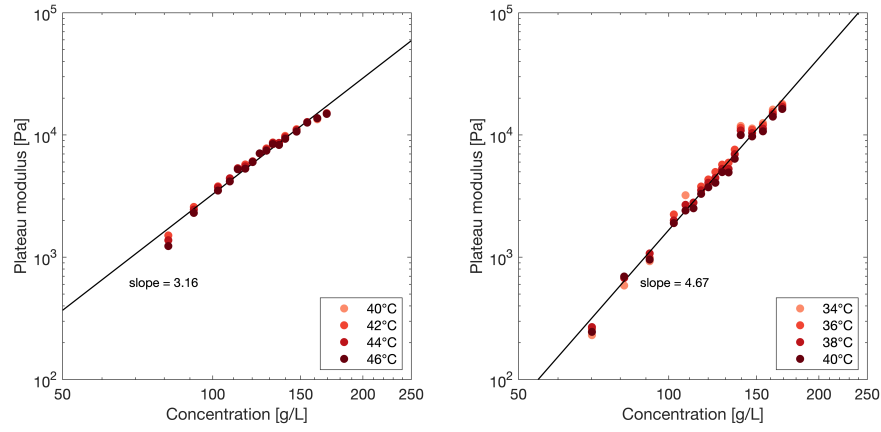

Figure B.6: Evolution of the plateau modulus G_0 versus concentration at different temperatures (> CMT) for (a) EG312 and (b) EG412. The solid lines represent power law fits with the exponents indicated in the graph.

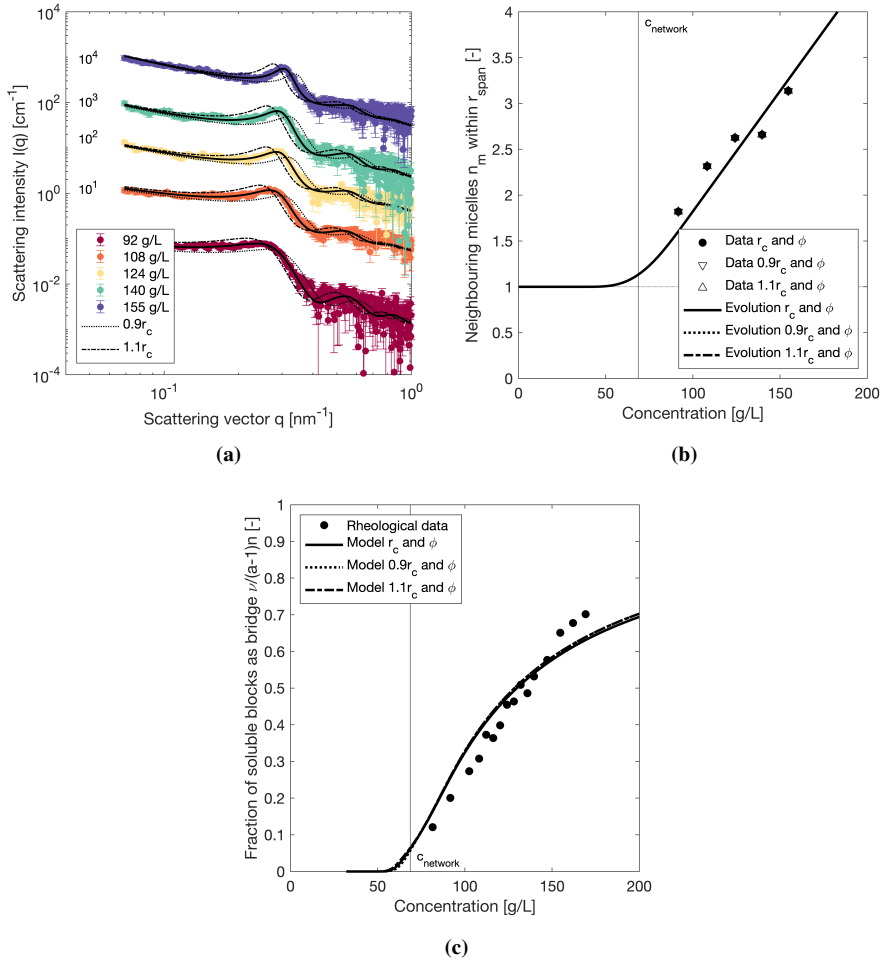

Figure B.7: Sensitivity analysis using 10% variation in the core radius r_c for different concentrations of EG312 at 46°C: (a) effect on SAXS intensity profiles, (b) effect on n_m and its evolution with concentration and (c) effect on the model prediction of the fraction of soluble PEO chain active as an elastic bridge.

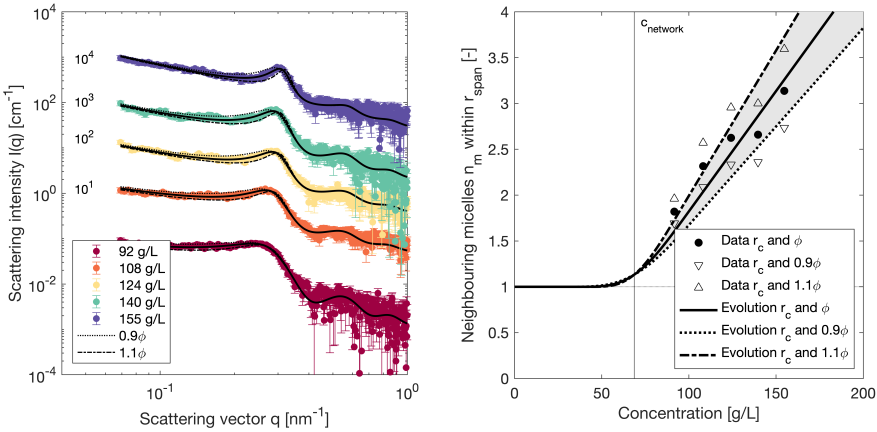

Figure B.8: Sensitivity analysis using 10% variation in micellar volume fraction ϕ for different concentrations of EG312 at 46°C: (a) effect on SAXS intensity profiles, (b) effect on n_m and its evolution with concentration and (c) effect on the model prediction of the fraction of soluble PEO chain active as an elastic bridge.

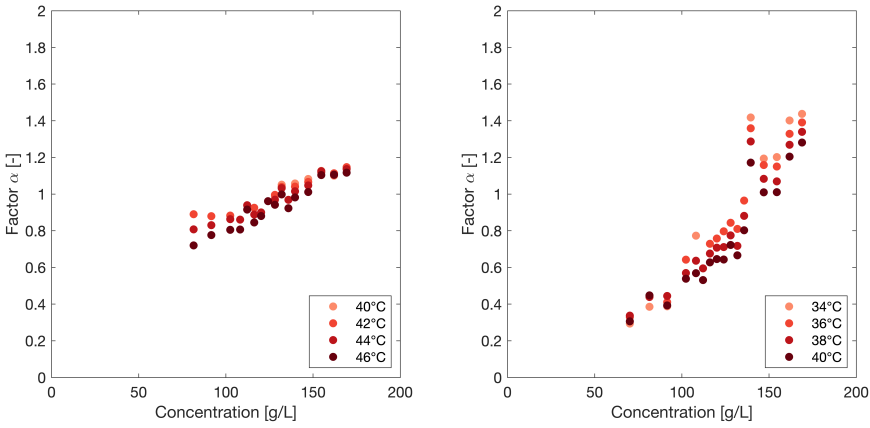

(a) **(b)**

Figure B.9: Evolution of α factor versus concentration at different temperatures(> CMT) for (a) EG312 and (b) EG412. The α factor is determined as the ratio of the actual data as inferred from the plateau modulus G_0 compared to the model prediction.

List of Figures

2.1 Binding energies of non-covalent interactions 6

2.2 Typical amphiphile phase diagram 8

2.3 Phase behavior and rheology of Pluronic F127® 11

2.4 Phase behavior and rheology of PEO-PPO multiblock copolymeren . 13

2.5 Different metallo-supramolecular polymer architectures 15

2.6 Divalent metal ion-terpyridine bis-complex 15

2.7 Network principles of amphiphilic block copolymers 18

2.8 Rheology of HEUR polymers 20

2.9 Concentration dependence of the rheogical properties of HEUR polymers 22

2.10 Rheology of hydrophobically modified PAM multiblock copolymers . 24

2.11 Different network principles of telechelic metallo-supramolecular polymers 26

2.12 Rheology of 4-arm PEO hydrogels crosslinked by nickel(II)-histide . 28

2.13 Rheology of 4-arm PEO hydrogels crosslinked by metal(II)-terpyridine 29

2.14 Mechano-statistical model prediction of rheological properties of HEUR 34

2.15 Rheological sticky Rouse fingerprint 38

2.16 Rheological sticky reptation fingerprint 40

2.17 Relaxation time versus concentration in multisticker micellar model . 40

2.18 Original PAMPS-PAAm double network 42

2.19 Rheology of IPN combining two hydrophobically associating triblock copolymer networks 44

2.20 Rheology of IPN combining metal-ligand and dynamic covalent bonds 45

2.21 Rheology of DCN, IPN or DN combining metal-ligand and dynamic covalent bonds 46

3.1 Schematic overview of ExpertGel® molecules 48

3.2 FT-IR spectra of Pluronics® and ExpertGel® 50

3.3 Molecular weight distribution of Pluronics® and ExpertGel® 52

3.4 ^{1}H-NMR spectra of Pluronics® and ExpertGel® 53

3.5 Post-functionalization reaction scheme 58

3.6 ^{1}H-NMR spectrum of 4-arm terpyridine-functionalized PEO stars . . 59

3.7 UV-VIS calibration and spectra of terpyridine solutions, OH-PEO stars and tpy-PEO stars 61

3.8 Rheological response with peripheral oil layer and with solvent trap . 64

3.9 Rheological measurement protocol of single and double networks . . 66

3.10 Determination of the refractive index increment of Expertgel® 70

4.1 Temperature evolution of dilute EG312 solution probed by rheology and calorimetry 78

4.2 Temperature evolution of concentrated EG312 solution probed by rheology and calorimetry 80

4.3 Different network formation principles of Pluronics® and ExpertGel® . 82

4.4 Cloud point determination 83

4.5 Phase diagrams of EG312 and EG412 as probed by different techniques 85

4.6 Thermodynamic quantities of micellization of EG312 and EG412 at 1° C/min 89

4.7 ITC data analysis 93

4.8 Zoomed phase diagrams of EG312 and EG412 including ITC results . 95

4.9 DLS data analysis EG312 97

4.10 R_H from DLS at different temperatures, and R_{HS} from viscosity scaling, both as function of concentration for EG312 and EG412 99

4.11 Debye plots and resulting M_w and A_2 for EG312 and EG412 101

4.12 Synchrotron SAXS results for EG312 and EG412 102

4.13 Analysis for determination of the hard sphere radius R_{HS} 105

5.1 Dangling end, superloop and superbridge 114

5.2 Overview of the transient network model 116

5.3 Viscosity scaling with concentration for EG312 and determination of temperature dependent $c_{network}$ 120

5.4 SAXS intensity profiles of EG312 networks at 46°C 122

5.5 SAXS fitting parameter r_c and ϕ, and calculated values n_{mic} and N_{agg} for EG312 as function of network concentration 124

5.6 Determination of the amount of micellar cores n_m for EG312 network at 46°C 127

5.7 Schematic illustrations for the calculation of n_m from the radial distribution function 128

5.8 Evolution of n_m, and probabilities F_1 and F_2 versus concentration for EG312 networks at different temperatures 130

5.9 Rheological frequency sweeps of EG312 and EG412 networks 131

5.10 Model prediction and results for EG312 and EG412 133

5.11 Redundant bridge and entanglements between bridges and/or loops . . 135

6.1 Identification of characteristic relaxation times in multisticker networks 142

6.2 Temperature dependency of rheological network fingerprint 144

6.3 Temperature dependence of the relaxation times in micellar networks . 145

6.4 Concentration dependence of relaxation activation energies 145

6.5 Concentration dependence of the relaxation times in micellar networks 147

6.6 Temperature dependence of the power law exponents 147

6.7 Concentration dependence of different relaxation time indicators . . . 148

6.8 τ_N/τ_S data and adapted existing model predictions 151
6.9 Calculated τ_{chain} versus concentration 153

7.1 Linear rheology of HC single network 159
7.2 Stretched exponential stress relaxation fitting of HC single network . . 160
7.3 Temperature dependence of elastic fraction and single relaxation time of HC single network 161
7.4 Linear rheology of ML single network 164
7.5 Maxwellian fitting of ML single network 165
7.6 Temperature dependence of elastic fraction and single relaxation time of ML single network 166
7.7 DN build up as probed by rheology 167
7.8 Frequency sweep of steady state DN 168
7.9 Stress relaxation of DN at different decreasing temperatures 169
7.10 Fitting of DN stress relaxation with single and stretched exponential decay 170
7.11 Synergistic number density of elastically active chains in the DN . . . 171
7.12 Temperature dependence and delay of relaxation times in the DN . . . 173
7.13 Purple samples due to metal impurities 174
7.14 Reproducibility of DNs on different geometries 175

A.1 DSC data analysis 188
A.2 ASC data analysis 188
A.3 Rheological oscillatory temperature ramp data analysis 189
A.4 Temperature ramps during heating and cooling of a concentrated EG312 solution at 6.28 rad/s 189
A.5 Temperature ramps of ExpertGel® EG412 and Pluronic® F127 189
A.6 Determination of T_{gel} for different concentrations of EG312 190
A.7 DSC data using a heating rate of 0.1°C/min and 1°C/min 190

A.8 Thermodynamic quantities of micellization of EG312 and EG412 at 0.1°C/min and 1°C/min 191

A.9 Comparison ITC data analysis 191

A.10 DLS data analysis EG412 192

A.11 Viscosity of η_{sol} as a function of temperature and concentration for EG312 193

B.1 Temperature ramps during heating and cooling of a concentrated EG312 solution at 100 rad/s 198

B.2 Viscosity scaling with concentration for EG412 198

B.3 SAXS intensity profiles of EG412 networks at 40°C 199

B.4 SAXS fitting parameter r_c and ϕ, and calculated values n_{mic} and N_{agg} for EG412 as function of network concentration 200

B.5 Evolution of n_m, and probabilities F_1 and F_2 versus concentration for EG412 networks at different temperatures 201

B.6 Evolution of the plateau modulus G_0 versus concentration for EG312 and EG412 201

B.7 Sensitivity analysis using 10% variation in r_c for EG312 at 46°C . . . 202

B.8 Sensitivity analysis using 10% variation in ϕ for EG312 at 46°C . . . 203

B.9 Evolution of α factor versus concentration for EG312 and EG412 . . 204

List of Tables

2.1 Equilibrium constants of metal(II)-terpyridine complexes in water . . 16

2.2 Characteristics and scaling laws of different transient network models 31

2.3 As- and dissociation rates in (modified) Tanaka-Edwards models . . . 33

3.1 FT-IR peak positions and their origin in ExpertGel samples 49

3.2 Molecular weight characteristics of Pluronics® and ExpertGel® 51

3.3 ^{1}H-NMR peak positions and their origin in Pluronics® and ExpertGel® 54

3.4 Characteristics of ExpertGel® as determined by ^{1}H-NMR 55

3.5 Polymer parameters of the PEO and PPO blocks present in ExpertGel® 57

3.6 ^{1}H-NMR peak positions and their origin in 4-arm terpyridine-functionalized PEO stars 60

4.1 CMC of ExpertGel® and Pluronics® 87

4.2 Thermodynamic quantities of micellization for ExpertGel® and Pluronics® 90

4.3 ITC results of CMC and the thermodynamic quantities of micellization for ExpertGel® and Pluronic® F127 95

5.1 Example of the combinatorics approach for a chain with 4 hydrophobic stickers 113

B.1 Example of the combinatorics approach for a triblock copolymers . . 197

Bibliography

[1] Jean-Marie Lehn. Supramolecular Chemistry—Scope and Perspectives Molecules, Supermolecules, and Molecular Devices (Nobel lecture). *Angewandte Chemie International Edition in English*, 27(1):89–112, 1988.

[2] Sebastian Seiffert. *Supramolecular polymer networks and gels*, volume 268. Springer, 2015.

[3] David S. Lawrence, Tao Jiang, and Michael Levett. Self-assembling supramolecular complexes. *Chemical Reviews*, 95(6):2229–2260, 1995.

[4] Fanwen Zeng and Steven C. Zimmerman. Dendrimers in supramolecular chemistry: From molecular recognition to self-assembly. *Chemical Reviews*, 97(5):1681–1712, 1997.

[5] L. Brunsveld, B. J.B. Folmer, E. W. Meijer, and R. P. Sijbesma. Supramolecular polymers. *Chemical Reviews*, 101(12):4071–4097, 2001.

[6] Neralagatta M. Sangeetha and Uday Maitra. Supramolecular gels: Functions and uses. *Chemical Society Reviews*, 34(10):821–836, 2005.

[7] Sebastian Seiffert and Joris Sprakel. Physical chemistry of supramolecular polymer networks. *Chemical Society Reviews*, 41(2):909–930, 2012.

[8] Lenny Voorhaar and Richard Hoogenboom. Supramolecular polymer networks: Hydrogels and bulk materials. *Chemical Society Reviews*, 45(14):4013–4031, 2016.

[9] Viviane A. Friese and Dirk G. Kurth. From coordination complexes to coordination polymers through self-assembly. *Current Opinion in Colloid and Interface Science*, 14(2):81–93, 2009.

[10] Wolfgang H. Binder and Ronald Zirbs. Supramolecular polymers and networks with hydrogen bonds in the main- and side-chain. *Advances in Polymer Science*, 207(1):1–78, 2007.

[11] Tamaki Nakano. *π-Stacked Polymers and Molecules: Theory, Synthesis, and Properties*. Springer, 2014.

[12] Charl F.J. Faul. Ionic self-assembly for functional hierarchical nanostructured materials. *Accounts of Chemical Research*, 47(12):3428–3438, 2014.

[13] Ulrich S. Schubert and Christian Eschbaumer. Macromolecules containing bipyridine and terpyridine metal complexes: Towards metallosupramolecular polymers. *Angewandte Chemie - International Edition*, 41(16):2892–2926, 2002.

[14] Bas G.G. Lohmeijer and Ulrich S. Schubert. Playing LEGO with macromolecules: Design, synthesis, and self-organization with metal complexes. *Journal of Polymer Science, Part A: Polymer Chemistry*, 41(10):1413–1427, 2003.

[15] R. Hogg and R.G. Wilkins. Exchange studies of certain chelate compounds of the transition metals. *Journal of the American Chemical Society*, 341-350, 1962.

[16] Charles André Fustin, Pierre Guillet, Ulrich S. Schubert, and Jean François Gohy. Metallo-supramolecular block copolymers. *Advanced Materials*, 19(13):1665–1673, 2007.

[17] Adam O. Moughton and Rachel K. O'Reilly. Using metallo-supramolecular block copolymers for the synthesis of higher order nanostructured assemblies. *Macromolecular Rapid Communications*, 31(1):37–52, 2010.

[18] Clément Mugemana, Pierre Guillet, Charles André Fustin, and Jean François Gohy. Metallo-supramolecular block copolymer micelles: Recent achievements. *Soft Matter*, 7(8):3673–3678, 2011.

[19] Jérémy Brassinne, Arnaud M. Stevens, Evelyne Van Ruymbeke, Jean François Gohy, and Charles André Fustin. Hydrogels with dual relaxation and two-step gel-sol transition from heterotelechelic polymers. *Macromolecules*, 46(22):9134–9143, 2013.

[20] Jérémy Brassinne, Jean François Gohy, and Charles André Fustin. Orthogonal control of the dynamics of supramolecular gels from heterotelechelic associating polymers. *ACS Macro Letters*, 5(12):1364–1368, 2016.

[21] Dushyant B. Varshey, John R. G. Sander, Tomislav Friščić, and Leonard R. MacGillivray. Supramolecular interactions. *Supramolecular Chemistry*, 2012.

[22] Ian Hamley. *Block copolymers in solution: Fundamentals and applications*. John Wiley and Sons, 205.

[23] Yiyong Mai and Adi Eisenberg. Self-assembly of block copolymers. *Chemical Society Reviews*, 41(18):5969–5985, 2012.

[24] Domenico Lombardo, Mikhail A. Kiselev, Salvatore Magazù, and Pietro Calandra. Amphiphiles self-assembly: Basic concepts and future perspectives of supramolecular approaches. *Advances in Condensed Matter Physics*, 2015:151683, 2015.

[25] Christopher M. Bates and Frank S. Bates. 50th anniversary perspective: Block polymers-pure potential. *Macromolecules*, 50(1):3–22, 2017.

[26] Paschalis Alexandridis and Björn Lindman, editors. *Amphiphilic block copolymers*. Woodhead Publishing Limited, Amsterdam, 2000.

[27] G. Ulbricht, W. Hoffman, H. Wanka. Phase diagrams and aggregation behavior of poly(oxyethylene)-poly(oxypropylene)-poly(oxyethylene) triblock copolymers in aqueous solutions. *Macromolecules*, 27:4145–4159, 1994.

[28] Kaiwen Zhang, Kun Xue, and Xian Jun Loh. Thermo-responsive hydrogels: From recent progress to biomedical applications. *Gels*, 7(3):77, 2021.

[29] Rainer Haag. Supramolecular drug-delivery systems based on polymeric core-shell architectures. *Angewandte Chemie - International Edition*, 43(3):278–282, 2004.

[30] C. Gong, T. Qi, X. Wei, Y. Qu, Q. Wu, F. Luo, and Z. Qian. Thermosensitive polymeric hydrogels as drug delivery systems. *Current Medicinal Chemistry*, 20(1):79–94, 2013.

[31] Ranee A. Stile, Wesley R. Burghardt, and Kevin E. Healy. Synthesis and characterization of injectable poly(N-isopropylacrylamide)-based hydrogels that support tissue formation in vitro. *Macromolecules*, 32(22):7370–7379, 1999.

[32] Ji Sun Park, Dae Gyun Woo, Bo Kyung Sun, Hyung Min Chung, Su Jin Im, You Mee Choi, Kinam Park, Kang Moo Huh, and Keun Hong Park. In vitro and in vivo test of PEG/PCL-based hydrogel scaffold for cell delivery application. *Journal of Controlled Release*, 124(1-2):51–59, 2007.

[33] Tengfei Zhou, Xiaolong Li, Guo Li, Taoran Tian, Shiyu Lin, Sirong Shi, Jinfeng Liao, Xiaoxiao Cai, and Yunfeng Lin. Injectable and thermosensitive TGF-β1-loaded PCEC hydrogel system for in vivo cartilage repair. *Scientific Reports*, 7(1):1–13, 2017.

[34] He Liu, Yilong Cheng, Jinjin Chen, Fei Chang, Jincheng Wang, Jianxun Ding, and Xuesi Chen. Component effect of stem cell-loaded thermosensitive polypeptide hydrogels on cartilage repair. *Acta Biomaterialia*, 73:103–111, 2018.

[35] Jiabin Zhang, Ming Zhang, Rongcai Lin, Seonho Yun, Yuguang Du, Liming Wang, Qingqiang Yao, Andrew Zannettino, and Hu Zhang. Allogeneic primary mesenchymal stem/stromal cell aggregates within poly(N-isopropylacrylamide-co-acrylic acid) hydrogel for osteochondral regeneration. *Applied Materials Today*, 18:100487, 2020.

[36] Yipei Chen, Yuzhuo Li, Wenjia Shen, Kun Li, Lin Yu, Qinghua Chen, and Jiandong Ding. Controlled release of liraglutide using thermogelling polymers in treatment of diabetes. *Scientific Reports*, 6:1–13, 2016.

[37] Kun Xue, Xinxin Zhao, Zhongxing Zhang, Beiying Qiu, Queenie Shu Woon Tan, Kok Haur Ong, Zengping Liu, Bhav Harshad Parikh, Veluchamy Amutha Barathi, Weimiao Yu, Xiaomeng Wang, Gopal Lingam, Walter Hunziker, Xinyi Su, and Xian Jun Loh. Sustained delivery of anti-VEGFs from thermogel depots inhibits angiogenesis without the need for multiple injections. *Biomaterials Science*, 7(11):4603–4614, 2019.

[38] Paschalis Alexandridis. Amphiphilic copolymers and their applications. *Current Opinion in Colloid and Interface Science*, 1(4):490–501, 1996.

[39] John G. Curro and Amalie L. Frischknecht. Solution behavior of PEO: the ultimate biocompatible polymer. Technical report, 2004.

[40] Anaïs Pitto-Barry and Nicolas P.E. Barry. Pluronic® block-copolymers in medicine: From chemical and biological versatility to rationalisation and clinical advances. *Polymer Chemistry*, 5(10):3291–3297, 2014.

[41] Andrew M. Bodratti and Paschalis Alexandridis. Amphiphilic block copolymers in drug delivery: advances in formulation structure and performance. *Expert Opinion on Drug Delivery*, 15(11):1085–1104, 2018.

[42] Jana Herzberger, Kerstin Niederer, Hannah Pohlit, Jan Seiwert, Matthias Worm, Frederik R. Wurm, and Holger Frey. Polymerization of ethylene oxide, propylene oxide, and other alkylene oxides: Synthesis, novel polymer architectures, and bioconjugation. *Chemical Reviews*, 116(4):2170–2243, 2016.

[43] Paschalis Alexandridis, Josef F. Holzwarth, and T. Alan Hatton. Micellization of poly(ethylene oxide)-poly(propylene oxide)-poly(ethylene oxide) triblock copolymers in aqueous solutions: Thermodynamics of copolymer association. *Macromolecules*, 27(9):2414–2425, 1994.

[44] Paschalis Alexandridis and T. Alan Hatton. Poly(ethylene oxide)-poly(propylene oxide)-poly(ethylene oxide) block copolymer surfactants in aqueous solutions and at interfaces: Thermodynamics, structure, dynamics, and modeling. *Colloids and Surfaces A: Physicochemical and Engineering Aspects*, 96(1-2):1–46, 1995.

[45] Liem Chau Pham Trong, Madeleine Djabourov, and Alain Ponton. Mechanisms of micellization and rheology of PEO-PPO-PEO triblock copolymers with various architectures. *Journal of Colloid and Interface Science*, 328(2):278–287, 2008.

[46] Søren Hvidt, Erling B. Jørgensen, Wyn Brown, and Karin Schulen. Micellization and gelation of aqueous solutions of a triblock copolymer studied by rheological techniques and scanning calorimetry. *Journal of Physical Chemistry*, 98(47):12320–12328, 1994.

[47] Bo Nyström and Anna Lena Kjøniksen. Dynamic light scattering of a poly(ethylene oxide)-poly(propylene oxide)-poly(ethylene oxide) triblock copolymer in water. *Langmuir*, 13(17):4520–4526, 1997.

[48] Yingchun Liu, Sow Hsin Chen, and John S. Huang. Light-scattering studies of concentrated copolymer micellar solutions. *Macromolecules*, 31(18):6226–6233, 1998.

[49] Otto Glatter, Güther Scherf, Karin Schillén, and Wyn Brown. Characterization of a poly(ethylene oxide)-poly(propylene oxide) triblock copolymer (EO27-PO39-EO27) in aqueous solution. *Macromolecules*, 27(21):6046–6054, 1994.

[50] Kell Mortensen and Jan Skov Pedersen. Structural study on the micelle formation of poly(ethylene oxide)–poly(propylene oxide)–poly(ethylene oxide) triblock copolymer in aqueous solution. *Macromolecules*, 26(4):805–812, 1993.

[51] Lin Yang, Paschalis Alexandridis, David C. Steytler, Matthias J. Kositza, and Josef F. Holzwarth. Small-angle neutron scattering investigation of the temperature-dependent aggregation behavior of the block copolymer Pluronic L64 in aqueous solution. *Langmuir*, 16(23):8555–8561, 2000.

[52] Sijun Liu and Lin Li. Multiple phase transition and scaling law for poly(ethylene oxide)-poly(propylene oxide)-poly(ethylene oxide) triblock copolymer in aqueous solution. *ACS Applied Materials and Interfaces*, 7(4):2688–2697, 2015.

[53] Robert K. Prud'homme, Guangwei Wu, and Dieter K. Schneider. Structure and rheology studies of poly(oxyethylene-oxypropylene-oxyethylene) aqueous solution. *Langmuir*, 12(20):4651–4659, 1996.

[54] Kyu Hyun, Jung Gun Nam, Manfred Wilhellm, Kyung Hyun Ahn, and Seung Jong Lee. Large amplitude oscillatory shear behavior of PEO-PPO-PEO triblock copolymer solutions. *Rheologica Acta*, 45(3):239–249, 2006.

[55] Zukang Zhou and Benjamin Chu. Light-scattering study on the association behavior of triblock polymers of ethylene oxide and propylene oxide in aqueous solution. *Journal of Colloid And Interface Science*, 126(1):171–180, 1988.

[56] Franck Artzner, Sandrine Geiger, Audrey Olivier, Cécile Allais, Stéphanie Finet, and Florence Agnely. Interactions between poloxamers in aqueous solutions: Micellization and gelation studied by differential scanning calorimetry, small angle X-ray scattering, and rheology. *Langmuir*, 23(9):5085–5092, 2007.

[57] Thierry Nivaggioli, Paschalis Alexandridis, T. Alan Hatton, Ahmad Yekta, and Mitchell A. Winnik. Fluorescence probe studies of Pluronic copolymer solutions as a function of temperature. *Langmuir*, 11(3):730–737, 1995.

[58] H. Henning Winter and Francois Chambon. Analysis of linear viscoelasticity of a crosslinking polymer at the gel point. *Journal of Rheology*, 30(2):367–382, 1986.

[59] Kell Mortensen, Dietmar Schwahn, and Stefan Janssen. Pressure-induced melting of micellar crystal. *Physical Review Letters*, 71(11):1728–1731, 1993.

[60] A. F. Kostko, J. L. Harden, and M. A. McHugh. Dynamic light scattering study of concentrated triblock copolymer micellar solutions under pressure. *Macromolecules*, 42(14):5328–5338, 2009.

[61] Kawthar Bouchemal, Florence Agnely, Armand Koffi, and Gilles Ponchel. A concise analysis of the effect of temperature and propanediol-1,2 on Pluronic F127 micellization using isothermal titration microcalorimetry. *Journal of Colloid and Interface Science*, 338(1):169–176, 2009.

[62] Kazuhiro Kaizu and Paschalis Alexandridis. Micellization of polyoxyethylene-polyoxypropylene block copolymers in aqueous polyol solutions. *Journal of Molecular Liquids*, 210:20–28, 2015.

[63] Nivedita Pandit, Troy Trygstad, Scott Croy, Maria Bohorquez, and Cody Koch. Effect of salts on the micellization, clouding, and solubilization behavior of Pluronic F127 solutions. *Journal of Colloid and Interface Science*, 222(2):213–220, 2000.

[64] Yan Lei Su, Hui Zhou Liu, Jing Wang, and Jia Yong Chen. Study of salt effects on the micellization of PEO-PPO-PEO block copolymer in aqueous solution by FTIR spectroscopy. *Langmuir*, 18(3):865–871, 2002.

[65] J. P. Mata, P. R. Majhi, C. Guo, H. Z. Liu, and P. Bahadur. Concentration, temperature, and salt-induced micellization of a triblock copolymer Pluronic L64 in aqueous media. *Journal of Colloid and Interface Science*, 292(2):548–556, 2005.

[66] Uzma Ashraf, Oyais Ahmad Chat, Masrat Maswal, Suraya Jabeen, and Aijaz Ahmad Dar. An investigation of Pluronic P123-sodium cholate mixed system: Micellization, gelation and encapsulation behavior. *RSC Advances*, 5(102):83608–83618, 2015.

[67] Zhiqi He and Paschalis Alexandridis. Micellization thermodynamics of Pluronic P123 (EO20PO70EO20) amphiphilic block copolymer in aqueous ethylammonium nitrate (EAN) solutions. *Polymers*, 10:32, 2017.

[68] Dali Zhou, Paschalis Alexandridis, and Ali Khan. Self-assembly in a mixture of two poly(ethylene oxide)-b-poly(propylene oxide)-b-poly(ethylene oxide) copolymers in water. *Journal of Colloid and Interface Science*, 183(2):339–350, 1996.

[69] Vijender Singh, Poonam Khullar, Pragnesh N Dave, and Navjot Kaur. Micelles, mixed micelles, and applications of polyoxypropylene (PPO)-polyoxyethylene (PEO)-polyoxypropylene (PPO) triblock polymers. *International Journal of Industrial Chemistry*, 4(1):12, 2013.

[70] David Löf, Anna Niemiec, Karin Schillén, Watson Loh, and Gerd Olofsson. A calorimetry and light scattering study of the formation and shape transition of mixed micelles of EO20PO68EO20 triblock copolymer (P123) and nonionic surfactant (C12EO6). *Journal of Physical Chemistry B*, 111(21):5911–5920, 2007.

[71] Kell Mortensen, Wyn Brown, and Erling Jørgensen. Phase behavior of poly(propylene oxide)-poly(ethylene oxide)-poly(propylene oxide) triblock copolymer melt and aqueous solutions. *Macromolecules*, 27(20):5654–5666, 1994.

[72] Gerardino D'Errico, Luigi Paduano, and Ali Khan. Temperature and concentration effects on supramolecular aggregation and phase behavior for poly(propylene oxide)-b-poly(ethylene oxide)- b-poly(propylene oxide) copolymers of different composition in aqueous mixtures, 1. *Journal of Colloid and Interface Science*, 279(2):379–390, 2004.

[73] Gerardino D'Errico, Luigi Paduano, Ornella Ortona, Gaetano Mangiapia, Luigi Coppola, and Fabrizio Lo Celso. Temperature and concentration effects on supramolecular aggregation and phase behavior for poly(propylene oxide)-b-poly(ethylene oxide)-b-poly(propylene oxide) copolymers of different concentration in aqueous mixtures, 2. *Journal of Colloid and Interface Science*, 359(1):179–188, 2011.

[74] Eneko Larrañeta and José Ramón Isasi. Phase behavior of reverse poloxamers and poloxamines in water. *Langmuir*, 29(4):1045–1053, 2013.

[75] Bryna C. Kumi, Boualem Hammouda, and Sandra C. Greer. Self-assembly of the triblock copolymer 17R4 poly(propylene oxide)14-poly(ethylene oxide)24-poly(propylene oxide)14 in D2O. *Journal of Colloid and Interface Science*, 434:201–207, 2014.

[76] G. Ten Brinke and G. Hadziioannou. Topological constraints and their influence on the properties of synthetic macromolecular systems. 2. Micelle formation of triblock copolymers. *Macromolecules*, 20(3):486–489, 1987.

[77] N. P. Balsara, M. Tirrell, and T. P. Lodge. Micelle formation of BAB triblock Copolymers in solvents that preferentially dissolve the A block. *Macromolecules*, 24(8):1975–1986, 1991.

[78] Kyung Hwa Sun, Youn Soo Sohn, and Byeongmoon Jeong. Thermogelling poly(ethylene oxide-b-propylene oxide-b-ethylene oxide) disulfide multiblock copolymer as a thiol-sensitive degradable polymer. *Biomacromolecules*, 7(10):2871–2877, 2006.

[79] Kazuaki Rikiyama, Tasuku Horiuchi, Naoyuki Koga, Yusuke Sanada, Keisuke Watanabe, Misako Aida, and Yukiteru Katsumoto. Micellization of poly(ethylene oxide)-poly(propylene oxide) alternating multiblock copolymers in water. *Polymer*, 156:102–110, 2018.

[80] Alejandro Sosnik and Daniel Cohn. Reverse thermo-responsive poly(ethylene oxide) and poly(propylene oxide) multiblock copolymers. *Biomaterials*, 26(4):349–357, 2005.

[81] Nivedita K. Pandit and Richard McGowan. Gelation of pluronic® F127-polyethylene glycol mixtures: Relationship to PEG molecular weight. *Drug Development and Industrial Pharmacy*, 24(2):183–186, 1998.

[82] Abhinav Maheswaran Pragatheeswaran and Shing Bor Chen. Effect of chain length of PEO on the gelation and micellization of the pluronic F127 copolymer aqueous system. *Langmuir*, 29(31):9694–9701, 2013.

[83] Daniel Cohn, Alejandro Sosnik, and Avraham Levy. Improved reverse thermo-responsive polymeric systems. *Biomaterials*, 24(21):3707–3714, 2003.

[84] Daniel Cohn and Alejandro Sosnik. Novel reverse thermoresponsive injectable poly(ether carbonate)s. *Journal of Materials Science: Materials in Medicine*, 14(2):175–180, 2003.

[85] Jun Jiang, Ram Malal, Chunhua Li, Min Y. Lin, Ralph H. Colby, Dilip Gersappe, Miriam H. Rafailovich, Jonathan C. Sokolov, and Daniel Cohn. Rheology of thermoreversible hydrogels from multiblock associating copolymers. *Macromolecules*, 41(10):3646–3652, 2008.

[86] Yuexia Wang, Yebang Tan, Xiaoling Huang, Yuju Che, and Xu Du. Synthesis of biodegradable amphiphilic thermo-responsive multiblock polycarbonate and its self-aggregation behavior in aqueous solution. *Journal of Applied Polymer Science*, 112:1425–1435, 2009.

[87] Yuexia Wang, Yebang Tan, Xiaoling Huang, and Guiying Xu. Gelation behavior of thermo-responsive poly(ethylene oxide) and poly(propylene oxide) multiblock polycarbonates. *Journal of Macromolecular Science, Part A: Pure and Applied Chemistry*, 46(4):397–404, 2009.

[88] Tasuku Horiuchi, Takamasa Sakai, Yusuke Sanada, Keisuke Watanabe, Misako Aida, and Yukiteru Katsumoto. Association behavior of poly(ethylene oxide)-poly(propylene oxide) alternating multiblock copolymers in water toward thermally induced phase separation. *Langmuir*, 33(51):14649–14656, 2017.

[89] Tasuku Horiuchi, Kazuaki Rikiyama, Kenji Sakanaya, Yusuke Sanada, Keisuke Watanabe, Misako Aida, and Yukiteru Katsumoto. Effect of molecular weight on cloud point of aqueous solution of poly(ethylene oxide)– poly(propylene oxide) alternating multiblock copolymer. *Journal of Oleo Science*, 69(5):449–453, 2020.

[90] G. N. Lewis. The atom and the molecule. *Journal of the American Chemical Society*, 38(4):762–785, 1916.

[91] Jérémy Brassinne, Charles André Fustin, and Jean François Gohy. Polymer gels constructed through metal-ligand coordination. *Journal of Inorganic and Organometallic Polymers and Materials*, 23(1):24–40, 2013.

[92] Manuela Chiper, Richard Hoogenboom, and Ulrich S. Schubert. Toward main chain metallo-terpyridyl supramolecular polymers: "The metal does the trick". *Macromolecular Rapid Communications*, 30(8):565–578, 2009.

[93] Raja Shunmugam and Gregory N. Tew. Polymers that contain ligated metals in their side chain: Building a foundation for functional materials in opto-electronic applications with an emphasis on lanthanide ions. *Macromolecular Rapid Communications*, 29(16):1355–1362, 2008.

[94] Raja Shunmugam, Gregory J. Gabriel, Khaled A. Aamer, and Gregory N. Tew. Metal-ligand-containing polymers: Terpyridine as the supramolecular unit. *Macromolecular Rapid Communications*, 31(9-10):784–793, 2010.

[95] Xufeng Wu and Cassandra L. Fraser. Architectural diversity via metal template-assisted polymer synthesis: a macroligand chelation approach to linear and star-shaped polymeric ruthenium tris(bipyridine) complexes. *Macromolecules*, 33(11):4053–4060, 2000.

[96] Ravindra R. Pal, Masayoshi Higuchi, and Dirk G. Kurth. Optically active metallo-supramolecular polymers derived from chiral bis-terpyridines. *Organic Letters*, 11(16):3562–3565, 2009.

[97] Blayne M. McKenzie and Stuart J. Rowan. *Metallosupramolecular polymers, networks, and gels*. John Wiley and Sons, 2008.

[98] H Irving and R J P Williams. The stability of transition-metal complexes. *Journal of the American Chemical Society*, 3192-3210, 1953.

[99] Joseph I. Bullock and Peter W.G. Simpson. Effect of temperature on the protonation constants of terpyridyl and the stability constant of the bis-terpyridyl iron(II) cation. *Journal of the Chemical Society, Faraday Transactions 1*, 7711:1991–1997, 1981.

[100] R. Farina, R. Hogg, and R.G. Wilkins. Rate-pH profile for the dissociation of Iron(II)-and Cobalt(II)-terpyridine complexes. *Inorganic Chemistry*, 7(1):170–172, 1967.

[101] Torsten Rossow, Axel Habicht, and Sebastian Seiffert. Relaxation and dynamics in transient polymer model networks. *Macromolecules*, 47(18):6473–6482, 2014.

[102] Stuart J. Rowan and J. Benjamin Beck. Metal-ligand induced supramolecular polymerization: A route to responsive materials. *Faraday Discussions*, 128:43–53, 2005.

[103] R.H. Holyer, C.D. Hubbard, S.F.A. Kettle, and Wilki. The kinetics of replacement reactions of complexes of the transition metals with terpyridine. *Inorganic Chemistry*, 5(6):622–625, 1966.

[104] Amir Jangizehi, Mostafa Ahmadi, and Sebastian Seiffert. Emergence, evidence, and effect of junction clustering in supramolecular polymer materials. *Materials Advances*, 2(5):1425–1453, 2021.

[105] Patricia Y.W. Dankers, Thomas M. Hermans, Travis W. Baughman, Yuko Kamikawa, Roxanne E. Kieltyka, Maartje M.C. Bastings, Henk M. Janssen, Nico A.J.M. Sommerdijk, Antje Larsen, Marja J.A. Van Luyn, Anton W. Bosman, Eliane R. Popa, George Fytas, and E. W. Meijer. Hierarchical formation of supramolecular transient networks in water: A modular injectable delivery system. *Advanced Materials*, 24(20):2703–2709, 2012.

[106] Roxanne E. Kieltyka, A. C.H. Pape, Lorenzo Albertazzi, Yoko Nakano, Maartje M.C. Bastings, Ilja K. Voets, Patricia Y.W. Dankers, and E. W. Meijer. Mesoscale modulation of supramolecular ureidopyrimidinone-based poly(ethylene glycol) transient networks in water. *Journal of the American Chemical Society*, 135(30):11159–11164, 2013.

[107] Mingyu Guo, Louis M. Pitet, Hans M. Wyss, Matthijn Vos, Patricia Y.W. Dankers, and E. W. Meijer. Tough stimuli-responsive supramolecular hydrogels with hydrogen-bonding network junctions. *Journal of the American Chemical Society*, 136(19):6969–6977, 2014.

[108] Han Gao, Ning Wang, Xiufeng Hu, Wenjing Nan, Yanjiao Han, and Wenguang Liu. Double hydrogen-bonding pH-sensitive hydrogels retaining high-strengths over a wide pH range. *Macromolecular Rapid Communications*, 34(1):63–68, 2013.

[109] Xiaobo Hu, Mohammad Vatankhah-Varnoosfaderani, Jing Zhou, Qiaoxi Li, and Sergei S. Sheiko. Weak hydrogen bonding enables hard, strong, tough and elastic hydrogels. *Advanced Materials*, 27(43):6899–6905, 2015.

[110] Martien A. Cohen Stuart, Bas Hofs, Ilja K. Voets, and Arie De Keizer. Assembly of polyelectrolyte-containing block copolymers in aqueous media. *Current Opinion in Colloid and Interface Science*, 10(1-2):30–36, 2005.

[111] Marc Lemmers, Joris Sprakel, Ilja K. Voets, Jasper Van Der Gucht, and Martien A. Cohen Stuart. Multiresponsive reversible gels based on chargedriven assembly. *Angewandte Chemie - International Edition*, 49(4):708–711, 2010.

[112] Jasmine N. Hunt, Kathleen E. Feldman, Nathaniel A. Lynd, Joanna Deek, Luis M. Campos, Jason M. Spruell, Blanca M. Hernandez, Edward J. Kramer, and Craig J. Hawker. Tunable, high modulus hydrogels driven by ionic coacervation. *Advanced Materials*, 23(20):2327–2331, 2011.

[113] Matthew S. Menyo, Craig J. Hawker, and J. Herbert Waite. Versatile tuning of supramolecular hydrogels through metal complexation of oxidation-resistant catechol-inspired ligands. *Soft Matter*, 9(43):10314–10323, 2013.

[114] Florian D. Jochum, Jérémy Brassinne, Charles André Fustin, and Jean François Gohy. Metallo-supramolecular hydrogels based on copolymers bearing terpyridine side-chain ligands. *Soft Matter*, 9(7):2314–2320, 2013.

[115] Guosong Chen and Ming Jiang. Cyclodextrin-based inclusion complexation bridging supramolecular chemistry and macromolecular self-assembly. *Chemical Society Reviews*, 40(5):2254–2266, 2011.

[116] Guiting Liu, Qijuan Yuan, Geoffrey Hollett, Wei Zhao, Yang Kang, and Jun Wu. Cyclodextrin-based host-guest supramolecular hydrogel and its application in biomedical fields. *Polymer Chemistry*, 9(25):3436–3449, 2018.

[117] Deniz C. Tuncaboylu, Murat Sari, Wilhelm Oppermann, and Oguz Okay. Tough and self-healing hydrogels formed via hydrophobic interactions. *Macromolecules*, 44(12):4997–5005, 2011.

[118] Insu Jeon, Jiaxi Cui, Widusha R.K. Illeperuma, Joanna Aizenberg, and Joost J. Vlassak. Extremely stretchable and fast self-healing hydrogels. *Advanced Materials*, 28(23):4678–4683, 2016.

[119] Leqi Fan, Xuemei Ge, Yebin Qian, Minyan Wei, Zirui Zhang, Wei En Yuan, and Yuanming Ouyang. Advances in synthesis and applications of self-healing hydrogels. *Frontiers in Bioengineering and Biotechnology*, 8:1–14, 2020.

[120] Constantinos Tsitsilianis. Responsive reversible hydrogels from associative "smart" macromolecules. *Soft Matter*, 6(11):2372–2388, 2010.

[121] Jiaul Hoque, Nivedita Sangaj, and Shyni Varghese. Stimuli-responsive supramolecular hydrogels and their applications in regenerative medicine. *Macromolecular Bioscience*, 19(1):1–16, 2019.

[122] Jiaojiao Shang, Xiaoxia Le, Jiawei Zhang, Tao Chen, and Patrick Theato. Trends in polymeric shape memory hydrogels and hydrogel actuators. *Polymer Chemistry*, 10(9):1036–1055, 2019.

[123] Liang Dong and Hongrui Jiang. Autonomous microfluidics with stimuli-responsive hydrogels. *Soft Matter*, 3(10):1223–1230, 2007.

[124] Esra Su, Mine Yurtsever, and Oguz Okay. A self-healing and highly stretchable polyelectrolyte hydrogel via cooperative hydrogen bonding as a superabsorbent polymer. *Macromolecules*, 52(9):3257–3267, 2019.

[125] J. Zachary Hilt, Amit K. Gupta, Rashid Bashir, and Nicholas A. Peppas. Ultrasensitive biomens sensors based on microcantilevers patterned with environmentally responsive hydrogels. *Biomedical Microdevices*, 5(3):177–184, 2003.

[126] Nuri Park and Jaeyun Kim. Hydrogel-based artificial muscles: overview and recent progress. *Advanced Intelligent Systems*, 2(4):1900135, 2020.

[127] Christophe Chassenieux, Taco Nicolai, and Lazhar Benyahia. Rheology of associative polymer solutions. *Current Opinion in Colloid and Interface Science*, 16(1):18–26, 2011.

[128] Elham Eghbali, Olivier Colombani, Markus Drechsler, Axel H.E. Müller, and Heinz Hoffmann. Rheology and phase behavior of poly(n-butyl acrylate)-block-poly(acrylic acid) in aqueous solution. *Langmuir*, 22(10):4766–4776, 2006.

[129] Michihiro Ogura, Hiroyuki Tokuda, Shin Ichiro Imabayashi, and Masayoshi Watanabe. Preparation and solution behavior of a thermoresponsive diblock copolymer of poly(ethyl glycidyl ether) and poly(ethylene oxide). *Langmuir*, 23(18):9429–9434, 2007.

[130] Jeppe Madsen and Steven P. Armes. (Meth)acrylic stimulus-responsive block copolymer hydrogels. *Soft Matter*, 8(3):592–605, 2012.

[131] Chengming Li, Niklaas J. Buurma, Ihtshamul Haq, Colin Turner, Steven P. Armes, Valeria Castelletto, Ian W. Hamley, and Andrew L. Lewis. Synthesis and characterization of biocompatible, thermoresponsive ABC and ABA triblock copolymer gelators. *Langmuir*, 21(24):11026–11033, 2005.

[132] V. Castelletto, I. W. Hamley, X. F. Yuan, A. Kelarakis, and C. Booth. Structure and rheology of aqueous micellar solutions and gels formed from an associative poly(oxybutylene)-poly(oxyethylene)-poly(oxybutylene) triblock copolymer. *Soft Matter*, 1(2):138–145, 2005.

[133] Soo Jin Bae, Ju Myung Suh, Youn Soo Sohn, You Han Bae, Sung Wan Kim, and Byeongmoon Jeong. Thermogelling poly(caprolactone-b-ethylene glycol-b-caprolactone) aqueous solutions. *Macromolecules*, 38(12):5260–5265, 2005.

[134] Naomi Sanabria-DeLong, Sarvesh K. Agrawal, Surita R. Bhatia, and Gregory N. Tew. Impact of synthetic technique on PLA-PEO-PLA physical hydrogel properties. *Macromolecules*, 40(22):7864–7873, 2007.

[135] Sarvesh K. Agrawal, Naomi Sanabria-DeLong, Gregory N. Tew, and Surita R. Bhatia. Structural characterization of PLA-PEO-PLA solutions and hydrogels: Crystalline vs. amorphous PLA domains. *Macromolecules*, 41(5):1774–1784, 2008.

[136] Yiyong He, Paul G. Boswell, Philippe Bühlmann, and Timothy P. Lodge. Ion gels by self-assembly of a triblock copolymer in an ionic liquid. *Journal of Physical Chemistry B*, 111(18):4645–4652, 2007.

[137] Yiyong He and Timothy P. Lodge. Thermoreversible ion gels with tunable melting temperatures from triblock and pentablock copolymers. *Macromolecules*, 41(1):167–174, 2008.

[138] Michelle E. Seitz, Wesley R. Burghardt, K. T. Faber, and Kenneth R. Shull. Self-assembly and stress relaxation in acrylic triblock copolymer gels. *Macromolecules*, 40(4):1218–1226, 2007.

[139] M. E. Cates and S. J. Candau. Statics and dynamics of worm-like surfactant micelles. *Journal of Physics: Condensed Matter*, 2(33):6869–6892, 1990.

[140] M. E. Cates and S. M. Fielding. Rheology of giant micelles. In *Advances in Physics*, volume 55(7-8), pages 799–879. Taylor and Francis, 2006.

[141] S. Förster, B. Berton, H. P. Hentze, E. Krämer, M. Antonietti, and P. Lindner. Lyotropic phase morphologies of amphiphilic block copolymers. *Macromolecules*, 34(13):4610–4623, 2001.

[142] You Yeon Won, Kristofer Paso, H. Ted Davis, and Frank S. Bates. Comparison of original and cross-linked wormlike micelles of poly(ethylene oxide-b-butadiene) in water: Rheological properties and effects of poly(ethylene oxide) addition. *Journal of Physical Chemistry B*, 105(35):8302–8311, 2001.

[143] Sumeet Jain and Frank S. Bates. On the origins of morphological complexity in block copolymer surfactants. *Science*, 300(5618):460–464, 2003.

[144] Sumeet Jain and Frank S. Bates. Consequences of Nonergodicity in Aqueous Binary PEO-PB Micellar Dispersions. *Macromolecules*, 37(4):1511–1523, 2004.

[145] Antonio Tavera-Vázquez, Brisa Arenas-Gómez, Cristina Garza, Yun Liu, and Rolando Castillo. Structure, rheology, and microrheology of wormlike micelles made of PB-PEO diblock copolymers. *Soft Matter*, 14(35):7264–7276, 2018.

[146] Ronald G. Larson, Antony K. Van Dyk, Tirtha Chatterjee, and Valeriy V. Ginzburg. Associative thickeners for waterborne paints: Structure, characterization, rheology, and modeling. *Progress in Polymer Science*, 129:101546, 2022.

[147] Tom Annable, Richard Buscall, Rammile Ettelaie, and Diane Whittlestone. The rheology of solutions of associating polymers: Comparison of experimental behavior with transient network theory. *Journal of Rheology*, 37(4):695–726, 1993.

[148] Tom Annable, Richard Buscall, and Rammile Ettelaie. Network formation and its consequences for the physical behaviour of associating polymers in solution. *Colloids and Surfaces A: Physicochemical and Engineering Aspects*, 112(2-3):97–116, 1996.

[149] W. K. Ng, K. C. Tam, and R. D. Jenkins. Lifetime and network relaxation time of a HEUR-C20 associative polymer system. *Journal of Rheology*, 44(1):137–147, 2000.

[150] Linda Pellens, Rogelio Gamez Corrales, and Jan Mewis. General nonlinear rheological behavior of associative polymers. *Journal of Rheology*, 48(2):379–393, 2004.

[151] Linda Pellens, Kyun Hyun Ahn, Seung Jong Lee, and Jan Mewis. Evaluation of a transient network model for telechelic associative polymers. *Journal of Non-Newtonian Fluid Mechanics*, 121(2-3):87–100, 2004.

[152] Anubhav Tripathi, Kam C. Tam, and Gareth H. McKinley. Rheology and dynamics of associative polymers in shear and extension: Theory and experiments. *Macromolecules*, 39(5):1981–1999, 2006.

[153] Michael Rubinstein and Ralph H. Colby. *Polymer Physics*. Oxford University Press, Oxford, 2003.

[154] Rui Wang, Alfredo Alexander-Katz, Jeremiah A. Johnson, and Bradley D. Olsen. Universal cyclic topology in polymer networks. *Physical Review Letters*, 116(18):1–5, 2016.

[155] Mingjiang Zhong, Rui Wang, Ken Kawamoto, Bradley D. Olsen, and Jeremiah A. Johnson. Quantifying the impact of molecular defects on polymer network elasticity. *Science*, 353(6305):1264–1268, 2016.

[156] Xiao-Xia Meng and William B. Russel. Rheology of telechelic associative polymers in aqueous solutions. *Journal of Rheology*, 50(2):189–205, 2006.

[157] Tsutomu Indei. Rheological study of transient networks with junctions of limited multiplicity. *Journal of Chemical Physics*, 127(14), 2007.

[158] Jean François Berret, Damien Calvet, André Collet, and Michel Viguier. Fluorocarbon associative polymers. *Current Opinion in Colloid and Interface Science*, 8(3):296–306, 2003.

[159] G Marrucci, S Bhargava, and S.L Cooper. Models of shear-thickening behavior in physically cross-linked networks. *Macromolecules*, 26:6483–6488, 1993.

[160] Linda Pellens, Jan Vermant, and Jan Mewis. Deviations from the stress-optical rule in telechelic associative polymer solutions. *Macromolecules*, 38(5):1911–1918, 2005.

[161] Joris Sprakel, Jasper Van Der Gucht, Martien A. Cohen Stuart, and Nicolaas A.M. Besseling. Brownian particles in transient polymer networks. *Physical Review E - Statistical, Nonlinear, and Soft Matter Physics*, 77(6):1–10, 2008.

[162] Naomi Sanabria-DeLong, Sarvesh K. Agrawal, Surita R. Bhatia, and Gregory N. Tew. Controlling hydrogel properties by crystallization of hydrophobic domains. *Macromolecules*, 39(4):1308–1310, 2006.

[163] Sarvesh K. Agrawal, Naomi Sanabria-DeLong, Gregory N. Tew, and Surita R. Bhatia. Rheological characterization of biocompatible associative polymer hydrogels with crystalline and amorphous endblocks. *Journal of Materials Research*, 21(8):2118–2125, 2006.

[164] Soo Jin Bae, Min Kyung Joo, Yuri Jeong, Sung Wook Kim, Woo Kul Lee, Youn Soo Sohn, and Byeongmoon Jeong. Gelation behavior of poly(ethylene glycol) and polycaprolactone triblock and multiblock copolymer aqueous solutions. *Macromolecules*, 39(14):4873–4879, 2006.

[165] Dharmista Mistry, Tom Annable, Xue Feng Yuan, and Colin Booth. Rheological behavior of aqueous micellar solutions of a triblock copolymer of ethylene oxide and 1,2-butylene oxide: B10e410B 10. *Langmuir*, 22(7):2986–2992, 2006.

[166] Tina Vermonden, Nicolaas A.M. Besseling, Mies J. Van Steenbergen, and Wim E. Hennink. Rheological studies of thermosensitive triblock copolymer hydrogels. *Langmuir*, 22(24):10180–10184, 2006.

[167] Tina Vermonden, Sidhartha S Jena, David Barriet, Roberta Censi, Jasper Van Der, Wim E Hennink, and Ronald A Siegel. Macromolecular diffusion in self-assembling biodegradable thermosensitive hydrogels. *Macromolecules*, 43(2):782–789, 2010.

[168] Enrique Jiménez Regalado, Joseph Selb, and Françoise Candau. Viscoelastic behavior of semidilute solutions of multisticker polymer chains. *Macromolecules*, 32(25):8580–8588, 1999.

[169] Charles L. McCormick, Takamasa Nonaka, and C. Brent Johnson. Water-soluble copolymers: 27. Synthesis and aqueous solution behaviour of associative acrylamide N-alkylacrylamide copolymers. *Polymer*, 29(4):731–739, 1988.

[170] Edgar Volpert, Joseph Selb, and Francoise Candau. Associating behaviour of polyacrylamides hydrophobically modified with dihexylacrylamide. *Polymer*, 39(5):1025–1033, 1998.

[171] Alain Hill, Françoise Candau, and Joseph Selb. Properties of hydrophobically associating polyacrylamides: Influence of the method of synthesis. *Macromolecules*, 26(17):4521–4532, 1993.

[172] F S Hwang. Effects of water-soluble spacers on the hydrophobic association of fluorocarbon-modified poly(acrylamide). *Macromolecules*, 28(9):3328–3335, 1995.

[173] Françoise Candau and Joseph Selb. Hydrophobically-modified polyacrylamides prepared by micellar polymerization. *Advances in Colloid and Interface Science*, 79(2-3):149–172, 1999.

[174] Sandra L. Cram, Hugh R. Brown, Geoffrey M. Spinks, Dominique Hourdet, and Costantino Creton. Hydrophobically modified dimethylacrylamide synthesis and rheological behavior. *Macromolecules*, 38(7):2981–2989, 2005.

[175] Laurence Petit, Carole Karakasyan, Nadège Pantoustier, and Dominique Hourdet. Synthesis of graft polyacrylamide with responsive self-assembling properties in aqueous media. *Polymer*, 48(24):7098–7112, 2007.

[176] Laura M. Gouveia, Bruno Grassl, and Alejandro J. Müller. Synthesis and rheological properties of hydrophobically modified polyacrylamides with lateral chains of poly(propylene oxide) oligomers. *Journal of Colloid and Interface Science*, 333(1):152–163, 2009.

[177] Jisun Lee, You Han Bae, Youn Soo Sohn, and Byeongmoon Jeong. Thermogelling aqueous solutions of alternating multiblock copolymers of poly(L-lactic acid) and poly(ethylene glycol). *Biomacromolecules*, 7(6):1729–1734, 2006.

[178] Jin Woo Lee, Feng jun Hua, and Doo Sung Lee. Thermoreversible gelation of biodegradable poly(ε-caprolactone) and poly(ethylene glycol) multiblock copolymers in aqueous solutions. *Journal of Controlled Release*, 73(2-3):315–327, 2001.

[179] Jin Sun Ahn, Ju Myung Suh, Minyung Lee, and Byeongmoon Jeong. Slow eroding biodegradable multiblock poloxamer copolymers. *Polymer International*, 54(5):842–847, 2005.

[180] Jos M.J. Paulusse, D. J.M. Van Beek, and Pint P. Sijbesma. Reversible switching of the sol-gel transition with ultrasound in rhodium(I) and iridium(I) coordination networks. *Journal of the American Chemical Society*, 129(8):2392–2397, 2007.

[181] Tina Vermonden, Wiebe M. De Vos, Antonius T.M. Marcelis, and Ernst J.R. Sudhölter. 3-D water-soluble reversible neodymium(III) and lanthanum(III) coordination polymers. *European Journal of Inorganic Chemistry*, 14:2847–2852, 2004.

[182] S. Schmatloch and U. S. Schubert. Engineering with metallo-supramolecular polymers: Linear coordination polymers and networks. *Macromolecular Symposia*, 199:483–498, 2003.

[183] Mutsumi Kimura, Yasushi Nakagawa, Naoya Adachi, Yoko Tatewaki, Tadashi Fukawa, and Hirofusa Shirai. Metallosupramolecular gels made of four-armed poly(ethylene glycol)s having terpyridine termini. *Chemistry Letters*, 38(4):382–383, 2009.

[184] Harald Hofmeier and Ulrich S. Schubert. Supramolecular branching and crosslinking of terpyridine-modified copolymers: Complexation and decomplexation studies in diluted solution. *Macromolecular Chemistry and Physics*, 204(11):1391–1397, 2003.

[185] Christina Ott, Christoph Ulbricht, Richard Hoogenboom, and Ulrich S. Schubert. Metallo-supramolecular materials based on amine-grafting onto polypentafluorostyrene. *Macromolecular Rapid Communications*, 33(6-7):556–561, 2012.

[186] Robert M. Meudtner and Stefan Hecht. Responsive backbones based on alternating triazole-pyridine/benzene copolymers: From helically folding polymers to metallosupramolecularly crosslinked gels. *Macromolecular Rapid Communications*, 29(4):347–351, 2008.

[187] C. Huber, F. Bangerter, W. R. Caseri, and C. Weder. Complexation of unsaturated carbon-carbon bonds in π-conjugated polymers with transition metals. *Journal of the American Chemical Society*, 123(17):3857–3863, 2001.

[188] Hiroshi Yokoi, Satoshi Kawata, and Masamoto Iwaizumi. Interaction modes between heavy metal ions and water-soluble polymers. 2. Spectroscopic and magnetic reexamination of the aqueous solutions of cupric ions and poly(acrylic acid). *Journal of the American Chemical Society*, 108(12):3361–3365, 1986.

[189] E. Pezron, A. Ricard, F. Lafuma, and R. Audebert. Reversible gel formation induced by ion complexation. 1. Borax-galactomannan Interactions. *Macromolecules*, 21(4):1121–1125, 1988.

[190] Kenji Kamide, Katsunari Yasuda, and Kunihiko Okajima. C-NMR study on gelation of aqueous carboxyethylcellulose with total degree of substitution of solution induced by metal cations. *Polymer Journal*, 20(3):259–268, 1988.

[191] Jinchun Yuan, Xiuli Fang, Lingxing Zhang, Guangning Hong, Yangju Lin, Qifeng Zheng, Yuanze Xu, Yonghong Ruan, Wengui Weng, Haiping Xia, and Guohua Chen. Multi-responsive self-healing metallo-supramolecular gels based on "click" ligand. *Journal of Materials Chemistry*, 22(23):11515–11522, 2012.

[192] Xavier De Hatten, Nicholas Bell, Nataliya Yufa, Gabriel Christmann, and Jonathan R. Nitschke. A dynamic covalent, luminescent metallopolymer that undergoes sol-to-gel transition on temperature rise. *Journal of the American Chemical Society*, 133(9):3158–3164, 2011.

[193] Tina Vermonden, Mies J. Van Steenbergen, Nicolaas A.M. Besseling, Antonius T.M. Marcelis, Wim E. Hennink, Ernst J.R. Sudhölter, and Martien A. Cohen Stuart. Linear rheology of water-soluble reversible neodymium(III) coordination polymers. *Journal of the American Chemical Society*, 126(48):15802–15808, 2004.

[194] Scott C. Grindy, Martin Lenz, and Niels Holten-Andersen. Engineering elasticity and relaxation time in metal-coordinate cross-linked hydrogels. *Macromolecules*, 49(21):8306–8312, 2016.

[195] Niels Holten-Andersen, Matthew J. Harrington, Henrik Birkedal, Bruce P. Lee, Phillip B. Messersmith, Ka Yee C. Lee, and J. Herbert Waite. pH-induced metal-ligand cross-links inspired by mussel yield self-healing polymer networks with near-covalent elastic moduli. *Proceedings of the National Academy of Sciences of the United States of America*, 108(7):2651–2655, 2011.

[196] Bruce P. Lee, Jeffrey L. Dalsin, and Phillip B. Messersmith. Synthesis and gelation of DOPA-modified poly(ethylene glycol) hydrogels. *Biomacromolecules*, 3(5):1038–1047, 2002.

[197] Dominic E. Fullenkamp, Lihong He, Devin G. Barrett, Wesley R. Burghardt, and Phillip B. Messersmith. Mussel-inspired histidine-based transient network metal coordination hydrogels. *Macromolecules*, 46(3):1167–1174, 2013.

[198] Torsten Rossow and Sebastian Seiffert. Supramolecular polymer gels with potential model-network structure. *Polymer Chemistry*, 5(8):3018–3029, 2014.

[199] F. Tanaka and S. F. Edwards. Viscoelastic properties of physically cross-linked networks. Transient network theory. *Macromolecules*, 25(5):1516–1523, 1992.

[200] F. Tanaka and S. F. Edwards. Viscoelastic properties of physically crosslinked networks. Part 1. Non-linear stationary viscoelasticity. *Journal of Non-Newtonian Fluid Mechanics*, 43(2-3):247–271, 1992.

[201] F. Tanaka and S.F. Edwards. Viscoelastic properties of physically crosslinked networks. *Journal of Non-Newtonian Fluid Mechanics*, 43(2-3):289–309, 1992.

[202] F. Tanaka and S. F. Edwards. Viscoelastic properties of physically crosslinked networks. Part 3. Time-dependent phenomena. *Journal of Non-Newtonian Fluid Mechanics*, 43(2-3):289–309, 1992.

[203] M. E. Cates. Reptation of living polymers: dynamics of entangled polymers in the presence of reversible chain-scission reactions. *Macromolecules*, 20(9):2289–2296, 1987.

[204] A. N. Semenov, J. F. Joanny, and A. R. Khokhlov. Associating polymers: Equilibrium and linear viscoelasticity. *Macromolecules*, 28(4):1066–1075, 1995.

[205] L. G. Baxandall. Dynamics of reversibly cross-linked chains. *Macromolecules*, 22(4):1982–1988, 1989.

[206] Alexander N. Semenov and Michael Rubinstein. Thermoreversible gelation in solutions of associative polymers. 1. Statics. *Macromolecules*, 31(4):1373–1385, 1998.

[207] Alexander N. Semenov and Michael Rubinstein. Thermoreversible gelation in solutions of associative polymers. 2. Linear dynamics. *Macromolecules*, 31(4):1386–1397, 1998.

[208] Ludwik Leibler, Michael Rubinstein, and Ralph H. Colby. Dynamics of reversible networks. *Macromolecules*, 24(16):4701–4707, 1991.

[209] Michael Rubinstein and Alexander N. Semenov. Dynamics of entangled solutions of associating polymers. *Macromolecules*, 34(4):1058–1068, 2001.

[210] A. N. Semenov and Michael Rubinstein. Dynamics of entangled associating polymers with large aggregates. *Macromolecules*, 35(12):4821–4837, 2002.

[211] M. S. Green and A. V. Tobolsky. A new approach to the theory of relaxing polymeric media. *Journal of Chemical Physics*, 14(2):80–92, 1946.

[212] Misazo Yamamoto. The visco-elastic properties of network structure I. General formalism. *Journal of the Physical Society of Japan*, 11(4):413–421, 1956.

[213] A S Lodge. A network theory of flow birefringence and stress in concentrated polymer solutions. *Transactions of the Faraday Society*, 52:120–130, 1956.

[214] A. Vaccaro and G. Marrucci. A model for the nonlinear rheology of associating polymers. *Journal of Non-Newtonian Fluid Mechanics*, 92(2-3):261–273, 2000.

[215] B. H.A.A. van den Brule and P. J. Hoogerbrugge. Brownian dynamics simulation of reversible polymeric networks. *Journal of Non-Newtonian Fluid Mechanics*, 60(2-3):303–334, 1995.

[216] J. G. Hernández Cifre, T. M.A.O.M. Barenbrug, J. D. Schieber, and B. H.A.A. van den Brule. Brownian dynamics simulation of reversible polymer networks under shear using a non-interacting dumbbell model. *Journal of Non-Newtonian Fluid Mechanics*, 113(2-3):73–96, 2003.

[217] Shi Qing Wang. Transient network theory for shear-thickening fluids and physically crosslinked networks. *Macromolecules*, 25(25):7003–7010, 1992.

[218] Kyung Hyun Ahn and Kunihiro Osaki. Mechanism of shear thickening investigated by a network model. *Journal of Non-Newtonian Fluid Mechanics*, 56(3):267–288, 1995.

[219] I. A. Nyrkova and A. N. Semenov. Correlation effects in dynamics of living polymers. *Europhysics Letters*, 79(6):66007, 2007.

[220] W. Knoben, N. A.M. Besseling, L. Bouteiller, and M. A.Cohen Stuart. Dynamics of reversible supramolecular polymers: Independent determination of the dependence of linear viscoelasticity on concentration and chain length by using chain stoppers. *Physical Chemistry Chemical Physics*, 7(11):2390–2398, 2005.

[221] W. Knoben, N. A.M. Besseling, and M. A. Cohen Stuart. Rheology of a reversible supramolecular polymer studied by comparison of the effects of temperature and chain stoppers. *Journal of Chemical Physics*, 126(2), 2007.

[222] Q. T. Pham, W. B. Russel, J. C. Thibeault, and W. Lau. Micellar solutions of associative triblock copolymers: the relationship between structure and rheology. *Macromolecules*, 32(15):5139–5146, 1999.

[223] Dipesh Amin, Alexei E. Likhtman, and Zuowei Wang. Dynamics in supramolecular polymer networks formed by associating telechelic chains. *Macromolecules*, 49(19):7510–7524, 2016.

[224] Bai Xu, Ahmad Yekta, Lin Li, Zahra Masoumi, and Mitchell A. Winnik. The functionality of associative polymer networks: The association behavior of hydrophobically modified urethane-ethoxylate (HEUR) associative polymers in aqueous solution. *Colloids and Surfaces A: Physicochemical and Engineering Aspects*, 112(2-3):239–250, 1996.

[225] Anton Mordvinkin, Diana Döhler, Wolfgang H. Binder, Ralph H. Colby, and Kay Saalwächter. Terminal flow of cluster-forming supramolecular polymer networks: Single-chain relaxation or micelle reorganization? *Physical Review Letters*, 125(12):127801, 2020.

[226] Anton Mordvinkin, Diana Döhler, Wolfgang H. Binder, Ralph H. Colby, and Kay Saalwächter. Rheology, sticky chain and sticker dynamics of supramolecular elastomers based on cluster-forming telechelic linear and star polymers. *Macromolecules*, 54(11):5065–5076, 2021.

[227] Milad Golkaram and Katja Loos. A critical approach to polymer dynamics in supramolecular polymers. *Macromolecules*, 52(24):9427–9444, 2019.

[228] R. H. W. Wientjes, R. J. J. Jongschaap, M. H. G. Duits, and J. Mellema. A new transient network model for associative polymer networks. *Journal of Rheology*, 43(2):375–391, 1999.

[229] R. J.J. Jongschaap, R. H.W. Wientjes, M. H.G. Duits, and J. Mellema. Generalized transient network model for associative polymer networks. *Macromolecules*, 34(4):1031–1038, 2001.

[230] Tsutomu Indei and Jun Ichi Takimoto. Linear viscoelastic properties of transient networks formed by associating polymers with multiple stickers. *Journal of Chemical Physics*, 133(19), 2010.

[231] Robert D. Groot and Wim G.M. Agterof. Monte Carlo study of associative polymer networks. II. Rheologic aspects. *The Journal of Chemical Physics*, 100(2):1657–1664, 1994.

[232] Robert D. Groot and Wim G.M. Agterof. Dynamic viscoelastic modulus of associative polymer networks: Off-lattice simulations, theory and comparison to experiments. *Macromolecules*, 28(18):6284–6295, 1995.

[233] Quan Chen, Zhijie Zhang, and Ralph H. Colby. Viscoelasticity of entangled random polystyrene ionomers. *Journal of Rheology*, 60(6):1031–1040, 2016.

[234] Zhijie Zhang, Quan Chen, and Ralph H. Colby. Dynamics of associative polymers. *Soft Matter*, 14(16):2961–2977, 2018.

[235] Joon Seop Kim, Katsuyuki Yoshikawa, and Adi Eisenberg. Molecular weight dependence of the viscoelastic properties of polystyrene-based ionomers. *Macromolecules*, 27(22):6347–6357, 1994.

[236] Kathleen E. Feldman, Matthew J. Kade, E. W. Meijer, Craig J. Hawker, and Edward J. Kramer. Model transient networks from strongly hydrogen-bonded polymers. *Macromolecules*, 42(22):9072–9081, 2009.

[237] Donghua Xu and Stephen L. Craig. Scaling laws in supramolecular polymer networks. *Macromolecules*, 44(13):5465–5472, 2011.

[238] Sebastian Hackelbusch, Torsten Rossow, and Peter Van Assenbergh. Chain dynamics in supramolecular polymer networks. *Macromolecules*, 46(15):6273–6286, 2013.

[239] Jente Verjans, Alexis André, Evelyne Van Ruymbeke, and Richard Hoogenboom. Physically cross-linked polybutadiene by quadruple hydrogen bonding through side-chain incorporation of ureidopyrimidinone with branched alkyl side chains. *Macromolecules*, 55(3):928–941, 2022.

[240] Piotr Kujawa, Annie Audibert-Hayet, Joseph Selb, and Françoise Candau. Effect of ionic strength on the rheological properties of multisticker associative polyelectrolytes. *Macromolecules*, 39(1):384–392, 2006.

[241] Quan Chen, Gregory J. Tudryn, and Ralph H. Colby. Ionomer dynamics and the sticky Rouse model. *Journal of Rheology*, 57(5):1441–1462, 2013.

[242] Quan Chen, Chongwen Huang, R. A. Weiss, and Ralph H. Colby. Viscoelasticity of reversible gelation for ionomers. *Macromolecules*, 48(4):1221–1230, 2015.

[243] Zhijie Zhang, Chang Liu, Xiao Cao, Longcheng Gao, and Quan Chen. Linear viscoelastic and dielectric properties of strongly hydrogen-bonded polymers near the sol-gel transition. *Macromolecules*, 49(23):9192–9202, 2016.

[244] Aamir Shabbir, Irakli Javakhishvili, Silvina Cerveny, Søren Hvilsted, Anne L. Skov, Ole Hassager, and Nicolas J. Alvarez. Linear viscoelastic and dielectric relaxation response of unentangled UPy-based supramolecular networks. *Macromolecules*, 49(10):3899–3910, 2016.

[245] Guanghui Cui, Victor A. H. Boudara, Qian Huang, Guilhem P. Baeza, Andrew J. Wilson, Ole Hassager, Daniel J. Read, and Johan Mattsson. Linear shear and nonlinear extensional rheology of unentangled supramolecular side-chain polymers. *Journal of Rheology*, 62(5):1155–1174, 2018.

[246] B. J. Gold, C. H. Hövelmann, N. Lühmann, N. K. Székely, W. Pyckhout-Hintzen, A. Wischnewski, and D. Richter. Importance of compact random walks for the rheology of transient networks. *ACS Macro Letters*, 6(2):73–77, 2017.

[247] B. J. Gold, C. H. Hövelmann, N. Lühmann, W. Pyckhout-Hintzen, A. Wischnewski, and D. Richter. The microscopic origin of the rheology in supramolecular entangled polymer networks. *Journal of Rheology*, 61(6):1211–1226, 2017.

[248] David Myung, Dale Waters, Metedith Wiseman, Pierre-Emile Duhamel, Jaan Noolandi, Christopher N. Ta, and Curtis W. Frank. Progress in the development of interpenetrating polymer networks. *Polymers for Advanced Technologies*, 19(6):647–657, 2008.

[249] Ecaterina Stela Dragan. Design and applications of interpenetrating polymer network hydrogels. A review. *Chemical Engineering Journal*, 243:572–590, 2014.

[250] Qiang Chen, Hong Chen, Lin Zhu, and Jie Zheng. Engineering of tough double network hydrogels. *Macromolecular Chemistry and Physics*, 217(9):1022–1036, 2016.

[251] Xinxin Huang, Jingchao Li, Jing Luo, Qiang Gao, An Mao, and Jianzhang Li. Research progress on double-network hydrogels. *Materials Today Communications*, 29(May):102757, 2021.

[252] Xiaowen Xu, Valentin Victor Jerca, and Richard Hoogenboom. Bioinspired double network hydrogels: From covalent double network hydrogels: Via hybrid double network hydrogels to physical double network hydrogels. *Materials Horizons*, 8(4):1173–1188, 2021.

[253] A. V. Shibaev and O. E. Philippova. New approaches to the design of double polymer networks: A review. *Polymer Science - Series C*, 64(1):26–39, 2022.

[254] Jian Ping Gong, Yoshinori Katsuyama, Takayuki Kurokawa, and Yoshihito Osada. Double-network hydrogels with extremely high mechanical strength. *Advanced Materials*, 15(14):1155–1158, 2003.

[255] Jian Ping Gong. Why are double network hydrogels so tough? *Soft Matter*, 6(12):2583–2590, 2010.

[256] Jian Ping Gong. Materials both tough and soft. *Science*, 344(6180):161–162, 2014.

[257] Xuanhe Zhao, Xiaoyu Chen, Hyunwoo Yuk, Shaoting Lin, Xinyue Liu, and German Parada. Soft materials by design: Unconventional polymer networks give extreme properties. *Chemical Reviews*, 121(8):4309–4372, 2021.

[258] Progyateg Chakma and Dominik Konkolewicz. Dynamic covalent bonds in polymeric materials. *Angewandte Chemie - International Edition*, 58(29):9682–9695, 2019.

[259] A. Klymenko, T. Nicolai, L. Benyahia, C. Chassenieux, O. Colombani, and E. Nicol. Multiresponsive hydrogels formed by interpenetrated self-assembled polymer networks. *Macromolecules*, 47(23):8386–8393, 2014.

[260] Hui Yang, Sina Ghiassinejad, Evelyne Van Ruymbeke, and Charles André Fustin. Tunable Interpenetrating Polymer Network Hydrogels Based on Dynamic Covalent Bonds and Metal-Ligand Bonds. *Macromolecules*, 53(16):6956–6967, 2020.

[261] Hui Yang, Evelyne Van Ruymbeke, and Charles André Fustin. Influence of network topology on the viscoelastic properties of double dynamics hydrogels. *Macromolecules*, 55(12):5058–5070, 2022.

[262] Anna Pagnoux, Marc Dolatkhani, and Patricia Chaffaux. Thermosensitive polymers and thermoreversible gels obtained from these polymers (patent US 7,339,013 B2), 2008.

[263] Geng Li and James SaNogueira. Robust sunscreen compositions, 2021.

[264] Anastasiia Galakhova, Fabian Kadisch, Gregor Mori, Susanne Heyder, Helmut Wieser, Bernhard Sartory, and Simon Burger. Corrosion of stainless steel by urea at high temperature. *Corrosion and Materials Degradation*, 2(3):461–473, 2021.

[265] Theodor Stern. Conclusive chemical deciphering of the consistently occurring double-peak carbonyl-stretching FTIR absorbance in polyurethanes. *Polymers for Advanced Technologies*, 30(3):675–687, 2019.

[266] Søren Hvidt and Walther Batsberg. Characterization and micellization of a poloxamer block copolymer. *International Journal of Polymer Analysis and Characterization*, 12(1):13–22, 2007.

[267] Kell Mortensen, Walther Batsberg, and Søren Hvid. Effects of PEO-PPO diblock impurities on the cubic structure of aqueous PEO-PPO-PEO pluronics micelles: Fee and bcc ordered structures in F127. *Macromolecules*, 41(5):1720–1727, 2008.

[268] Vincent Testard, Julian-Oberdisse, and Christian Ligoure. Monte Carlo simulations of colloidal pair potential induced by telechelic polymers: Statistics of loops and bridges. *Macromolecules*, 41(19):7219–7226, 2008.

[269] P. J. Flory and J. E. Mark. The configuration of the polyoxyethylene chain. *Journal of the American Chemical Society*, 87(7):1415–1423, 1965.

[270] Akihiro Abe, Tsuneo Hirano, and Teiji Tsuruta. Conformational energies and the random-coil configuration of poly(oxypropylene). *Macromolecules*, 12(6):1092–1100, 1979.

[271] Shinsuke Kokubo and Philipp Vana. Easy access to the characteristic ratio of polymers using ion-mobility mass spectrometry. *Macromolecular Chemistry and Physics*, 218(1):1–10, 2017.

[272] G. Allen, C. Booth, and C. Price. III-The unperturbed dimensions of poly(propylene oxide). *Polymer*, 8(C):397–401, 1967.

[273] Edward W. Merrill, Kathleen A. Dennison, and Cynthia Sung. Partitioning and diffusion of solutes in hydrogels of poly(ethylene oxide). *Biomaterials*, 14(15):1117–1126, 1993.

[274] Ulrich S. Schubert, Oliver Hien, and Christian Eschbaumer. Functionalized polymers with metal complexing segments: A simple and high-yield entry towards terpyridine-based oligomers. *Macromolecular Rapid Communications*, 21(16):1156–1161, 2000.

[275] Jan Leys, Patricia Losada-Pérez, Eli Slenders, Christ Glorieux, and Jan Thoen. Investigation of the melting behavior of the reference materials biphenyl and phenyl salicylate by a new type adiabatic scanning calorimeter. *Thermochimica Acta*, 582:68–76, 2014.

[276] Jan Leys, Benoît Duponchel, Stéphane Longuemart, Christ Glorieux, and Jan Thoen. A new calorimetric technique for phase change materials and its application to alkane-based PCMs. *Materials for Renewable and Sustainable Energy*, 5:4, 2016.

[277] Jan Leys, Patricia Losada-Pérez, Christ Glorieux, and Jan Thoen. The melting behaviour of water and water–sodium chloride solutions studied by high-resolution Peltier-element-based adiabatic scanning calorimetry. *Journal of Thermal Analysis and Calorimetry*, 129(3):1727–1739, 2017.

[278] Stephen W. Provencher. A constrained regularization method for inverting data represented by linear algebraic or integral equations. *Computer Physics Communications*, 27(3):213–227, 1982.

[279] Alexey Sivokhin and Oleg A. Kazantsev. Temperature dependence of the Rayleigh ratio for toluene: Thermoresponsive polymers characterization. *ChemistrySelect*, 6(35):9499–9502, 2021.

[280] Jerome K. Percus and George J. Yevick. Analysis of classical statistical mechanics by means of collective coordinates. *Physical Review*, 110(1):1–13, 1958.

[281] Eleonora Russo and Carla Villa. Poloxamer hydrogels for biomedical applications. *Pharmaceutics*, 11(12):1–17, 2019.

[282] Almudena Naharros-Molinero, María Ángela Caballo-González, Francisco Javier de la Mata, and Sandra García-Gallego. Direct and reverse Pluronic micelles: Design and characterization of promising drug delivery nanosystems. *Pharmaceutics*, 14(12):1–25, 2022.

[283] Ivana Jarak, Carla L. Varela, Elisiário Tavares da Silva, Fernanda F.M. Roleira, Francisco Veiga, and Ana Figueiras. Pluronic-based nanovehicles: Recent advances in anticancer therapeutic applications. *European Journal of Medicinal Chemistry*, 206:112526, 2020.

[284] Jialin Yu, Huayu Qiu, Shouchun Yin, Hebin Wang, and Yang Li. Polymeric drug delivery system based on pluronics for cancer treatment. *Molecules*, 26(12):1–23, 2021.

[285] Karine Cappuccio de Castro, Julia Cedran Coco, Érica Mendes dos Santos, Janaína Artem Ataide, Renata Miliani Martinez, Mônica Helena Monteiro do Nascimento, João Prata, Pedro Ricardo Martins Lopes da Fonte, Patrícia Severino, Priscila Gava Mazzola, André Rolim Baby, Eliana Barbosa Souto, Daniele Ribeiro de Araujo, and André Moreni Lopes. Pluronic® triblock copolymer-based nanoformulations for cancer therapy: A 10-year overview. *Journal of Controlled Release*, 353:802–822, 2023.

[286] Payam Zarrintaj, Joshua D. Ramsey, Ali Samadi, Zhaleh Atoufi, Mohsen Khodadadi Yazdi, Mohammad Reza Ganjali, Leila Mohammadi Amirabad, Ehsan Zangene, Mehdi Farokhi, Krzysztof Formela, Mohammad Reza Saeb, Masoud Mozafari, and Sabu Thomas. Poloxamer: A versatile tri-block copolymer for biomedical applications. *Acta Biomaterialia*, 110:37–67, 2020.

[287] Y. L. Wu, R. Sprik, W. C.K. Poon, and E. Eiser. Effect of salt on the phase behaviour of F68 triblock PEO/PPO/PEO copolymer. *Journal of Physics Condensed Matter*, 18(19):4461–4470, 2006.

[288] Salvatore Costanzo, Alfonso Di Sarno, Marina D'Apuzzo, Pietro Renato Avallone, Ernesto Raccone, Annalisa Bellissimo, Finizia Auriemma, Nino Grizzuti, and Rossana Pasquino. Rheology and morphology of Pluronic F68 in water. *Physics of Fluids*, 33(4):043113, 2021.

[289] Jan Thoen. Thermal investigations of phase transitions in thermotropic liquid crystals. *International journal of modern physics B*, 9(18-19):2157–2218, 1995.

[290] F.A. Morrison. *Understanding rheology*. Oxford University Press, 1998.

[291] Wyn Brown, Karin Schilllen, Mats Almgren, Soeren Hvidt, and Pratap Bahadur. Micelle and gel formation in a poly(ethylene oxide)/poly(propylene oxide)/poly(ethylene oxide) triblock copolymer in water solution: dynamic and static light scattering and oscillatory shear measurements. *Journal of Physical Chemistry*, 95(4):1850–1858, 1991.

[292] Germán Pérez-Sánchez, Filipa A. Vicente, Nicolas Schaeffer, Inês S. Cardoso, Sónia P.M. Ventura, Miguel Jorge, and João A.P. Coutinho. Rationalizing the phase behavior of triblock copolymers through experiments and molecular simulations. *Journal of Physical Chemistry C*, 123(34):21224–21236, 2019.

[293] Kawthar Bouchemal, Florence Agnely, Armand Koffi, Madeleine Djabourov, and Gilles Ponchel. What can isothermal titration microcalorimetry experiments tell us about the self-organization of surfactants into micelles? *Journal of Molecular Recognition*, 23(4):335–342, 2010.

[294] Pankaj Singla, Shruti Chabba, and Rakesh Kumar Mahajan. A systematic physicochemical investigation on solubilization and in vitro release of poorly water soluble oxcarbazepine drug in pluronic micelles. *Colloids and Surfaces A: Physicochemical and Engineering Aspects*, 504:479–488, 2016.

[295] Julia F. Alopaeus, Ellen Hagesæther, and Ingunn Tho. Micellisation mechanism and behaviour of soluplus®–furosemide micelles: Preformulation studies of an oral nanocarrier-based system. *Pharmaceuticals*, 12(1):1–23, 2019.

[296] Pooja Prasanthan and Nand Kishore. Self-assemblies of Pluronic micelles in partitioning of anticancer drugs and effectiveness of this system towards target protein. *RSC Advances*, 11(36):22057–22069, 2021.

[297] Yoshihito David Saito, Shandiz Tehrani, Manko M. Okamoto, Henry H. Chang, and Phoebe Dea. Calorimetry studies of chlorpromazine hydrochloride in solution. *Langmuir*, 16(16):6391–6395, 2000.

[298] Watson Loh, César Brinatti, and Kam Chiu Tam. Use of isothermal titration calorimetry to study surfactant aggregation in colloidal systems. *Biochimica et Biophysica Acta - General Subjects*, 1860(5):999–1016, 2016.

[299] Niels Erik Olesen, René Holm, and Peter Westh. Determination of the aggregation number for micelles by isothermal titration calorimetry. *Thermochimica Acta*, 588:28–37, 2014.

[300] Yun Yan, Ludger Harnau, Nicolaas A.M. Besseling, Arie De Keizer, Matthias Ballauff, Sabine Rosenfeldt, and Martien A.Cohen Stuart. Spherocylindrical coacervate core micelles formed by a supramolecular coordination polymer and a diblock copolymer. *Soft Matter*, 4(11):2207–2212, 2008.

[301] Wolfgang Schärtl. *Light scattering from polymer solutions and nanoparticle dispersions*. Springer, 2007.

[302] Marc Lemmers, Ilja K. Voets, Martien A. Cohen Stuart, and Jasper Van Der Gucht. Transient network topology of interconnected polyelectrolyte complex micelles. *Soft Matter*, 7(4):1378–1389, 2011.

[303] Irvin M. Krieger and Thomas J. Dougherty. A Mechanism for non-Newtonian flow in suspensions of rigid spheres. *Transactions of the Society of Rheology*, 3:137–148, 1959.

[304] Joona Bang, Karthik Viswanathan, Timothy P. Lodge, Moon Jeong Park, and Kookheon Char. Temperature-dependent micellar structures in poly(styrene-b-isoprene) diblock copolymer solutions near the critical micelle temperature. *Journal of Chemical Physics*, 121(22):11489–11500, 2004.

[305] J. C. Castaing, C. Allain, P. Auroy, and L. Auvray. Rheology of nanosized hairy grain suspensions. *European Physical Journal B*, 10(1):61–70, 1999.

[306] Bo Nyström, Harald Walderhaug, and Finn Knut Hansen. Dynamic crossover effects observed in solutions of a hydrophobically associating water-soluble polymer. *Journal of Physical Chemistry*, 97(29):7743–7752, 1993.

[307] Harald Walderhaug, Finn Knut Hansen, Susanna Abrahmsén, Karin Persson, and Peter Stilbs. Associative thickeners. NMR self-diffusion and rheology studies of aqueous solutions of hydrophobically modified poly(oxyethylene) polymers. *Journal of Physical Chemistry*, 97(31):8336–8342, 1993.

[308] Tom Annable, Richard Buscall, Rammile Ettelaie, Philip Shepherd, and Diane Whittlestone. Influence of surfactants on the rheology of associating polymers in solution. *Langmuir*, 10(4):1060–1070, 1994.

[309] Abdel Azim A. Abdel-Azim, Aiman M. Atta, Medhat S. Farahat, and Wagdy Y. Boutros. Determination of intrinsic viscosity of polymeric compounds through a single specific viscosity measurement. *Polymer*, 39(26):6827–6833, 1998.

[310] Talib Omer Kashmola and Estabraq Saad Kamil. Structure rheology of polyethylene oxide solution. *Iraqi Journal of Chemical and Petroleum Engineering*, 15(1):23–32, 2014.

[311] Ralph H. Colby. Structure and linear viscoelasticity of flexible polymer solutions: Comparison of polyelectrolyte and neutral polymer solutions. *Rheologica Acta*, 49(5):425–442, 2010.

[312] Koblan Wilfried Ebagninin, Adel Benchabane, and Karim Bekkour. Rheological characterization of poly(ethylene oxide) solutions of different molecular weights. *Journal of Colloid and Interface Science*, 336(1):360–367, 2009.

[313] Ensong Zhang, Xueming Dai, Zhixin Dong, Xuepeng Qiu, and Xiangling Ji. Critical concentration and scaling exponents of one soluble polyimide - From dilute to semidilute entangled solutions. *Polymer*, 84:275–285, 2016.

[314] Richard Chudoba, Jan Heyda, and Joachim Dzubiella. Temperature-dependent implicit-solvent model of polyethylene glycol in aqueous solution. *Journal of Chemical Theory and Computation*, 13(12):6317–6327, 2017.

[315] Bryan Raubenolt, Gaurav Gyawali, Wenwen Tang, Katy S. Wong, and Steven W. Rick. Coarse-grained simulations of aqueous thermoresponsive polyethers. *Polymers*, 10(5):1–16, 2018.

[316] Jianing Liu, Hans Joachim Schöpe, and Thomas Palberg. An improved empirical relation to determine the particle number density of fluid-like ordered charge-stabilized suspensions. *Particle and Particle Systems Characterization*, 17(5-6):206–212, 2000.

[317] Xiaohan Zhang, Konstantinos Kyriakos, Maria Rikkou-Kalourkoti, Elina N. Kitiri, Costas S. Patrickios, and Christine M. Papadakis. Amphiphilic single and double networks: a small-angle X-ray scattering investigation. *Colloid and Polymer Science*, 294(6):1027–1036, 2016.

[318] J. L. Yarnell, M. J. Katz, R. G. Wenzel, and S. H. Koenig. Structure factor and radial distribution function for liquid argon at 85K. *Physical Review A*, 7(6):2130–2144, 1973.

[319] Loup Verlet and Jean Jacques Weis. Equilibrium theory of simple liquids. *Physical Review A*, 5(2):939–952, 1972.

[320] Jonas Riest, Thomas Eckert, Walter Richtering, and Gerhard Nägele. Dynamics of suspensions of hydrodynamically structured particles: Analytic theory and applications to experiments. *Soft Matter*, 11(14):2821–2843, 2015.

[321] Chenyang Liu, Jiasong He, Evelyne van Ruymbeke, Roland Keunings, and Christian Bailly. Evaluation of different methods for the determination of the plateau modulus and the entanglement molecular weight. *Polymer*, 47(13):4461–4479, 2006.

[322] L. C. Case. Branching in polymers. I. Network defects. *Journal of Polymer Science*, 45(146):397–404, 1960.

[323] Paulina J. Skrzeszewska, Frits A. De Wolf, Marc W.T. Werten, Antoine P.H.A. Moers, Martien A. Cohen Stuart, and Jasper Van Der Gucht. Physical gels of telechelic triblock copolymers with precisely defined junction multiplicity. *Soft Matter*, 5(10):2057–2062, 2009.

[324] Evelyne Van Ruymbeke and Dimitris Vlassopoulos. Macromolecular Rheology. In *Macromolecular Engineering*, pages 1–56. Wiley, 2022.

[325] Tingzi Yan, Klaus Schröter, Florian Herbst, Wolfgang H. Binder, and Thomas Thurn-Albrecht. What controls the structure and the linear and nonlinear rheological properties of dense, dynamic supramolecular polymer networks? *Macromolecules*, 50(7):2973–2985, 2017.

[326] Ana West and James T. Kindt. On the relationship between plateau modulus and shear relaxation time in transient networks. *Macromolecular Theory and Simulations*, 24(3):208–217, 2015.

[327] Kendra A. Erk and Jack F. Douglas. Stretched exponential stress relaxation in a thermally reversible, physically associating block copolymer solution. *Materials Research Society Symposium Proceedings*, 1418:1–8, 2012.

[328] Joachim Wuttke. Laplace-fourier transform of the stretched exponential function: Analytic error bounds, double exponential transform, and open-source implementation "libkww". *Algorithms*, 5(4):604–628, 2012.

[329] Rong Wang, Mike Geven, Pieter J. Dijkstra, Penny Martens, and Marcel Karperien. Hydrogels by supramolecular crosslinking of terpyridine end group functionalized 8-arm poly(ethylene glycol). *Soft Matter*, 10(37):7328–7336, 2014.

[330] Flanco Zhuge, Jérémy Brassinne, Charles André Fustin, Evelyne Van Ruymbeke, and Jean François Gohy. Synthesis and rheology of bulk metallo-supramolecular polymers from telechelic entangled precursors. *Macromolecules*, 50(13):5165–5175, 2017.

[331] Walther Burchard. Solution properties of branched macromolecules. *Advances in Polymer Science*, 143:114–194, 1999.

[332] Takuya Katashima. Rheological studies on polymer networks with static and dynamic crosslinks. *Polymer Journal*, 53(10):1073–1082, 2021.

[333] F. Di Lorenzo and S. Seiffert. Nanostructural heterogeneity in polymer networks and gels. *Polymer Chemistry*, 6(31):5515–5528, 2015.

[334] Sebastian Seiffert. Scattering perspectives on nanostructural inhomogeneity in polymer network gels. *Progress in Polymer Science*, 66:1–21, 2017.

[335] Takamasa Sakai, Takuro Matsunaga, Yuji Yamamoto, Chika Ito, Ryo Yoshida, Shigeki Suzuki, Nobuo Sasaki, Mitsuhiro Shibayama, and Ung-il Chung. Design and fabrication of a high-strength hydrogel with ideally homogeneous network structure from tetrahedron-like macromonomers. *Macromolecules*, 41:5379–5384, 2008.

[336] Hidemitsu Furukawa, Kazuyuki Horie, Ryunosuke Nozaki, and Mamoru Okada. Swelling-induced modulation of static and dynamic fluctuations in polyacrylamide gels observed by scanning microscopic light scattering. *Physical Review E*, 68:031406, 2003.

[337] Martha Franziska Koziol, Phuong Loan Nguyen, Shannon Gallo, Bradley D. Olsen, and Sebastian Seiffert. Hierarchy of relaxation times in supramolecular polymer model networks. *Physical Chemistry Chemical Physics*, 24(8):4859–4870, 2022.

[338] Shengchang Tang, Muzhou Wang, and Bradley D. Olsen. Anomalous self-diffusion and sticky Rouse dynamics in associative protein hydrogels. *Journal of the American Chemical Society*, 137(11):3946–3957, 2015.

[339] Shengchang Tang and Bradley D. Olsen. Relaxation processes in supramolecular metallogels based on histidine-nickel coordination bonds. *Macromolecules*, 49(23):9163–9175, 2016.

[340] Shengchang Tang, Axel Habicht, Shuaili Li, Sebastian Seiffert, and Bradley D. Olsen. Self-Diffusion of associating star-shaped polymers. *Macromolecules*, 49(15):5599–5608, 2016.

[341] Amir Jangizehi, S. Reza Ghaffarian, Willi Schmolke, and Sebastian Seiffert. Dominance of chain entanglement over transient sticking on chain dynamics in hydrogen-bonded supramolecular polymer networks in the melt. *Macromolecules*, 51(8):2859–2871, 2018.

[342] Alexander Patist, James R. Kanicky, Pavan K. Shukla, and Dinesh O. Shah. Importance of micellar kinetics in relation to technological processes. *Journal of Colloid and Interface Science*, 245(1):1–15, 2002.

[343] Paola Nicolella, Daniel Lauxen, Mostafa Ahmadi, and Sebastian Seiffert. Reversible hydrogels with switchable diffusive permeability. *Macromolecular Chemistry and Physics*, 222(16):1–8, 2021.

[344] Taiki Tominaga, Vijay R. Tirumala, Eric K. Lin, Jian Ping Gong, Hidemitsu Furukawa, Yoshihito Osada, and Wen li Wu. The molecular origin of enhanced

toughness in double-network hydrogels: A neutron scattering study. *Polymer*, 48(26):7449–7454, 2007.

Curriculum vitae

An-Sofie Huysecom, born on the 3rd of May 1994 in Leuven, Belgium, graduated high school focusing on Latin and mathematics at Heilige-Drievuldigsheidscollege in Leuven in 2012. Owing to her interest in STEM courses, she enrolled at KU Leuven to pursue a degree in Engineering Science. She obtained her bachelor's degree (magna cum laude) in 2015 with a major in Chemical Engineering and a minor in Living System's Technology and Materials Engineering. She then started her master studies in Chemical Engineering at KTH Royal Institute of Technology in Stockholm, Sweden, as part of a one semester exchange program, after which she continued her studies at KU Leuven. During her master studies, An-Sofie obtained hands-on experience in the chemical industry during engineering internships at BASF, Antwerp (Belgium) and SABIC, Geleen (The Netherlands). She graduated (summa cum laude) in 2017 with a major in Product Engineering and a master thesis entitled 'Developing conducting polymer blends by tuning their phase separated morphology and carbon nanotube network: Effect of compatibilization strategies', which was conducted in the Soft Matter, Rheology and Technology (SMaRT) division of the Department of Chemical Engineering under the supervision of Prof. dr. ir. Paula Moldenaers. For this research, she obtained the CIT-IAR master thesis award.

Afterwards, An-Sofie continued her collaboration with Prof. dr. ir. Paula Moldenaers as a PhD Researcher at SMaRT, co-supervised by Prof. dr. ir. Ruth Cardinaels. She fully exploited her passion for research during a 5-year PhD project about supramolecular single and double networks formed by hydrophobic association. In October 2018, she was granted a personal fellowship from Research Foundation Flanders (FWO), for her fundamental research on multi-dynamic polymer networks in collaboration with UCLouvain in Louvain-la-Neuve, Belgium. For her didactical contribution to the Department of Chemical Engineering, An-Sofie received the student award 'Gouden Krijtje' for best teaching assistant in 2019 and 2021. An-Sofie finalized her PhD thesis entitled 'Transient networks formed by hydrophobically associating multiblock copolymers' early 2023. After her PhD journey at SMaRT, An-Sofie started as a Scientist Poly(propylene) Products at SABIC in Geleen.

List of publications

Publications in international journals with peer review

Huysecom, A., Glorieux, C., Thoen, J., Thielemans, W., Fustin, C., Moldenaers, P., Cardinaels, R., Phase behavior of medium-length hydrophobically associating PEO-PPO multiblock copolymers in aqueous media. *Journal of Colloid and Interface Science*, 641:521-538, 2023, doi:10.1016/j.jcis.2023.03.013

Huysecom, A., Thielemans, W., Moldenaers, P., Cardinaels, R., A generalized mechano-statistical transient network model for unravelling the network topology and elasticity of hydrophobically associating multiblock copolymers in aqueous solutions, *Macromolecules*, 56(2):612-633, 2023, doi:10.1021/acs.macromol.2c01500

Houben, S., Aldana, A.A., **Huysecom, A.**, Mpinganzim, W., Cardinaels, R., Baker, M.B., Pitet, L.M., Hybrid hydrogels with orthogonal transient crosslinking exhibiting highly tunable mechanical properties. *ACS Applied Polymer Materials*, 5(3):1819-1827, 2023, doi:10.1021/acsapm.2c01906

Anand, R., Salar Amoli, M., **Huysecom, A.**, Amorim, P., Agten, H., Geris, L., Bloemen, V., A tunable gelatin-hyaluronan dialdehyde/methacryloyl gelatin interpenetrating polymer network hydrogel for additive tissue manufacturing. *Biomedical Materials*, 17(4):045027, 2022, doi:10.1088/1748-605X/ac78b8

Staffa, L. H., **Huysecom, A.**, Prado Bettini, S. H., Moldenaers, P., Chinelatto, M. A., Effect of molecular structure of PEG/PCL multiblock copolymers on the morphology and interfacial properties of PLA/PCL blends. *Journal of Polymer Research*, 29(9):388, 2022, doi:10.1007/s10965-022-03239-4

Hosseini, M.H., Javadi, A., **Huysecom, A.**, Schmit, P., Anderson, P.D., Cardinaels, R., Nazockdast, H., Double percolation of multi-walled carbon nanotubes (MWNTs) in poly(lactic acid)/poly(styrene-co-acrylonitrile) (PLA/SAN) co-continuous blends, *in preparation for submission (manuscript available)*

Bharati, A., **Huysecom, A.**, Van Der Donck, T., Kar, G.P., Bose, S., Seo, J.W., Wubbenhorst, M., Moldenaers, P., Cardinaels, R., Tuning the phase-separated morphology and carbon nanotube network in bi-phasic polymer blends of PαMSAN and PMMA: effect of novel compatibilizers on electrical properties, *in preparation for submission (manuscript available)*

Cover pages in international journals

Huysecom, A., Thielemans, W., Moldenaers, P., Cardinaels, R., A generalized mechano-statistical transient network model for unravelling the network topology and elasticity of hydrophobically associating multiblock copolymers in aqueous solutions, *Macromolecules*, 56(2), 2023 (front cover)

Abstracts presented at international conferences and symposia (first author contributions only)

Huysecom, A., Thielemans, W., Cardinaels, R., Moldenaers, P., A generalized mechano-statistical transient network model to unravel the network topology, elasticity and relaxation dynamics of associative multiblock copolymer solutions. *Society of Rheology annual meeting*, Chicago (United States of America), October 2022.

Huysecom, A., Thielemans, W., Cardinaels, R., Moldenaers, P., Network topology, elasticity and dynamics of transient networks formed by hydrophobically associating multiblock copolymers in aqueous solutions. *Rheology in Action, Joint Symposium of the Dutch Society of Rheology and the Belgian Group of Rheology*, Leuven (Belgium), July 2022.

Huysecom, A., Thielemans, W., Cardinaels, R., Moldenaers, P., Transient networks of hydrophobically associating multiblock copolymers in aqueous solutions: micellar network topology, elasticity and relaxation dynamics. *EPF European Polymer Congress*, Prague (Czech Republic), June 2022.

Huysecom, A., Thielemans, W., Moldenaers, P., Cardinaels, R., Unravelling the network topology and elasticity of hydrophobically associating multiblock copolymers in aqueous solutions using a novel mechano-statistical transient network model. *Annual European Conference on Rheology*, Sevilla (Spain), April 2022.

Huysecom, A., Thielemans, W., Cardinaels, R., Moldenaers, P., Unravelling the transient network topology of hydrophobically associating multiblock copolymers and their resulting elasticity and relaxation times. *Society of Rheology annual meeting* (online), October 2021.

Huysecom, A., Thielemans, W., Cardinaels, R., Moldenaers, P., Unravelling the transient network topology of hydrophobically associating multiblock copolymers. *SoftComp annual meeting* (online), May 2021.

Huysecom, A., Van Ruymbeke, E., Fustin, C. -A., Cardinaels, R., Moldenaers, P., Rheological insights in the behavior of supramolecular double networks - the synergy investigated? *SoftComp annual meeting*, Portonovo (Italy), October 2019.

Huysecom, A., Bharati, A., Cardinaels, R., Moldenaers, P., Predicting the localization and interconnectivity of carbon nanotubes in compatibilized bi-phasic polymer blends. *10th Conference on Broadband Dielectric Spectroscopy and its Applications*, Brussels (Belgium), August 2018.

Huysecom, A., Bharati, A., Cardinaels, R., Moldenaers, P., Uniquely developing tunable morphologies and carbon nanotube localization in bi-phasic polymer blends by compatibilizer grafting. *SoftComp annual meeting*, Primosten (Croatia), May 2018.

Huysecom, A., Bharati, A., Cardinaels, R., Moldenaers, P., Inducing electrical conductivity by tuning the phase-separated morphology and carbon nanotube network in bi-phasic polymer blends with free and grafted (co)polymers. *Rheology - 360° Joint Symposium of the Belgian Group of Rheology and the German Rheological Society*, Luxembourg (Luxembourg), March 2018.

FACULTY OF ENGINEERING SCIENCE
DEPARTMENT OF CHEMICAL ENGINEERING
SOFT MATTER, RHEOLOGY AND TECHNOLOGY
Celestijnenlaan 200J box 2424
B-3001 Leuven
ansofie.huysecom@kuleuven.be
https://cit.kuleuven.be/smart